



Virginia Commonwealth University
VCU Scholars Compass

Theses and Dissertations


Graduate School

2020

Peridynamic Approaches for Damage Prediction in Carbon Fiber and Carbon Nanotube Yarn Reinforced Polymer Composites

Forrest E. Baber
Virginia Commonwealth University

Follow this and additional works at: <https://scholarscompass.vcu.edu/etd>

 Part of the [Applied Mechanics Commons](#), [Computer-Aided Engineering and Design Commons](#), and the [Structures and Materials Commons](#)

© The Author

Downloaded from

<https://scholarscompass.vcu.edu/etd/6209>

This Dissertation is brought to you for free and open access by the Graduate School at VCU Scholars Compass. It has been accepted for inclusion in Theses and Dissertations by an authorized administrator of VCU Scholars Compass. For more information, please contact libcompass@vcu.edu.

VIRGINIA COMMONWEALTH UNIVERSITY

COLLEGE OF ENGINEERING

Dissertation

**PERIDYNAMIC APPROACHES FOR DAMAGE PREDICTION IN
CARBON FIBER AND CARBON NANOTUBE YARN
REINFORCED POLYMER COMPOSITES**

by

FORREST BABER

B.S., Virginia Commonwealth University, 2015

A dissertation submitted in partial fulfillment of the
requirements for the degree of Doctor of Philosophy
at Virginia Commonwealth University.

May 2020

© May 2020 by
FORREST BABER
All rights reserved

Approved by

First Reader

Ibrahim Guven, PhD
Virginia Commonwealth University

Second Reader

Padmasiri Vipul Ranatunga, PhD
Air Force Research Laboratory

Third Reader

Stewart Silling, PhD
Sandia National Laboratory

Fourth Reader

John Speich, PhD
Virginia Commonwealth University

Fifth Reader

Karla Mossi, PhD
Virginia Commonwealth University

Acknowledgments

First, I would like to thank my family and friends for all of their support and encouragement over the years, and a special thanks to Collette Ward for her unwavering support throughout my PhD journey.

I would also like to acknowledge all of my lab mates for their discussions and insights on my research. In particular, Riley and Rachel for their significant help debugging and troubleshooting EMU, Susie for her expertly developed graphics, and Kyle for our machine learning discussions.

I am very thankful to have had constant support from my advisor, Dr. Ibrahim Guven. Not only has he helped propel the research, but I am thankful for the opportunities he provided and the personal growth he spurred by encouraging the presentation my work at conferences over the years. Finally, I would like to thank the US-COMP institute, The Boeing Company, and the Air Force Research Laboratory for providing funding and support of this project. These organizations not only provided financial support, but they helped significantly in fostering my growth as an engineer.

**PERIDYNAMIC APPROACHES FOR DAMAGE PREDICTION IN
CARBON FIBER AND CARBON NANOTUBE YARN
REINFORCED POLYMER COMPOSITES**

FORREST BABER

Virginia Commonwealth University, College of Engineering, May 2020

Chairperson: Ibrahim Guven, PhD

Assistant Professor, Department of Mechanical and
Nuclear Engineering, VCU

ABSTRACT

Aerospace structures are increasingly utilizing advanced composites because of their high specific modulus and specific strength. While the introduction of these material systems can dramatically decrease weight, they pose unique certification challenges, often requiring extensive experimental testing in each stage of the design cycle. The expensive and time-consuming nature of experimental testing necessitates the advancement of simulation methodologies to both aid in the certification process and assist in the exploration of the microstructure design space.

Peridynamic (PD) theory, originating from Sandia National Labs in the early 2000s, is a nonlocal continuum-based method that reformulates the equation of motion into an integral equivalent form. The integral form, on which the theory is based, is well suited to explore discontinuity rich phenomena such as damage and material failure.

This dissertation develops PD-based simulation approaches to investigate two polymer based composite material systems of different maturity: carbon fiber and carbon nanotube (CNT) yarn. For carbon fiber reinforced composites, simulation approaches were developed to predict damage resulting from low-velocity impact, an important part of the certifi-

cation process because often damage associated with this loading goes undetected leading to premature structural failure. In contrast to the more established carbon fiber, CNT yarn is a promising constituent material still very much in the developmental process. With this in mind, PD simulation approaches were developed with a different objective, which was to systematically explore microstructure property relationships, providing early feedback in the material design process.

Contents

1	Introduction	1
1.1	Motivation	1
1.2	Failure Mechanisms of Polymer Matrix Composites	3
1.3	Introduction to Peridynamics	5
1.4	Research Objectives	13
1.5	Outline	14
1.6	Unique Contributions	15
2	Carbon Fiber Reinforced Composites	17
2.1	Peridynamic Approach for Laminated Composites	20
2.2	Objective Approach for Determining PD Material Parameters	30
2.2.1	2D Isotropic Scenario	32
2.2.2	Intralaminar Fiber and Matrix Bonds	34
2.2.3	Intralaminar Shear Nonlinearity	42
2.2.4	Interlaminar Constitutive Response	45
2.2.5	PD Strength Parameters	48
2.3	Quasi-Static Off-Axis Tension Simulation Results	54
2.4	Strain Rate Dependence	65
2.4.1	Dynamic Off-Axis Tension Simulation Results	67
2.5	Low-Velocity Impact Simulation Results	83
2.5.1	Problem Description	83
2.5.2	Simulation Approach Improvement Summary	85
2.5.3	Simulation Results	90

2.5.4	Increasing Impact Energy	126
2.5.5	Decreasing Longitudinal Strength	128
2.5.6	Comparing Increased Energy with Decreasing Longitudinal Strength	134
2.6	Hat-Stiffened Panel Impact Simulation Results	138
2.7	Through-Thickness Reinforcement Simulation Results	143
2.7.1	Considerations for Through-Thickness Reinforcement	143
2.7.2	Through-Thickness Reinforcement Simulation Results	145
3	CNT Yarn Reinforced Polymer Composites	151
3.1	Background	151
3.2	Experimental Work	153
3.3	Microstructure Characterization	156
3.3.1	X-ray CT Imaging	156
3.3.2	Thresholding Process	156
3.3.3	Manipulation of the Grid Spacing	158
3.3.4	Characterization of Segmented X-ray CT Data	161
3.4	Peridynamic Modeling Approach	171
3.4.1	Bond Types	171
3.4.2	Off-Axis Modulus Function	173
3.4.3	PD Material Constants	175
3.4.4	Simulation Procedure	181
3.4.5	PD Simulation Results	181
3.5	Synthetic Microstructure Reconstruction	190
4	Conclusions and Future Work	203

List of Tables

1.1	Categorization of peridynamic types based upon force state vectors.	9
2.1	Intralaminar material interactions considered in the PD laminated composite model.	23
2.2	Example of the number of bond types for fiber and matrix material points.	30
2.3	Comparison of analytical and numerical bond constants given the engineering constants.	34
2.4	Correspondence between CCM and PD RO parameters.	43
2.5	Spring constants as functions of intralaminar grid spacing.	56
2.6	Example of the calculated fiber bond and matrix bond constants when the intralaminar grid spacing is held constant, but the horizon is changed.	59
2.7	PD material parameters for shear nonlinearity.	61
2.8	Comparison of strain rate and PD simulation parameters.	72
2.9	Ramberg-Osgood parameters for the material system as a function of strain rate calculated using the numerical approach.	78
2.10	Discretization related parameters for off-axis dynamic validation.	78
2.11	PD discretization parameters used for low-velocity impact simulations.	84
2.12	Calculated PD material parameters utilizing the numerical approach.	84
2.13	Calculated PD RO material parameters at various strain rates.	84
2.14	Failure parameters input in the PD model.	85
2.15	Quantitative comparison of experiments and PD simulations at all energy levels.	122
2.16	Summary of decrease in longitudinal strength.	129
2.17	Approximate stitched geometric parameters.	147

2.18	Normal and shear bond stitched material parameters.	147
3.1	Material properties of CNT yarn polymer composite. ^a As reported by the manufacturer.	154
3.2	Number of material points extracted from BMP images with changing grid spacing.	159
3.3	Relationship between material association, alignment, and behavior for various bonds.	172
3.4	Incorporation of clusters into the model	194
3.5	Summary of simulations performed to explore the structure.	197

List of Figures

1-1	Summary of primary failure mechanisms: (a) fiber crushing, (b) fiber breakage, (c) delamination, (d) fiber bridging, (e) matrix cracking [4, 13, 14].	4
1-2	Failure mechanisms associated with low-velocity impact of CFRP composites [12].	5
1-3	Pairwise response function reproduced from [34].	10
1-4	Potential constitutive relationships.	11
1-5	Schematic example showing the relation between damage and crack formation [22].	13
2-1	Explicit representation of fiber (dark) and matrix (light) regions for various fiber orientations.	21
2-2	Bond types associated with a fiber material point.	23
2-3	Bond types associated with a matrix material point.	24
2-4	Schematic demonstrating the shear bond kinematics with an undeformed (left) and deformed (right) configurations.	25
2-5	Isolated view of shear bond kinematics and associated shear angles.	26
2-6	Schematic illustration of surface correction factors reproduced from [22].	27
2-7	Local and global coordinate systems for surface correction factors.	29
2-8	Typical example of a 2D isotropic family of material point i	32
2-9	(a) Matrix material point and family under transverse loading. (b) Fiber material point and family under transverse loading.	36
2-10	(a) Matrix material point and family loaded in fiber direction. (b) Fiber material point and family loaded in fiber direction.	40
2-11	PD lamina material constant calculation summary.	42

2-12	Steps of the numerical approach for nonlinear constitutive relationships using an optimization-based approach.	44
2-13	Example of an interlaminar shear bond (Red) and material points involved in determining the shear angle.	46
2-14	Visualization of energy-based failure criterion for a matrix material point. An intralaminar matrix family is shown with colors representing different calculated matrix critical stretch. Importantly, each PD bond despite having different critical stretch values, has the same critical bond energy.	50
2-15	Schematic showing shear nonlinearity energy density factor calculation.	53
2-16	Lamina geometry and boundary regions used in verification.	55
2-17	An example of utilizing PD load steps (orange) to simulate a stress vs. strain curve.	56
2-18	Comparison of intralaminar refinement with colors representing fiber and matrix material regions.	57
2-19	Comparison of PD and experimental stress vs. strain curve for (a) 0° oriented fiber and (b) 90° oriented fiber.	58
2-20	Matrix and fiber material points families with a horizon of (a) $3.015 \times \Delta x$ (top row), and (b) $1.90 \times \Delta x$ (bottom row).	59
2-21	Comparison of PD and experimental stress vs. strain curve for two horizon values for (a) 0° oriented fiber and (b) 90° oriented fiber.	60
2-22	Linear (dashed line), Ramberg-Osgood (square symbols), and hyperbolic (circle symbols) constitutive relationships PD results compared against experimental (solid line) stress vs. strain curve for 5 fiber orientations.	63
2-23	Comparison of PD and experimental 8-ply laminate stress vs. strain curves for (a) 0° oriented fiber and (b) 90° oriented fiber.	64

2-24	Linear (dashed line), Ramberg-Osgood (square symbols), and hyperbolic (circle symbols) constitutive relationships PD results compared against experimental (solid line) stress vs. strain curve for 45° fiber orientation and 8-ply laminate.	65
2-25	An example of subdomains on a 3-ply laminate.	66
2-26	Flow chart for introducing strain rate dependence into the PD model.	68
2-27	Displacement field associated with a 370 /s strain rate case.	69
2-28	Verification of the applied strain rate methodology with the strain rate calculated from displacement field over each iteration.	70
2-29	(a) Example rectangular simulation domain and a chosen material point (red). (b) Individual bonds of the chosen material point colored by strain rate magnitude.	71
2-30	Example of strain rate variation vs. iteration for a 370/s input strain rate.	73
2-31	Schematic demonstrating the bond angles present with a uniform intralaminar grid spacing.	74
2-32	Strain rate as a function of bond orientation.	74
2-33	Comparison of individual bond orientation strain rate and the average strain rate of all bonds.	75
2-34	Comparison of strain rate vs. iteration for two different intralaminar discretizations.	76
2-35	Strain rate dependent constitutive response for a composite laminate.	77
2-36	Comparison of PD stress vs. strain predictions and experimental stress vs. strain response for a) 370 /s b) 0.8 /s and c) 0.0001 /s strain rates.	79
2-37	PD simulations with strain rates in-between the known experimental Ramberg-Osgood parameters.	80
2-38	Schematic with stretch rate subdomains.	81
2-39	Comparison of the local strain rate on each subdomain “D” vs. iteration.	82

2-40	Comparison of stress vs. strain response for 1 stretch rate domain (blue) vs. 5 stretch rate subdomains (red).	82
2-41	Quasi-static tests used for PD material parameter calibration. 1.) longitudinal tension (fiber bond material parameter), 2) transverse tension (matrix bond material parameter), 3.) interlaminar shear (interlaminar shear bond material parameter), 4.) interlaminar normal (interlaminar normal bond material parameter)	86
2-42	Force vs. time response predicted by legacy PD approach (PD01) compared against experimental measurements for 225 in-lbf impact energy.	87
2-43	Force vs. displacement response predicted by legacy PD approach (PD01) compared against experimental measurements for 225 in-lbf impact energy.	87
2-44	Force vs. time response predicted by objective baseline PD approach (PD02) compared against experimental measurements for 225 in-lbf impact energy.	88
2-45	Force vs. displacement response predicted by objective baseline PD approach (PD02) compared against experimental measurements for 225 in-lbf impact energy.	89
2-46	Force vs. time response predicted by objective baseline PD with shear nonlinearity approach (PD03) compared against experimental measurements for 225 in-lbf impact energy.	90
2-47	Force vs. displacement response predicted by objective baseline PD with shear nonlinearity approach (PD03) compared against experimental measurements for 225 in-lbf impact energy.	90
2-48	Force vs. time response predicted by objective baseline PD with shear nonlinearity and strain rate dependent material properties approach (PD04) compared against experimental measurements for 150 in-lbf impact energy.	91

2-49	Force vs. time response predicted by objective baseline PD with shear nonlinearity and strain rate dependent material properties approach (PD04) compared against experimental measurements for 187.5 in-lbf impact energy.	92
2-50	Force vs. time response predicted by objective baseline PD with shear nonlinearity and strain rate dependent material properties approach (PD04) compared against experimental measurements for 225 in-lbf impact energy.	92
2-51	Force vs. time response predicted by objective baseline PD with shear nonlinearity and strain rate dependent material properties approach (PD04) compared against experimental measurements for 262.5 in-lbf impact energy.	93
2-52	Force vs. displacement response predicted by objective baseline PD with shear nonlinearity and strain rate dependent material properties approach (PD04) compared against experimental measurements for 150 in-lbf impact energy.	94
2-53	Force vs. displacement response predicted by objective baseline PD with shear nonlinearity and strain rate dependent material properties approach (PD04) compared against experimental measurements for 187.5 in-lbf impact energy.	95
2-54	Force vs. displacement response predicted by objective baseline PD with shear nonlinearity and strain rate dependent material properties approach (PD04) compared against experimental measurements for 225 in-lbf impact energy.	95
2-55	Force vs. displacement response predicted by objective baseline PD with shear nonlinearity and strain rate dependent material properties approach (PD04) compared against experimental measurements for 262.5 in-lbf impact energy.	96

2-56	Energy vs. time response predicted by objective baseline PD with shear nonlinearity and strain rate dependent material properties approach (PD04) compared against experimental measurements for 150 in-lbf impact energy. .	97
2-57	Energy vs. time response predicted by objective baseline PD with shear nonlinearity and strain rate dependent material properties approach (PD04) compared against experimental measurements for 187.5 in-lbf impact energy. .	98
2-58	Energy vs. time response predicted by objective baseline PD with shear nonlinearity and strain rate dependent material properties approach (PD04) compared against experimental measurements for 225 in-lbf impact energy. .	98
2-59	Energy vs. time response predicted by objective baseline PD with shear nonlinearity and strain rate dependent material properties approach (PD04) compared against experimental measurements for 262.5 in-lbf impact energy. .	99
2-60	Experimental c-scan results for each energy level: (a) 150 in-lbf, (b) 187.5 in-lbf, (c) 225 in-lbf, and (d) 262.5 in-lbf.	100
2-61	Laminate back face for (a) 225 in-lbf energy and (b) 262.5 in-lbf energy. . .	101
2-62	Delamination (color variation indicates ply depth from impact side) predicted by PD04 approach compared against experimental measurements (outline overlaid) for 150 in-lbf impact energy.	103
2-63	Delamination (color variation indicates ply depth from impact side) predicted by PD04 approach compared against experimental measurements (outline overlaid) for 187.5 in-lbf impact energy.	104
2-64	Delamination (color variation indicates ply depth from impact side) predicted by PD04 approach compared against experimental measurements (outline overlaid) for 225 in-lbf impact energy.	105
2-65	Delamination (color variation indicates ply depth from impact side) predicted by PD04 approach compared against experimental measurements (outline overlaid) for 262.5 in-lbf impact energy.	106

2-66	Ply-by-ply total damage predicted by PD04 approach for 150 in-lbf impact energy.	108
2-67	Ply-by-ply total damage predicted by PD04 approach for 187.5 in-lbf impact energy.	109
2-68	Ply-by-ply total damage predicted by PD04 approach for 225 in-lbf impact energy.	110
2-69	Ply-by-ply total damage predicted by PD04 approach for 262.5 in-lbf impact energy.	111
2-70	Ply-by-ply fiber damage predicted by PD04 approach for 150 in-lbf impact energy.	112
2-71	Ply-by-ply fiber damage predicted by PD04 approach for 187.5 in-lbf impact energy.	113
2-72	Ply-by-ply fiber damage predicted by PD04 approach for 225 in-lbf impact energy.	114
2-73	Ply-by-ply fiber damage predicted by PD04 approach for 262.5 in-lbf impact energy.	115
2-74	Ply-by-ply interlaminar damage predicted by PD04 approach for 150 in-lbf impact energy.	116
2-75	Ply-by-ply interlaminar damage predicted by PD04 approach for 187.5 in-lbf impact energy.	117
2-76	Ply-by-ply interlaminar damage predicted by PD04 approach for 225 in-lbf impact energy.	118
2-77	Ply-by-ply interlaminar damage predicted by PD04 approach for 262.5 in-lbf impact energy.	119
2-78	(a) Comparison of force response and delaminated area over time for 262.5 in-lbf impact energy (b) fiber damage footprint at selected times (c) interlaminar damage footprint at selected times.	120

2-79	Ply-by-ply views of (a) fiber damage before event (b) fiber damage after event (c) interlaminar damage before event (d) interlaminar damage after event.	121
2-80	Quantitative comparison between PD (blue) and experimental (black) peak force (lbf) for each energy level.	123
2-81	Quantitative comparison between PD (blue) and experimental (black) peak displacement (in) for each energy level.	123
2-82	Quantitative comparison between PD (blue) and experimental (black) delaminated area (in ²) for each energy level.	124
2-83	Quantitative comparison between PD (blue) and experimental (black) absorbed energy (in-lbf) for each energy level.	125
2-84	Force vs. time response prediction for 282.42 (red) in-lbf impact energy compared against experimental 262.5 (black) in-lbf and the PD prediction for 262.5 (blue) in-lbf.	126
2-85	Force vs. displacement response prediction for 282.42 (red) in-lbf impact energy compared against experimental 262.5 (black) in-lbf and the PD prediction for 262.5 (blue) in-lbf.	127
2-86	Energy vs. time response prediction for 282.42 (red) in-lbf impact energy compared against experimental 262.5 (black) in-lbf and the PD prediction for 262.5 (blue) in-lbf.	128
2-87	Delamination (color variation indicates ply depth from impact side and black indicates fiber failure) prediction at 262.5 in-lbf compared against prediction for 282.42 in-lbf impact energy.	128
2-88	Force vs. time response predicted with 15% (green) less, 10 % (red) less, and original longitudinal strength (blue) compared against experimental measurements for 262.5 in-lbf impact energy.	130

2-89	Displacement vs. time response predicted with 15% (green) less, 10 % (red) less, and original longitudinal strength (blue) compared against experimental measurements for 262.5 in-lbf impact energy.	131
2-90	Energy vs. time response predicted with 15% (green) less, 10 % (red) less, and original longitudinal strength (blue) compared against experimental measurements for 262.5 in-lbf impact energy.	131
2-91	Delamination predicted with the original longitudinal strength (a) and with the 10% less longitudinal strength (b).	132
2-92	Force vs. time comparison of decreasing longitudinal strength at 225 in-lbf. .	132
2-93	Force vs. displacement comparison of decreasing longitudinal strength at 225 in-lbf.	133
2-94	Energy vs. time comparison of decreasing longitudinal strength at 225 in-lbf.	133
2-95	Energy vs. time response predicted with energy 282.4 in-lbf (green), 10 % (red) less longitudinal strength, and original longitudinal strength (blue) compared against experimental measurements for 262.5 in-lbf impact energy.	134
2-96	Delamination predicted with the original longitudinal strength (a) and with the 10% less longitudinal strength (b).	135
2-97	Fiber damage associated with a 10% decrease in longitudinal strength. . . .	136
2-98	Fiber damage associated with an impact energy of 282.42 in-lbf.	137
2-99	Hat-stiffened panel geometry.	138
2-100	Hat-stiffened cross-section geometry.	138
2-101	Discretized hat-stiffened panel with the hat-stiffener (red) and laminate (blue).	139
2-102	PD hat-stiffener cross-section discretization.	139
2-103	Force (lbf) vs. time (s) prediction for the hat-stiffened panel.	140
2-104	Force (lbf) vs. displacement (in) prediction for the hat-stiffened panel. . . .	141
2-105	Energy (in-lbf) vs. time (s) prediction for the hat-stiffened panel.	141
2-106	Z-displacement contours of the hat-stiffened panel.	142
2-107	PD damage prediction in the hat-stiffened panel.	142

2-108	Schematic demonstrating the stitched bond approach.	143
2-109	Example of a stitched pattern and the identified stitched PD material points (red) shown from a top view.	144
2-110	Flow chart for introducing through-thickness reinforcements.	145
2-111	Stitch schematic showing the dimensions of the stitched frame with respect to the laminate.	146
2-112	Force (lbf) vs. displacement (in) response for the stitch material.	147
2-113	Converted stress (ksi) vs. strain (%) response of the stitched material.	148
2-114	Comparison of stitch reinforced and unreinforced simulations at 225 in-lbf.	148
2-115	Force (lbf) vs. displacement (in) curve comparing a stitched laminate simulation with an unreinforced laminate simulation.	149
2-116	Energy (in-lbf) vs. time (s) curve comparing stitched and unreinforced PD simulations.	150
2-117	Comparison of stacked delamination between the two stitched scenarios.	150
3-1	(a) Custom-made aluminum fixture and (b) unidirectional CNT yarn/cyanate ester composite.	154
3-2	Experimentally obtained representative stress vs. strain curve.	155
3-3	Fully failed CNT yarn composite specimen.	155
3-4	Cross-sectional x-ray CT BMP image of a unidirectional CNT yarn polymer composite.	156
3-5	Comparison of BMP image and PD simulation grid after the thresholding process.	157
3-6	Example of determining constituent materials by means of a secondary threshold.	158
3-7	Comparison of differing levels of refinement. Notation on the left side of the image indicates grid spacing.	159

3-8	(a) BMP image containing yarn, resin, and void pixels. (b) A 2D PD slice of the composite specimen with yarn (blue) and resin (red) material points. (c) Stack of 11 different 2D PD slices with an exaggerated spacing in the x-direction. (d) A fully reconstructed section of the composite specimen.	160
3-9	Partitioning of x-ray CT into four distinct cells of high resolution.	162
3-10	A comparison of the number of material points in each cell.	163
3-11	A comparison of the average thickness of each cell.	164
3-12	Visualization of the two different methods used for approximating the thickness of each BMP slice.	164
3-13	A comparison of the volume fraction of each cell.	165
3-14	Visualization of the surface undulation colored by z-coordinate position.	166
3-15	Approximating the undulation of the surface.	167
3-16	Visualization of void fraction on a slice.	168
3-17	A comparison of the void fraction of each cell.	168
3-18	Visualization of yarn, resin, and void material on a slice.	170
3-19	The resulting clusters identified by application of first the K-nearest then the DBSCAN algorithm to detect shape, size, and quantity of resin clusters of the microstructure.	170
3-20	Schematic showing the possible bond types.	173
3-21	Schematic representation of the constitutive relationships.	174
3-22	Flow chart for obtaining elastic constants.	179
3-23	Variation in yarn material constant.	180
3-24	Variation in matrix material constant.	180
3-25	Demonstration of load steps.	182
3-26	Peridynamic stress-strain % curves.	183
3-27	Damage contours at the failure strain of each cell at various orientations.	184
3-28	Damage overlay in different YZ planes for cell 1.	185
3-29	Damage initiation for cell 1 at different YZ planes.	186

3-30	Damage initiation for cell 2 at different YZ planes.	187
3-31	Damage initiation for cell 3 at different YZ planes.	188
3-32	Damage initiation for cell 4 at different YZ planes.	189
3-33	Example of PDF generation and comparison with sampled statistics for synthetic reconstruction.	191
3-34	Probability density functions for each microstructural descriptor.	192
3-35	PD grid development using PDFs.	192
3-36	Synthetic reconstruction process.	193
3-37	Demonstration of cluster implementation.	195
3-38	Comparison of the original PDFs (A) and modified PDFs (B).	196
3-39	Visualization of PDF modification and the resulting microstructure on a 2D slice.	197
3-40	Visualization of microstructure descriptors for each simulation scenario.	198
3-41	Visualization of microstructure modifications on 2D PD slices.	200
3-42	Overview of the final damage contours for each microstructure scenario.	201
3-43	Stress vs. strain curves for each simulation scenario compared against the original PDFs (scenario A).	202

List of Abbreviations

BMP	Bitmap
BVID	Barely Visible Impact Damage
CCM	Classical Continuum Mechanics
CFRP	Carbon Fiber Reinforced Polymer
CLT	Classical Laminate Theory
CNT	Carbon Nanotube
CT	Computed Tomography
DBSCAN	Density Based Spatial Clustering of Applications with Noise
EXP	Experimental
FE	Finite Element
FEA	Finite Element Analysis
FEM	Finite Element Method
LVI	Low-Velocity Impact
PD	Peridynamics
PDF	Probability Density Function
PDFA	Progress Damage and Failure Analysis
PMC	Polymer Matrix Composite
RO	Ramberg-Osgood
SE	Strain Energy
SED	Strain Energy Density
SEM	Scanning Electron Microscope
PDF	Probability Distribution Function
V&V	Verification and Validation
VID	Visible Impact Damage

Chapter 1

Introduction

1.1 Motivation

Polymer matrix composites (PMCs) have several significant advantages compared to other material systems. One important benefit is their high stiffness and strength to weight ratios [1–3]. For aerospace and other applications in which weight is of supreme importance [2], PMC utilization has dramatically increased over the years. However, the weight advantage of PMCs comes at a cost with the primary disadvantages being low fracture toughness, expensive fabrication, and difficult repair [1].

The low fracture toughness of PMCs is particularly challenging in industries, such as aerospace, where brittle abrupt fracture can have devastating and life-altering consequences. As a result, large safety factors and design cautions are required. While advanced and automated manufacturing is consistently lowering the fabrication cost [3], creating parts of complex geometry is still time intensive and extremely costly [1]. Finally, because the initial detection of failure in composite materials is difficult [4], flaws in composite structures may go unnoticed, making repair of the part challenging [1]. Despite these challenges, the weight advantage has made it an increasingly popular design choice, with several recently built aircraft having greater than 50% weight composite material [3]. There is great potential for PMCs, especially if some of these challenges can be addressed and mitigated.

While there are many different types of reinforcing materials used in PMCs, this dissertation will focus on two: carbon fiber and carbon nanotube (CNT) yarn. Carbon fiber reinforced polymer matrix (CFRP) composites have been around for decades and were

first used in aerospace structures in the early 1960s [3]. Over this time, the manufacturing process has greatly improved, the cost of production has dropped, and the properties of the carbon fibers themselves have gotten better [3]. Despite their long existence, CFRPs continue to pose unique challenges from a computational perspective. They are highly anisotropic, heterogeneous, and as a result, have complex failure mechanisms. These difficulties exist in all length scales of the material, from interactions at the atomic scale, all the way to the stacking sequence at the macroscale.

Compared to carbon fiber, CNT yarn is still in the early stages of the material life cycle. Carbon nanotubes offer an even higher tensile modulus and strength [5] than traditional fiber. This significantly magnifies the weight advantage. While CNTs have the potential to become a part of the next generation of composite material, there are difficulties translating the material properties from the nanoscale to the macroscale. Recently developed CNT yarn, a macro-assemblage of CNTs, is commonly viewed as a path for transitioning to these larger scales [6]. Similar to carbon fiber, the CNT yarn has a complex hierarchical structure with a wide range of failure mechanisms. To fully realize its potential, a better understanding of these mechanisms is needed.

This dissertation is focused on developing computational-based simulation approaches that are complementary to experimental methods. When computational methods are used in tandem with experiments, a more fundamental understanding of the material systems can be obtained. Computational methods provide the means to investigate various loading conditions and part designs in short succession. They can inspire experimental work and help guide an experiment towards a new understanding. Well-verified and validated simulation approaches ultimately lower costs and improve resource allocation. A major focus of this work is on predicting failure mechanisms of both carbon fiber and CNT yarn reinforced PMCs. New computational methodologies allow for the exploration of material interaction across length scales, will aid in the future designs of experimental testing, and allow for a more fundamental understanding of damage development.

1.2 Failure Mechanisms of Polymer Matrix Composites

The failure mechanisms of PMCs can often be difficult to parse and identify because they have abrupt and catastrophic failure [7], which makes a post-mortem identification of root causes difficult. However, in recent years, new techniques have been developed for in-situ monitoring of the composite under a variety of loading conditions [4], elucidating the damage mechanisms involved. Failure mechanisms of PMCs can be broadly classified by their loading type, material origins, and location within the composite.

In CFRP composites, fiber failure can occur via two different mechanisms: fiber breakage and fiber crushing/kinking. Because fibers are the primary load-carrying constituent material, this type of failure is extremely detrimental to the composite's performance [4]. Fiber breakage occurs in tension and results in the fiber being split into two separate pieces. Because there is a distribution of fiber diameters and ultimate strengths, not all fibers break at the same load level [4]. The second fiber-related mechanism, fiber crushing, arises from a compressive loading component in the direction of the fiber. This mechanism is generally considered to be a multi-step process in which defects in the microstructure, such as fiber waviness [7, 8] and misorientations of the fiber with respect to the compressive load, result in fiber kinking and ultimately fiber crushing [4, 7].

A second failure morphology, matrix cracking, occurs in the polymer and reduces the ability of the composite to transfer load, a major role of the matrix material. The polymer matrix exists to transfer load to the fiber, protect the fiber from damage, and stabilize the fiber alignment [4, 9]. Matrix cracking, which can be induced by tensile, compressive, and shear loading, can significantly reduce the ultimate strength of the composite. Another important type of matrix failure, interlaminar delamination, occurs in resin-rich regions between plies of different fiber orientations [9, 10] and is often induced by interlaminar shear stresses [11, 12]. These failure mechanisms are summarized schematically and through SEM images (Figure 1-1).

Damage arising from impact related events is a common concern for aerospace structures [3, 4]. In low-velocity impact conditions, matrix cracking, fiber failure, and delam-

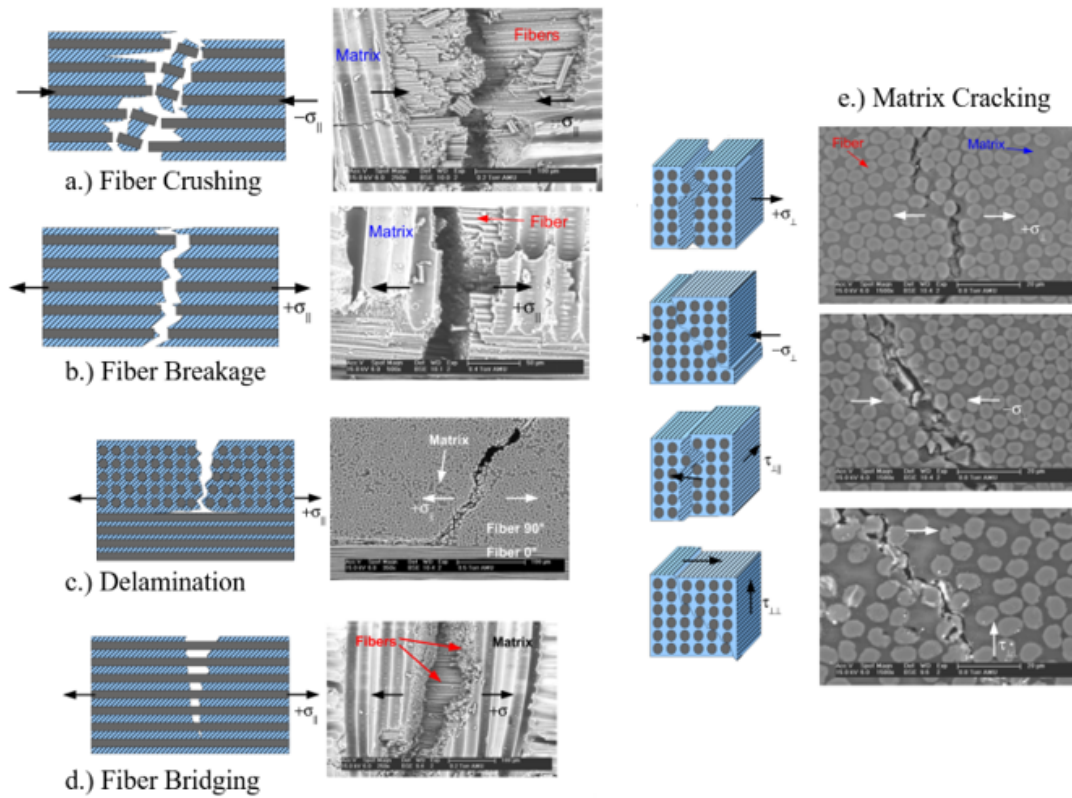


Figure 1-1: Summary of primary failure mechanisms: (a) fiber crushing, (b) fiber breakage, (c) delamination, (d) fiber bridging, (e) matrix cracking [4, 13, 14].

ination all interact with each other [9]. Bending stresses associated with LVI can initiate matrix cracking, which migrates and influences delamination at the ply interfaces [4, 13]. An example of this interaction and occurrence throughout the composite (Figure 1-2) is given in [12], where compressive failure occurs directly underneath the impactor, tensile failure of the fiber occurs due to the bending of the back face, and interlaminar shear driven delamination occurs throughout the composite.

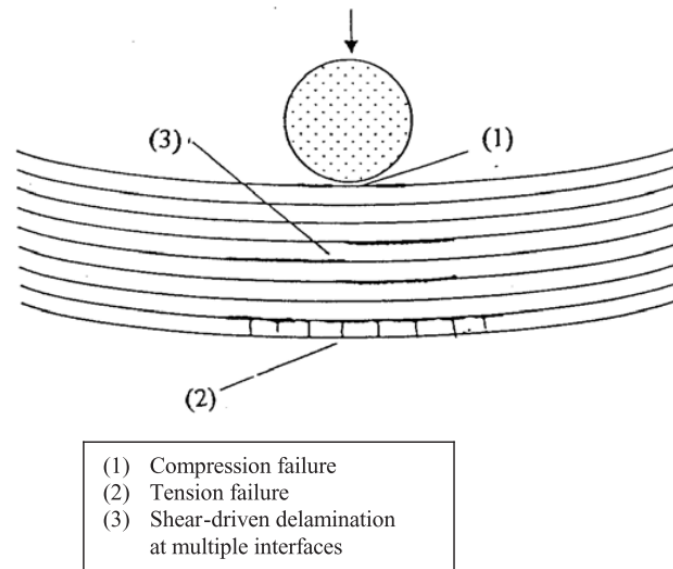


Figure 1-2: Failure mechanisms associated with low-velocity impact of CFRP composites [12].

Carbon fiber and CNT yarn reinforced composites have similar failure behavior in the polymer, but distinctly different mechanisms in the reinforcement. Zhang et al. [15] examined the failure of CNT yarn at different strain rates. At low rates they observed a more ductile failure mode and attributed this type of failure to the redistribution and sliding of the CNTs. At higher strain rates, when the CNTs are not given sufficient time to redistribute loading, they observed a more brittle failure similar to carbon fiber. The interaction between CNTs, the redistribution of loading, and differing degrees of CNT alignment all lead to very unique and complex failure traits. The complexity and wide range of damage mechanisms motivates the use of Peridynamic (PD) theory, which is introduced in the following section.

1.3 Introduction to Peridynamics

Finite element method (FEM) has been the main modeling approach for analysis of CFRP composites. Since its development in the mid-20th century, FEM has served the aerospace

industry extremely well, aiding in the design and manufacture of stronger and lighter structures. Because FEM is based on continuum mechanics formulations involving spatial derivatives, the computations suffer from reduced accuracy when discontinuities are present in the solution domain. Sharp corners, material interfaces, and crack faces/tips are examples of such discontinuities where a spatial derivative is not well defined. As a result, in the FEM, treatment of failure and fracture is not as robust and accurate as the other simulation output such as displacements. Additionally, because FEM relies on the concept of meshing with connectivity that works on the basis of nodes defining elements, and because fracture and failure would require these fundamental definitions to be modified as the simulation progresses, its use for dynamic fracture problems has major drawbacks. Improvements have been introduced starting in the 1990s to address these issues with two particular methods gaining wide recognition: (1) cohesive zone models [16], and (2) extended FEM (X-FEM) [17, 18].

Cohesive zone models (CZMs) place additional surface elements (cohesive elements) between the conventional finite elements that allow a discontinuity to develop and progress based on a material-specific traction-separation law. CZMs can be calibrated for systems with specific geometries and materials so that the predictions are consistent with the experimental findings. This method works best when the fracture initiation sites are known *a priori* (e.g. pre-existing notches); if cohesive elements are utilized across the entire solution domain, the structure can potentially become unrealistically stiff. Also, using cohesive elements excessively leads to non-trivial increases in the computational load. Thus, there are two main difficulties analysts must overcome in using CZMs: (i) finding a set of traction-separation law material parameters based on continuum mechanics, and (ii) identifying the potential failure/fracture sites prior to the analysis.

The extended FEM provides a convenient methodology such that the initial connectivity of the mesh is no longer a major roadblock in problems involving dynamic propagation of failure [17, 18]. An element may be divided into two or three smaller elements with clear definition of fracture surfaces defined by the newly generated surfaces of those ele-

ments. The method has been used by a large number of researchers studying failure and fracture of materials including composites. The main disadvantage is the requirement of using external criteria to grow fractures. As a result, X-FEM prediction of crack branching leading to complex fracture patterns remains a challenge. Both the CZMs and X-FEM can be extremely useful in analyzing certain problems. For example, quasi-static growth of delaminations in laminated composites can be simulated using CZMs with great success [19, 20]. Similarly, self-similar crack propagation under quasi-static conditions can be satisfactorily predicted using X-FEM [18]. However, there is need for a computational simulation method that naturally captures initiation and propagation of distinctly different failure modes under dynamic loading conditions in fiber reinforced laminated composites.

To more accurately represent the different damage mechanisms and the interactions between these mechanisms, this dissertation is focused on the use of Peridynamic (PD) theory. PD theory, introduced by Silling [21], is a reformulation of classical continuum theory that avoids using spatial derivatives. Instead, dynamic equilibrium is expressed in terms of integration. By doing so, failure initiation and propagation is inherently included in the theory.

Over the years, much PD work has been performed relating to laminated composite structures [22–30]. Early investigations of low-velocity impact damage on composites [23, 31] accounted for directional dependent material properties of lamina by adjusting the material point force interactions according to their relative direction with respect to the fiber orientation. Theoretical derivations of nonlocal potentials governing internal interactions were presented by matching the PD and classical continuum mechanics (CCM) strain energy density expressions [24]; application of this development was demonstrated by considering a thin plate with a central slit undergoing quasi-static in-plane tensile loading. Failure propagation of CFRP laminate under a combined thermal and mechanical load was investigated in [25]. A combined PD and FE approach was demonstrated by simulating mode I and II crack propagations in a stiffened curved composite laminate [26]. Representation of a CFRP composite in a PD setting by modeling the fiber and matrix materials

explicitly was presented [27] by considering a panel under quasi-static tensile loading. The non-isotropic behavior of CFRP composites were modeled by defining several distinct material behaviors and damage parameters [30]. Hu et al. developed a model specifying different damage parameters to correspond to different failure modes (e.g., delamination, fiber breakage) [28].

In all of this previous work concerning CFRP composite modeling using PD theory, only [27] considered fiber and matrix materials as separate constituents in the model. It is believed that this approach should be explored further because it allows for an unambiguous definition and separation of different damage mechanisms. Additionally, such an approach permits the representation of arbitrary ply orientations with no requirement of having plies oriented in multiples of 45 degrees (i.e., 0° , -45° , 90°).

As mentioned previously, peridynamics recasts the partial differential equations of CCM into an equivalent integro-differential equation. The integration in this equation introduces the concept of nonlocality into the governing equation. In this context, nonlocality implies that a material point interacts not only with its nearest neighbors, but also with material points inside a sphere of radius, δ , termed the horizon. The interactions that develop between two material points are referred to as bonds. This unique mathematical formulation of PD makes it well suited for exploring discontinuity-rich phenomena such as failure initiation and propagation in a solid body.

While only bond-based PD is used in this dissertation, it is important to introduce the variants or “flavors” of PD that have been developed in recent years [32]. They can be distinguished from each other by the manner in which they conserve angular momentum. In particular, restrictions are placed on the internal force states that enable conservation of angular momentum. Table 1.1 lists these variants and the associated restrictions placed on the force state vectors. For bond-based PD, the force state vectors are equal in magnitude and oriented parallel to the deformed bond vector. In ordinary state-based PD, the force state vectors are unequal in magnitude, but still oriented along the deformed bond vector. Finally, in non-ordinary state-based PD, the force state vectors are unequal in magnitude

and not parallel to the deformed bond vector. In other words, descending the table removes restrictions on the force state vectors. Both bond- and state-based PD theory are described in the literature with more details [22, 33, 34].

Table 1.1: Categorization of peridynamic types based upon force state vectors.

Peridynamic Types:	Force State Vectors	
	Magnitude	Orientation w/ Deformed Bond Vector
Bond-Based	Equal	Parallel
Ordinary State-Based	Unequal	Parallel
Nonordinary State-Based	Unequal	Nonparallel

As derived by [21], the PD bond-based equation of motion can be written as

$$\rho \frac{\partial^2 \mathbf{u}}{\partial t^2} = \int_{H_x} \mathbf{f}(\mathbf{u}' - \mathbf{u}, \mathbf{x}' - \mathbf{x}, t) dH_x + \mathbf{b}(\mathbf{x}, t) \quad (1.1)$$

for a material point \mathbf{x} at time t . The left hand side of Equation (1.1) contains the mass density, ρ , and the acceleration term, $\frac{\partial^2 \mathbf{u}}{\partial t^2}$. The interaction between two material points can be expressed by the pairwise response function, $\mathbf{f}(\mathbf{u}' - \mathbf{u}, \mathbf{x}' - \mathbf{x}, t)$. In the simplest form, the response function takes a linear expression given by

$$f_{ij} = cs_{ij} \quad (1.2)$$

where f_{ij} is the bond force density associated with the interaction between material point i and j . The stiffness of the interaction is determined by the material constant c , often referred to in the literature as the bond constant. The bond stretch, s_{ij} , between material points i and j is defined through the kinematics of Figure 1.3.

Figure 1.3, originally from Gerstle [34], shows the kinematics of two particles within a body. This figure has been reproduced with slight modifications in notation. In this figure, two particles are shown, particle P and P' . The initial spatial locations of these particles are

\mathbf{X} and \mathbf{X}' with respect to a reference coordinate system. The undeformed reference vector between these two material points is given by \mathbf{r} , and can be related to the initial particle locations as shown in Equation (1.3).

$$\mathbf{r} = \mathbf{X}' - \mathbf{X} \quad (1.3)$$

Upon displacement of particles P and P' , their new locations (in light blue) are given by \mathbf{x} and \mathbf{x}' respectively. The displacement vector of each individual particle is written as \mathbf{u} and \mathbf{u}' . The deformed bond vector, \mathbf{p} , is expressed by Equation (1.4).

$$\mathbf{p} = (\mathbf{X}' - \mathbf{X}) + (\mathbf{u}' - \mathbf{u}) \quad (1.4)$$

Using these definitions, one can define a scalar quantity, termed stretch, between two interacting material points.

$$s = \frac{|\mathbf{p}| - |\mathbf{r}|}{|\mathbf{r}|} \quad (1.5)$$

This stretch quantity is akin to extensional strain in classical continuum theory.

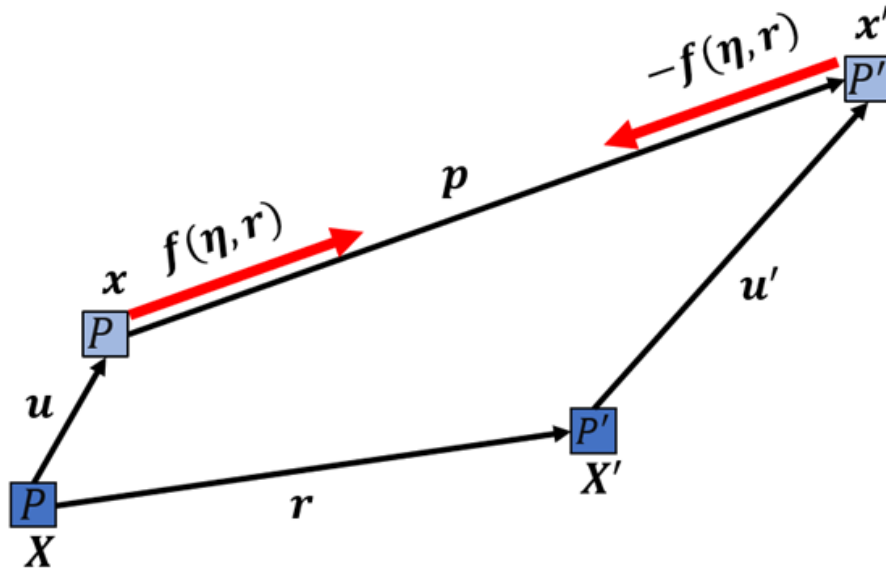


Figure 1-3: Pairwise response function reproduced from [34].

Constitutive relationships between the bond force density and the stretch of material points have been derived for various material models (see [22], [32] among others). As the solution domain is subjected to external stimuli, forces and stretches between material points develop. In the literature, this relationship often takes a linear form. However, it should be mentioned that the constitutive relationship is not limited to this form. A *linear-flat* relationship between the bond force and bond stretch is also possible and illustrated in Figure 1-4. This figure shows several different examples of constitutive relationships. Additionally, three distinct paths are shown. The blue path represents the loading curve, the green arrows represent the unload path, and the red arrow represents the failure path.

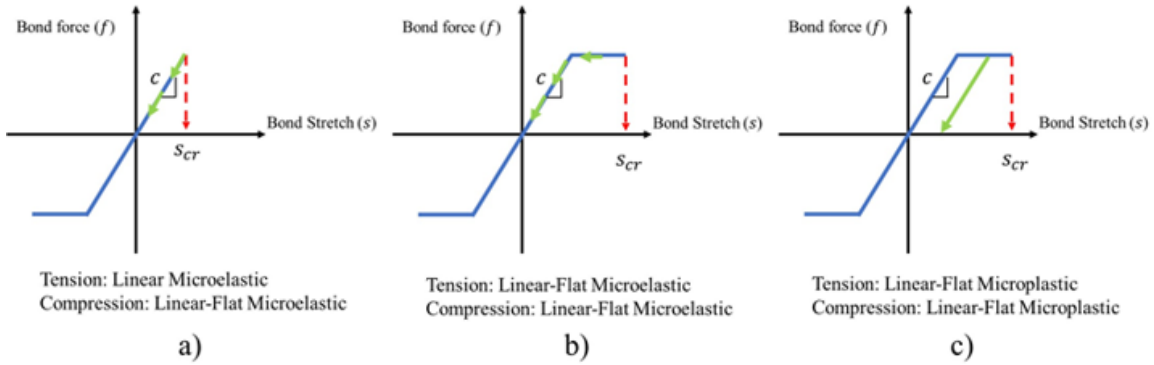


Figure 1-4: Potential constitutive relationships.

Figure 1-4 (a) shows a microelastic linear constitutive relationship with a linear-flat relationship in compression. In this material model, the bond force is related linearly to the stretch through the material constant, c , coined the bond constant. In compression, bond force and stretch are linearly related to each other up to a certain force value, after which the bond cannot carry additional load but is still able to further deform. The second material model, Figure 1-4 (b), demonstrates a linear-flat constitutive relationship in both tension and compression. Additionally, it shows the unloading path is elastic and thus follows the loading curve. Finally, Figure 1-4 (c) shows an example of a microplastic material model. This model, like the one in Figure 1-4 (b), is linear-flat in tension and compression. However, unlike the previous models, the bond experiences permanent deformation upon reaching the flat portion. If a bond reaches the flat portion but not the critical stretch,

the unloading takes place from its current stretch value following a path parallel to the original loading curve. The deformation of the bond may continue to a value that leads to its breakage. The stretch value at this state is called the critical stretch, s_{cr} . Silling and Askari [35] formulated a relationship between the fracture energy G_o and bulk modulus κ of the material, and its PD critical stretch as:

$$s_{cr} = \sqrt{\frac{5G_o}{9\kappa\delta}} \quad (1.6)$$

It should be noted that the critical stretch expression given in Equation (1.6) assumes only a linear relationship between the bond force and bond stretch, without the flat portions shown in Figure 1-4 (a). Failure in PD theory is accounted for in the constitutive law. As a PD bond fails, its load is redistributed to other bonds within the horizon. This increases the strain on the neighboring bonds, potentially leading to further failure. During the PD simulation, the number of bonds connected to each material point is monitored at every time step. A scalar parameter, damage, is defined at every material point. Its value is defined as the ratio of number of the broken bonds to the initial number of bonds at the material point. All material points have a damage value of zero at the beginning of a simulation, while a value of unity indicates a material point that is disconnected from all of its original family members. Equation (1.7) shows the equation defining the scalar damage parameter ϕ [22, 35]. In this equation, μ is a history dependent scalar quantity of value 0 or 1 used to tabulate the failure of a bond.

$$\phi(\mathbf{X}, t) = 1 - \frac{\int_H \mu(\mathbf{X}' - \mathbf{X}, t) dV'}{\int_H dV'} \quad (1.7)$$

Typically, when the local damage of a material point reaches a value of 0.5, a crack is considered to have formed [22]. Consider the example presented in Figure 1-5. In the initial state, the material point (red) and its bonds (blue) are fully connected. As the simulation progresses to the deformed state, t_2 , the applied load has caused half of the material point's bonds to exceed their critical stretch. This leads to a local damage of 0.5 and no longer any

bonds connecting with the upper surface (green semi-circle).

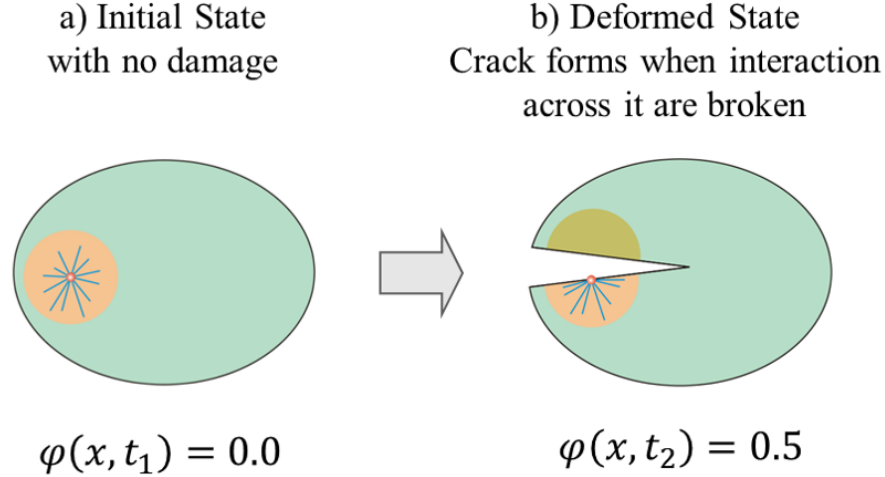


Figure 1.5: Schematic example showing the relation between damage and crack formation [22].

As discussed prominently in the literature [21, 22, 34], a microelastic pairwise response function f can be related to an elastic potential $w(\eta, \mathbf{r})$. In the literature, this is termed as the micropotential [21, 22] of a bond or the pairwise potential function. Equation (1.8) shows this relationship.

$$f(\eta, \mathbf{r}) = \frac{\partial w}{\partial \eta}(\eta, \mathbf{r}) \quad (1.8)$$

1.4 Research Objectives

This dissertation contains computational simulation approaches for carbon fiber and carbon nanotube yarn reinforced polymer matrix composites. The objective of this work is to aid in the developmental process of these materials through the accurate prediction of damage morphology and evolution. As a consequence of material maturity, these two simulations are performed at different length scales. The more mature and commonly utilized CFRP composites are analyzed at the macroscale and subjected to more advanced loading conditions, such as low-velocity impact and off-axis dynamic testing. Simulation approaches

developed for carbon fiber are geared towards aiding the certification process and learning more about the interaction of failure mechanisms.

On the other hand, CNT yarn is still in the initial stages of material development. Perhaps even more so than CFRP, CNT yarn is a truly complex and hierarchical structure that necessitates a multiscale modeling approach. For this reason, simulations are geared towards tailoring and learning about the microstructure material property relationships. Methods were created to analyze and systematically explore the microstructure itself under pure tensile loading.

These two differing material systems and length scales demonstrate the versatility of peridynamics.

1.5 Outline

This dissertation is broken up into four chapters. The first chapter is intended to provide an introduction to PMCs, common failure mechanisms, PD theory, and the objectives of this research. In the second chapter, the PD simulation approach for CFRP matrix composite is developed and explored. This chapter contains a brief background on the low-velocity impact problem and its importance from a certification and analysis perspective. The PD laminate approach is provided with focus on the objective determination of material parameters. Verification and validation of the approach is given through the simulation of off-axis static and dynamic tension tests. Finally, simulation results for low-velocity impact at four different energies is given and compared against experiments. Additionally, an approach for simulating a hat stiffened panel and a method for including through-thickness reinforcements are provided.

The third chapter introduces CNT yarn reinforced composites. A framework using PD theory is developed and demonstrated for deformation and failure analysis of carbon nanotube (CNT) yarn-based structural composites. Experimental work involving tension testing of a CNT yarn/polymer composite resulting in stress-strain response up to and including failure and was provided by researchers at NASA Langley. The as-prepared specimen was

characterized using x-ray micro computed tomography (CT), which was then converted into voxel-based data with CNT yarn, polymer, and void phases as well as surface undulation. A Density-Based Spatial Clustering of Applications with Noise (DBSCAN) algorithm was applied to detect and quantify the clusters of voids, of CNT-rich, and of resin-rich regions. The voxel data, with all microstructural details, were used in PD simulations. These demonstrate the critical roles of resin and void clusters and surface undulation in fracture initiation and propagation. Additional analysis was performed to construct probability density functions (PDFs) of different phases (yarn, resin, void) with the goal of constructing synthetic virtual composite specimens. The synthetically reconstructed models correctly captured the experimental stress vs. strain response. The similarities and differences between the failure (initiation and propagation) behaviors predicted by x-ray CT-based and PDF-based simulations are presented in detail and discussed.

The final chapter provides concluding remarks and a discussion on future work that can be undertaken.

1.6 Unique Contributions

As mentioned in the objective section, the focus of this dissertation is on developing PD simulation approaches that can help other computational and experimental researchers learn more about the material systems. A list of contributions to the community contained within this dissertation is provided as follows:

1. Introduced an approach to calculate PD elastic and strength material constants within an explicit fiber and matrix laminate representation. (Section 2.2)
2. Incorporated intralaminar shear nonlinearity into the PD laminate model using a numerical approach. A Ramberg-Osgood and hyperbolic constitutive relationship were explored through off-axis tension testing. (Section 2.2.3)
3. Intralaminar strain rate dependence was introduced using a new method of calculating a local PD strain rate and a rate dependent Ramberg-Osgood constitutive rela-

tionship was demonstrated through off-axis dynamic tensile testing. (Section 2.4)

4. A systematic exploration of the numerical approach, intralaminar shear nonlinearity, and strain rate dependence was performed. The influence of each of these additional modeling features was explored through low-velocity impact testing. (Section 2.5)
5. Created a method for converting x-ray CT microstructural data into an explicit simulation domain. The methodology developed is not limited to PD or CNT yarn. (Section 3.3)
6. Developed characterization routines for classifying void and resin clusters. Unsupervised clustering algorithms were used to quantify void and resin clusters of the microstructure. This information was used directly in the developed PD simulations. (Section 3.3.4)
7. Developed a unique PD approach to simulate CNT yarn reinforced composites was used to explore the microstructure process-property relationships of the composite under tensile loading. (Section 3.4)
8. Created a method for synthetic manipulation of microstructures within PD by using probability density functions (PDFs). This provides a convenient way of exploring and testing different structural influences on the mechanical behavior. (Section 3.5)

Chapter 2

Carbon Fiber Reinforced Composites

The aerospace industry is continually increasing the use of Carbon Fiber Reinforced Polymer (CFRP) matrix composites to manufacture light-weight structural parts. These material systems provide strengths comparable to advanced metal alloys at a fraction of the weight due to their lower density. However, the inherent inhomogeneity of CFRPs bring a great deal of complexity in their deformation behavior and failure patterns. For example, CFRPs experience distinctly different failure modes including matrix cracking, fiber breakage, and delamination. These structures undergo various loading scenarios during their service life. One class of loading conditions involve low-velocity/low-energy impact on laminates (e.g. tool drop). This type of impact event may cause damages that are not visible and hard to detect. Such internal damages may lead to unexpected larger-scale component failures.

A common failure mode observed in CFRPs under low-velocity impact conditions is delamination. Individual plies that make up a laminate may separate from each other due to dynamic transverse loading. When the transient load is no longer acting, the structure may go back to its near-original shape with internal delaminations present. This category of damage is coined “Barely Visible Impact Damage” (BVID) [36]. Because delaminations do not change the overall appearance of the laminate, they may not be easily detected but may serve as initiation sites for additional failure that significantly degrades the strength and stiffness of the component. Therefore, the presence of delaminations in a laminate poses considerable safety risk for the structural integrity of aerospace components.

The incorporation of advanced composite material systems into aerospace structures is a time-consuming and expensive process [37]. Structures built with carbon fiber material

are certified by extensive physical testing at every stage in the design cycle [38]. Recent years have seen the development of progressive damage and failure analysis (PDFA) methods, which aim to expedite the certification process by reducing the amount of physical testing needed to be performed. Currently however, the maturity level of PDFA methods need to be established to ensure confidence in the analyses being performed [39]. Recent work [37–39] has focused on creating a framework of best practices for verifying and validating (V & V) PDFA methods.

The verification and validation of a material constitutive response is a fundamental aspect of every PDFA method. The material response of advanced PDFA methods typically contains four key characteristics: the elastic response, the pre-peak response, the failure criteria, and the post-peak behavior [39]. For matrix material, the elastic response governs undamaged behavior, the pre-peak response softens the stress vs. strain curve to account for microdamage and degradation, a failure criteria is used to determine the transition into post-peak behavior, and the post-peak response determines the method in which energy is then dissipated [39]. As suggested by [37], each individual characteristic needs to be captured appropriately to prevent the compounding and propagation of errors in the simulation.

Most computational work in composites have been performed using the finite element method (FEM) because of its ability to capture mechanical behavior of a wide variety of systems. In recent years, various FEM based models have utilized the V & V framework. A relatively new method, PD theory, has also been used to simulate composite problems. In part because of its novelty, PD theory has yet to be assessed under the V & V framework developed by [39].

Peridynamics is a nonlocal continuum theory that reformulates the traditional partial differential equation of motion into an integral equivalent form. The integral form introduces nonlocality in the system, which has several advantages. In an integral based equation, the underlying mathematics are not disturbed by the traditional differential equation singularities such as cracks and material interfaces. The main objective of this work is to put forth a PD model within the context of the PDFA V & V framework.

For nonlocal methods, such as PDs, the $V \& V$ of the material response centers around the proper determination of nonlocal material constants. Correctly determining nonlocal material parameters is a challenging endeavor in a composite system because the assumptions on which analytical expressions have previously been built [35], specifically that isotropy and homogeneity, are no longer valid. It should be mentioned that most PD work in composites retain the homogenized assumption and incorporate anisotropy by varying PD material parameters with bond orientation. Early work with such a representation has been shown by Askari et al. in [23], in which low-velocity impact on a 32-ply laminate was simulated at 90 and 45 joules of impacting energy. Utilizing such a representation, the researchers were able to capture ply level delaminations and interaction with intralaminar matrix cracking. Nonlocal material parameters were calibrated to match ply level properties at a particular discretization. In another homogenized composite model, Hu et al. [24] developed an analytical expression for the nonlocal material parameters and simulated pre-existing central crack in a thin rectangular plate of M55J/M18 carbon/epoxy composite. Similarly, the work by Oterkus et al. [25], used a homogenized model to simulate both mechanical and thermal loading of composite laminates. In this work and later in [22], nonlocal material parameters were found analytically.

While most PD work, including all the work described above, has been conducted using a homogenized approach, Kilic et al. [27], developed an explicit representation of a composite and simulated pre-existing center crack tension tests. This type of representation poses an additional challenge in the calculation of nonlocal parameters because of the violation of both isotropy and homogeneity. In the work by Kilic et al. [27], and in previous work by Baber et al. [40], this unique challenge has been overcome by utilizing the inverse method put forth by [40, 41], in which the nonlocal material parameters are found by iteratively calibrating using full-scale simulations under various loading conditions. In this method, nonlocal material parameters are determined through comparison with local analytical expressions or continuum-based elastic modeling efforts. While simple and effective, the disadvantage to this sort of approach is that re-calibration is necessary with any

changes to the discretization or material system. Furthermore, while the inverse method is simple for linear constitutive relationships with a single material constant, the method becomes increasingly challenging and unreliable as additional material constants are added to the constitutive relation. In the current work, an objective approach for determining PD material constants is developed. This approach allows for immediate, on-the-fly calculation of nonlocal parameters regardless of discretization or material system. The approach is used to calculate the nonlocal material constants for both linear and nonlinear relationships. The method is validated by performing PD tensile simulations and the resulting numerical stress vs. strain curves are compared with the experimental work of [37].

The current PD development work includes: (i) development of an objective approach for determining PD material parameters (Section 2.2), (ii) implementation of nonlinear intralaminar material response (Section 2.2.3), (iii) implementation of nonlinear interlaminar material response (Section 2.2.4), and (iv) implementation of strain rate dependence of material response (Section 2.4). These developments allow for immediate, on-the-fly calculation of nonlocal parameters regardless of discretization or material system. This development work is verified and validated using off-axis quasi-static (Section 2.3) and dynamic tension tests (Section 2.4). Low-velocity impact simulations were performed at four energy levels and compared against experimental results (Section 2.5). Finally, the developed methods were extended to incorporate a through-thickness reinforcement and hat stiffener (Section 2.6-2.7.1).

2.1 Peridynamic Approach for Laminated Composites

The current PD work treats the anisotropy and heterogeneity of a laminated composite through an explicit representation of fiber and matrix material regions. A lamina is considered to consist of a single layer of PD material points that have alternating sequences of fiber and matrix material association (Figure 2-1). This type of explicit representation is readily able to incorporate different fiber orientations (Figure 2-1, column 1 for 0° , column 2 for 45° , column 3 for 90° , and column 4 for -45°), which leads to the discretization pro-

cess in which the representative fiber and matrix bands are discretized as PD material points of finite volumes (Figure 2-1, rows 2 and 3). Importantly, throughout the discretization process, the material points retain their material association. Anisotropic behavior associated with a lamina is captured by carefully curating the interactions between the material regions. These interactions can be categorized as intralaminar (in-plane) and interlaminar (out-of-plane).

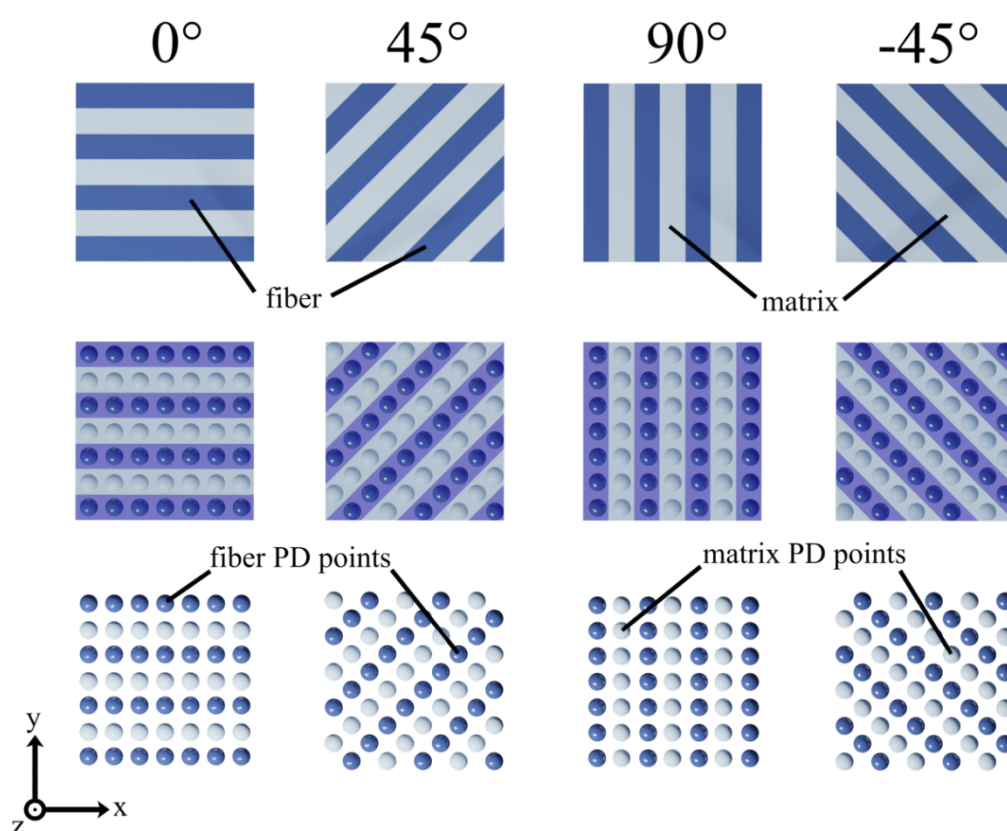


Figure 2-1: Explicit representation of fiber (dark) and matrix (light) regions for various fiber orientations.

Intralaminar Interactions

Two distinct material points interact with each other through a force density, Equation (1.1). In the case of a domain with a single homogeneous isotropic material, this interaction is uniform across the domain. Because fiber reinforced polymer composites are

heterogeneous and anisotropic, five distinct intralaminar material point interaction types (bond types) are needed, (Table 2.1). In a PD representation of a lamina, there are five distinct bond types (Table 2.1, rows 1-5) depending on the material associations of points x and x' (Table 2.1, columns 2 and 3). When the material association of the material points are dissimilar, bond types 3 and 4 (Table 2.1, rows 3-4), the interaction behavior is considered to be that of the interface. If both material points are that of matrix association, bond type 5 (Table 1, row 5), the interaction behavior is considered to be that of matrix material. Finally, if both material points are of fiber association, bond types 1 and 2, (Table 2.1, rows 1-2), the alignment of the bond with respect to the lamina fiber orientation must be considered. Fiber to fiber bonds aligned parallel to the lamina fiber orientation are considered to have fiber behavior, while all other fiber-fiber bond orientations are considered to have matrix behavior.

Each interaction behavior is given a unique constitutive relationship as follows:

$$f_f = c_f s \quad (2.1)$$

$$f_m = c_m s \quad (2.2)$$

$$f_i = c_i s \quad (2.3)$$

where c_f is the fiber micromodulus, c_m is the matrix micromodulus, and c_i is the interface micromodulus. For simplicity, the interface micromodulus is assumed to be equal that of the matrix.

Bond types associated with a fiber material point in a lamina can be visualized in Figure 2.2. Employing the color notation used earlier in Figure 2.1, dark blue circles are representative of fiber material points, while light gray circles are representative of matrix material points. In this example, the red material point in the center of the image has fiber material association. Because the lamina fiber orientation is -45° in this example, the interactions shown in dark blue between the red fiber point and the dark blue fiber points have fiber behavior (bond type 1). All other fiber-fiber interactions, shown in light blue, are not parallel to the lamina fiber orientation and as a result have the matrix material behavior (bond type

Table 2.1: Intralaminar material interactions considered in the PD laminated composite model.

Bond Type	Point X	Point X'	Alignment	Behavior
1	Fiber	Fiber	Parallel	Fiber
2	Fiber	Fiber	Nonparallel	Matrix
3	Fiber	Matrix	NA	Interface
4	Matrix	Fiber	NA	Interface
5	Matrix	Matrix	NA	Matrix

2). Interactions between the red fiber point and light gray matrix points are considered to have interface behavior (bond type 3), and are shown in gray.

An alternate scenario in which the center point is a matrix material point may also be considered is provided in Figure 2-3. In this case, only two bond types are possible. The first, a matrix-fiber interaction is shown by the gray connections between the red matrix point and the dark blue fiber points. This interaction type has interface behavior (bond type 4). Finally, the light gray interactions, shown between the matrix material point in red and matrix material points in light gray, have matrix behavior (bond type 5).

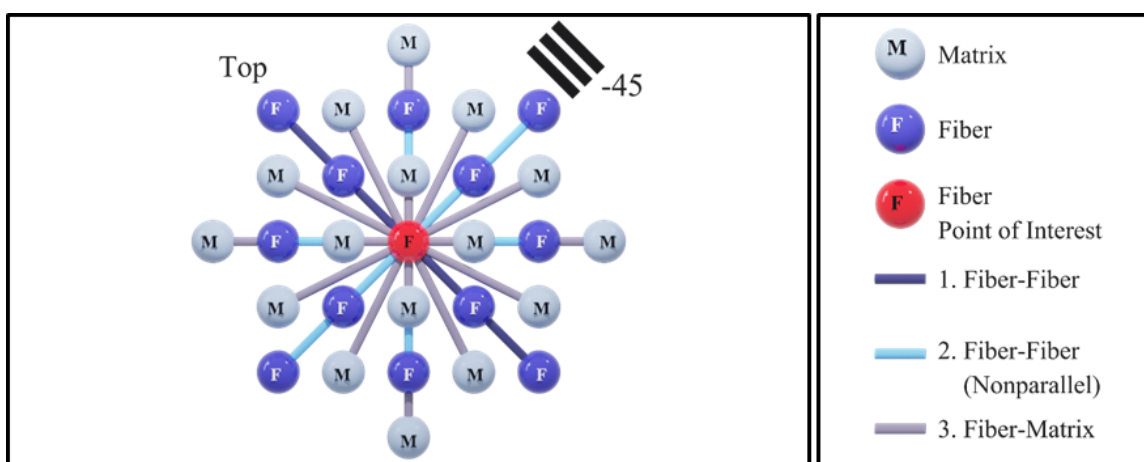


Figure 2-2: Bond types associated with a fiber material point.

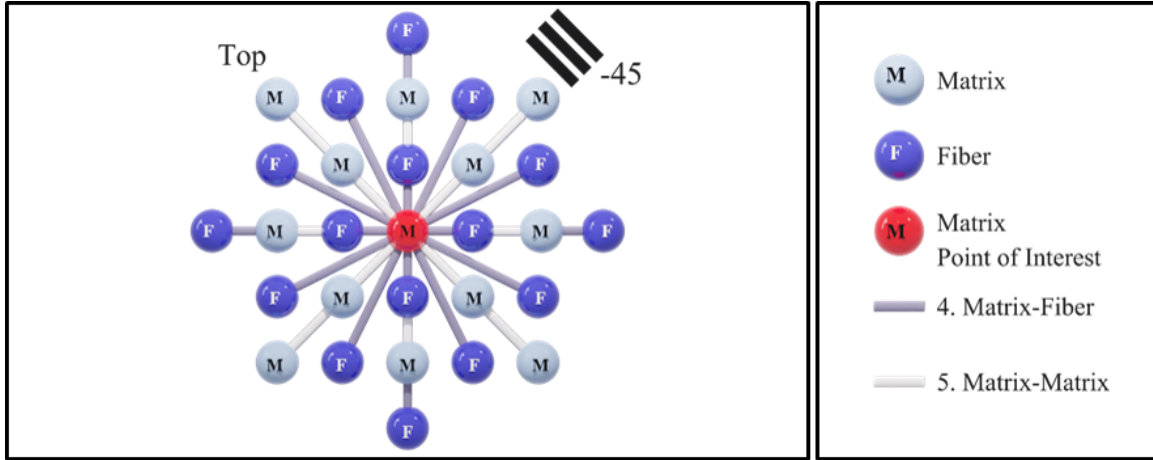


Figure 2-3: Bond types associated with a matrix material point.

Interlaminar Interactions

In the interlaminar direction (between ply), two different interaction types are considered: interlaminar normal and interlaminar shear. As the name suggests, interlaminar normal bonds exist between two material points of different plies with the interaction normal to the ply. The force density for a normal bond is defined

$$f_n = c_n s \quad (2.4)$$

where c_n is the normal bond constant.

The standard bond-based PD implementation was modified to improve the simulation's ability to capture the deformation behavior in the thickness direction. Following the work of Oterkus and Madenci in [25], the deformation of the interlaminar shear bonds are governed by a different constitutive law which is given in Equation (2.5)

$$f_s = c_s \phi_s \Delta x^2 \quad (2.5)$$

where c_s is the interlaminar shear bond constant, ϕ_s is the shear angle, and Δx is the intralaminar grid spacing. Figure 2-4 depicts the shear bond kinematics used in the current approach. There are three material points shown in Figure 2-4 and their initial positions are given by points a , b , c , and d . The bonds between material points a and d as well as b and c

are separated by a ply thickness of t and are considered to be normal bonds. Alternatively, shear bonds are shown between material points ab and dc . These bonds have the initial lengths of r_{ab} and r_{dc} , respectively. The red circles are representative of their new positions after subjected to pure shear deformation.

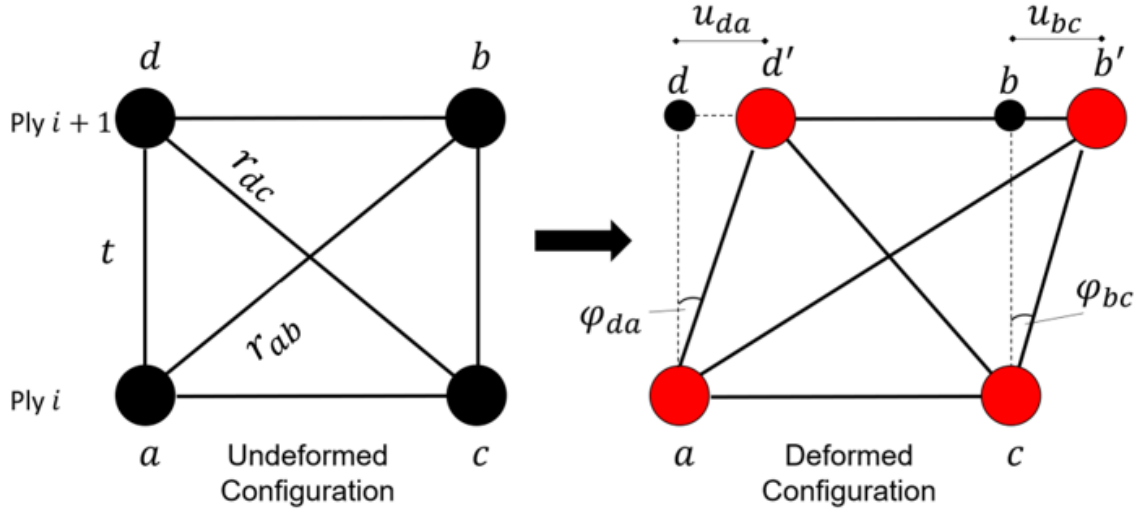


Figure 2-4: Schematic demonstrating the shear bond kinematics with an undeformed (left) and deformed (right) configurations.

The shear angle associated with the applied shear deformation can be found by evaluating the geometric relationship between material points a , b , c and d . An isolated view of the associated geometry is shown in Figure 2-5.

First, the displacement u_{da} and u_{bc} are needed and can be found from Equation (2.6) and Equation (2.7), respectively.

$$u_{da} = |(r_{dc} + \eta_{dc})| - |r_{dc}| \quad (2.6)$$

$$u_{bc} = |(r_{ba} + \eta_{ba})| - |r_{ba}| \quad (2.7)$$

The shear angle can then be found by utilizing a small angle approximation as shown in the equations below.

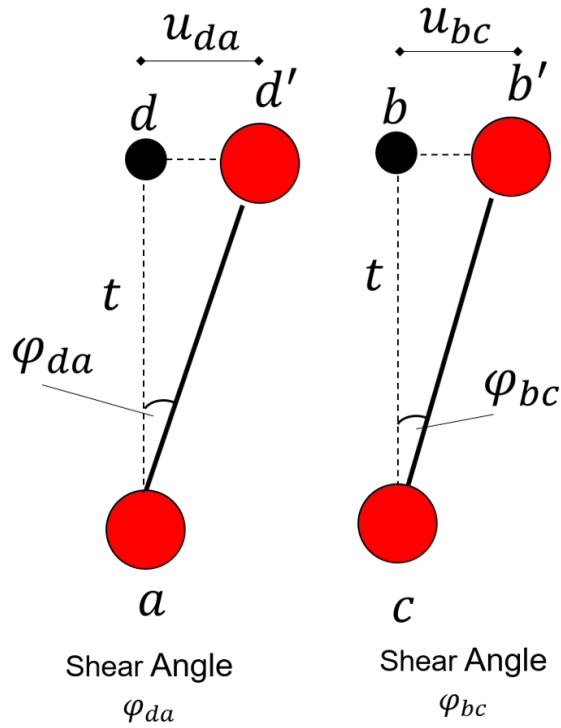


Figure 2-5: Isolated view of shear bond kinematics and associated shear angles.

$$\tan \varphi_{da} \approx \varphi_{da} \approx \frac{u_{da}}{t} \quad (2.8)$$

$$\tan \varphi_{bc} \approx \varphi_{bc} \approx \frac{u_{bc}}{t} \quad (2.9)$$

Finally, the shear angle is found by averaging the individual angles. The negative sign arises because the shear bond dc is in compression.

$$\varphi_{shear} = \frac{(\varphi_{bc} - \varphi_{da})}{2} \quad (2.10)$$

Surface Correction Factors

Surface correction factors, discussed extensively in the literature [22, 25, 35], are used to account for missing family members at the free surfaces of material regions. This correc-

tion operation is necessary as material points located near the boundaries have fewer bonds (Figure 2-6). Truncated material point families without surface correction introduces errors into the simulations because they unnaturally reduce the material stiffness in such regions.

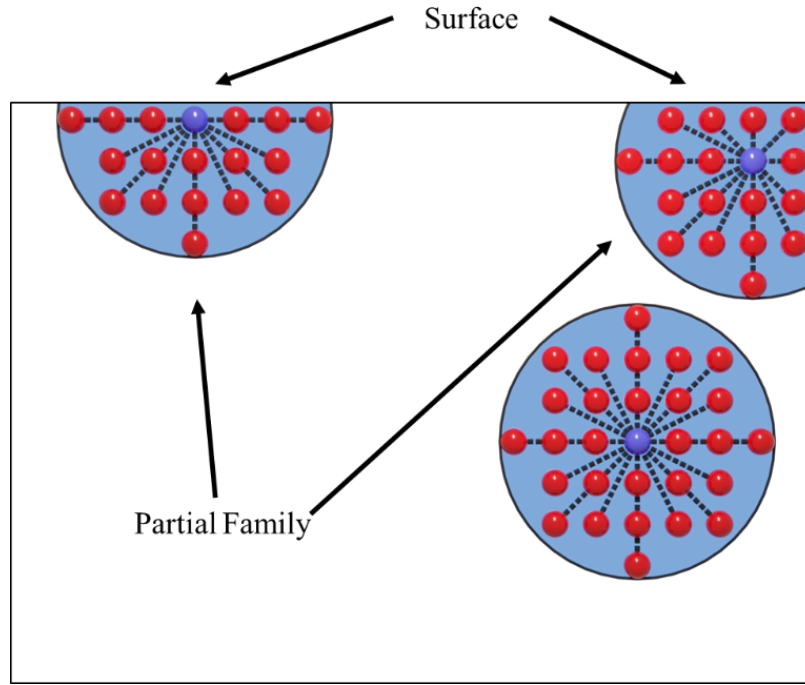


Figure 2-6: Schematic illustration of surface correction factors reproduced from [22].

A simple remedy for this low material stiffness is to increase the bond constants, through the application of surface correction factors, for points containing missing family members. Discussed extensively in [22], surface correction factors can be obtained by calculating the strain energy density (SED) of a material point under simple loading conditions and ensuring equality with classical continuum mechanics (CCM) solutions. In this approach, the SED of a material point located near the boundary W_b is multiplied with a surface correction factor sf to equate to the CCM SED associated with the loading condition, W_{CCM} , as follows

$$W_{CCM} = sfW_b. \quad (2.11)$$

In PD numerical implementation, the bond constant is increased through the application of the surface correction factor as reflected in the constitutive equations

$$f = (sf)cs \quad (2.12)$$

where f is the bond force density, sf is the surface correction factor associated with the material point x , c is the bond constant, and s is the bond stretch.

This simple procedure increases in complexity when anisotropy and heterogeneity are required, as in the current PD lamina model. In contrast to the previously described method, the lamina model contains an explicit representation of material regions, two distinct bond constants, and directionally dependent behavior. As a result, the SED of a material point i is decomposed into separate strain energy densities based upon bond types

$$W_i = W_f + W_m \quad (2.13)$$

where W_f is the SED contribution from the fiber constitutive relationship and W_m is the SED contribution from matrix bonds. The PD SED, $W_{f-(i)}$, for a fiber material point can be written as

$$W_{f-(i)} = \frac{1}{2} \sum_{j=1}^{N_f} \frac{1}{2} c_f s_{ij}^2 r_{ij} V_{ij} s f_{ij} + \frac{1}{2} \sum_{j=1}^{N_m} \frac{1}{2} c_m s_{ij}^2 r_{ij} V_{ij} s f_{ij} \quad (2.14)$$

in which N_f and N_m are the number of fiber and matrix bonds. The fiber and matrix bond constants are c_f and c_m , respectively, with units of lbf/in⁶. The bond stretch is given by s_{ij} , r_{ij} is the undeformed bond length, V_{ij} is the average volumes of material points i and j , and $s f_{ij}$ is the volume correction factor for the fiber material point i .

Using the same notation, the PD SED for a matrix material point, $W_{m-(i)}$, can be written as

$$W_{m-(i)} = \frac{1}{2} \sum_{j=1}^{N_m} \frac{1}{2} c_m s_{ij}^2 r_{ij} V_{ij} s f_{ij} \quad (2.15)$$

A local coordinate system is used to calculate correction factors in the longitudinal and transverse directions (Figure 2.7). The 1 direction of the local coordinate system coincides

with the lamina fiber direction while the 2 direction designates the intralaminar transverse direction (Figure 2-7). The global coordinate system uses x, y, and z. A correction factor

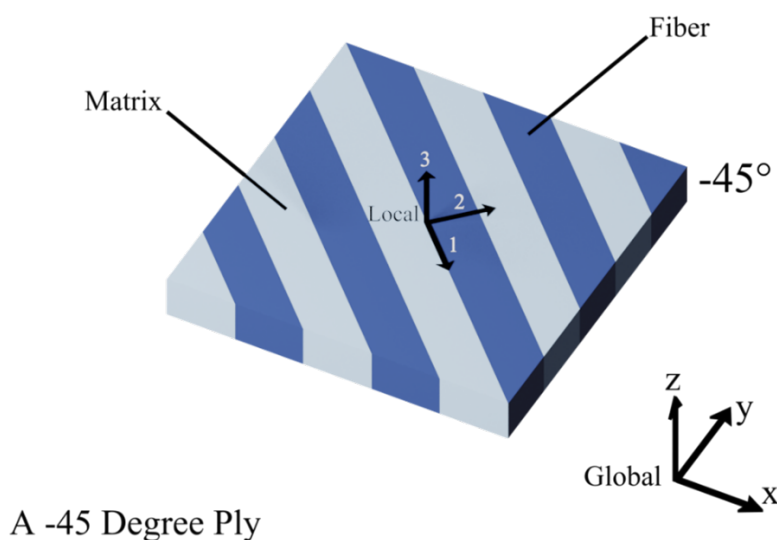


Figure 2-7: Local and global coordinate systems for surface correction factors.

is then determined via a direct comparison with the SED developed within the bulk of the composite. First, a fiber and a matrix point are chosen far from the boundaries. Each point is subjected to loading in the 1 direction and 2 direction of the local coordinate system, and their corresponding SED values are recorded. The same procedure is applied to points located near the boundaries. Both the boundary and bulk value SED values in each direction are forced to equal through the application of a correction factor as a multiplier to the boundary SED values. For a lamina, this process culminates in four separate correction factors as follows:

$$W_{(\theta)(mm)bulk} = sf_{(\theta)(mm)} W_{(\theta)(mm)bdry} \quad (2.16)$$

where the first index describes the local coordinate system direction, the second index the material association, and the third indicates whether the material point is in the bulk or near a boundary. These directional correction factors can be used as principal values in an

ellipse as shown by in [22]. The developed term is then applied to the bond constant.

Alternative Surface Correction Factor Calculations

The formulation presented above works well for unidirectional laminates. However, because the number of fiber bonds for a fiber material point differs depending on ply orientation (Table 2.2), an alternative surface correction factor calculation was created for fiber and matrix material points. The surface correction factor sf for a material point i are calculated on a per ply orientation basis θ by counting the number of each bond type (fiber, matrix, shear, and normal) n in a family and normalizing by a full family of that same bond type (F):

$$sf_{(i)}^{(n)} = \frac{F_{(\theta)}^{(mp)(n)}}{A_{(i)(\theta)}^{(mp)(n)}} \quad (2.17)$$

In this equation, the superscript mp denotes material point type. Because each material point has its own interaction domain, they need to be distinguished from each other.

Table 2.2: Example of the number of bond types for fiber and matrix material points.

Ply	Fiber		Matrix		Interlaminar	
	Fiber Bonds	Matrix Bonds	Fiber Bonds	Matrix Bonds	Normal Bonds	Shear Bonds
45	4	24	0	28	6	168
-45	4	24	0	28	6	168
0	6	22	0	28	6	168
90	6	22	0	28	6	168

Based on bond type, the surface correction factors can then be applied to the bond force density calculation.

2.2 Objective Approach for Determining PD Material Parameters

The determination of nonlocal material parameters is an important task in the PD modeling process. In most work to date, nonlocal PD material parameters are found by establishing

a link between local classical theory with the nonlocal counterpart. For bond-based PDs, a link between local and nonlocal theory is SED. An expression for the SED of a material point subjected to a certain loading condition is equated with the local classical theory SED. Implicit in both local and nonlocal SED expressions are the material constants of interest. An example of this methodology is given in the early PD work [35] in which, the bond constant is found analytically by subjecting a homogeneous body to isotropic expansion. This methodology of equating SED results in an analytical form of the bond constant as a function of engineering constants and discretization parameters. In two-dimensional (2D) problems of elasticity, this is derived as [22]

$$c = \frac{12\kappa}{\pi h \delta^3} \quad (2.18)$$

where κ is the bulk modulus, h is the thickness, and δ is the nonlocal horizon. Relationships such as Equation (2.18), are significant because they enable the user to modify the material system and discretization with ease and objectivity.

In the current work, the integration performed in [22] for a 2D isotropic body is carried out numerically. The intent of such reproduction is to introduce the process on a simple system, after which, the additional complexities of the explicit lamina representation and anisotropy are demonstrated.

Steps of analysis for obtaining nonlocal PD material parameters are tabulated as follows:

- Set up material point family
- Calculate volume of each material point
- Apply strain to PD material points
- Calculate PD strain energy density w/o bond constant
- Calculate CCM strain energy density
- Equate strain energy densities and solve for PD bond constant

At the beginning of the process, in the current PD approach for laminated composites, families of material points are set up with the intralaminar and interlaminar grid spacings, which are different from each other due to the thin nature of laminated composites. In

the second step, the volume is calculated for each of the bond interactions. Based on the literature [22], the volume of the interaction is calculated as the average of the volume of the two interaction material points. An accurate accounting of each material point volume is needed for accurate calculation SED. As a result, volume correction factors are generally applied to material points on the edge of a family. These correction factors are used to more accurately capture the interaction volume. For reference, volume correction factors are discussed in detail in [22]. In the third step, an extensional strain is applied to each of the PD interactions. Care must be taken to ensure that the strain applied to the PD interactions accurately reflects the strain from classical theory. With an equivalent deformation field between the two theories, the PD constant is chosen to ensure the SED of both theories are also equivalent.

2.2.1 2D Isotropic Scenario

Following the steps outlined above, a material point far from the boundaries is chosen and the reference locations of its family members are tabulated. The family members associated with the material point are dependent upon the discretization, specifically grid spacing and horizon, chosen (Figure 2-8).

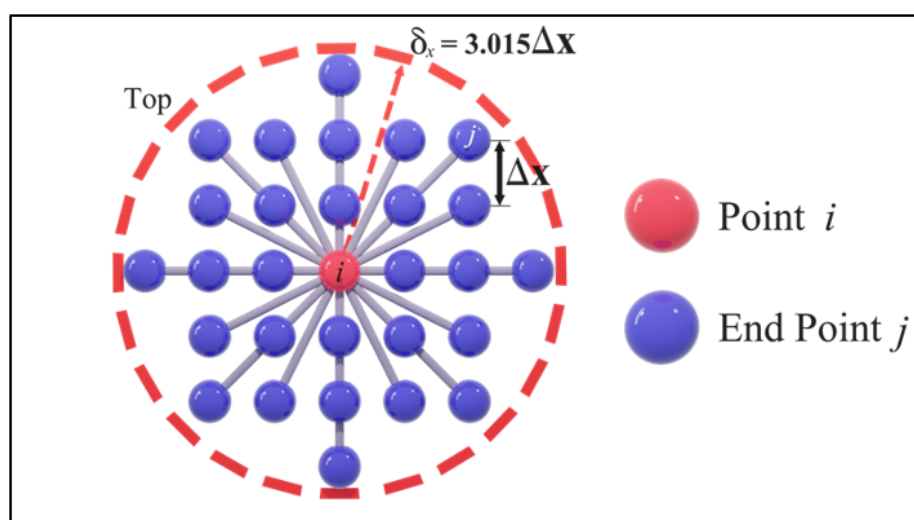


Figure 2-8: Typical example of a 2D isotropic family of material point i .

Let the center point of the family be i , with the familial endpoints, j . Typically, the intralaminar horizon δ_x in PD analyses is chosen slightly larger than 3 times the intralaminar grid spacing Δx . With the family of interactions established, the undeformed bond length between the center point i and the endpoints j can be calculated as

$$r_{ij} = |x_j - x_i| \quad (2.19)$$

where r_{ij} is the undeformed bond length, x_j is reference position of point j , and x_i is the reference position of point i .

The deformed bond length can be calculated assuming a uniform isotropic expansion

$$p_{ij} = |y_j - y_i| = (1 + \varepsilon)r_{ij} \quad (2.20)$$

where y_j and y_i are the deformed positions of point j and i respectively, ε is a chosen strain, and r_{ij} is the previously calculated undeformed bond length. The relative displacement of each bond u_{ij} can be written as the difference between the deformed and undeformed bond lengths, and is then given by

$$u_{ij} = p_{ij} - r_{ij}. \quad (2.21)$$

The strain energy density of material point i can be calculated by summing the SED contributions from each bond in discretized from as:

$$W_{(i)} = \frac{1}{2} \sum_{j=1}^N \frac{1}{2} k_i u_{ij}^2 V_{ij} \frac{\delta}{r_{ij}} \quad (2.22)$$

where k_i is the spring constant of material point i and has the units (lbf/in⁷). The term V_{ij} is the mean of the volumes of material points i and j in the reference configuration. The one half term in front of the summation arises because half of the energy of the bond is allocated to material point i [22, 34, 35] with the remaining half allocated to point j . The only unknown in this equation is the spring constant k_i . Finally, the SED from classical

continuum mechanics given this deformation can be calculated as

$$W_{CCM} = 2\kappa\varepsilon^2 \quad (2.23)$$

in which κ is the bulk modulus and ε is the applied strain. Equating the strain energy densities from Equations (2.22) and (2.23) and solving for the spring constant k_i leads to

$$k_i = \frac{2\kappa\varepsilon^2}{\frac{1}{2} \sum_{j=1}^N \frac{1}{2} u_{ij}^2 V_{ij} \frac{\delta}{r_{ij}}} \quad (2.24)$$

The bond constant can then be calculated by multiplying the intralaminar horizon δ with the spring constant:

$$c_i = k_i \delta. \quad (2.25)$$

This result is compared with the analytical expression given by Equation (2.18) by considering an example (Table 2.3). For a specified set of elastic material properties of elastic modulus $E = 23.83\text{e}6$ psi and shear modulus $\kappa = 35.74\text{e}6$ psi, and PD grid properties of horizon $\delta_x = 0.2374$ in, grid spacing $\Delta x = 0.0787$ in, and thickness $\Delta z = 0.0787$ in, the resulting numerical bond constant is approximately 2 % lower than the analytical calculation (Table 2.3), which is deemed satisfactory.

Table 2.3: Comparison of analytical and numerical bond constants given the engineering constants.

E	κ	δ_x (in)	$\Delta x = \Delta z$	c_{2d}	c_i	Diff
(psi)	(psi)	(in)	(in)	(lbf/in6)	(lbf/in6)	(%)
23.83e6	35.74e6	0.2374	0.0787	1.298e11	1.274e11	-1.77

2.2.2 Intralaminar Fiber and Matrix Bonds

The numerical procedure described above can be extended for a lamina with a few simple modifications. Recall that anisotropic behavior is incorporated through an explicit representation of fiber and matrix material regions. The implication of such a representation is

that the material points have unique families depending on their material type. This effectively changes the family of interactions (interaction domain) developed for each material point. Furthermore, to account for the anisotropic behavior, two constitutive material relationships are considered: fiber and matrix. These differences lead to two unknown nonlocal material constants and therefore two distinct loading conditions are needed.

The first loading scenario involves the interaction family of a matrix material point (Figure 2.9 (a)) while the second loading scenario places a fiber material point at the focal point (Figure 2.9 (b)) and works with its interaction domain. For the sake of completeness, these two families show five different bond types: fiber-fiber, nonparallel fiber-fiber, fiber-matrix, matrix-fiber, and matrix-matrix.

These unique interaction types are simplified in the current work and are described by either a fiber or a matrix constitutive relationship. For matrix behavior, the constitutive relationship is given by

$$f_{ij} = k_m u_{ij} \quad (2.26)$$

where f_{ij} is the bond force density with units lbf/in⁶, k_m is the matrix related material constant with units lbf/in⁷, and u_{ij} is the relative displacement between point i and point j . Similarly, the fiber constitutive relationship is written as

$$f_{ij} = k_f u_{ij} \quad (2.27)$$

with k_f representing the fiber related material constant. The material constants can be found by subjecting the family to simple loading conditions. With this representation, two distinct loading conditions are needed to solve for the two unknowns k_f and k_m . To isolate the matrix response, the first loading condition considered is transverse loading (i.e. normal to fiber direction). In this scenario, as a result of the orientation, the bonds supporting the transverse load are: nonparallel fiber-fiber, fiber-matrix, matrix-fiber, and matrix-matrix interactions. Each of these bonds is considered to have matrix behavior and uses the constitutive relationship dictated by Equation (2.26).

To calculate the constant k_m , first consider the relationship between the transverse mod-

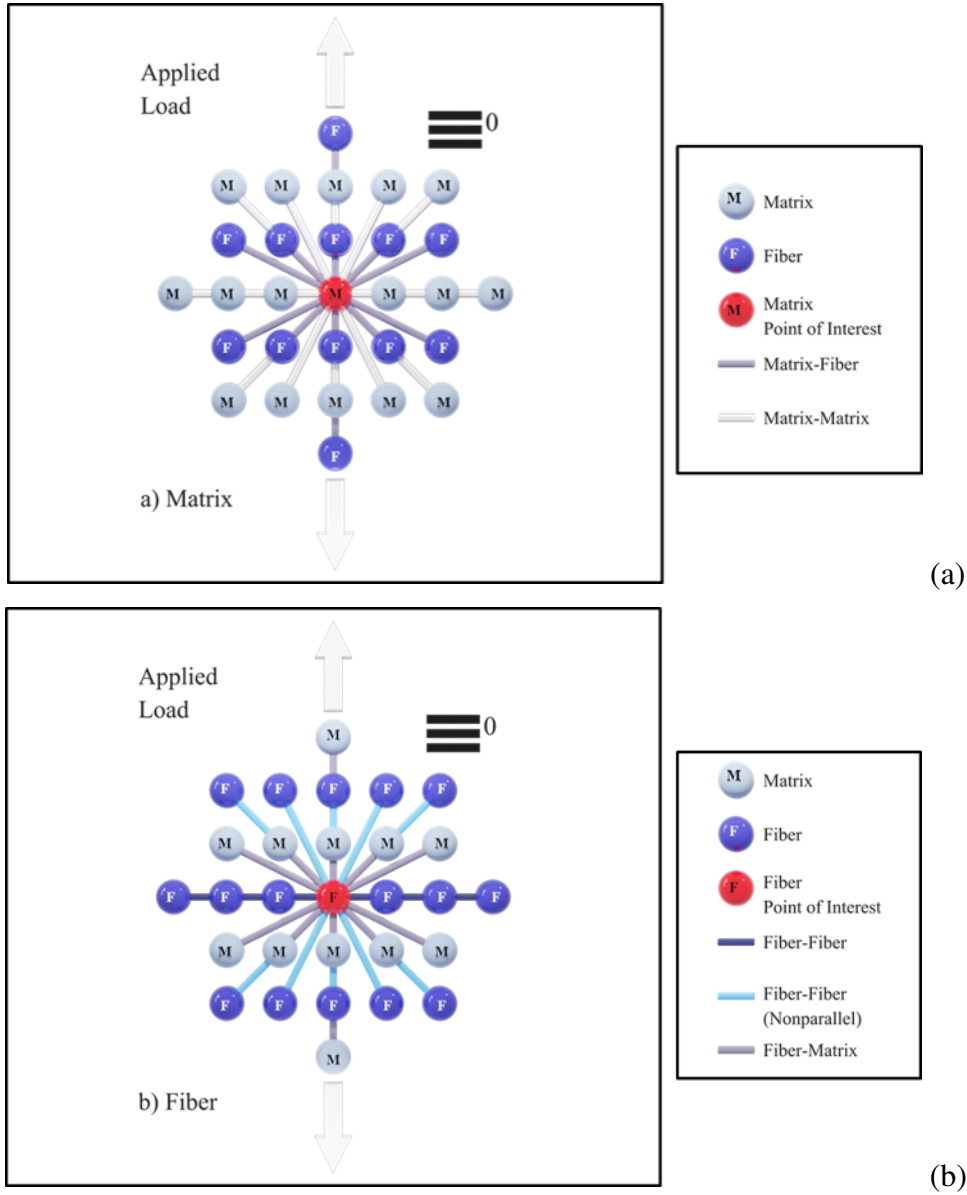


Figure 2.9: (a) Matrix material point and family under transverse loading. (b) Fiber material point and family under transverse loading.

ulus and the local SED with this loading scenario. From classical laminate theory (CLT) [1], the transverse modulus E_{22} , the major Poisson's ratio ν_{12} , and the minor Poisson's ratio ν_{21} can be related to the reduced stiffness term Q_{22} via

$$Q_{22} = \frac{E_{22}}{(1 - \nu_{21}\nu_{12})}. \quad (2.28)$$

The transverse stress σ_{22} can be found using Hooke's law with the longitudinal strain ε_{11} and the shear strain γ_{12} set to 0, as follows

$$\begin{Bmatrix} \sigma_{11} \\ \sigma_{22} \\ \tau_{12} \end{Bmatrix} = \begin{bmatrix} Q_{11} & Q_{12} & 0 \\ Q_{12} & Q_{22} & 0 \\ 0 & 0 & Q_{66} \end{bmatrix} \begin{Bmatrix} 0 \\ \varepsilon_{22} \\ 0 \end{Bmatrix}. \quad (2.29)$$

The relationship between transverse stress and strain under these conditions is then

$$\sigma_{22} = Q_{22}\varepsilon_{22}. \quad (2.30)$$

The local SED can be written as

$$W = \frac{1}{2}(\sigma_{11}\varepsilon_{11} + \sigma_{22}\varepsilon_{22} + \tau_{12}\gamma_{12}) \quad (2.31)$$

with σ_{11} and ε_{11} being the longitudinal stress and strain, respectively, and τ_{12} and γ_{12} representing the shear stress and strain, respectively. From Equations (2.30) and (2.31), the local SED resulting from only transverse loading is written as

$$W_{22} = \frac{1}{2}Q_{22}\varepsilon_{22}^2. \quad (2.32)$$

Following the isotropic and homogeneous scenario described earlier, the nonlocal PD material constant can be found by developing an expression for the PD SED of a material point and equating with the local SED, Equation (2.32). It is important to ensure that the deformation field applied in PD matches with that assumed in CLT. Meaning that a relationship between the CLT strain field and the stretch of bonds must be developed. The stretch, s_{ij} of a bond can be thought of an extensional strain of a line segment. In the literature [42], extensional strain has been related to traditional strain components via the following equation

$$s_{ij} = \varepsilon_{11} \cos^2 \theta_{ij} + \gamma_{12} \cos \theta_{ij} \sin \theta_{ij} + \varepsilon_{22} \sin^2 \theta_{ij} \quad (2.33)$$

where θ_{ij} is the orientation of points i and j with respect to the horizontal axis. Recall that in the development of Equation (2.32), the longitudinal strain ε_{11} and the shear strain γ_{12}

were assumed to be 0. To ensure equality and to develop the same deformation field, these terms must also drop out of the stretch-extensional strain relationship of Equation (2.33). This simplification results in

$$s_{ij} = \varepsilon_{22} \sin^2 \theta_{ij} \quad (2.34)$$

where s_{ij} is the stretch between points i and j , ε_{22} is the applied transverse strain, and θ_{ij} is the angle the bond makes with the horizontal axis. The relative displacement u_{ij} can be related to stretch via

$$u_{ij} = s_{ij} r_{ij} \quad (2.35)$$

where r_{ij} is the undeformed bond length. Substituting Equation (2.34) into Equation (2.35) leads to

$$u_{ij} = \varepsilon_{22} \sin^2 \theta_{ij} r_{ij} \quad (2.36)$$

The SED of a PD material point i can be written as

$$W_i = W_m + W_f \quad (2.37)$$

where W_m is SED contribution from matrix constitutive behavior and W_f is SED contribution from fiber constitutive behavior. All fiber-fiber bonds are oriented along the horizontal and have a bond angle θ_{ij} of 0 degrees (Figure 2.9b). Equation (2.34) shows that bonds oriented at 0 degrees will not have any extensional strain. Therefore, fiber bonds do not contribute to the local PD SED with transverse loading. With this in mind, the local SED of a PD material point can be written as

$$W_{22-(i)} = W_m = \frac{1}{2} \sum_{j=1}^{N_m} \frac{1}{2} k_m u_{ij}^2 V_{ij} \frac{\delta}{r_{ij}} \quad (2.38)$$

where N_m is the number of matrix bonds in the family of material point i , V_{ij} is the average volume of material points i and j , δ the horizon, and r_{ij} the undeformed bond length. Equating Equations (2.31) and (2.38) and rearranging leads to an expression for the desired

unknown k_m

$$k_m = \frac{\frac{1}{2}Q_{22}\varepsilon_{22}^2}{\frac{1}{2}\sum_{j=1}^{N_m} \frac{1}{2}u_{ij}^2 V_{ij} \frac{\delta}{r_{ij}}}. \quad (2.39)$$

With this final development, some key characteristics are observed. Several discretization parameters appear in Equation (2.39). Most notably N_m which is the number of matrix bonds in the family of point i . This parameter corresponds with the selection of the horizon δ . Another discretization-based parameter is the volume V_{ij} , which is related to both the intralaminar and interlaminar grid spacings. The spring constant k_m is dependent on the lamina property Q_{22} and as the transverse stiffness increases, so does the nonlocal parameter. Finally, it should be noted that while the transverse strain ε_{22} appears in the numerator, it drops out of the equation because of the term u_{ij} , which includes ε_{22} in its definition.

With the matrix constant calculated, a similar methodology can be employed to calculate the fiber constant k_f in which the loading is applied along the fiber direction (Figure 2.10). While this scenario is similar to the transverse case, it poses some unique differences which must be considered.

Consider once again CLT and the SED that develops as a result of longitudinal loading. In this scenario, if the transverse strain and shear strain are set to 0, the local SED can be written as

$$W_{11} = \frac{1}{2}Q_{11}\varepsilon_{11}^2 \quad (2.40)$$

where Q_{11} is the CLT longitudinal reduced stiffness term and ε_{11} is the longitudinal strain. The stretch in a bond developed between two material points i and j can be related to the longitudinal strain as follows

$$s_{ij} = \varepsilon_{11} \cos^2 \theta_{ij}. \quad (2.41)$$

At this juncture, consider the differences in interactions between a matrix family (Figure 2.10a) and a fiber family (Figure 2.10b). For the family of a matrix material point, matrix-fiber and matrix-matrix bonds sustain load. Alternatively, for the family of a fiber material point, fiber-fiber, fiber-fiber (nonparallel), and fiber-matrix interactions carry load. The difference in behavior between the material points means that the local SED will be different

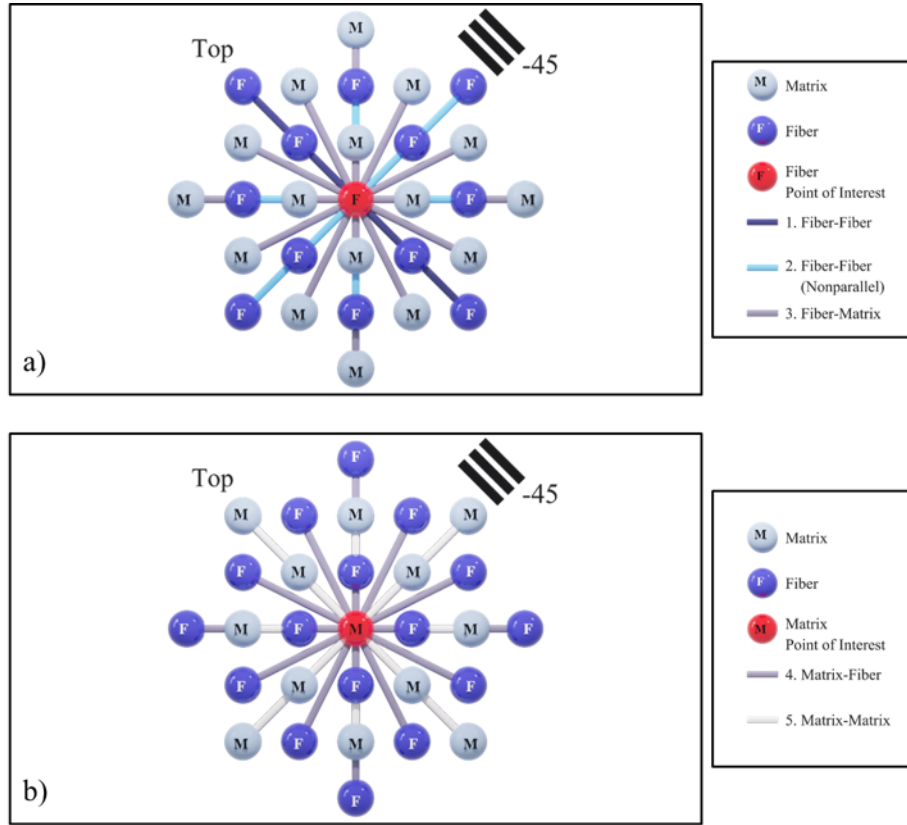


Figure 2-10: (a) Matrix material point and family loaded in fiber direction. (b) Fiber material point and family loaded in fiber direction.

depending upon whether the point has fiber or matrix association. Seeing as half of the material points on a lamina are fiber and the other half are matrix, if the CLT SED is matched to that of a fiber point, the SED for the lamina would not be captured. To account for this variation in SED among material points, the SED of a fiber material point is amplified so that the SED matches that of CLT, as follows

$$W_{11} = \frac{1}{2}(W_{PD-f} + W_{PD-m}). \quad (2.42)$$

In Equation (2.42), W_{PD-f} is the SED of a fiber material point loaded in the fiber direction and W_{PD-m} is the SED of a matrix material point loaded in the fiber direction. As indicated, the average of these SEDs is forced to equal that of CLT. The SED of a matrix material point loaded in the fiber direction is simply equal to that of W_{22} . Equation (2.42)

can be rearranged as

$$W_{PD-f} = 2W_{11} - W_{PD-m} = Q_{11}\varepsilon^2 - \frac{1}{2}Q_{22}\varepsilon^2. \quad (2.43)$$

The strain energy density of a fiber point loaded in the fiber direction can be written as

$$W_{PD-f} = W_m + W_f \quad (2.44)$$

where W_m and W_f are the SED contributions from matrix and fiber bonds, respectively. Equation (2.44) can be written in terms of the matrix and fiber constants as

$$W_{PD-f} = \frac{1}{2} \sum_{j=1}^{N_m} \frac{1}{2} k_m u_{ij}^2 V_{ij} \frac{\delta}{r_{ij}} + \frac{1}{2} \sum_{j=1}^{N_f} \frac{1}{2} k_f u_{ij}^2 V_{ij} \frac{\delta}{r_{ij}} \quad (2.45)$$

in which N_m and N_f are, respectively, the number of matrix and fiber bonds in the family of the fiber point. Rearranging and equating with Equation (2.43) leads to the following expression for the fiber constant

$$k_f = \frac{Q_{11}\varepsilon^2 - \frac{1}{2}Q_{22}\varepsilon^2 - \frac{1}{2} \sum_{j=1}^{N_m} \frac{1}{2} k_m u_{ij}^2 V_{ij} \frac{\delta}{r_{ij}}}{\frac{1}{2} \sum_{j=1}^{N_f} \frac{1}{2} u_{ij}^2 V_{ij} \frac{\delta}{r_{ij}}}. \quad (2.46)$$

It should be noted that the fiber constant k_f is dependent upon both the longitudinal modulus and the transverse modulus, as well as the matrix PD constant k_m . With this in mind, the matrix constant k_m must be found first. In summary, the following steps are used in the numerical approach for the calculation of k_f and k_m .

Require: Engineering material properties: E_{11}, E_{22}, ν_{12}

Calculate reduced stiffness coefficients: Q_{11}, Q_{22}

Calculate strain energy densities analytically: W_{11}, W_{22}

Apply tensile strain ϵ_{22} to PD family

Calculate PD strain energy density: W_{22-PD}

Equate with local theory to **find:** k_m

Apply tensile strain ϵ_{11} to PD family

Calculate PD strain energy density: W_{11-PD}

Equate with local theory to **find:** k_f

Figure 2.11: PD lamina material constant calculation summary.

2.2.3 Intralaminar Shear Nonlinearity

The numerical approach described above is extended to incorporate nonlinear constitutive responses. The generalized PD approach is first developed considering a Ramberg-Osgood (RO) relationship given by [43]. In order to demonstrate the general-purpose applicability of the current approach, a hyperbolic relationship is also considered. The RO stress vs. strain relationship under consideration is given by

$$\sigma = \frac{E_o}{\left(1 + \left(\frac{E_o \epsilon}{\sigma_o}\right)^\eta\right)^{\frac{1}{\eta}}} \epsilon \quad (2.47)$$

where σ is the axial stress, E_o is the initial Young's modulus, σ_o is the asymptotic stress, and η is a shape parameter. This relationship is first converted into a PD relationship in terms of bond force density f_{ij} and relative displacement u_{ij} as shown in

$$f_{ij} = \frac{k_o}{\left(1 + \left(\frac{k_o |u_{ij}|}{f_o}\right)^\eta\right)^{\frac{1}{\eta}}} u_{ij} \quad (2.48)$$

in which where k_o is the PD initial stiffness, f_o is the asymptotic bond force density, and η the shape parameter. A correspondence between the conventional stress vs. strain Equation (2.47) and the PD RO Equation (2.48) leads to analogous CCM-PD pairs (Table 2.4).

It is important to note that this is a three-parameter constitutive relationship as compared to a linear relationship which only contains a single material constant. A three-parameter constitutive relationship highlights the importance of a numerical approach because the determination would be exceedingly difficult using an inverse/calibrated approach.

While there is not a unique solution for these parameters, an optimization approach can be used to accurately find the desired parameters, which requires several modifications to the previously described approach while the core of the approach remains the same.

Table 2.4: Correspondence between CCM and PD RO parameters.

CCM	PD	PD Description
σ	f_{ij}	PD bond force density
ε	u_{ij}	PD relative displacement
E_o	k_o	PD initial stiffness
σ_o	f_o	PD asymptotic bond force density
η	η	PD shape factor

The initial step in this approach integrates a desired nonlinear stress vs. strain curve into a cumulative SED vs. strain curve (Figure 2.12 - inset). This conversion allows for the more natural comparison between PD local SED and CLT SED.

The three material constants for PD Ramberg-Osgood model (k_o , f_o , and η) are determined so that at each strain % level, the PD cumulative SED matches the experimental SED within a set convergence criteria. In order to ensure a proper comparison when equating the experimental and PD SED, an accurate PD deformation field must be imposed on the family of interest. Axial stress σ_x and axial strain ε_x are known from the inputted stress vs. strain curve. The global y-component of strain ε_y and the global shear strain component γ_{xy}

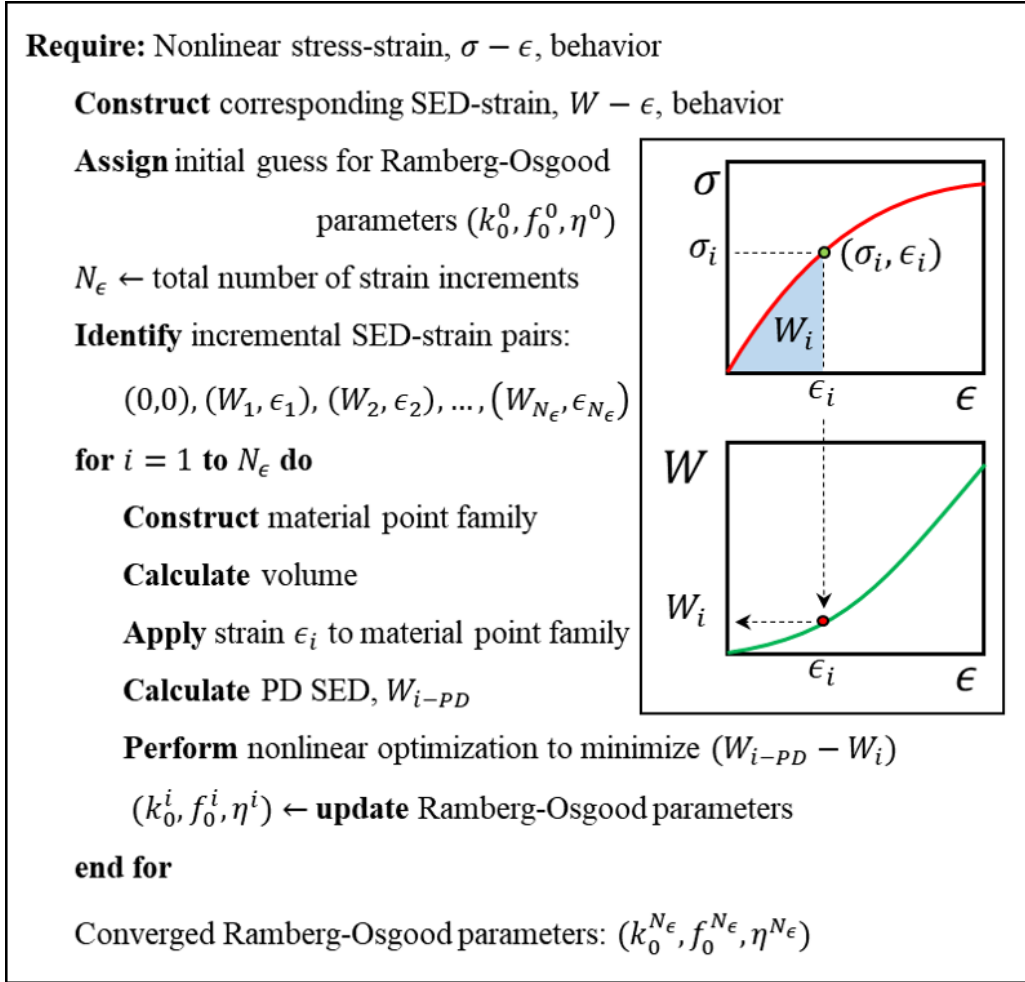


Figure 2.12: Steps of the numerical approach for nonlinear constitutive relationships using an optimization-based approach.

can be approximated using the CLT relationship as

$$\begin{Bmatrix} \epsilon_x \\ \epsilon_y \\ \gamma_{xy} \end{Bmatrix} = \begin{bmatrix} \bar{S}_{11} & \bar{S}_{12} & \bar{S}_{13} \\ \bar{S}_{21} & \bar{S}_{22} & \bar{S}_{23} \\ \bar{S}_{31} & \bar{S}_{32} & \bar{S}_{33} \end{bmatrix} \begin{Bmatrix} \sigma_x \\ \sigma_y \\ \tau_{xy} \end{Bmatrix}. \quad (2.49)$$

With the assumption that σ_y and τ_{xy} are 0 for loading in longitudinal direction, the global y and shear strain components can be written as

$$\epsilon_y = \bar{S}_{12} \sigma_x \quad (2.50)$$

and

$$\tau_{xy} = \bar{S}_{16}\sigma_x, \quad (2.51)$$

respectively. Given the strain field, the extensional strain/stretch s_{ij} can be written using Equation (2.33) and the relative displacement u_{ij} can be written using Equation (2.36). The strain energy density for a fiber material point $W_{f-(i)}$ can be written as

$$W_{f-(i)} = \frac{1}{2} \sum_{j=1}^{N_m} \left[\int_0^{u_{ij}} \frac{k_o}{\left(1 + \left(\frac{k_o|u_{ij}|}{f_o}\right)^\eta\right)^{\frac{1}{\eta}}} u_{ij} du_{ij} \right] V_{ij} \frac{\delta}{r_{ij}} + \frac{1}{2} \sum_{j=1}^{N_f} \frac{1}{2} k_f u_{ij}^2 V_{ij} \frac{\delta}{r_{ij}} \quad (2.52)$$

and the strain energy density for a matrix material point $W_{m-(i)}$ can be written as

$$W_{m-(i)} = \frac{1}{2} \sum_{j=1}^{N_m} \left[\int_0^{u_{ij}} \frac{k_o}{\left(1 + \left(\frac{k_o|u_{ij}|}{f_o}\right)^\eta\right)^{\frac{1}{\eta}}} u_{ij} du_{ij} \right] V_{ij} \frac{\delta}{r_{ij}}, \quad (2.53)$$

respectively. The strain energy density of the lamina is assumed to be the average of the strain energy density of the fiber and matrix material point:

$$W_{PD-(i)} = \frac{1}{2} (W_{f-(i)} + W_{m-(i)}). \quad (2.54)$$

The strain energy density from classical laminate theory is simply the integral of the experimental stress vs. strain curve:

$$W_{CLT} = \int_0^{\varepsilon_f} \sigma d\varepsilon. \quad (2.55)$$

Finally, the PD nonlinear material parameters are found using nonlinear least squares optimization with the objective function Ψ as

$$\Psi(\varepsilon) = \min(W_{PD-(i)} - W_{CLT}). \quad (2.56)$$

2.2.4 Interlaminar Constitutive Response

The interlaminar shear response was developed following the approach of [25] through the introduction of an interlaminar shear constitutive response. In contrast to a standard bond

kinematics, shear bonds interact through shear angle ϕ which can be found by monitoring the deformation of the bonds between material points (k and l) and (j and i) (Figure 2-13).

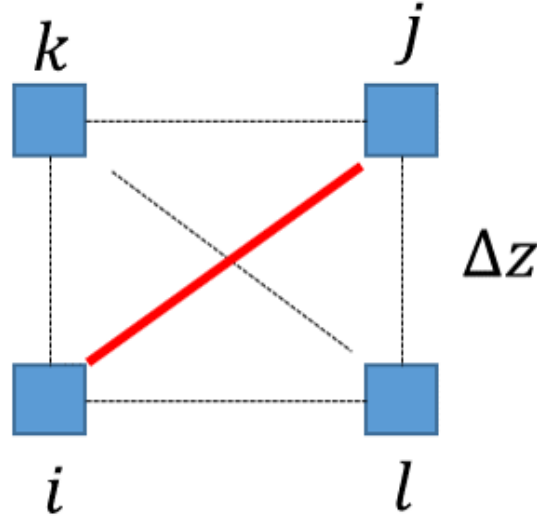


Figure 2-13: Example of an interlaminar shear bond (Red) and material points involved in determining the shear angle.

Using a similar numerical methodology as presented in the preceding sections, the interlaminar shear constant can be calculated by considering a single family of shear bonds and virtually applying a simple shear loading condition. A displacement field was applied to the family, which can be envisioned as fixing the bottom most material points of the family and applying a displacement to the top most material points of the family

$$\begin{Bmatrix} u_x \\ u_y \\ u_z \end{Bmatrix} = \begin{Bmatrix} r_z \tan \gamma_{xz} \\ 0 \\ 0 \end{Bmatrix}. \quad (2.57)$$

The reference bond lengths between material points (i and j) and (k and l) can be calculated using

$$|x_{ij}| = |\vec{x}_j - \vec{x}_i| \quad (2.58)$$

$$|x_{kl}| = |\vec{x}_k - \vec{x}_l|. \quad (2.59)$$

Similarly, the two deformed bond lengths can be expressed as

$$|y_{ij}| = |(\vec{x}_j + \vec{u}_j) - (\vec{x}_i + \vec{u}_i)| \quad (2.60)$$

$$|y_{kl}| = |(\vec{x}_k + \vec{u}_k) - (\vec{x}_l + \vec{u}_l)|. \quad (2.61)$$

The relative displacement of the two bonds is given by

$$|u_{ij}| = |y_{ij}| - |x_{ij}| \quad (2.62)$$

$$|u_{kl}| = |y_{kl}| - |x_{kl}| \quad (2.63)$$

and the shear angle of bond between material points i and j can be calculated with Equations (2.64 - 2.66)

$$du = \frac{1}{2}(|u_{ij}| - |u_{kl}|) \quad (2.64)$$

$$dz = \frac{1}{2}(|x_{3k} - x_{3i}| - |x_{3j} - x_{3l}|) \quad (2.65)$$

$$\tan \phi \cong \phi = \frac{du}{dz}. \quad (2.66)$$

The local CCM-based SED can be written as

$$W_{CCM} = \frac{1}{2}G\gamma_{xz}^2 \quad (2.67)$$

where G is the interlaminar shear modulus. The previous PD equations were written in terms of individual material points (i , j , k , and l). To simplify slightly the notation, the PD SED of material point i , can be calculated by summing each individual bond contributions as follows

$$W_{PD-(i)} = \frac{1}{2} \sum_{k=1}^{N_s} \frac{1}{2} k_s \phi_k^2 V_k \frac{\delta}{r_k} \quad (2.68)$$

where the subscript k represents each interlaminar shear bond in the family of the material point of interest, N_s the total number of shear bonds in the family, ϕ_k the shear angle associated with the bond, and k_s is the PD shear material constant. Equating the SED's

and rearranging leads to an expression of the PD shear material constant as a function of interlaminar shear modulus as follows

$$k_s = \frac{\frac{1}{2}G\gamma_{xz}^2}{\frac{1}{2}\sum_{k=1}^{N_s}\frac{1}{2}\phi_k^2V_k\frac{\delta}{r_k}}. \quad (2.69)$$

The interlaminar normal bond material constant was calculated by applying a normal strain in the interlaminar direction:

$$\begin{Bmatrix} u_x \\ u_y \\ u_z \end{Bmatrix} = \begin{Bmatrix} 0 \\ 0 \\ \varepsilon_z r_z \end{Bmatrix}. \quad (2.70)$$

The local CCM-based SED can be calculated as

$$W_{CCM} = \frac{1}{2}E_{22}\varepsilon_z^2 \quad (2.71)$$

where ε_z is the applied strain and it is assumed that the transverse modulus E_{22} is equal to the interlaminar modulus E_{33} . The PD equivalent SED for material point i can be calculated as

$$W_{PD-(i)} = \frac{1}{2}\sum_{k=1}^{N_n}\frac{1}{2}k_n s_k^2 V_k \frac{\delta}{r_k} \quad (2.72)$$

where k_n is the interlaminar normal bond type material constant, N_n is the number of normal bonds in the family and k the number of bonds. Equating the local CCM SED and PD SED and rearranging leads to an expression for the interlaminar normal bond spring constant as a function of transverse modulus:

$$k_n = \frac{\frac{1}{2}E_{22}\varepsilon_z^2}{\frac{1}{2}\sum_{k=1}^{N_n}\frac{1}{2}s_k^2V_k\frac{\delta}{r_k}}. \quad (2.73)$$

2.2.5 PD Strength Parameters

In the literature, there exist multiple formulations for PD strength parameters [22, 28, 35]. Most of these relationships are developed by relating strain energy release rate to PD critical stretch. These formulations are typically created using simplifying assumptions of homogeneity and uniform discretization. A new approach is needed as a result of the ex-

explicit representation of the laminate model. Unlike most work, which is based on critical stretch, the current work utilized a critical energy failure criterion.

An energy-based failure criterion was developed specifically for intralaminar bond types (fiber and matrix). The classical continuum mechanics-based transverse strain energy at failure Φ_{22}^f is approximated using the transverse strength σ_{22}^f and the transverse failure strain ϵ_{22}^f as

$$\Phi_{22}^f = \frac{1}{2} \sigma_{22}^f \epsilon_{22}^f V. \quad (2.74)$$

In PD, the total strain energy of a matrix material point Φ_m is approximated by summing the strain energy contributions of each bond l at the stretch s_{lm} as follows:

$$\Phi_m = \Phi_{22} = \frac{1}{2} \sum_{l=1}^{N_m} \frac{1}{2} k_m (s_{lm})^2 \delta r_l V_l^2. \quad (2.75)$$

For simplification, the total failure strain energy Φ_{22}^f is evenly distributed across all bonds in the family:

$$e_{cm} = \frac{\Phi_{22}^f}{N_m}. \quad (2.76)$$

The term e_{cm} represents the critical energy of a single matrix bond and when exceeded, the bond is considered to have failed. The strain energy of a single matrix bond e_{lm} can be written as

$$e_{lm} = \frac{1}{4} k_m (s_{lm})^2 \delta r_l V_l^2 \quad (2.77)$$

where the subscript l represents the current bond and the subscript m represents the matrix bond type. An energy based failure criterion can be implemented to many PD codes with only minor modifications by setting the critical energy of a single matrix bond Equation (2.76) equal to the strain energy of a single bond Equation (2.77)

$$e_{cm} = \frac{1}{4} k_m (s_{lm}^f)^2 \delta r_l V_l^2 \quad (2.78)$$

where a super script f has been added to the matrix stretch to indicate the stretch at failure. An important observation is that because bond length r_l varies within a family, so will

the matrix failure critical stretch s_{lm}^f in order to keep the critical energy e_{cm} constant. In particular, as a matrix bond length increases the critical stretch will decrease (Figure 2.14).

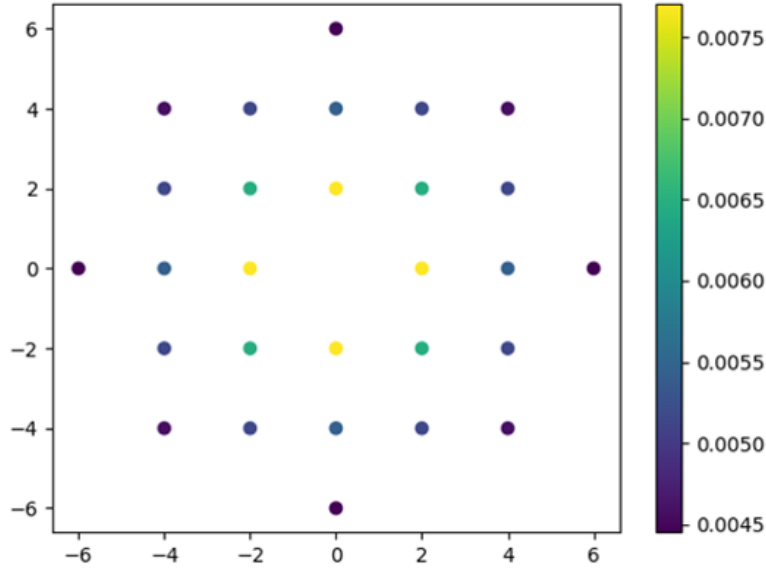


Figure 2-14: Visualization of energy-based failure criterion for a matrix material point. An intralaminar matrix family is shown with colors representing different calculated matrix critical stretch. Importantly, each PD bond despite having different critical stretch values, has the same critical bond energy.

Rearranging Equation (2.78) leads to an expression for the critical stretch of a matrix bond s_{lm}^f as a function of the discretization related parameters and transverse strength/failure strain:

$$s_{lm}^f = \sqrt{\frac{4e_{cm}}{k_m \delta r_l V_l^2}}. \quad (2.79)$$

When shear nonlinearity is included, through a RO or any other nonlinear response, the critical stretch associated with the nonlinear response is calculated by including a failure strain nonlinearity ratio q^* . This is simply the ratio of the nonlinear failure strain ϵ_n^f to the transverse failure strain:

$$q^* = \frac{\varepsilon_n^f}{\varepsilon_{22}^f}. \quad (2.80)$$

The failure strain nonlinearity ratio can then be multiplied with the critical stretch of a matrix bond to obtain a nonlinear critical stretch term s_{ln}^f :

$$s_{ln}^f = q^* s_{lm}^f. \quad (2.81)$$

Using a similar methodology, the longitudinal failure strain energy Φ_{11}^f can be expressed in terms of the longitudinal strength σ_{11}^f and the longitudinal failure strain ε_{11}^f :

$$\Phi_{11}^f = \frac{1}{2} \sigma_{11}^f \varepsilon_{11}^f V. \quad (2.82)$$

However, unlike in the transverse direction, the alternating sequences of fiber and matrix strands in the PD laminate model need to be accounted for. The strain energy in the longitudinal direction is considered to be an average of the strain energies of a fiber and matrix material points:

$$\Phi_{11} = \frac{1}{2} (\Phi_f + \Phi_m). \quad (2.83)$$

The failure strain energy of a fiber material point Φ_f^f can be written in terms of the longitudinal failure strain energy Φ_{11}^f and the failure strain energy of a matrix material point Φ_m^f :

$$\Phi_f^f = 2\Phi_{11}^f + \Phi_m^f. \quad (2.84)$$

The total strain energy of the fiber material point is comprised of a contribution from both fiber and matrix bonds as

$$\Phi_f = \frac{1}{2} \sum_{l=1}^{N_f} \frac{1}{2} k_f (s_{lf})^2 \delta r_l V_l^2 + \frac{1}{2} \sum_{l=1}^{N_m} \frac{1}{2} k_m (s_{lm})^2 \delta r_l V_l^2 \quad (2.85)$$

Similar to the matrix representation, the fiber related failure strain energy of a point is

divided evenly across the bonds as

$$\Phi_f^f = N_f \left(\frac{1}{4} k_f (s_{lf})^2 \delta r_l V_l^2 \right) + N_m \left(\frac{1}{4} k_m (s_{lm})^2 \delta r_l V_l^2 \right) \quad (2.86)$$

This expression can be rearranged to introduce the concept of a critical fiber bond energy:

$$e_{cf} = \frac{\Phi_f^f - N_m \left(\frac{1}{4} k_m (s_{lm})^2 \delta r_l V_l^2 \right)}{N_f}. \quad (2.87)$$

Again, for implementation purposes, this equation is rearranged to show the fiber bond critical stretch that is dependent on bond length and its matrix bond counterparts:

$$s_{lf}^f = \sqrt{\frac{2\Phi_{11}^f + \Phi_m^f - N_m \left(\frac{1}{4} k_m (s_{lm}^f)^2 \delta r_l V_l^2 \right)}{N_f \left(\frac{1}{4} k_f \delta r_l V_l^2 \right)}}. \quad (2.88)$$

Unlike the intralaminar bonds, the interlaminar bond failure criteria is based on a constant critical stretch and formulated using the more traditional strain energy release rate. This permits the use of the commonly available mode-I and mode-II energy release rates. Peridynamic interlaminar critical stretch formulations have been created in the past [25] and are used as the foundation for the current work.

Following the work of [25], the normal bond critical stretch is calculated and extended to include an arbitrary interlaminar horizon size using a geometric progression where Δz is the interlaminar grid spacing, and m is defined as its multiple:

$$G_{Ic} = \frac{\int F u}{A} = \left(\frac{1}{2} c_n s_n^2 V \Delta z \right) \frac{[\Delta z - (m+1)\Delta z^{m+1} + m\Delta z^{m+2}]}{(1 - \Delta z)^2} \quad (2.89)$$

$$m = \frac{\delta}{\Delta z}. \quad (2.90)$$

Rearranging leads to a direct expression for the interlaminar normal critical stretch as a

function of mode-I strain energy release rate as:

$$s_n = \sqrt{\frac{2G_{Ic}(1 - \Delta z)^2}{c_n V \Delta z [\Delta z - (m+1)\Delta z^{m+1} + m\Delta z^{m+2}]}}. \quad (2.91)$$

Similarly, following the work of [22, 28], and extending to an arbitrary interlaminar horizon size, an expression was developed for the interlaminar shear bond critical stretch:

$$G_{IIc} = \frac{\int F u}{A} = \frac{\sum_{l=1}^{N_s} \left[\frac{1}{2} k_s \Delta x^2 \phi_{cl} \frac{\delta}{r_l} V_l \cos \alpha_l \right] \phi_{cl} r_l}{\Delta x^2}. \quad (2.92)$$

When including shear nonlinearity, a shear nonlinearity energy density factor p^* is calculated as the ratio between the nonlinear SED and a linearized SED (Figure 2-15) as follows:

$$p^* = \frac{\int_0^{\epsilon_n^f} \sigma d\epsilon}{\frac{1}{2} E_o (\epsilon_n^f)^2}. \quad (2.93)$$

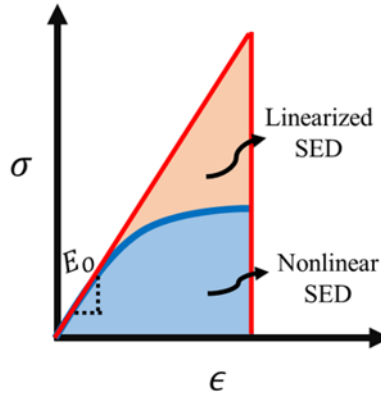


Figure 2-15: Schematic showing shear nonlinearity energy density factor calculation.

The linear-flat shear constitutive response-based energy calculation is given as

$$\Phi_{yld} = \sum_{l=1}^{N_s} \frac{1}{2} \left[k_s \Delta x^2 \phi_{yld} \frac{\delta}{r_l} V_l \cos \alpha_l \right] \phi_{yld} r_l + \sum_{l=1}^{N_s} \frac{1}{2} \left[k_s \Delta x^2 \phi_{yld} \frac{\delta}{r_l} V_l \cos \alpha_l \right] (\phi_c - \phi_{yld}) r_l \quad (2.94)$$

and compared with its linearized counterpart:

$$\Phi_c = \sum_{l=1}^{N_s} \frac{1}{2} \left[k_s \Delta x^2 \phi_c \frac{\delta}{r_l} V_l \cos \alpha_l \right] \phi_c r_l. \quad (2.95)$$

Because there are two unknowns, the shear yield ϕ_{yld} and the shear critical angle ϕ_c the shear nonlinearity energy density factor Equation (2.93) is used as a constraint equation as:

$$\Psi_1 = \frac{\Phi_{yld}}{\Phi_c} - p^*. \quad (2.96)$$

The second equation can be constructed as the difference between the mode-II strain energy release rate G_{IIc} and the PD equivalent mode-II energy release rate as

$$\Psi_s = \frac{\Phi_{yld}}{\Delta x^2} - G_{IIc} \quad (2.97)$$

Nonlinear optimization routines are then used to solve for the two unknowns by minimizing the square difference of the two equations:

$$\min(\Psi) = (\Psi_1 - \Psi_2)^2. \quad (2.98)$$

2.3 Quasi-Static Off-Axis Tension Simulation Results

The verification of the numerical approach was accomplished by simulating tension tests with 0° and 90° fiber orientations. The composite system IM7/8552 and associated engineering constants were used to obtain the PD nonlocal material parameters. The resulting simulated stress vs. strain curves were compared against the experimental results found from [37]. Three constitutive relationships (linear, RO, and hyperbolic) were considered along with multiple discretizations.

Peridynamic simulations were performed on a square specimen with dimensions of 1 in. x 1 in. (Figure 2-16). Additional material points were added at the vertical boundary strips along which the horizontal tensile loading was applied (Figure 2-16 - red material points).

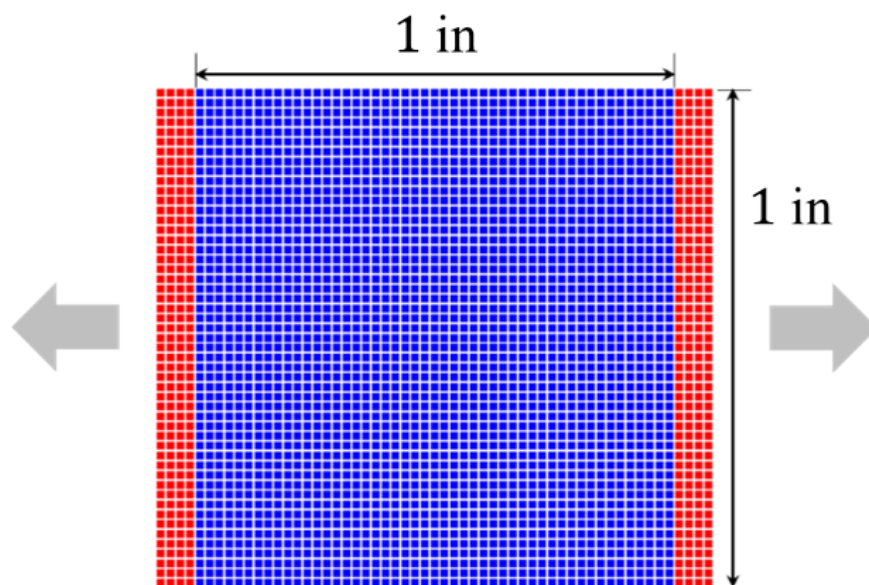


Figure 2-16: Lamina geometry and boundary regions used in verification.

Quasi-static simulations were performed by dividing the stress vs. strain response into discrete load steps and utilizing the adaptive dynamic relaxation procedure presented in [44]. In solving a quasi-static problem using PD approach in discrete load steps, displacements are applied at each end of the domain for each load step, and the cumulative force along a central plane normal to the applied load is monitored as the adaptive relaxation leads to a static equilibrium solution for that load step (Figure 2-17). Having the applied displacements and internal forces, strain and stress components can be calculated for the specimen, not unlike the experimental measurements. This approach allows for simulation of nonlinear stress vs. strain response.

To verify the objective determination of PD fiber and matrix material constants, the stress vs. strain response of 0° and 90° oriented lamina were simulated at various intralaminar grid spacings. The intralaminar grid spacing values used were 0.0787 in., 0.0394 in., and 0.0197 in. The interlaminar grid spacing was kept constant at 0.0075 in. and the intralaminar horizon was set to 3.015 times the intralaminar grid spacing. Using the objective approach developed in Section 2.2.2, fiber and matrix spring constants were calculated for

each intralaminar grid spacing (Table 2.5).

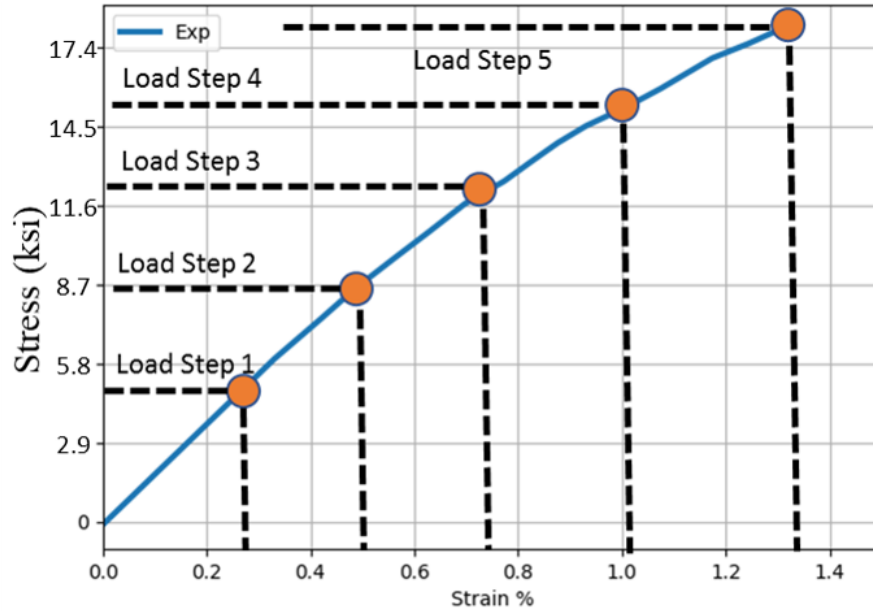


Figure 2-17: An example of utilizing PD load steps (orange) to simulate a stress vs. strain curve.

Table 2.5: Spring constants as functions of intralaminar grid spacing.

$\Delta x = \Delta y$ (in)	Δz (in)	δ_x (in)	k_f (lbf/in ⁷)	k_m (lbf/in ⁷)
0.0787	0.0052	0.2374	2.28e13	2.87e11
0.0394	0.0052	0.1187	3.66e14	4.58e12
0.0197	0.0052	0.0594	5.86e15	7.33e13

It is worth noting that with different levels of refinement (i.e., intralaminar grid spacing) the number of continuous fiber and matrix sequences in the fiber direction for a given intralaminar unit area changes (Figure 2-18). Coarser grids lead to fewer alternating fiber and matrix sequences, and vice versa. As the refinement is increased, the calculated spring constants increase in magnitude (Table 2.5).

At each intralaminar grid spacing, two simulations were performed leading to a total of

6 simulations. The first of two simulations was performed along the fiber direction and the second was performed in the transverse direction.

The results show close agreement between the PD simulations and experimental measurements (Figure 2-19).

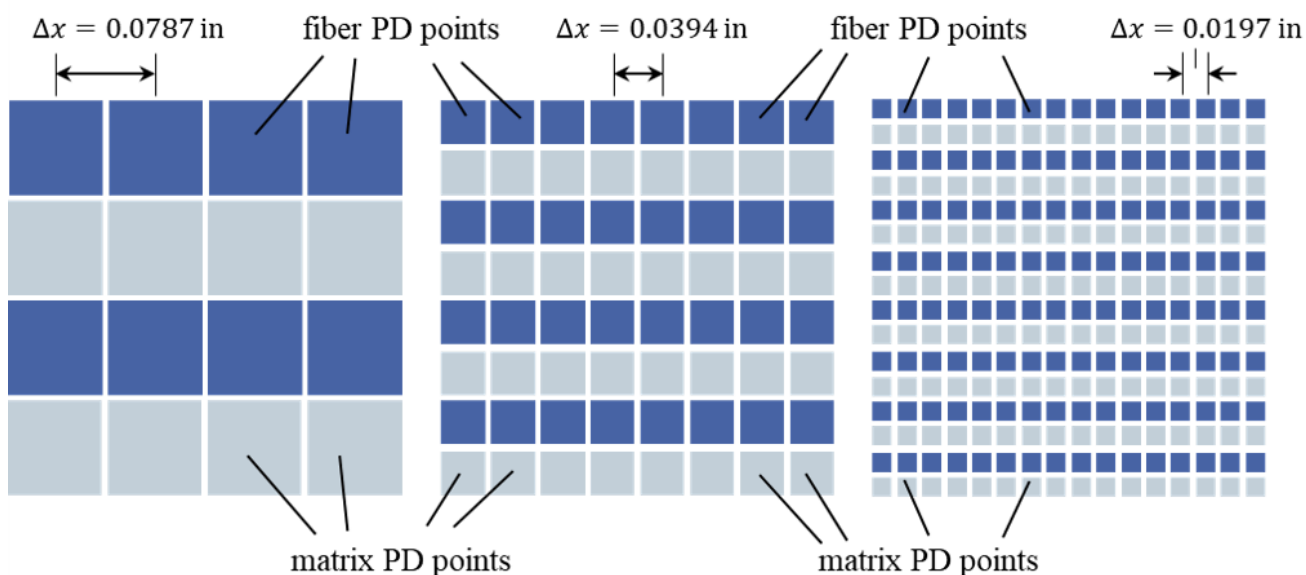


Figure 2-18: Comparison of intralaminar refinement with colors representing fiber and matrix material regions.

All six of the simulations compare well with the experimental results, and the large variation in refinement demonstrates the advantage of the developed numerical approach. At every discretization, the corresponding nonlocal material parameters can be found with ease. As further verification, the intralaminar horizon was significantly varied. Changing the horizon radius of a family of a matrix (Figure 2-20, top row, left) or a fiber (Figure 2-20, top row, right) material point from 3.015 times the intralaminar grid spacing to 1.90 times the intralaminar grid spacing drastically changes the number and type of bonds associated with a material point (Figure 2-20, bottom row). The difference in both shape and quantity of bonds between the families of radius $3.015 \times \Delta x$ and radius $1.90 \times \Delta x$ is striking (Figure 2-20). Additionally, for a fiber material point, the ratio of fiber bonds to matrix bonds is different between the two scenarios. The calculated values of fiber and matrix spring con-

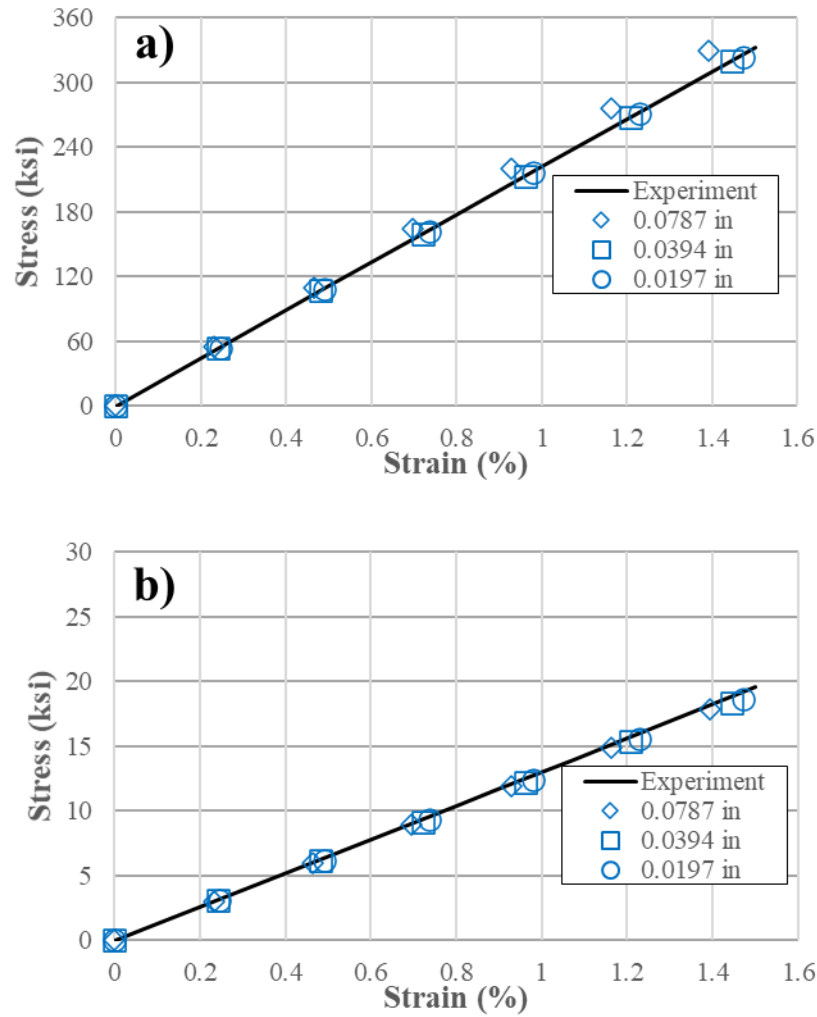


Figure 2-19: Comparison of PD and experimental stress vs. strain curve for (a) 0° oriented fiber and (b) 90° oriented fiber.

stants corresponding to $3.015 \times \Delta x$ and $1.90 \times \Delta x$ horizon values (Table 2.6) exhibit roughly one order of magnitude difference with the smaller horizon leading to larger spring stiffness values.

Four simulations were performed for verification of the calculated material constants and the results show very good agreement between PD simulations and the experimental measurements (Figure 2-21).

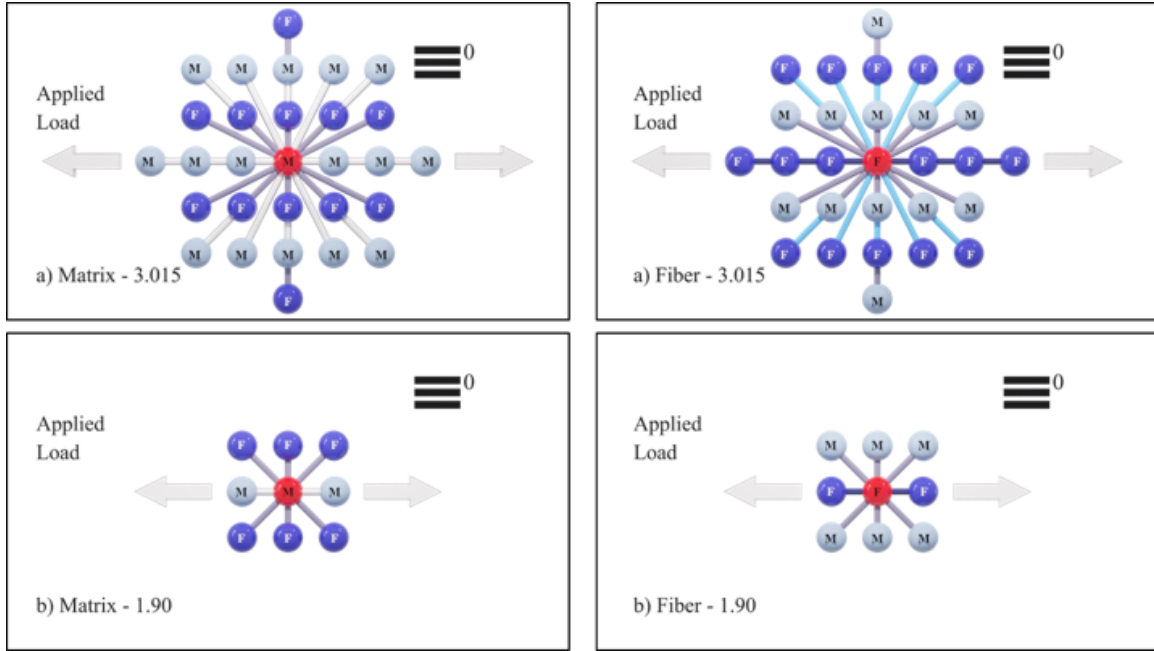


Figure 2-20: Matrix and fiber material points families with a horizon of (a) $3.015 \times \Delta x$ (top row), and (b) $1.90 \times \Delta x$ (bottom row).

Table 2.6: Example of the calculated fiber bond and matrix bond constants when the intralaminar grid spacing is held constant, but the horizon is changed.

Scenario	$\Delta x = \Delta y$ (in)	Δz (in)	δ_x (in)	k_f (lbf/in ⁷)	k_m (lbf/in ⁷)
A	0.0394	0.0052	0.2374	3.66e14	4.58e12
B	0.0394	0.0052	0.1187	1.81e15	3.17e13

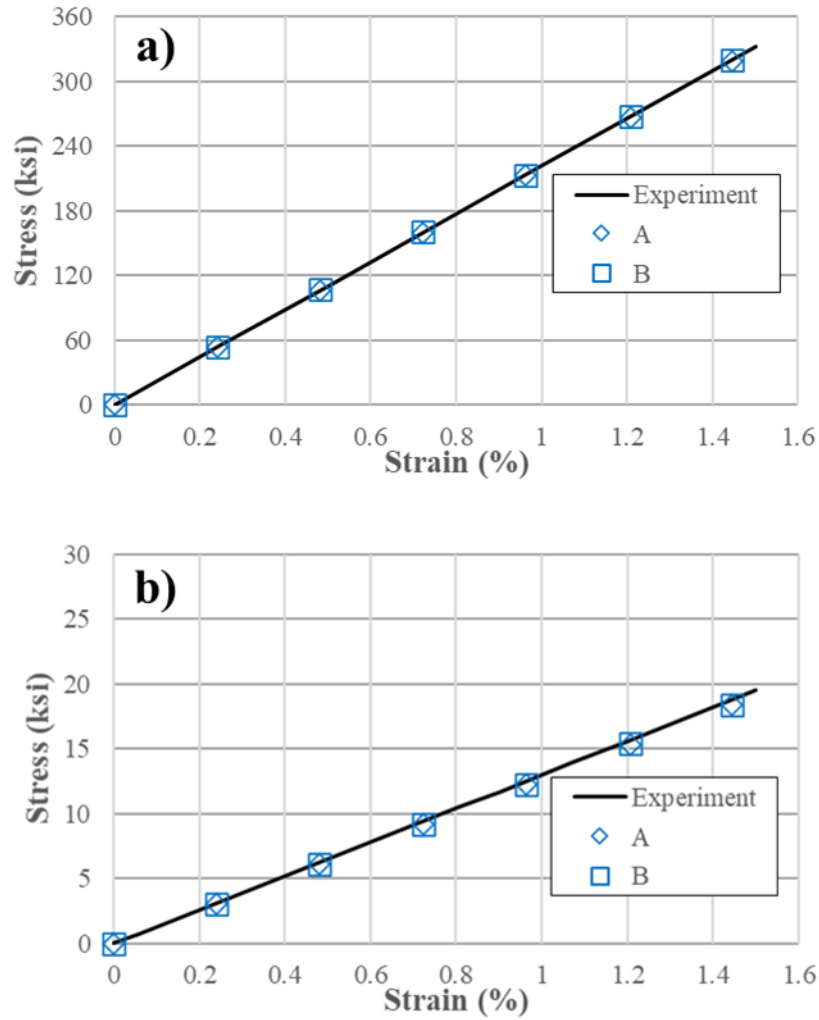


Figure 2-21: Comparison of PD and experimental stress vs. strain curve for two horizon values for (a) 0° oriented fiber and (b) 90° oriented fiber.

The validation of the improvements made to current PD approach in the area of shear nonlinearity was performed by considering lamina with ply orientations 15°, 30°, 45°, 60° and 75°. In order to further demonstrate the versatility of the current methodology, three different constitutive relationships were considered: linear, Ramberg-Osgood, and hyperbolic, as follows:

$$\textbf{Linear:} \quad f_{ij} = k_o u_{ij} \quad (2.99)$$

$$\textbf{Ramberg-Osgood:} \quad f_{ij} = \frac{k_o}{\left(1 + \left(\frac{k_o |u_{ij}|}{f_o}\right)^\eta\right)^{\frac{1}{\eta}}} u_{ij} \quad (2.100)$$

$$\textbf{Hyperbolic:} \quad f_{ij} = \frac{k_h}{\left(1 + \left(\frac{|u_{ij}|}{u_h}\right)\right)} u_{ij} \quad (2.101)$$

Following the approach detailed in Section 2.2.3, parameters for each of the constitutive relationships were found (Table 2.7) for intralaminar grid spacing $\Delta x = \Delta y = 0.0197$ in., interlaminar grid spacing $\Delta z = 0.0052$ in., and intralaminar horizon $\delta_x = \delta_y = 0.0594$ in. The linear constitutive relationship demonstrates that the initial stiffness of the system matches well with the determined constant. The spring constant decreases with an increase in angle, except for 60°, which is slightly lower than the 75° orientation.

Table 2.7: PD material parameters for shear nonlinearity.

Angle (°)	Linear	Ramberg-Osgood			Hyperbolic	
	k_o (lbf/in ⁷)	k_o (lbf/in ⁷)	f_o (lbf/in ⁶)	η	k_h (lbf/in ⁷)	u_h (in)
15	1.31e14	1.31e14	3.08e10	5.00	2.58e14	1.52e-4
30	1.06e14	1.06e14	4.22e10	3.24	1.36e14	5.71e-4
45	9.69e13	9.69e13	4.61e10	2.55	1.07e14	1.15e-3
60	8.43e13	8.43e13	3.79e10	3.78	8.86e13	2.39e-3
75	9.57e13	9.57e13	2.22e15	0.25	8.30e13	2.60e-3

Stress vs. strain curves for each of the different fiber orientations in the off-axis simulations using linear (Figure 2-22, dashed lines), Ramberg-Osgood (Figure 2-22, square symbols), and hyperbolic (Figure 2-22, circle symbols) constitutive relationships were compared against the experimental [37] measurements (Figure 2-22, solid lines). The linear constitutive relationship, as expected, does not capture the nonlinear stress vs. strain behavior exhibited in experiments for samples of 15° , 30° , and 45° fiber orientations while the nearly linear experimental responses of 60° and 75° agree quite well without any nonlinear constitutive relationship.

The Ramberg-Osgood relationship has three constants: k_o , f_o , and η , which were calculated using the numerical approach described in Section 2.2.3. The constitutive relation and parameters found capture well the nonlinearity of the 15° , 30° , and 45° cases. The greatest error lies in the 30° case, which matches well up to 0.75 %, at which point it begins to slightly overpredict the stress.

Unlike the three parameter RO relationship, the hyperbolic relationship has two parameters: k_h and u_h . The parameter k_h serves a similar purpose as the initial stiffness parameter k_o in the RO relationship. Much like the Ramberg-Osgood relationship, as the misalignment increases, the stiffness parameter decreases. The displacement-related constant u_h tends to increase with misalignment. The biggest difference between the Ramberg-Osgood and Hyperbolic constitutive relations is the shape difference in the 15° scenario. Similar to the RO scenario, the hyperbolic function overshoots the 30° case.

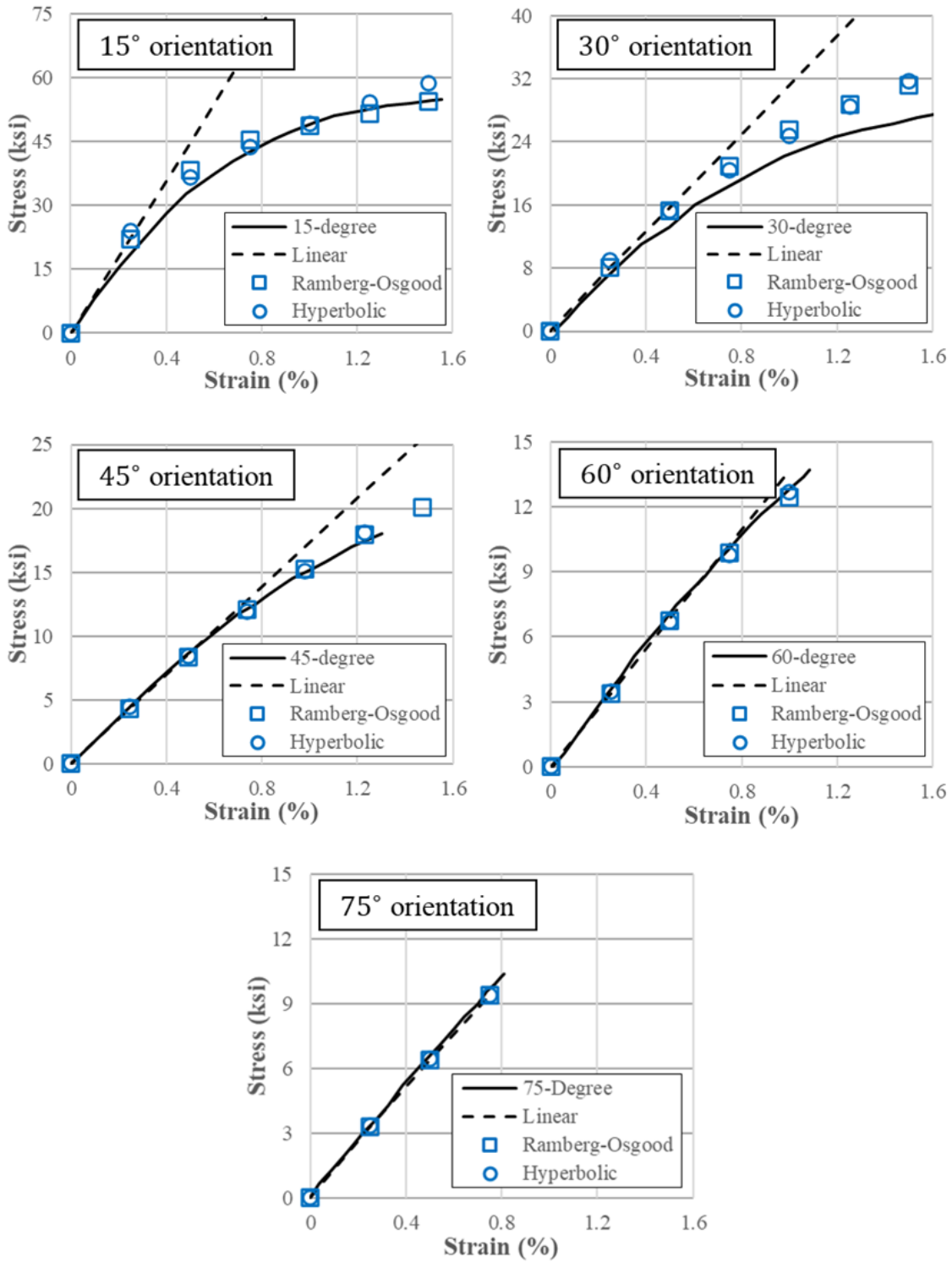
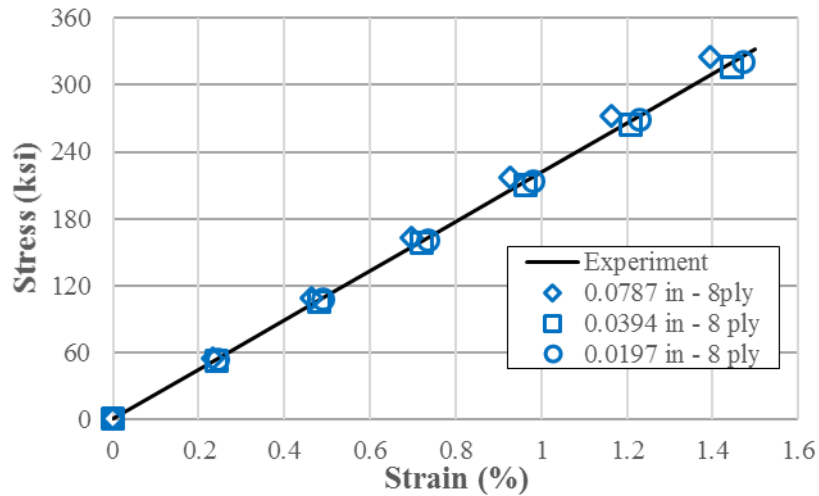


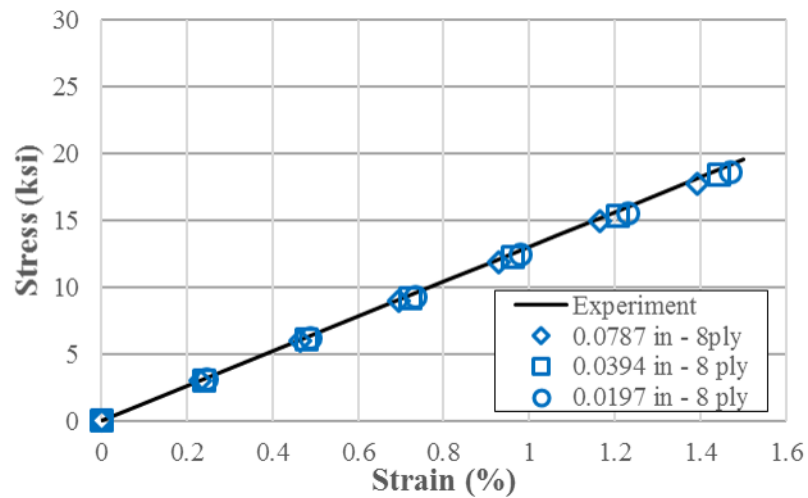
Figure 2-22: Linear (dashed line), Ramberg-Osgood (square symbols), and hyperbolic (circle symbols) constitutive relationships PD results compared against experimental (solid line) stress vs. strain curve for 5 fiber orientations.

8-ply Unidirectional Laminates:

Unidirectional 0° (Figure 2-23 (a)), 90° (Figure 2-23 (b)), and 45° (Figure 2-24) 8-ply laminates were simulated utilizing a similar approach to the one described in the preceding sections. The 8-ply laminates differ from the single ply through the introduction of inter-laminar shear and normal bonds. While the stress vs. strain response is slightly altered through the introduction of these bonds, the overall trends remain the same and the PD simulations and experiments remain in good agreement (Figure 2-23 and 2-24).



(a)



(b)

Figure 2-23: Comparison of PD and experimental 8-ply laminate stress vs. strain curves for (a) 0° oriented fiber and (b) 90° oriented fiber.

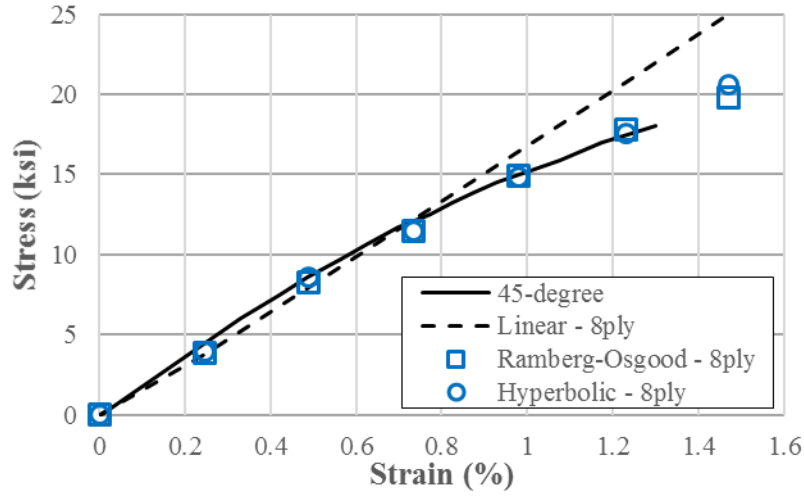


Figure 2-24: Linear (dashed line), Ramberg-Osgood (square symbols), and hyperbolic (circle symbols) constitutive relationships PD results compared against experimental (solid line) stress vs. strain curve for 45° fiber orientation and 8-ply laminate.

2.4 Strain Rate Dependence

A strain rate dependent constitutive response was introduced for intralaminar bonds by establishing a relationship between individual PD bond stretch rate and strain rate. A localized strain rate is obtained by dividing the model into subdomains (Figure 2-25). Although these subdomains can take any size and shape, to ease implementation, the subdomains are rectangular and follow ply boundaries. For example, in a 3-ply laminate with three subdomains in the x-direction and two in the y-direction, there are eighteen total subdomains (Figure 2-25).

The stretch rate $\dot{s}_{(l)(\theta)}^{(i)}$ of bond l with intralaminar bond orientation θ was calculated at each iteration i using a backward difference approximation, as follows:

$$\dot{s}_{(l)(\theta)}^{(i)} = \frac{s_{(l)(\theta)}^{(i)} - s_{(l)(\theta)}^{(i-1)}}{\Delta t}. \quad (2.102)$$

The timestep size Δt was calculated using the stability criterion provided in [22]. The current and previous bond stretch rates are $s_{(l)(\theta)}^{(i)}$ and $s_{(l)(\theta)}^{(i-1)}$, respectively. The intralaminar

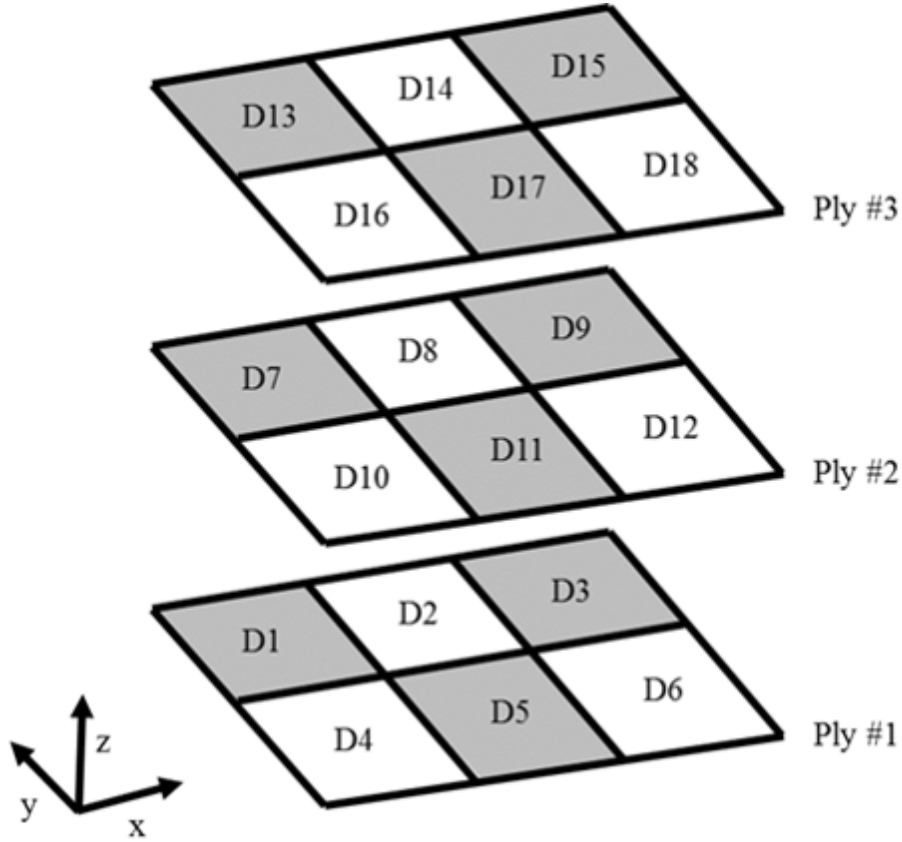


Figure 2-25: An example of subdomains on a 3-ply laminate.

bond orientation θ between material points i and j is defined using the arctangent function as

$$\theta = \tan^{-1} \left(\frac{|x_{2i} - x_{2j}|}{|x_{1i} - x_{1j}|} \right) \quad (2.103)$$

After calculating the nonlocal bond stretch rates, the local strain rate $\dot{\epsilon}_{(d)(\theta)}^{(i)}$ on each subdomain d at iteration i and orientation θ is approximated as the average of all bond stretch rates on the domain with the given orientation as follows:

$$\dot{\epsilon}_{(d)(\theta)}^{(i)} = \frac{\sum_{l=1}^N \dot{s}_{(l)(\theta)}^{(i)}}{N}. \quad (2.104)$$

The approximation of the local strain rate at each iteration provides the means for introducing a strain rate dependent constitutive response. Utilizing the aforementioned numerical

approach, PD Ramberg-Osgood parameters (k_o , f_o , η) were calculated as a function of strain rate ($\dot{\epsilon}_{(d)(\theta)}^{(i)}$). In this work, the PD parameters as functions of strain rate were found using experimental stress vs. strain curves at various strain rates. However, the PD parameters can also be found if traditional engineering Ramberg-Osgood parameters as functions of strain rate are known. Once the local strain rate and the PD Ramberg-Osgood parameters are found, piecewise linear interpolation is used to obtain the bond force density. A flow chart of the strain rate procedure is provided (Figure 2.26).

Several computational considerations are necessary for implementation. In particular, because backward difference approximation requires the stretch at the previous iteration, this information needs to be stored. For this purpose, the previous iteration displacement components are stored if a strain rate dependent constitutive model is used. This allows for the calculation of bond stretch at the previous iteration, but requires less memory than storing stretch of each bond. Additionally, to accommodate an easier implementation when parallel processing is used, the subdomains were chosen to coincide with processor boundaries. This reduces dramatically the amount of data that needs to be shared across processors in order to calculate the strain rate.

2.4.1 Dynamic Off-Axis Tension Simulation Results

The verification and validation of strain rate dependent constitutive behavior was considered in two parts: the verification of the relationship between stretch rate and strain rate and the verification of the off-axis response. First, the stretch rate formulation introduced in the preceding sections was verified by considering a 45° oriented lamina subjected to a constant strain rate. The intent of this first set of simulations was to verify the developed relationship between bond stretch rate and applied strain rate.

The applied strain rate was introduced into the system via a ramped displacement boundary condition with a final strain of 1.75%. This strain level was chosen because it allowed for clear visualization of the influence of strain rate without requiring excessive computational resources. The total simulation time t was calculated by dividing the axial

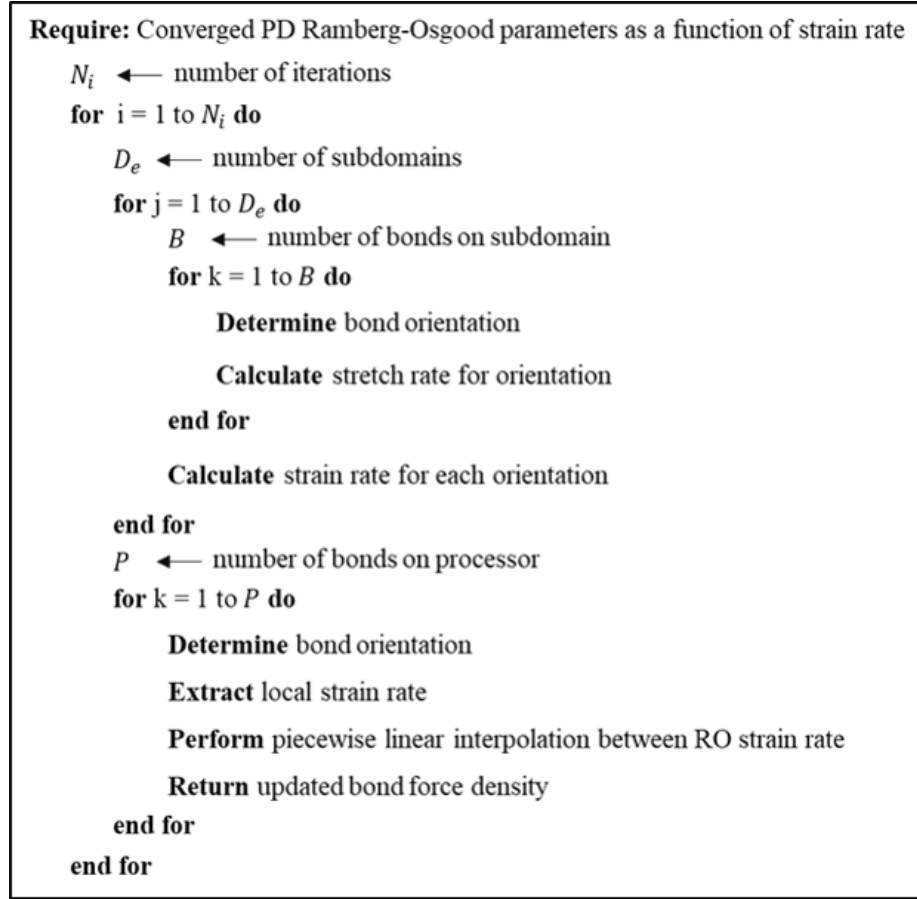


Figure 2.26: Flow chart for introducing strain rate dependence into the PD model.

strain ϵ_x by the strain rate $\dot{\epsilon}$ as

$$t = \frac{\epsilon_x}{\dot{\epsilon}}. \quad (2.105)$$

A stable time step size Δt was found following the stability criterion presented in [22]. A ramped displacement boundary condition was applied to both edges of the lamina that was equivalent to the desired strain. Because the time step is held constant to ensure numerical stability, the total number of iterations N_i are adjusted for each strain rate:

$$N_i = \frac{t}{\Delta t}. \quad (2.106)$$

The application of the strain rate was verified by tracking the displacement field (Figure 2-27) over time (Figure 2-28). In this example, a 370 /s strain rate was applied utilizing the ramped boundary condition. Every 100 time steps, the derivative of the x-displacement was taken to approximate the axial strain. Backwards difference was then used to calculate and verify the applied strain rate. While this simple methodology cannot be used for on-the-fly strain rate approximation, it provides confidence in the approach taken to introduce a constant strain rate to the material. The oscillatory response of the applied strain rate is to be expected because of the dynamics of the problem and the method of approximation.

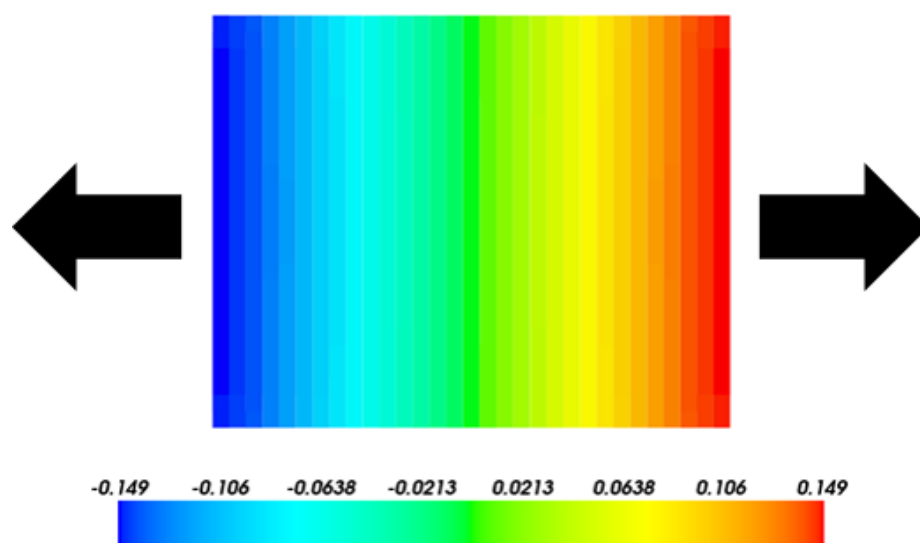


Figure 2-27: Displacement field associated with a 370 /s strain rate case.

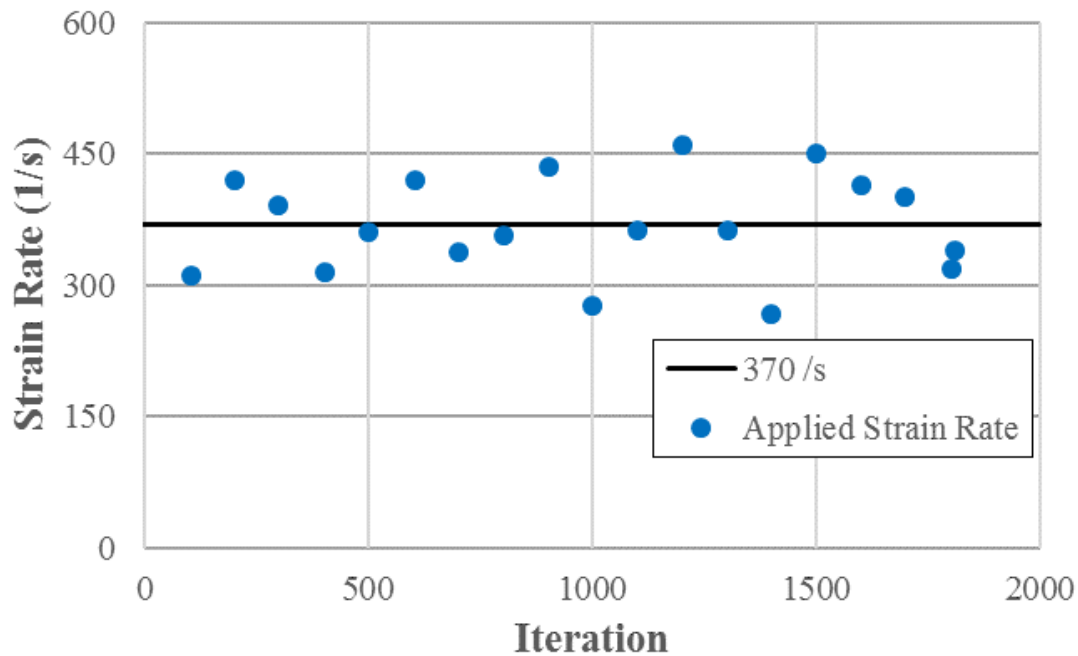


Figure 2-28: Verification of the applied strain rate methodology with the strain rate calculated from displacement field over each iteration.

The stretch rates of individual bonds can vary drastically within a family. Consider Figure 2-29 which demonstrates this variability. Figure 2-29 (a) shows the rectangular simulation domain (blue) and the chosen material point within the domain (red), which is located near the middle of the specimen. Using the methodology previously presented, stretch rate was introduced into the specimen using a ramped displacement boundary condition. Figure 2-29 (b) shows the interaction domain of the chosen material point colored by bond stretch rate. Because of the dynamics of the problem, and wave reflections on the domain, the individual bond stretch rate can vary significantly. This demonstrates some of the difficulties in calculating an engineering strain rate using a nonlocal method and illustrates the reason why subdomains are needed to approximate the strain rate.

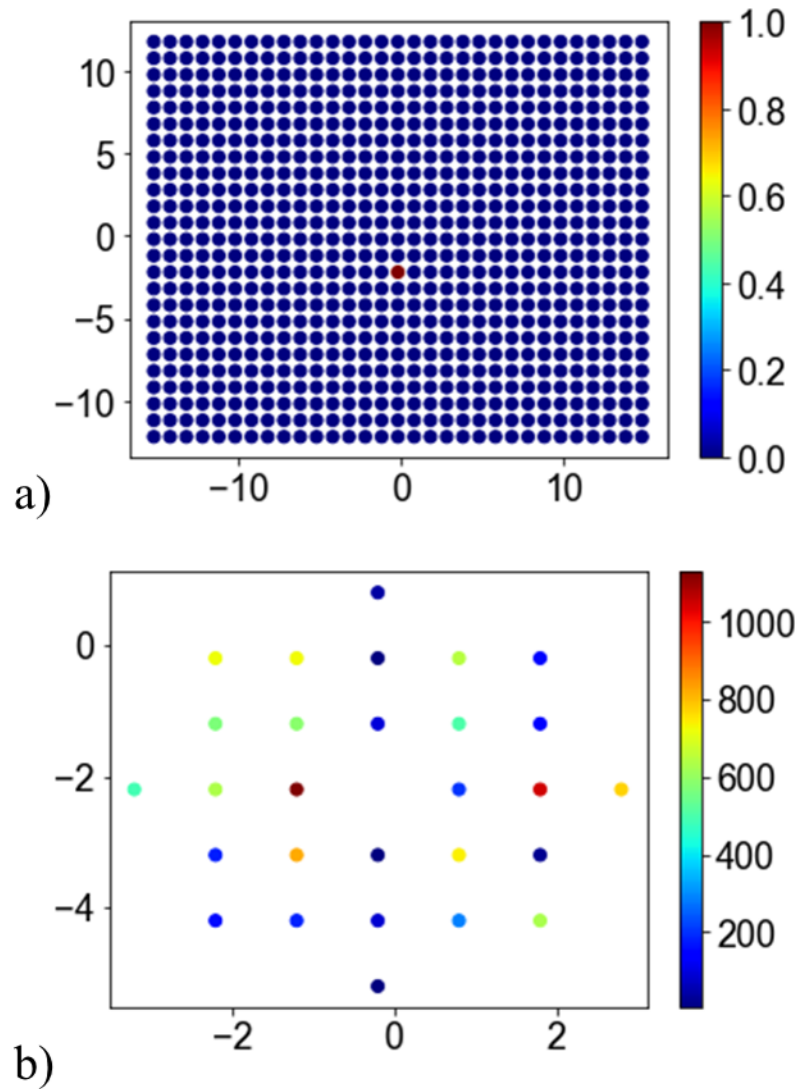


Figure 2-29: (a) Example rectangular simulation domain and a chosen material point (red). (b) Individual bonds of the chosen material point colored by strain rate magnitude.

Following the same methodology and for easy comparison, several strain rates and associated parameters used throughout this section are provided (Table 2.8).

Table 2.8: Comparison of strain rate and PD simulation parameters.

$\dot{\epsilon}$ (1/s)	Δt (s)	ϵ_x (in/in)	t (s)	N_i
1	1.33e-8	0.0175	1.75e-2	1315789
25	1.33e-8	0.0175	7.00e-4	52632
100	1.33e-8	0.0175	1.75e-4	13158
370	1.33e-8	0.0175	4.73e-5	3556

The PD strain rate formulation developed in Section 2.4 was tested by applying a 370 /s strain rate over 3556 iterations and recording the current stretch rate at each iteration (Figure 2.30). While the PD calculated strain rate oscillates (Figure 2.30 - blue curve) as the simulation progress with each iteration, the average PD calculated rate is similar to that of the applied strain rate (Figure 2.30 - black curve). This demonstrates the newly developed capability of effectively calculating a nonlocal PD strain rate.

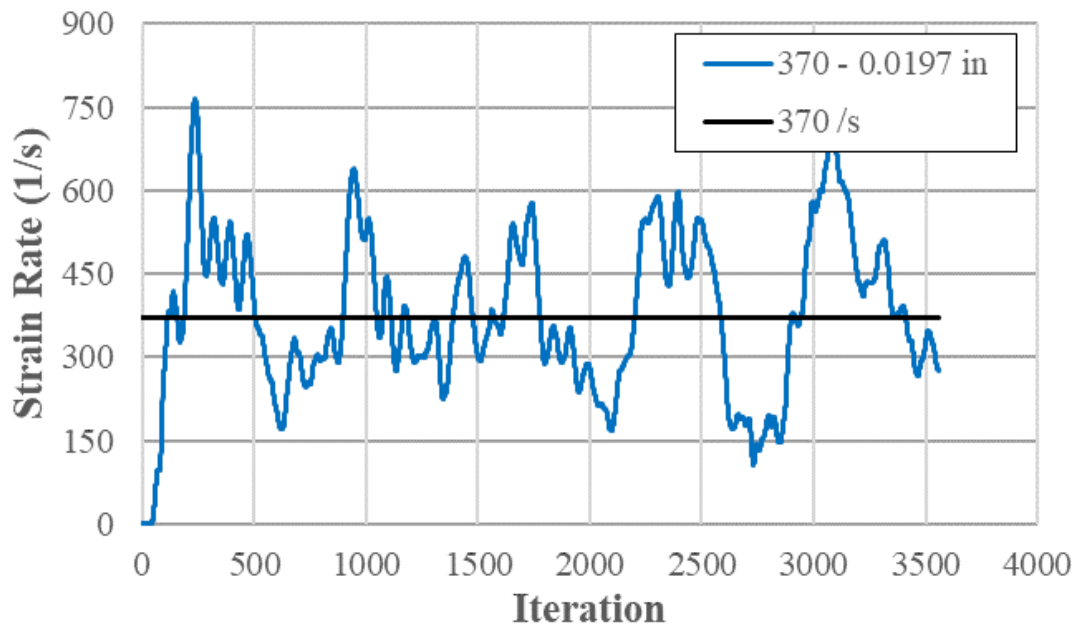


Figure 2-30: Example of strain rate variation vs. iteration for a 370/s input strain rate.

It is important to note that Figure 2-30 only visualizes bonds oriented parallel to the loading direction. The bond orientation θ of Equation (2.103) plays a key role in accurately capturing the local strain rate. For this purpose, the strain rate is decomposed based on bond orientation Equation (2.102). For a uniform intralaminar discretization and a horizon of $3.015\Delta x$, there are five different bond orientations (Figure 2-31): 0° (blue), 26.57° (yellow), 45° (gray), 63.43° (orange), and 90° (green).

As the bond orientation becomes less aligned with the loading direction, the strain rate decreases and becomes negative (Figure 2-32). If the average strain rate is used instead of the bond orientation decomposition (Figure 2-33 shown in red), the local strain rate will be significantly under predicted. For this reason, the stretch rate is calculated for each individual bond orientation and the piecewise linear interpolation is completed on an individual bond orientation basis.

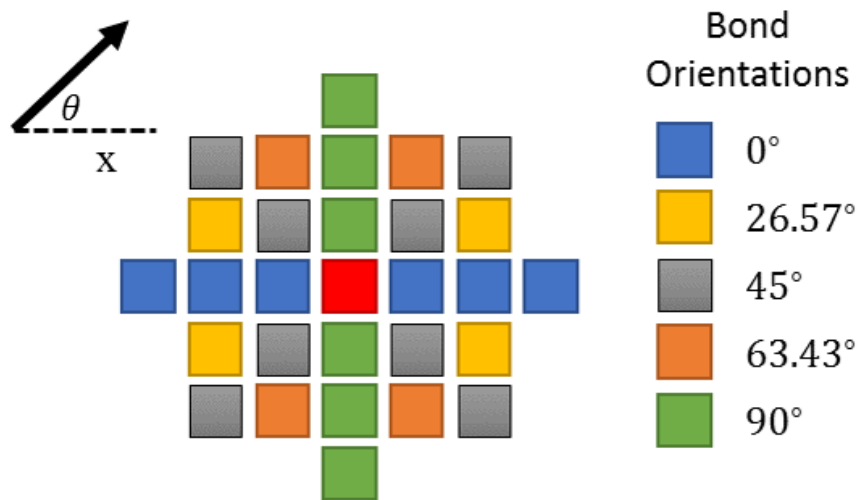


Figure 2-31: Schematic demonstrating the bond angles present with a uniform intralaminar grid spacing.

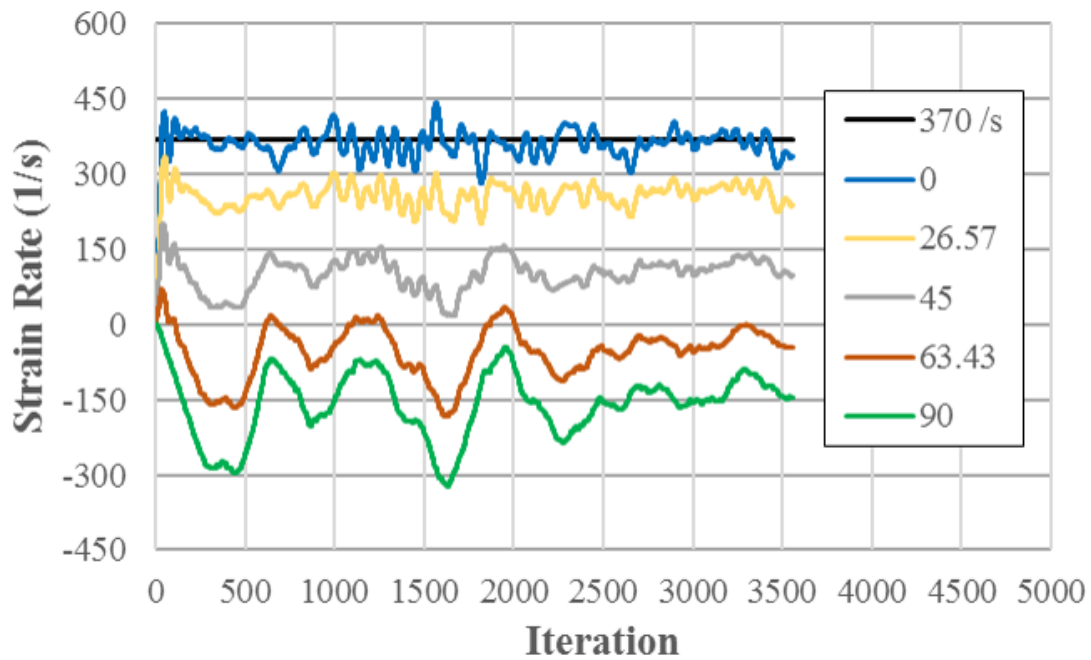


Figure 2-32: Strain rate as a function of bond orientation.

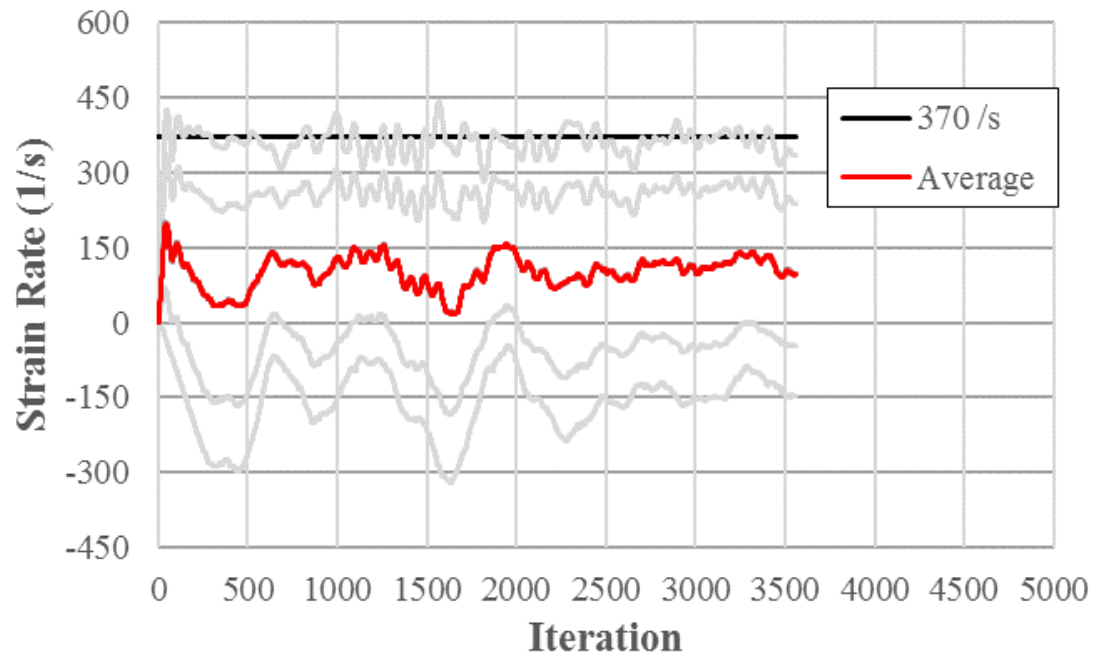


Figure 2-33: Comparison of individual bond orientation strain rate and the average strain rate of all bonds.

This simulation process was repeated (Figure 2.34) at a strain rate of 100 /s with two different intralaminar grid spacings: 0.0197 in. (Figure 2.34 - blue curve) and 0.0394 in. (Figure 2.34 - red curve). This is an important verification step as it demonstrates that the strain rate approach developed is both discretization and applied strain rate independent.

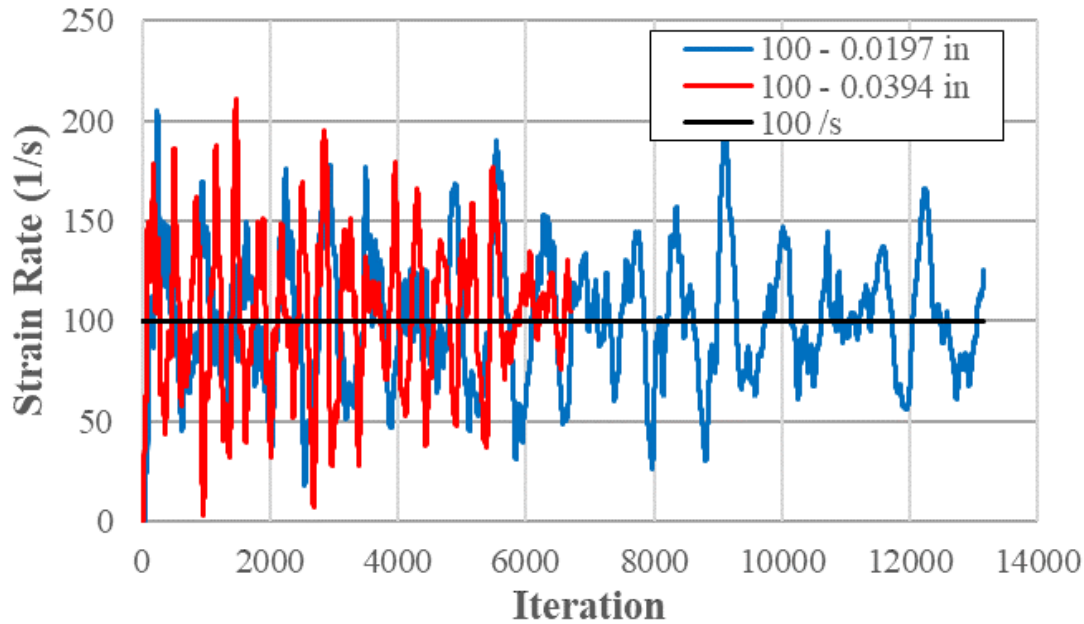


Figure 2.34: Comparison of strain rate vs. iteration for two different intralaminar discretizations.

The second part of the verification and validation consisted of performing off-axis dynamic tension simulations at three different strain rates and comparing the stress vs. strain response to experimental results. The experimental stress vs. strain response of a 45° oriented AS4/3501-6 material system published in [45] was used for comparison. For clarity, the response has been reproduced (Figure 2.35) and converted into imperial units.

Three different experimental strain rate responses are provided (0.0001 /s Quasi-Static, 0.8 /s, and 370 /s). While the stress vs. strain curves for AS4/3501-6 are significantly different than IM7/977-3, they show many of the common mechanical behaviors associated with increasing strain rate. In particular, as the strain rate is increased, the initial modulus also increases and the strain to failure decreases. Additionally, simulating with a different

material system is intended to demonstrate the objectivity of the developed approach. PD material parameters are calculated a priori as opposed to calibrated: a major milestone in the PD development process.

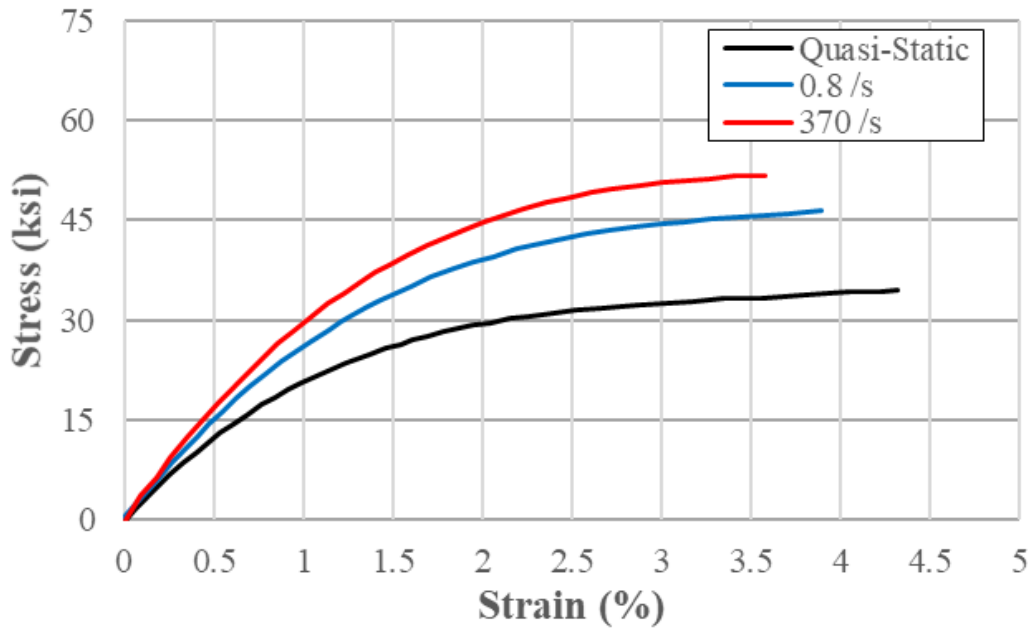


Figure 2-35: Strain rate dependent constitutive response for a composite laminate.

The first step in the PD simulation procedure was to obtain a PD functionalized representation of the three representative stress vs. strain curves. The shear nonlinearity numerical approach developed in Section 2.2.3 was used to calculate RO parameters at each rate (Table 2.9) using the discretization parameters of (Table 2.10).

A few observations can be made solely based on the calculated RO material parameters. First, following the experimental trend, as the strain-rate increases, the initial stiffness k_o increases. Similar to experiments, the difference in initial stiffness between the 0.8 /s strain rate and 370 /s strain rate is much smaller than the difference in initial stiffness between the quasi-static and 0.8 /s strain rates. The asymptotic bond force density f_o increases with increasing strain rate and hints at a change in shape of the stress vs. strain response. The shape parameter η does not appear to have a trend. Its influence on the stress vs. strain

Table 2.9: Ramberg-Osgood parameters for the material system as a function of strain rate calculated using the numerical approach.

$\dot{\epsilon}$ (1/s)	k_o (lbf/in ⁷)	f_o (lbf/in ⁶)	η
Quasi-Static	9.54e13	4.20e10	2.71
0.8	1.15e14	5.98e10	2.61
370	1.27e14	6.82e10	2.84

Table 2.10: Discretization related parameters for off-axis dynamic validation.

$\Delta x = \Delta y$ (in)	Δz (in)	δ_x (in)
0.019685	0.0075	0.05935

response should be explored in future work.

For each PD simulation, a force plane was placed in the middle of the specimen and was used to monitor force and in turn engineering stress for dynamic equilibrium. PD simulations were performed at 370 /s, 1 /s, and quasi-static strain rate conditions as opposed to the 370 /s, 0.8 /s, and 0.0001 /s experimental counterparts. The PD strain rate of 1 /s was chosen intentionally because it required considerably fewer iterations as compared to a 0.8 /s strain rate. As the strain rate is decreased, the simulations become increasingly more computationally expensive (Table 2.8). For this reason, the 370 /s and quasi-static simulations were run to 1.75% strain while the 0.8 /s strain rate simulation was run to approximately 1.25% strain. Additionally, as the strain rate decreases, the numerical stability of the simulation decreased. To help stabilize the system, a small viscous damping coefficient was applied to the 1 /s strain rate PD simulation. The application of a small viscous damping coefficient helped with numerical convergence (without inadvertently influencing the response) and is the reason for the much smoother stress vs. strain simulation response (Figure 2.36b). The PD quasi-static simulation (Figure 2.36c) was performed using an ex-

PLICIT solver with strain rate independent material properties. This enabled the simulation to be performed efficiently without any viscous damping. Overall, the PD and experimental stress vs. strain responses show great agreement (Figure 2.36).

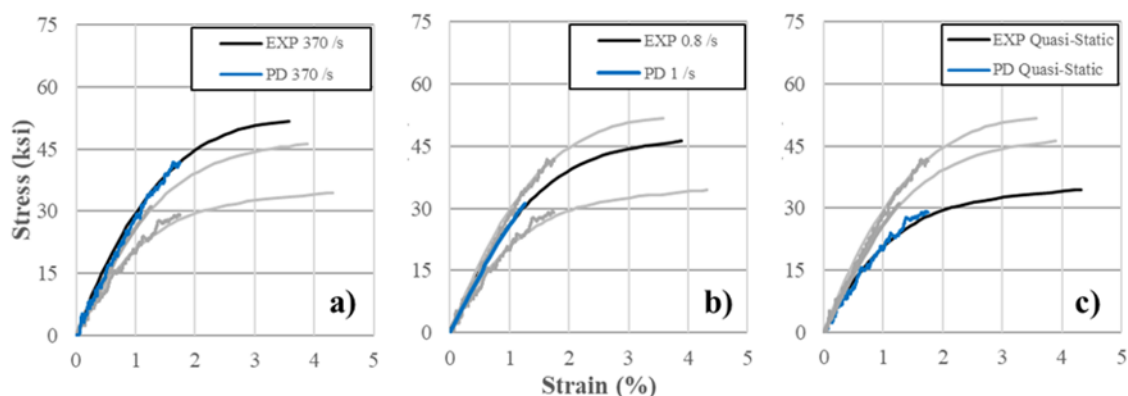


Figure 2.36: Comparison of PD stress vs. strain predictions and experimental stress vs. strain response for a) 370 /s b) 0.8 /s and c) 0.0001 /s strain rates.

For PD strain rates in-between the known RO parameters of (Table 2.9), piecewise linear interpolation is used. This was verified by running PD simulations at strain rates of 10 /s (Figure 2.37 - gray curve), 25 /s (Figure 27 - green curve), 37 /s (Figure 2.37 - gold curve), 100 /s (Figure 2.37 - purple curve), and 185 /s (Figure 2.37 - brown curve). As desired, each stress vs. strain response lies in-between the experimental 370 /s (Figure 2.37 - red curve) and 0.8 /s (Figure 2.37 - blue curve) strain rates.

The results presented thus far were completed using a single processor and stretch rate subdomain. Because low-velocity impact is a computationally expensive problem and has more localized strain-rates as compared to an off-axis tension test, it was important to introduce and verify the localized strain rate calculations presented in (Section 2.4) with multiple processors. To this end, the lamina was divided into 5 subdomains along the loading direction (x) (Figure 2.38). In the same manner as the previous off-axis dynamic simulations, a 370 /s strain rate was applied using a ramped displacement boundary condition to both ends of the lamina. The local strain rate was calculated on each subdomain for each iteration (Figure 2.39).

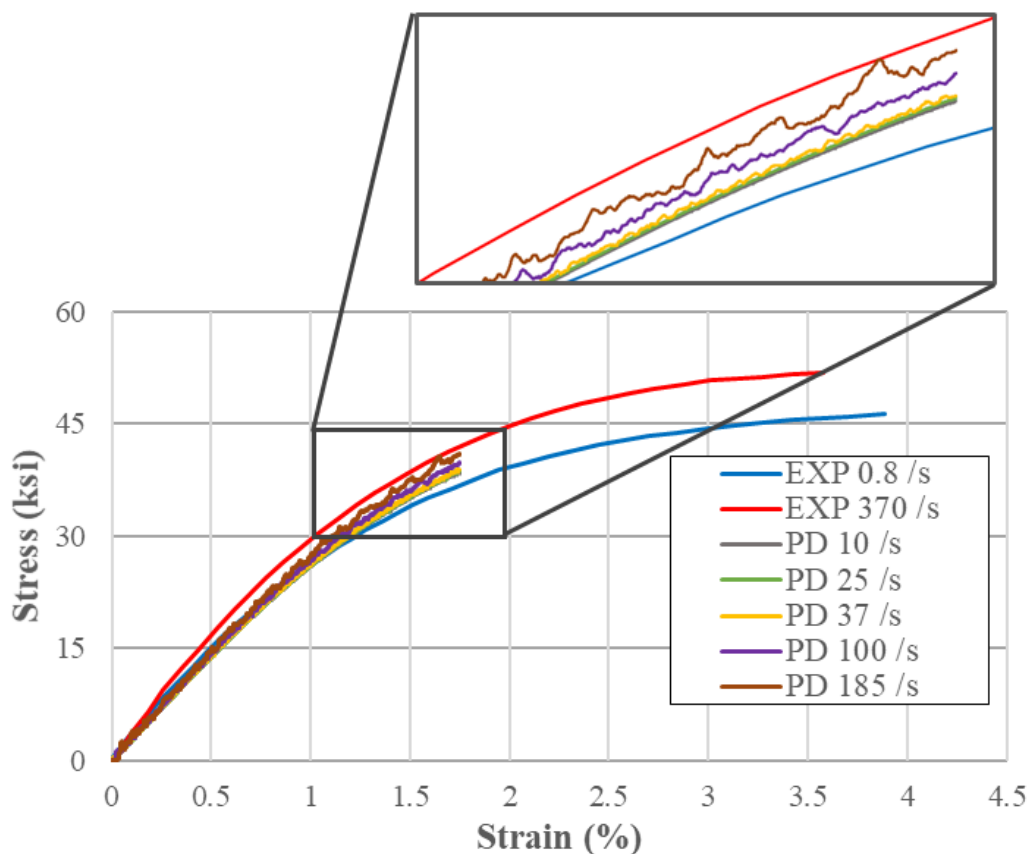


Figure 2-37: PD simulations with strain rates in-between the known experimental Ramberg-Osgood parameters.

As expected, each subdomain has a differing stretch rate oscillation. While there are extremes in the oscillation, such as the first subdomain, labeled D1 (Figure 29 - gray curve). Most subdomains have similar oscillation amplitudes and frequencies. Importantly, all of the subdomains oscillate about the applied 370 /s strain rate.

The stress vs. strain response between a PD simulation with 1 stretch rate domain (Figure 2-40 - blue curve) was compared to a PD simulation with 5 stretch rate subdomains (Figure 2-40 - red curve) with an applied strain rate of 370 /s. While there are slight differences in the oscillation of the response, the overall trend in the response is the same.

Future work should consider the influence of the size and shape of the subdomains on the calculated local strain rate. Additionally, nonuniform subdomains should be considered, which would allow for varying degrees of accuracy in the local strain rate calculations

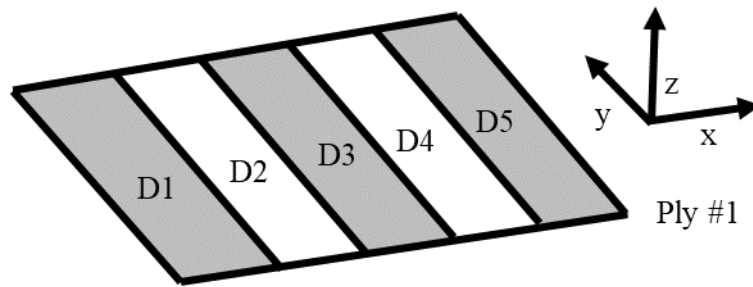


Figure 2-38: Schematic with stretch rate subdomains.

and would be beneficial when a region of strain rate sensitivity is known in advance.

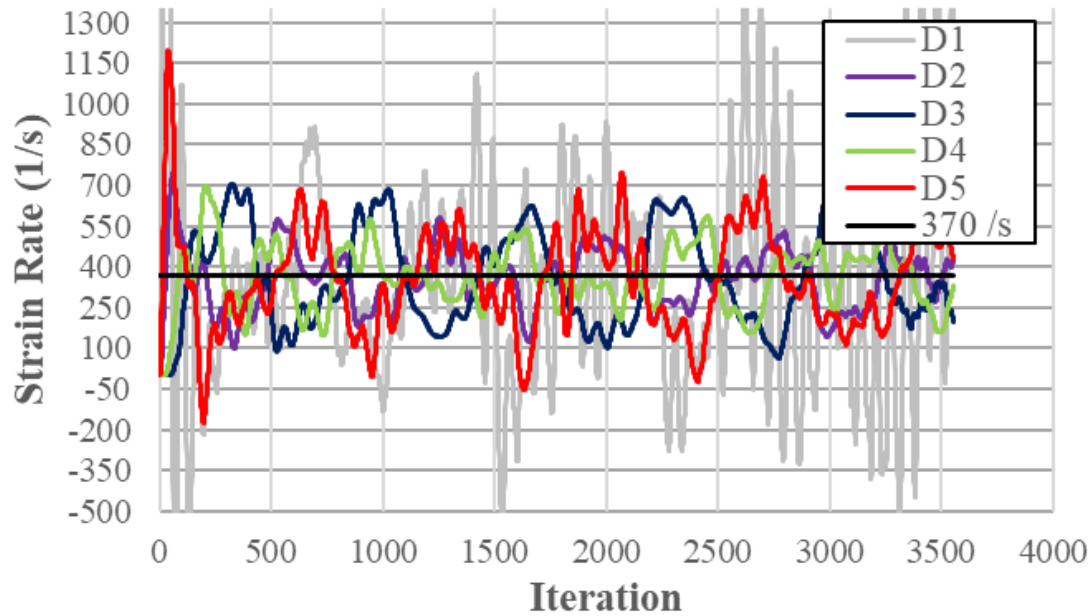


Figure 2-39: Comparison of the local strain rate on each subdomain “D” vs. iteration.

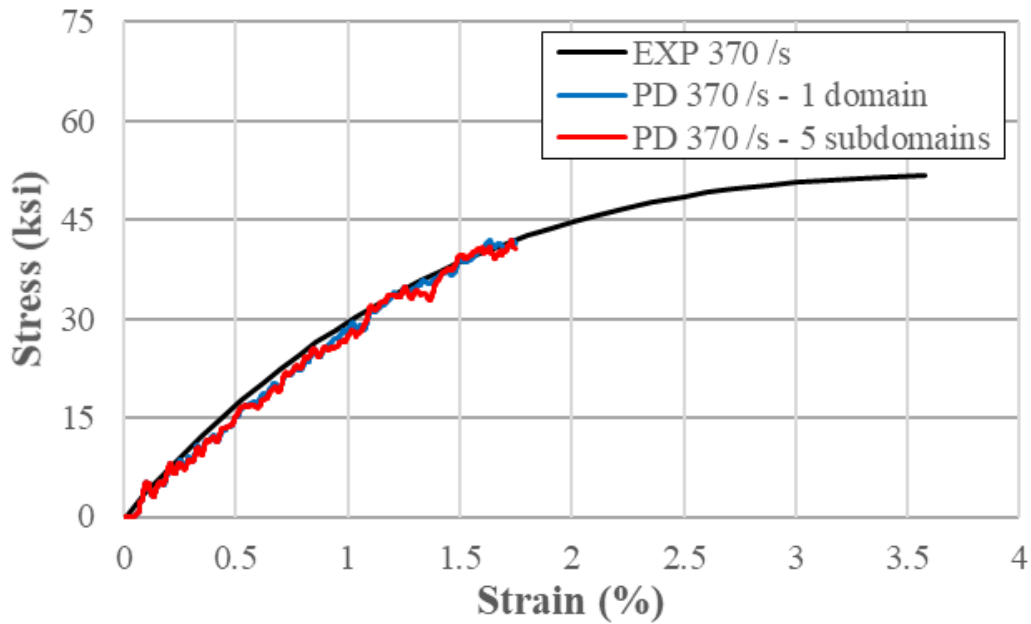


Figure 2-40: Comparison of stress vs. strain response for 1 stretch rate domain (blue) vs. 5 stretch rate subdomains (red).

2.5 Low-Velocity Impact Simulation Results

The developments made to the PD approach described in Section 2.2.3 and 2.4 have been applied to a multitude of problems with increasing complexity for validation purposes. First, a set of quasi-static off-axis tension tests were simulated using the improved formulation. Next, the off-axis tension simulations were repeated under dynamic loading conditions for a 45-degree lamina. In the subsequent sections, low-velocity impact simulations were performed to predict a laminate response under a range of energy levels. Simulation predictions were made at different stages of approach development (i.e., legacy, shear nonlinearity added, strain rate dependence added) and compared against the experimental measurements.

2.5.1 Problem Description

The PD approach with the improvements previously described were validated against experimental measurements on quasi-isotropic laminates subjected to low-velocity impact. A total of four impact energies were performed: 150 in-lbf, 187.5 in-lbf, 225 in-lbf, and 262.5 in-lbf. A 25 ply IM7/977-3 laminate with a quasi-isotropic stacking sequence, [(45/-45/0/90)3/0/(90/0/-45/45)3], was simulated using an intralaminar grid spacing of $7.87e-2$ in. and interlaminar grid spacing of $5.20e-3$ in. (Table 2.11). The interlaminar grid spacing was chosen to be equal to the ply thickness ensuring that there is only one layer of material points per ply. The intralaminar grid spacing was chosen to balance the need of accuracy and computational efficiency. The intralaminar and interlaminar horizons were set to $3.015\Delta x$ and $3.015\Delta z$, respectively. The intralaminar and interlaminar horizon were chosen based on previous experience in the literature [25].

The fiber, matrix, normal, and shear material parameters were calculated using the numerical approach described in (Section 2.2) and tabulated in (Table 2.9). Following the strain rate methodology outlined in (Section 2.4), the Ramberg-Osgood material parameters were calculated and input at two different strain rates: quasi-static and 0.53 /s (Table 2.13). The intralaminar and interlaminar input failure parameters, as described in (Sec-

tion 2.2.5), are provided in (Table 2.14). The simulation domain contained approximately 207,000 material points. Simulations were run on 56 processors and took approximately (50-60 hours) to reach a total simulation time of 7 ms. A total of 1,400 strain rate subdomains were used. There were 8 subdomains in the x-direction and 7 subdomains in the y-direction for each individual ply. Simulations were compared against experimental results provided by North Carolina State University collaborators under the IDAT (Impact Damage and Analysis Tools) project.

Table 2.11: PD discretization parameters used for low-velocity impact simulations.

$\Delta x = \Delta y$	Δz	V	δ_x	δ_z
(in)	(in)	(in ³)	(in)	(in)
7.87e-2	5.20e-3	3.22e-5	2.37e-1	1.57e-2

Table 2.12: Calculated PD material parameters utilizing the numerical approach.

k_f	k_m	k_n	k_s	ϕ_{yld}
(lbf/in ⁷)	(lbf/in ⁷)	(lbf/in ⁷)	(lbf/in ⁵)	(rads)
2.37e13	2.84e11	5.26e12	3.29e8	2.88e-3

Table 2.13: Calculated PD RO material parameters at various strain rates.

$\dot{\epsilon}$	k_o	f_o	η
(1/s)	(lbf/in ⁷)	(lbf/in ⁶)	
Quasi-Static	5.00e11	1.45e9	0.871
0.53	4.51e11	1.05e9	1.635

Table 2.14: Failure parameters input in the PD model.

σ_{11}^f	ϵ_{11}^f	σ_{22}^f	ϵ_{22}^f	G_{Ic}	G_{IIc}
(ksi)	(%)	(ksi)	(%)	(in-lbs/in ²)	(in-lbs/in ²)
421	1.84	13	1.09	1.47	2.94

2.5.2 Simulation Approach Improvement Summary

To highlight the differences made by each improvement, presented in the preceding sections, the energy level 225 in-lbf was selected and compared across four different developmental stages (PD01-PD04):

- PD01: Legacy approach: PD material parameters using the legacy approach are calibrated for the current discretization by simulating simple quasi-static tension tests and optimizing against benchmark solutions.
- PD02: Objective baseline: The PD elastic and strength parameters were objectively evaluated with no need for iteratively solving the problem in search of optimized values. Linear bond behavior for all bond types was used.
- PD03: Shear nonlinearity: In this solution, shear nonlinearity was added to the objective baseline.
- PD04: Strain rate dependence: This solution includes all improvements.

Prior to the implementation of the numerical approach (Section 2.2.2), PD material parameters for the laminate model were calibrated using an inverse approach first described in [41]. PD material parameters are calibrated in this approach by performing quasi-static simulations and comparing against FE or analytical solutions. This method, while well established, is cumbersome to perform and requires extensive user input and experience. Often, the calibration procedure can take the user several days to set up and perform the simulations. Errors at any stage in the process can be detrimental and ultimately give

incorrect PD material parameters. Furthermore, as the discretization of the system changes, re-calibration of the PD material parameters is necessary. These small details limit the users ability to explore the affect of nonlocality and discretization on the solution.

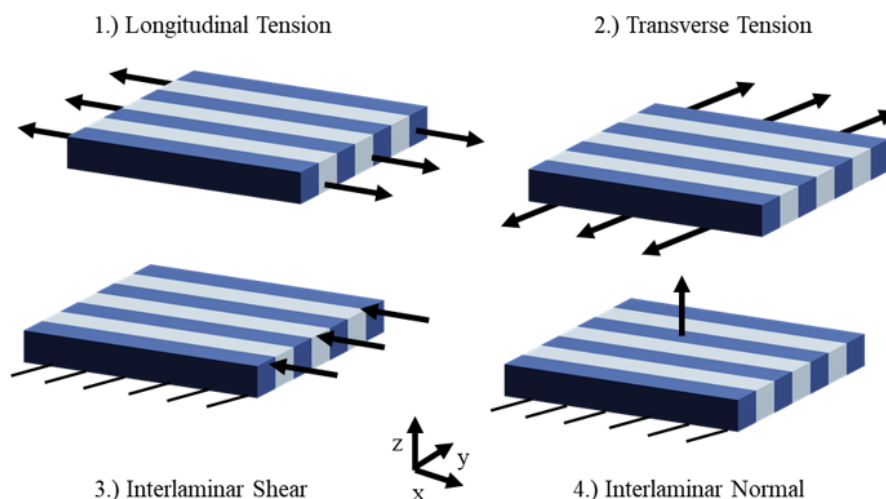


Figure 2-41: Quasi-static tests used for PD material parameter calibration. 1.) longitudinal tension (fiber bond material parameter), 2) transverse tension (matrix bond material parameter), 3.) interlaminar shear (interlaminar shear bond material parameter), 4.) interlaminar normal (interlaminar normal bond material parameter)

Figure 2-41 shows the quasi-static tests (longitudinal tension, transverse tension, interlaminar simple shear, and interlaminar normal) used to perform the PD material constant calibration. An 8-ply unidirectional laminate with approximate dimensions 2 in. \times 2 in. \times 0.0416 in. was used in each of the tests. The strain energy and internal force were compared against analytical solutions using the same boundary conditions. Because of the calibration involved, the legacy approach is a more time intensive and potentially less accurate than the numerical approach. It is included in this dissertation solely to provide a baseline on which to compare the progress and improvement of the current approach.

The legacy approach, PD01 (blue), overpredicted both maximum force and the time at which the maximum force is reached (Figure 2-42) while underpredicting the maximum impactor displacement (Figure 2-43) for impact energy 225 in-lbf. The slope of the force-time response is less than that of the experiments and ultimately leads to a an overprediction

of the impact duration. The simulation was stopped at approximately 6.5 ms as no further delamination or damage occurred.

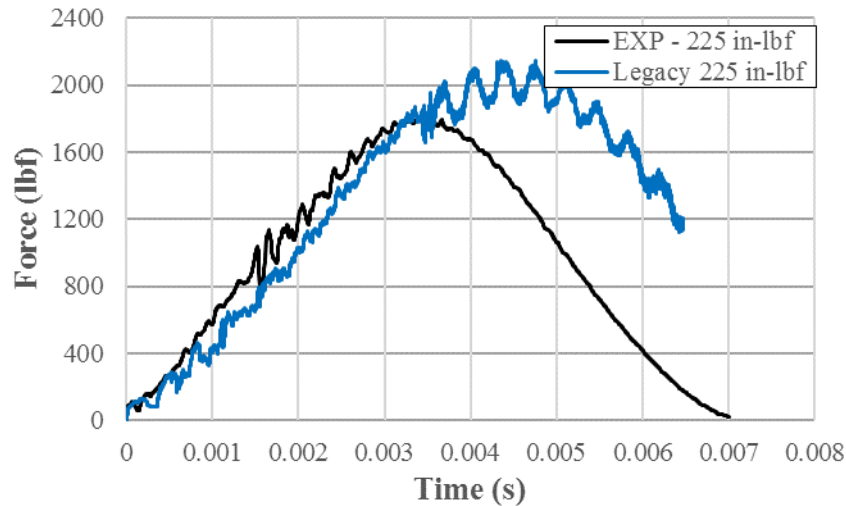


Figure 2-42: Force vs. time response predicted by legacy PD approach (PD01) compared against experimental measurements for 225 in-lbf impact energy.

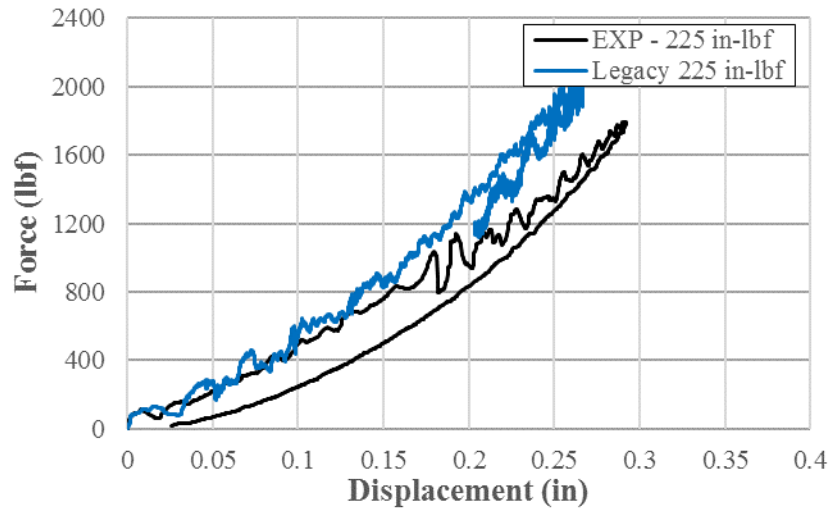


Figure 2-43: Force vs. displacement response predicted by legacy PD approach (PD01) compared against experimental measurements for 225 in-lbf impact energy.

The objective baseline approach, PD02, underpredicted the maximum force and the time at which the maximum force is reached (Figure 2-44) for impact energy 225 in-lbf; it also underpredicted the maximum impactor displacement (Figure 2-45) for the same case. It is worth noting that the force vs. time behavior exhibits a prolonged plateau near maximum force value before the unloading commences. This is also observed in the force vs. displacement behavior with a longer contact duration; local deformation and fiber bond failure near the impactor is thought to be responsible for this behavior. In comparison to the legacy approach, the simulation overpredicted the initial slope of the force vs. time response.

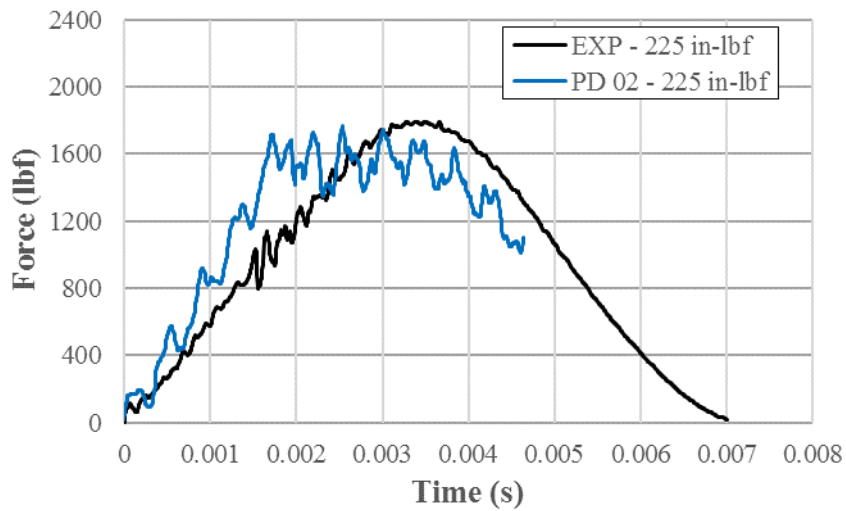


Figure 2-44: Force vs. time response predicted by objective baseline PD approach (PD02) compared against experimental measurements for 225 in-lbf impact energy.

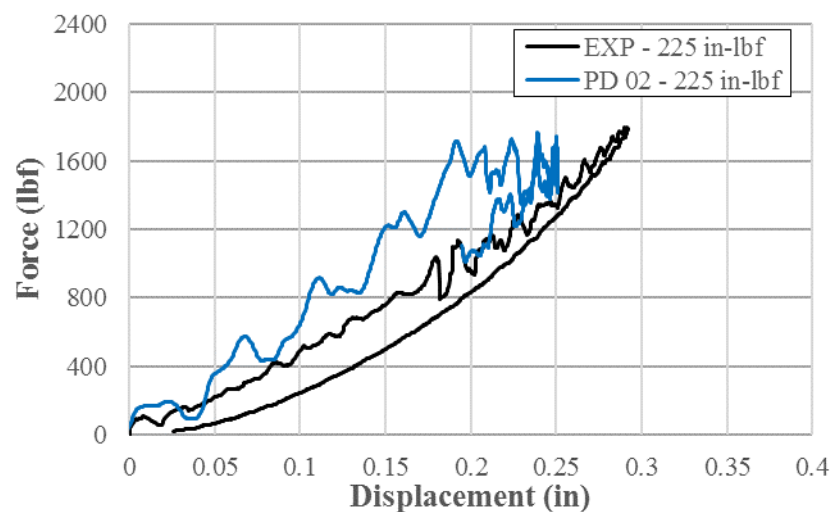


Figure 2-45: Force vs. displacement response predicted by objective baseline PD approach (PD02) compared against experimental measurements for 225 in-lbf impact energy.

The addition of shear nonlinearity proved to be most significant in improving the simulated impact response. Adding shear nonlinearity to the objective baseline captured well the experimentally measured force (Figure 2-46), displacement (Figure 2-47), and impact duration values with great accuracy. Nonlinearity of matrix and shear bond constitutive response provides a softening effect which manifests in a reduction of the initial slope of the force vs. time curve and allows for an increased peak displacement.

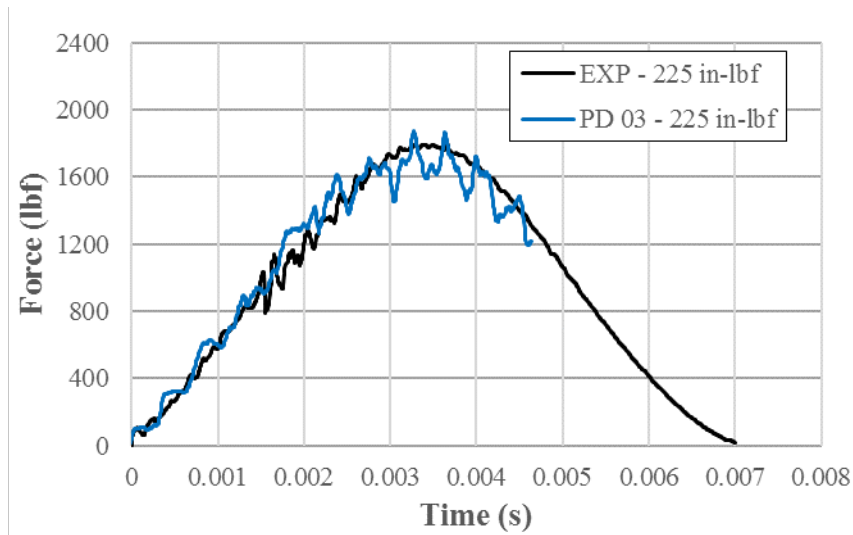


Figure 2-46: Force vs. time response predicted by objective baseline PD with shear nonlinearity approach (PD03) compared against experimental measurements for 225 in-lbf impact energy.

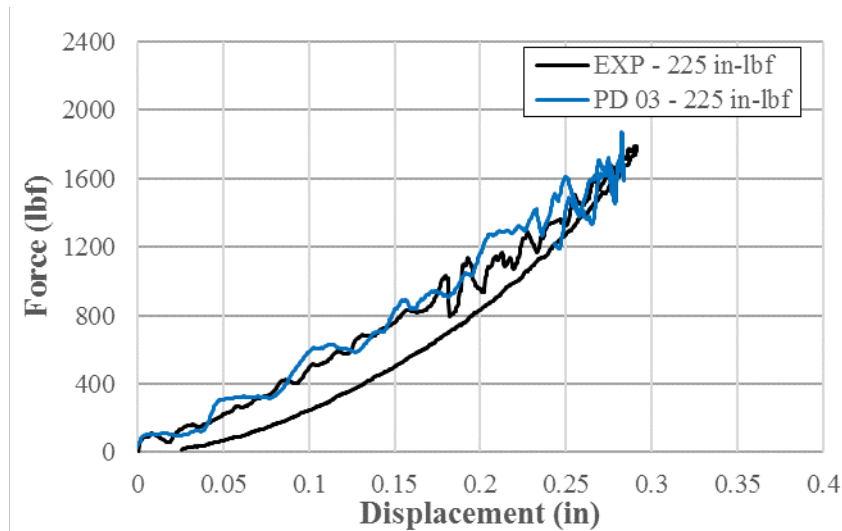


Figure 2-47: Force vs. displacement response predicted by objective baseline PD with shear nonlinearity approach (PD03) compared against experimental measurements for 225 in-lbf impact energy.

2.5.3 Simulation Results

The final improvement to the simulation approach consisted of incorporating intralaminar strain rate dependent material properties. This approach (PD04) was applied to all four en-

ergy levels. The force vs. time predictions for impact energies 150 in-lbf (Figure 2-48) and 187.5 in-lbf (Figure 2-49) exhibit remarkable agreement against the experimental measurements. However, the simulation approach slightly underpredicts the unloading portion of the response for impact energy 225 in-lbf (Figure 2-50). At the highest energy level, 262.5 in-lbf, the force drop, typically associated with back face fiber splitting, is not captured (Figure 2-51). Experimentally, this drop occurs close to the peak force at approximately 3 ms. The reasons for which the PD simulations do not capture this drop are explored in subsequent sections. Finally, the addition of strain rate dependence appears to have only minor influence on the overall response. This lack of influence could be related to the positioning or locality of the strain rate subdomains, or simply that the strain rate and therefore impact energy needs to be higher for a noticeable difference. Further exploration is needed in the future to fully analyze the influence of strain rate on LVI.

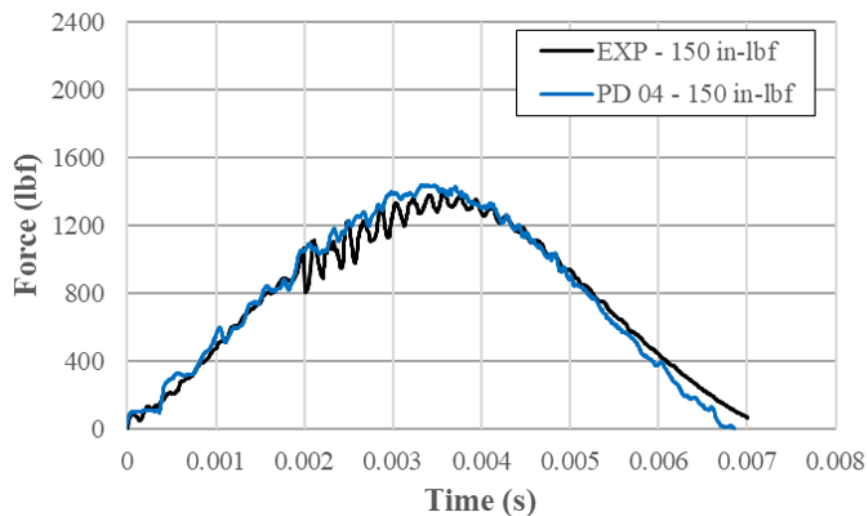


Figure 2-48: Force vs. time response predicted by objective baseline PD with shear nonlinearity and strain rate dependent material properties approach (PD04) compared against experimental measurements for 150 in-lbf impact energy.

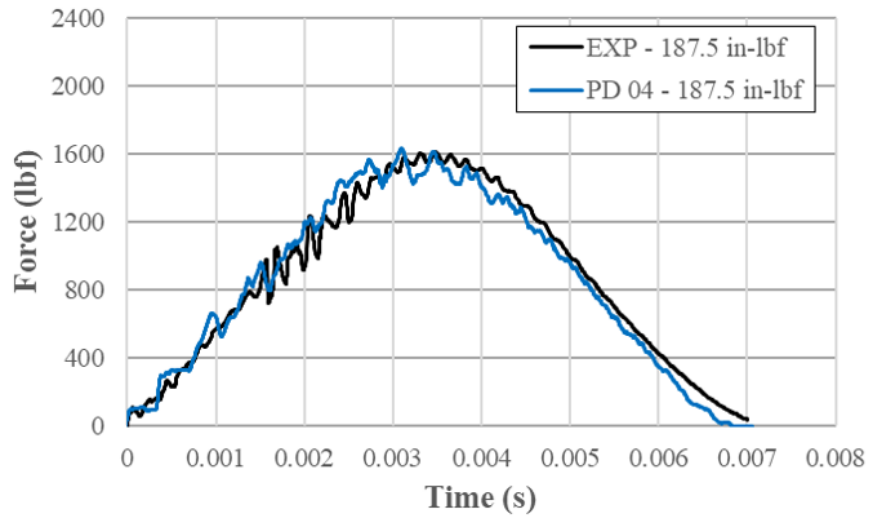


Figure 2-49: Force vs. time response predicted by objective baseline PD with shear nonlinearity and strain rate dependent material properties approach (PD04) compared against experimental measurements for 187.5 in-lbf impact energy.

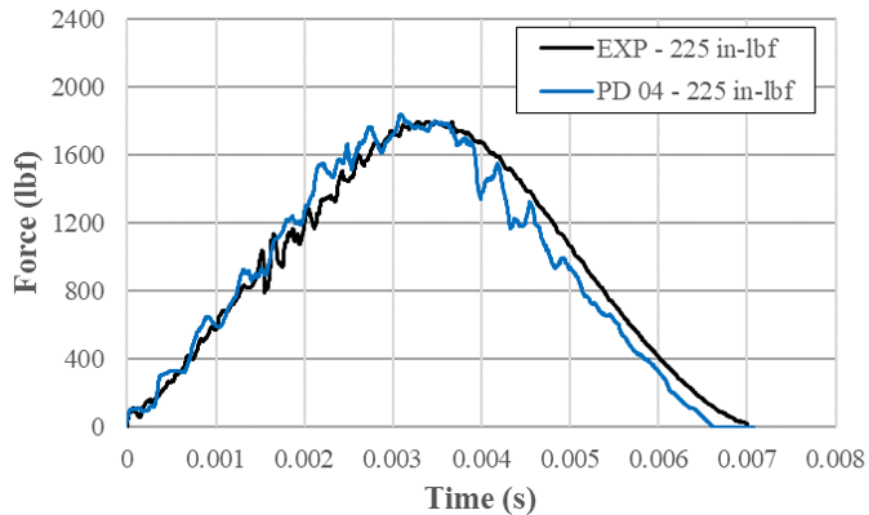


Figure 2-50: Force vs. time response predicted by objective baseline PD with shear nonlinearity and strain rate dependent material properties approach (PD04) compared against experimental measurements for 225 in-lbf impact energy.

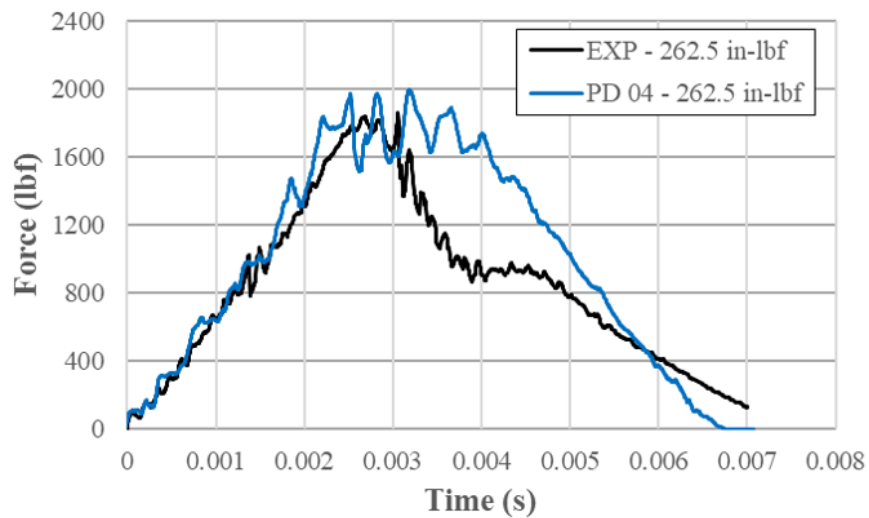


Figure 2-51: Force vs. time response predicted by objective baseline PD with shear nonlinearity and strain rate dependent material properties approach (PD04) compared against experimental measurements for 262.5 in-lbf impact energy.

Force vs. displacement responses for four energy levels were compared against the experiments. The comparisons concerning energy levels 150 in-lbf (Figure 2-52), 187.5 in-lbf (Figure 2-53), and 225 in-lbf (Figure 2-54) are considered to have high accuracy. The force vs. displacement response for the highest energy level, 262.5 in-lbf (Figure 2-55) predicted the loading portion as well as the maximum impactor displacement with great accuracy, but as with the force vs. time response, the sharp drop in force was not captured, which led to a departure between the two responses in the unloading portion.

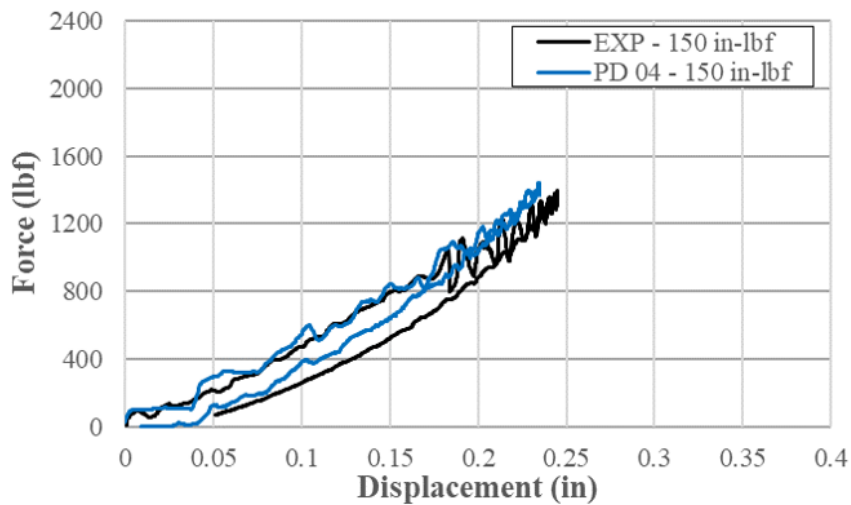


Figure 2-52: Force vs. displacement response predicted by objective base-line PD with shear nonlinearity and strain rate dependent material properties approach (PD04) compared against experimental measurements for 150 in-lbf impact energy.

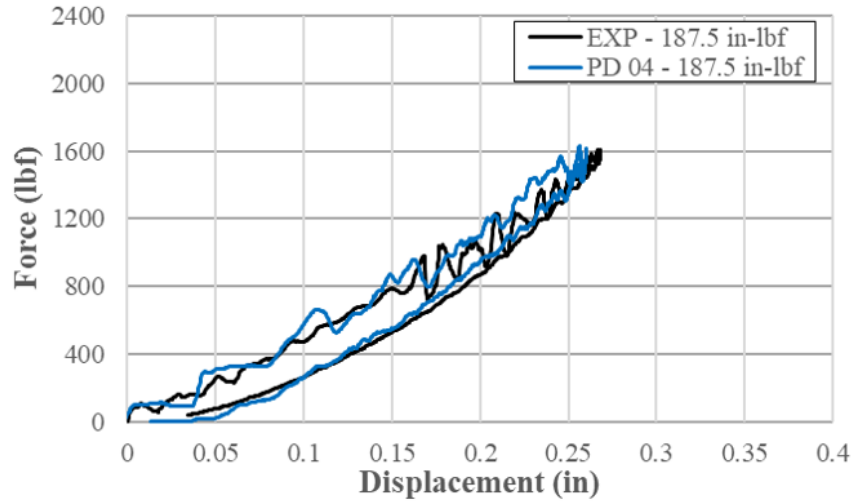


Figure 2-53: Force vs. displacement response predicted by objective baseline PD with shear nonlinearity and strain rate dependent material properties approach (PD04) compared against experimental measurements for 187.5 in-lbf impact energy.

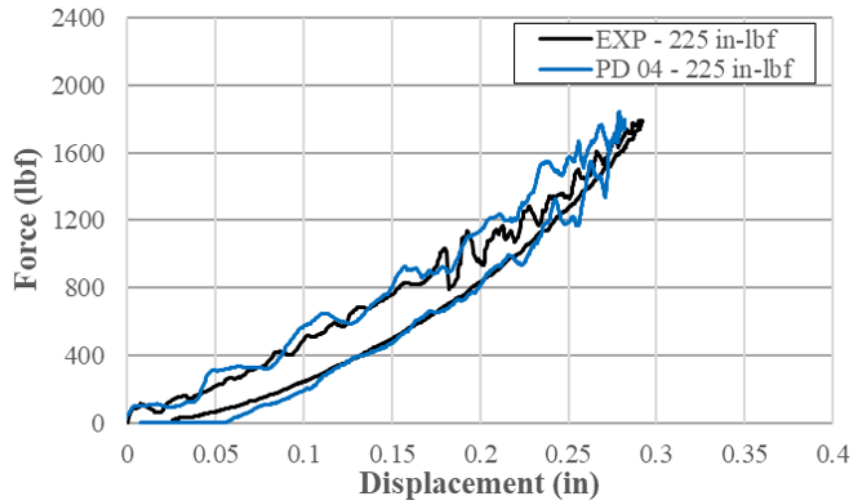


Figure 2-54: Force vs. displacement response predicted by objective baseline PD with shear nonlinearity and strain rate dependent material properties approach (PD04) compared against experimental measurements for 225 in-lbf impact energy.

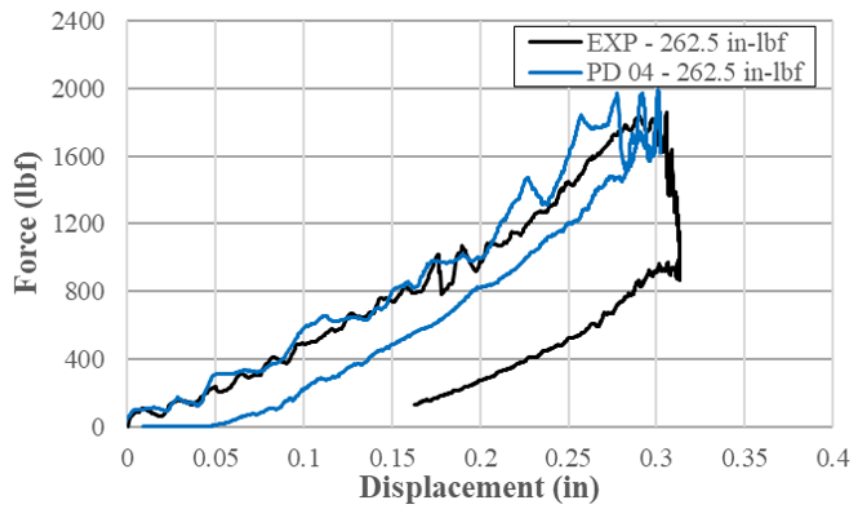


Figure 2-55: Force vs. displacement response predicted by objective base-line PD with shear nonlinearity and strain rate dependent material properties approach (PD04) compared against experimental measurements for 262.5 in-lbf impact energy.

Energy vs. time responses for each energy level were compared against the experiments: 150 in-lbf (Figure 2-56), 187.5 in-lbf (Figure 2-57), 225 in-lbf (Figure 2-58), and 262.5 in-lbf (Figure 2-59). The first energy level (Figure 2-56) slightly underpredicted the absorbed energy; alternatively, the second (Figure 2-57) and third (Figure 2-58) energy levels slightly overpredicted the absorbed energy. As expected, based on the force vs. time and force vs. displacement responses, the largest difference between the simulated and experimental results occurred at the highest energy level (Figure 2-59). While the simulated response continues the trend established by the previous energy levels, the experimental results showed a much larger absorbed energy. Similar to the force vs. time response, this departure is caused by the simulation not capturing complete fiber failure on the back surface.

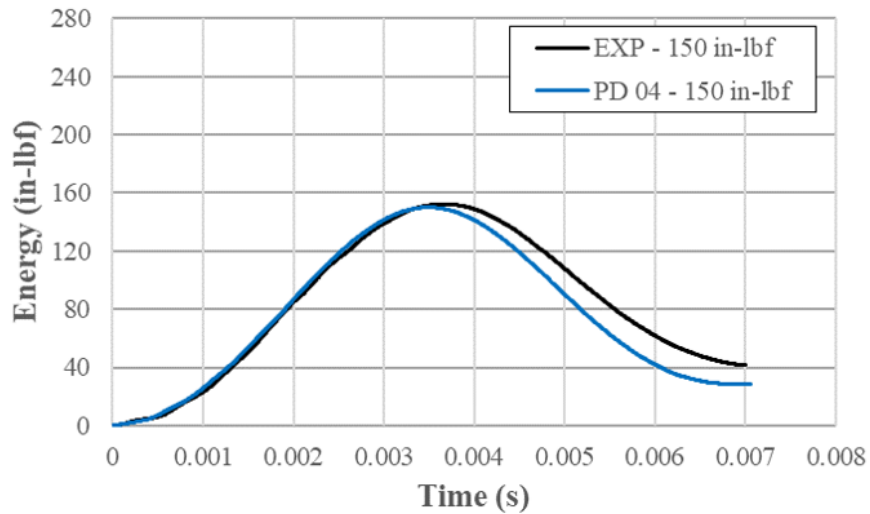


Figure 2-56: Energy vs. time response predicted by objective baseline PD with shear nonlinearity and strain rate dependent material properties approach (PD04) compared against experimental measurements for 150 in-lbf impact energy.

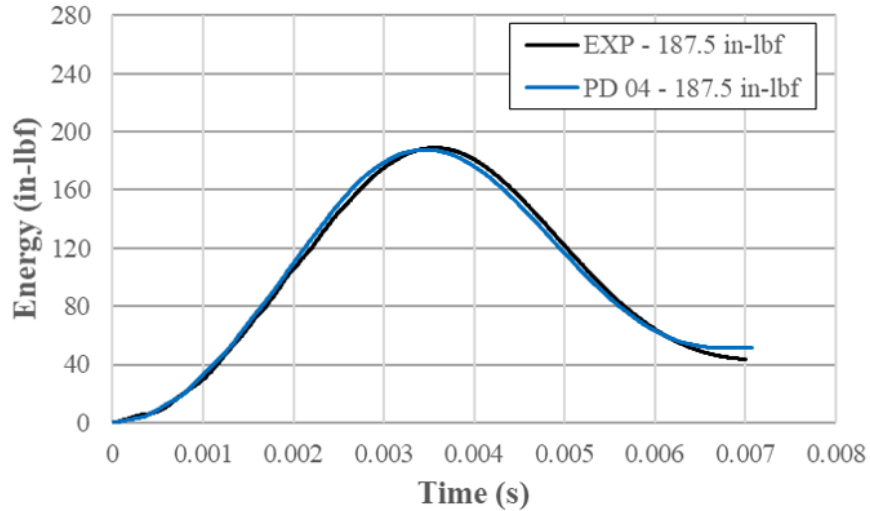


Figure 2-57: Energy vs. time response predicted by objective baseline PD with shear nonlinearity and strain rate dependent material properties approach (PD04) compared against experimental measurements for 187.5 in-lbf impact energy.

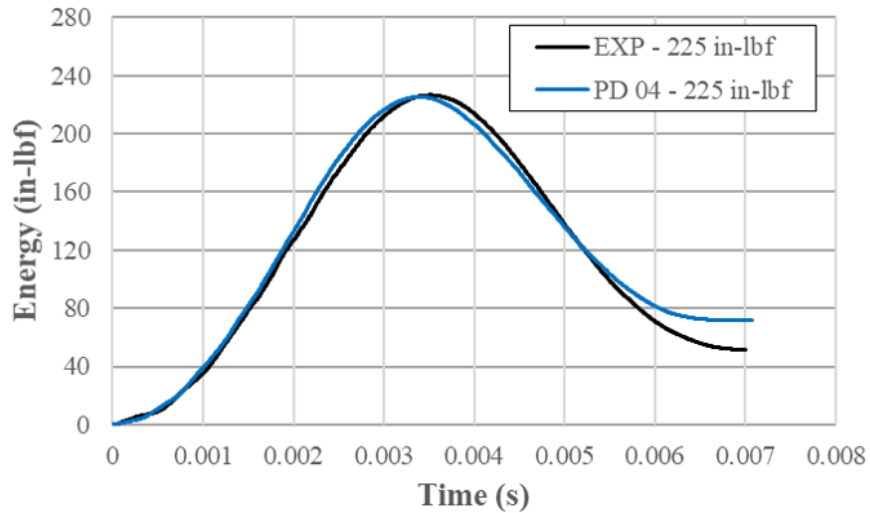


Figure 2-58: Energy vs. time response predicted by objective baseline PD with shear nonlinearity and strain rate dependent material properties approach (PD04) compared against experimental measurements for 225 in-lbf impact energy.

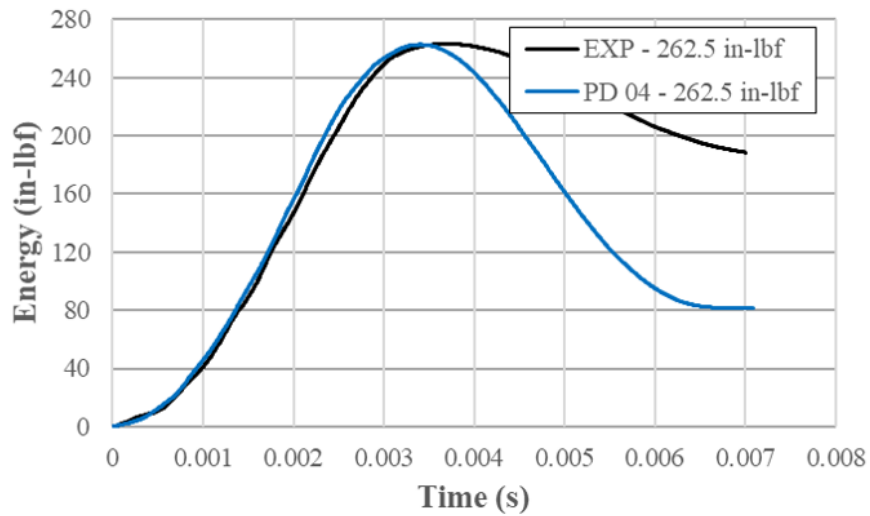


Figure 2-59: Energy vs. time response predicted by objective baseline PD with shear nonlinearity and strain rate dependent material properties approach (PD04) compared against experimental measurements for 262.5 in-lbf impact energy.

Experimental Damage Results

Experimental c-scans of the laminates after impact (Figure 2-60) were provided by North Carolina State University. The c-scan imaging provides an approximation of the delaminated area associated with each impact energy level (shown in red text). At the highest energy level (Figure 2-60 (d)) and in agreement with the previously presented experimental force vs. time, force vs. displacement, and energy vs. time curves; a completely different failure morphology can be observed. More specifically, a threshold energy has been reached which resulted in a transition from Barely Visible Impact Damage (BVID) to Visible Impact Damage (VID). This damage is oriented at a 45-degree angle from the horizontal and can be associated with back face fiber splitting. It is believed that this failure event causes the force drop shown in Figure 2-51.

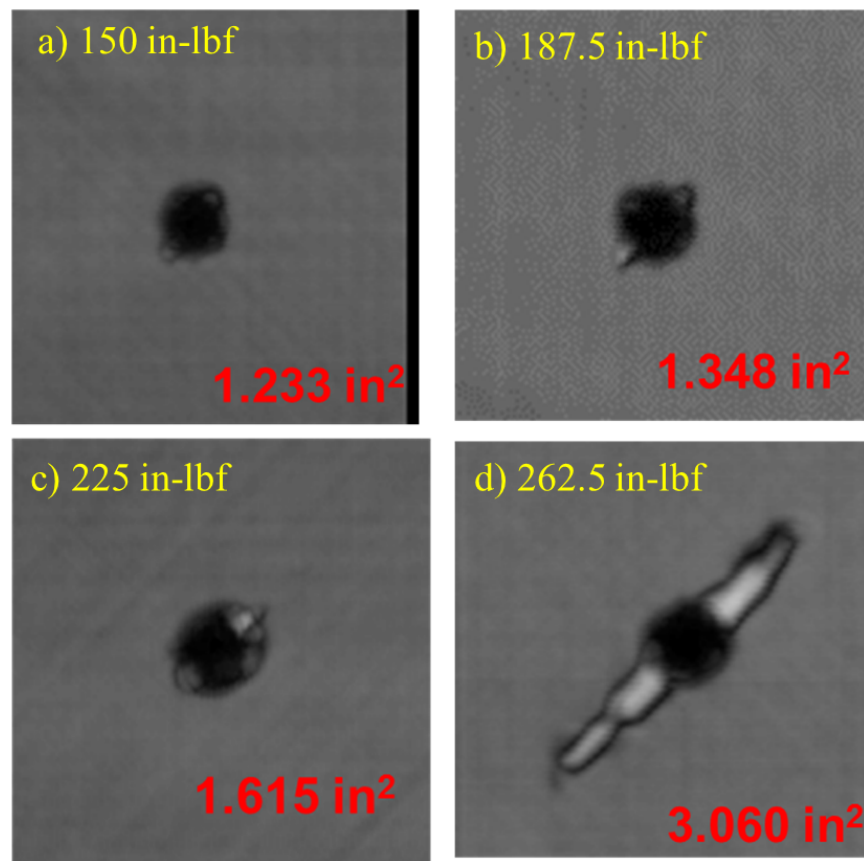


Figure 2-60: Experimental c-scan results for each energy level: (a) 150 in-lbf, (b) 187.5 in-lbf, (c) 225 in-lbf, and (d) 262.5 in-lbf.

The back face splitting extends nearly the entire diagonal of the panel (Figure 2-61 (b)) and stands in stark contrast to the other energy levels. The BVID impact of 225 in-lbf energy (Figure 2-61 (a)), does not show any visible signs of damage.

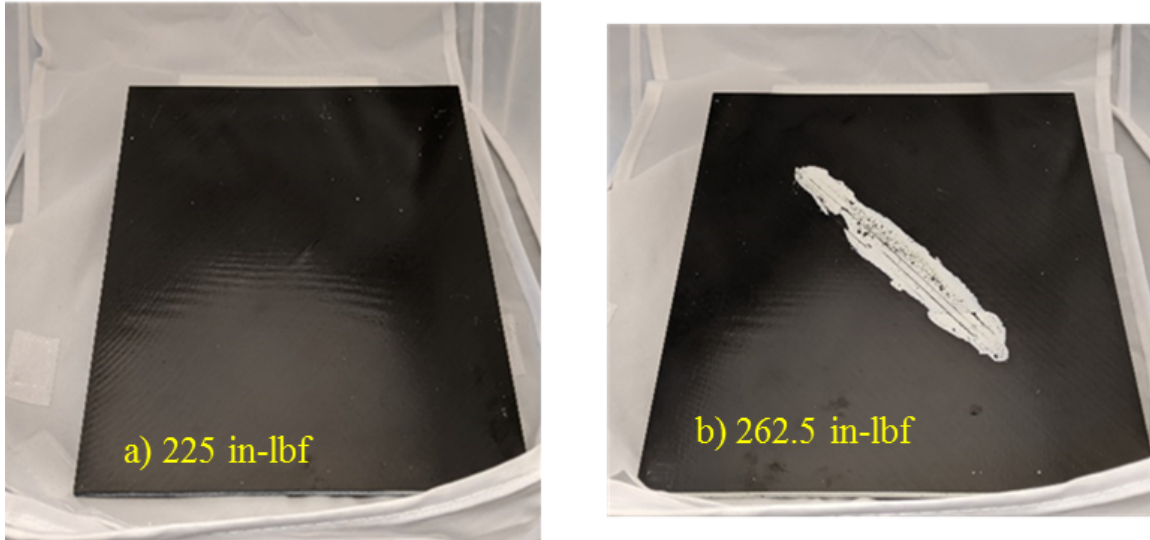


Figure 2-61: Laminate back face for (a) 225 in-lbf energy and (b) 262.5 in-lbf energy.

This threshold between BVID and VID impact behavior is an important aspect of LVI problems and is difficult to predict because of the interaction of different damage mechanisms. Peridynamic predictions of damage and this BVID/VID threshold is explored in the subsequent sections.

Peridynamic Damage Predictions

One particular advantage of the current PD approach is that it allows for examination of different failure modes on a ply-by-ply basis. The user has the ability to visualize total damage, intralaminar fiber damage, intralaminar matrix damage, and interlaminar damage. These damage metrics are defined as the ratio of the number of broken bonds, for a specific bond type, to the number of total possible interactions. These metrics provide insight into the type of damage that is occurring and when tracked over time help illuminate the interaction of these damage modes. As discussed in the introduction, most PD models consider material failure to occur when the damage of a material point reaches a value of 0.5,

indicating that 50% of the material points bonds have failed. The 0.5 threshold was used in this study for each bond type except for the fiber bonds. Because there are so few fiber bonds in the model, all fiber bond failure is considered to indicate significant damage in the laminate.

Interlaminar bond damage in the current PD approach is considered as analogous to experimentally evaluated delamination. Figures 2-62 - 2-65 compare the experimentally determined extent of delamination (black) with the PD predicted delamination (shown in color). These images are intended to be a natural comparison with the experimental c-scan images (Figure 2-60). The color in the center of the image shows the predicted delamination at different depths, with warmer colors being closer to the initial impact site. The black outlines show the experimentally determined delamination extent as measured from Figure 2-60. The yellow frame shows the boundary of the laminate and contextualizes the delamination extent with respect to the laminate dimensions.

Peridynamic predictions of delamination extent increased significantly from energy level 150 in-lbf (Figure 2-62) to 187.5 in-lbf (Figure 2-63), and increased slightly in the 225 in-lbf (Figure 2-64) scenario. A second significant increase in delamination was predicted from energy level 225 in-lbf to 262.5 in-lbf (Figure 2-65). When compared to the experimental measurements, the PD simulations underpredict the delamination for the 150 in-lbf (Figure 2-62) and 262.5 in-lbf (Figure 2-65) energy levels and more accurately predict the delamination for energy levels 187.5 in-lbf (Figure 2-63) and 225 in-lbf (Figure 2-64). The highest energy level (Figure 2-65) comparison shows a difference in failure morphology between the PD predictions and the experiments, which will be discussed further in the next sections.

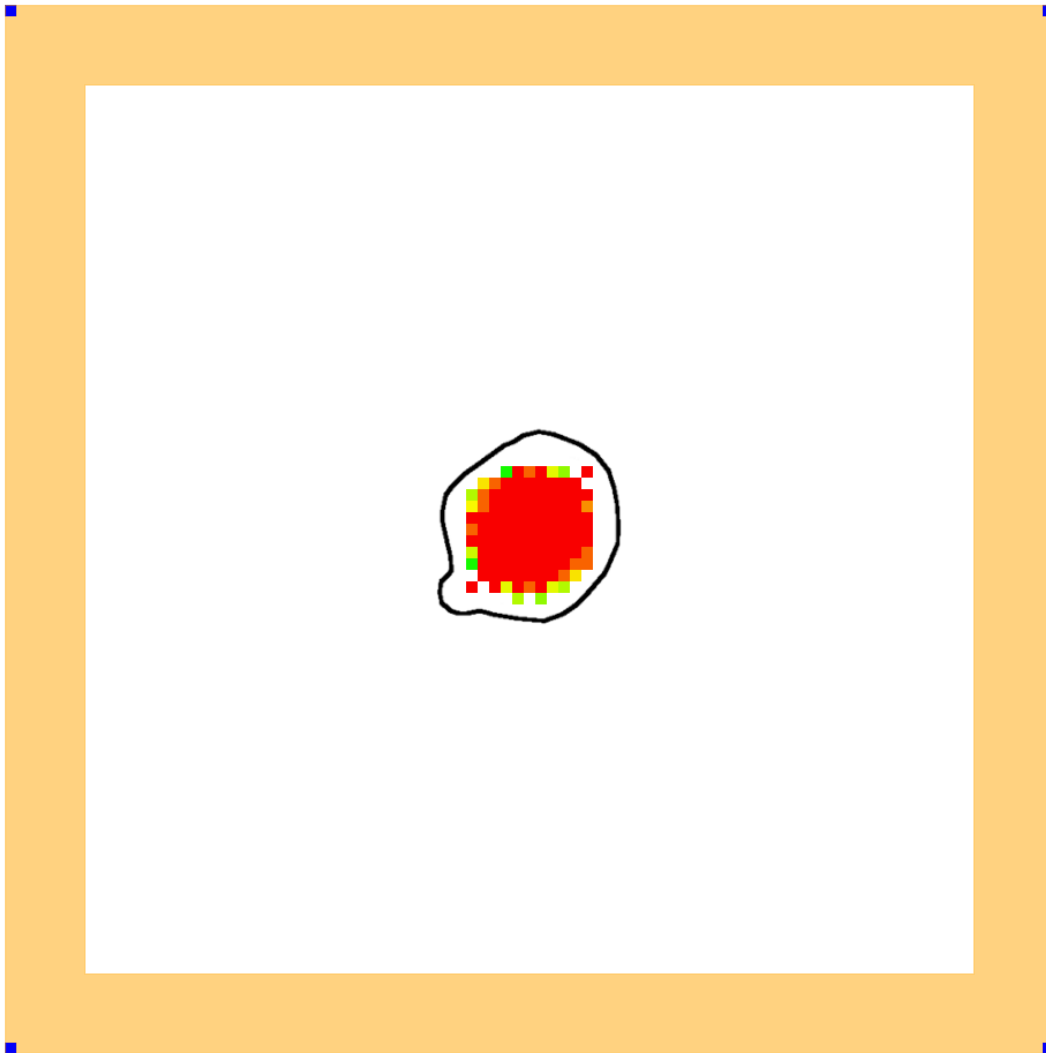


Figure 2-62: Delamination (color variation indicates ply depth from impact side) predicted by PD04 approach compared against experimental measurements (outline overlaid) for 150 in-lbf impact energy.

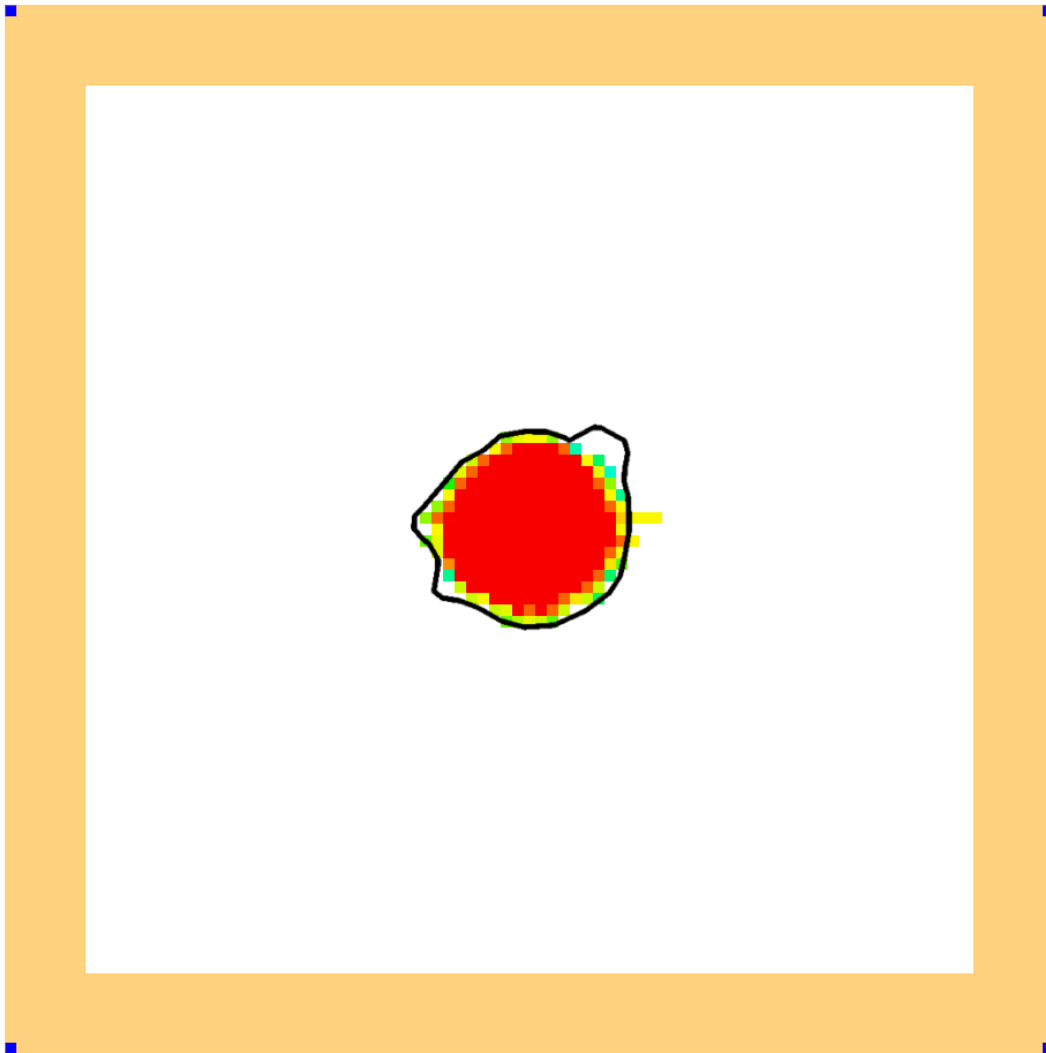


Figure 2-63: Delamination (color variation indicates ply depth from impact side) predicted by PD04 approach compared against experimental measurements (outline overlaid) for 187.5 in-lbf impact energy.

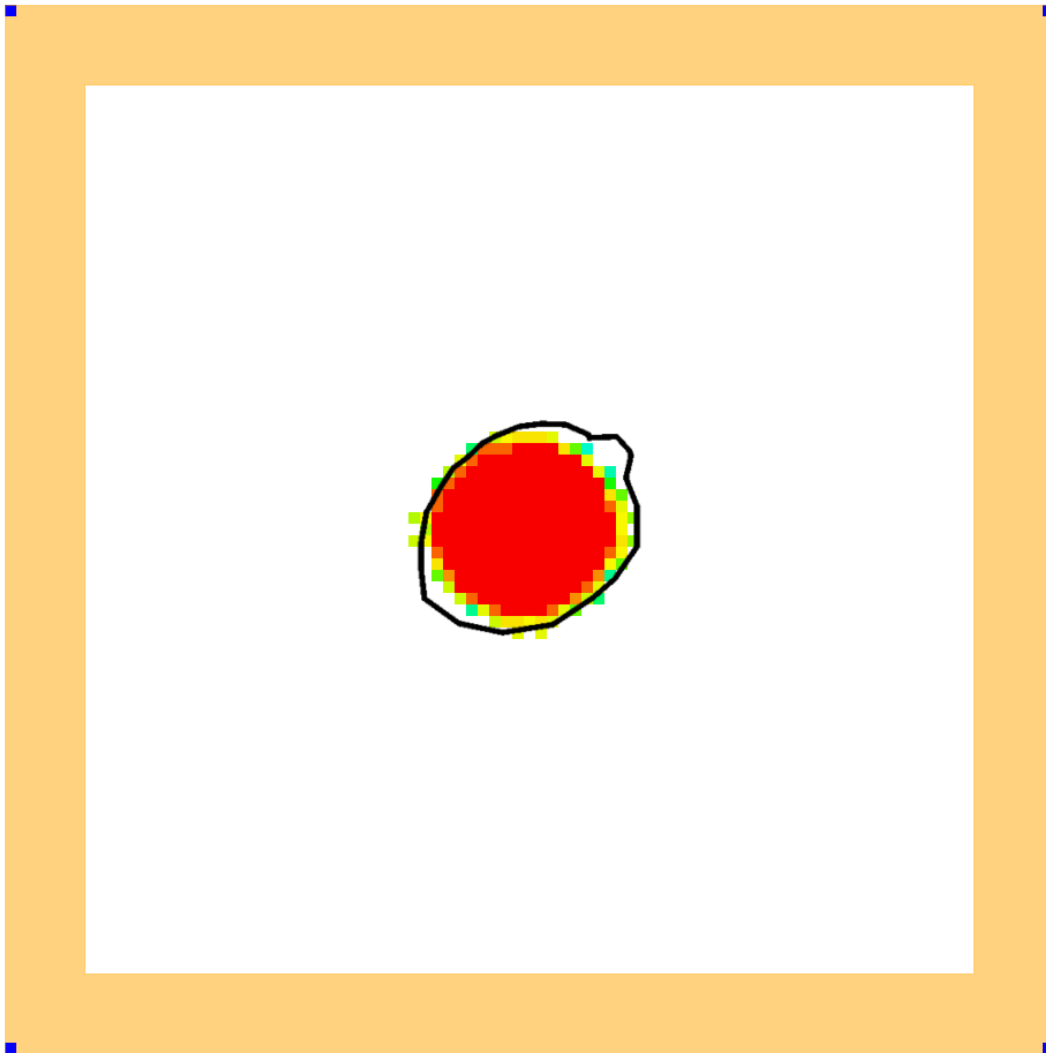


Figure 2-64: Delamination (color variation indicates ply depth from impact side) predicted by PD04 approach compared against experimental measurements (outline overlaid) for 225 in-lbf impact energy.

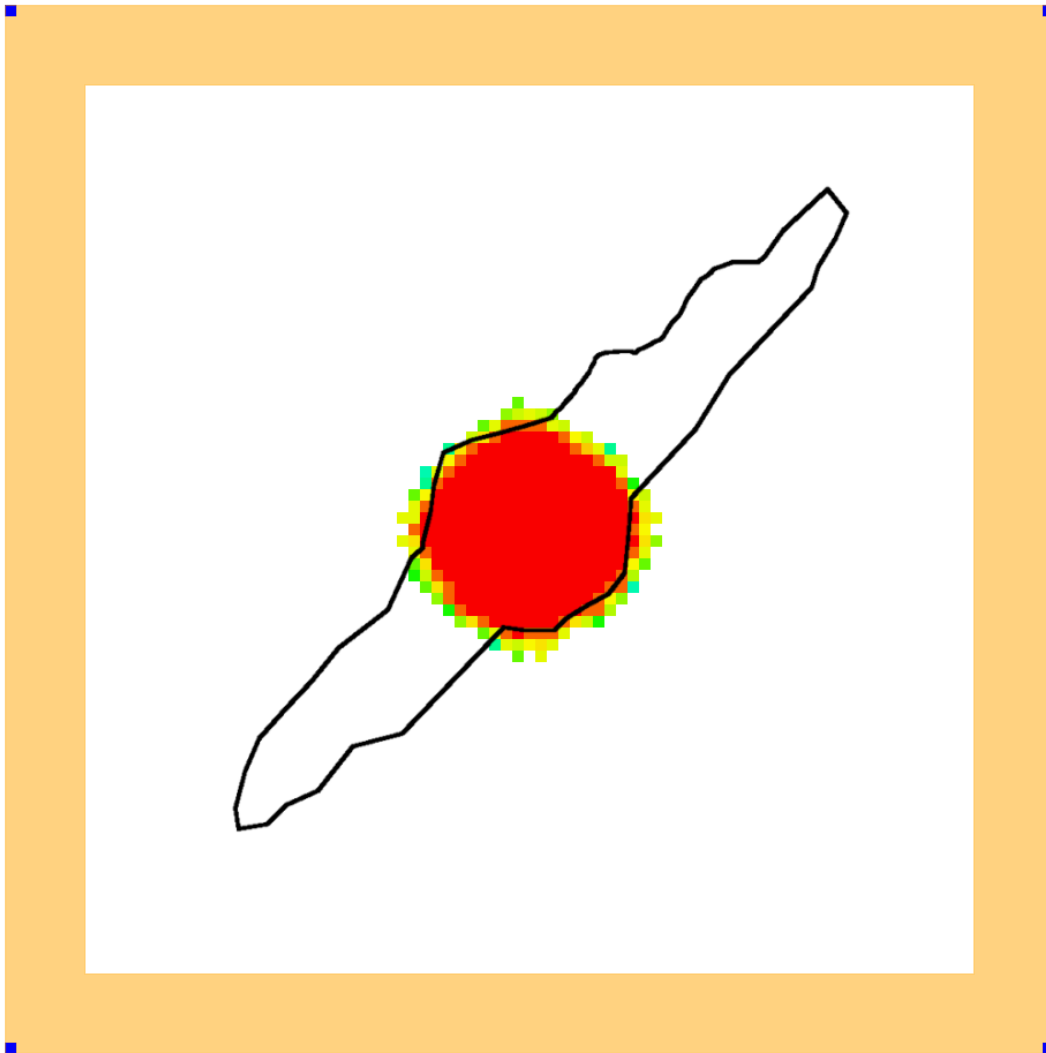


Figure 2-65: Delamination (color variation indicates ply depth from impact side) predicted by PD04 approach compared against experimental measurements (outline overlaid) for 262.5 in-lbf impact energy.

In addition to the stacked delamination visualization, PD predicted ply-by-ply damage can be obtained. This orientation is helpful in comparing damage with fiber orientation and depth. The plies are numbered “01-25” with 25 being closest to the initial impact site (impacting face). The fiber orientation is labeled in the bottom right corner of each ply for easy reference. While there appears to be some underlying directionality to the total damage, the failure is mainly circular throughout.

The increases in total damage (all damage modes contributing to a single scalar damage parameter for each material point) from energy level 150 in-lbf (Figure 2.66) to energy levels 187.5 in-lbf (Figure 2.67), 225 in-lbf (Figure 2.68), and 262.5 in-lbf (Figure 2.69) are clearly observed.

Fiber damage (Figure 2.70 to Figure 2.73) and interlaminar damage (Figure 2.74 to Figure 2.77) exhibit similar progression. Very few fiber material points are damaged in the low energy levels. This fiber damage occurs close to the impactor. At the highest energy level. Fiber damage occurs at the top most plies and begins to occur significantly in the back plies. One way to visualize the extent of damage in the LVI simulations is through an exploded isometric view (Figure 2.74 - 2.77). This orientation allows for easy visualization of the variation of delamination with depth.

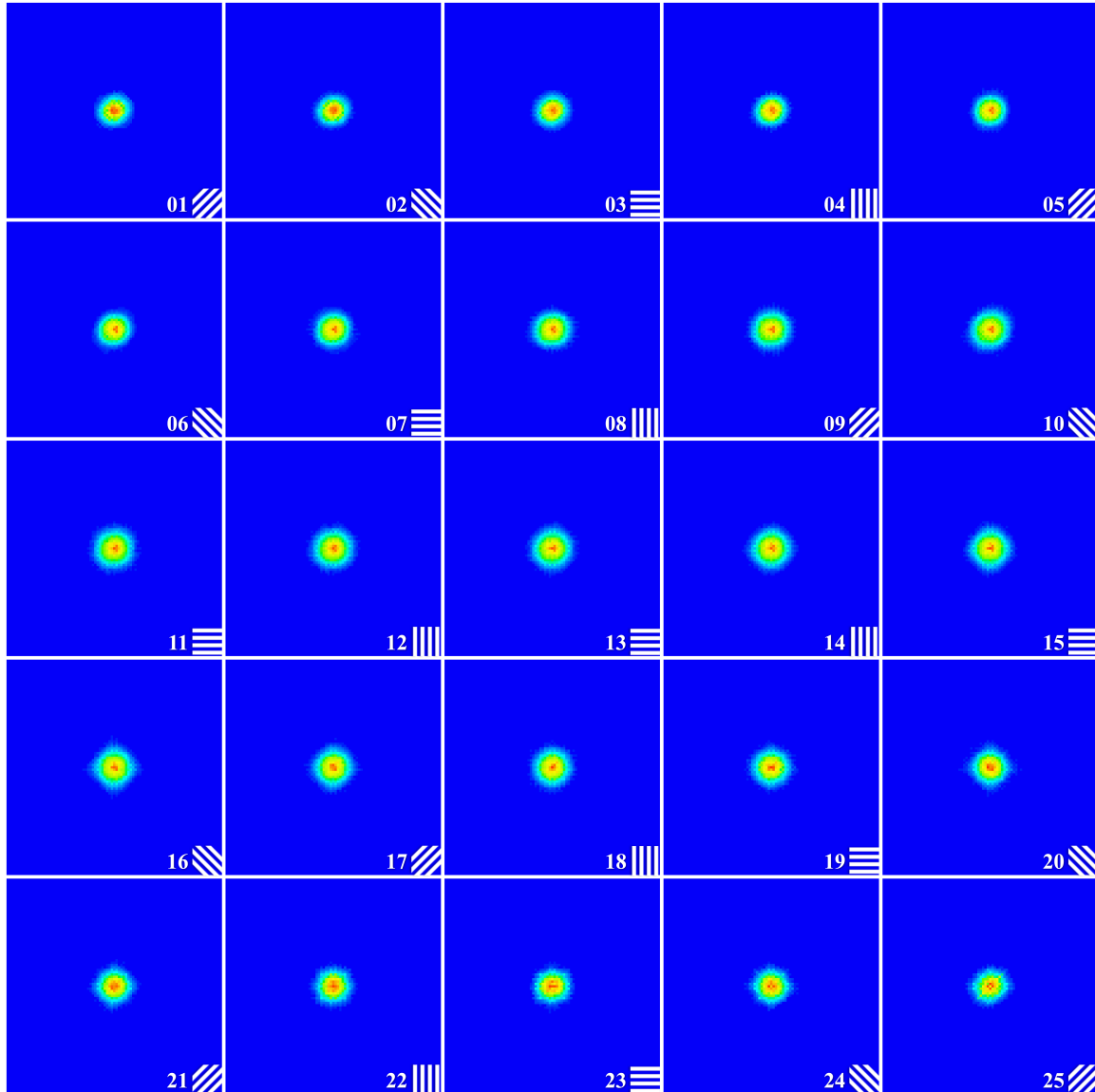


Figure 2-66: Ply-by-ply total damage predicted by PD04 approach for 150 in-lbf impact energy.

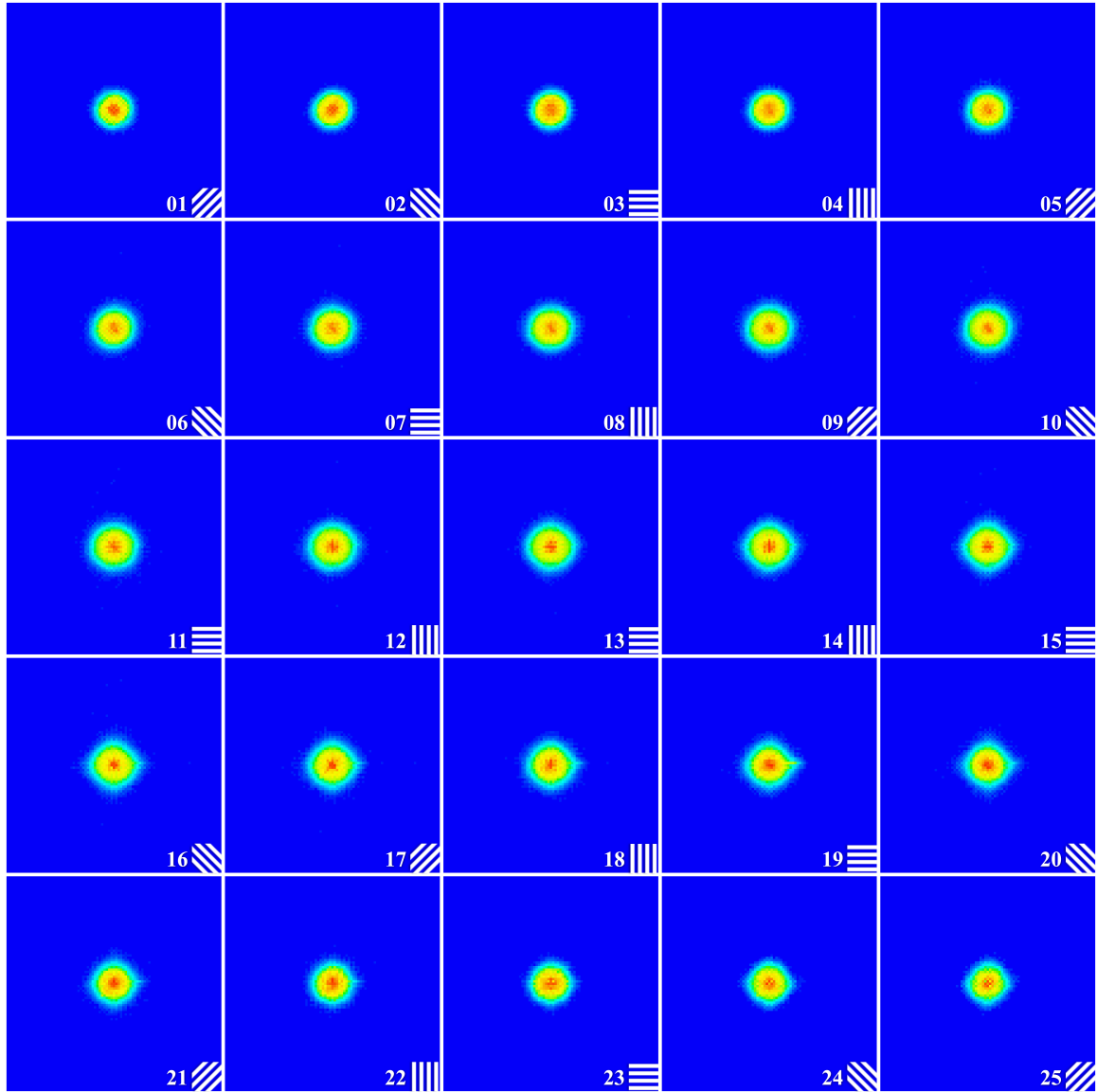


Figure 2-67: Ply-by-ply total damage predicted by PD04 approach for 187.5 in-lbf impact energy.

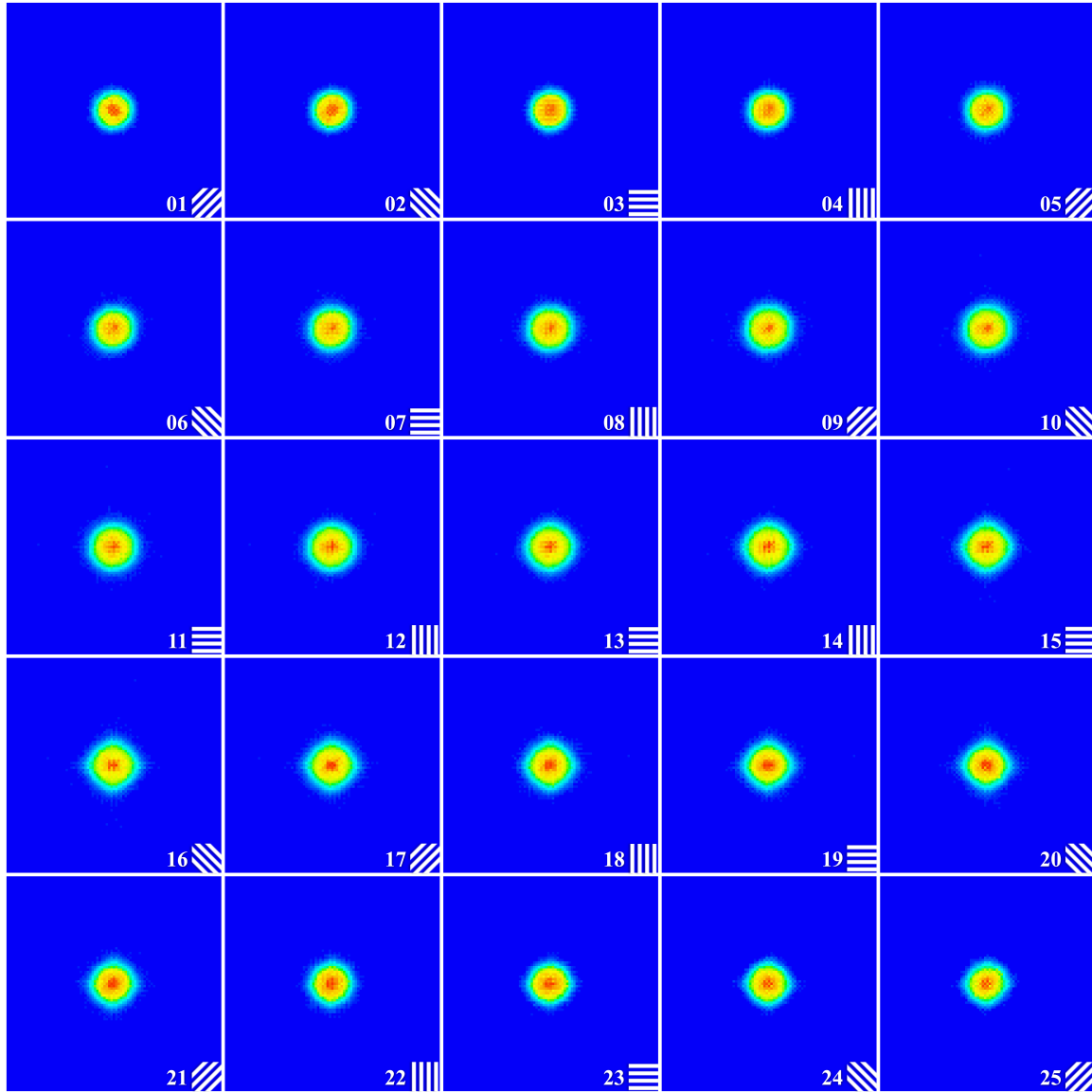


Figure 2-68: Ply-by-ply total damage predicted by PD04 approach for 225 in-lbf impact energy.

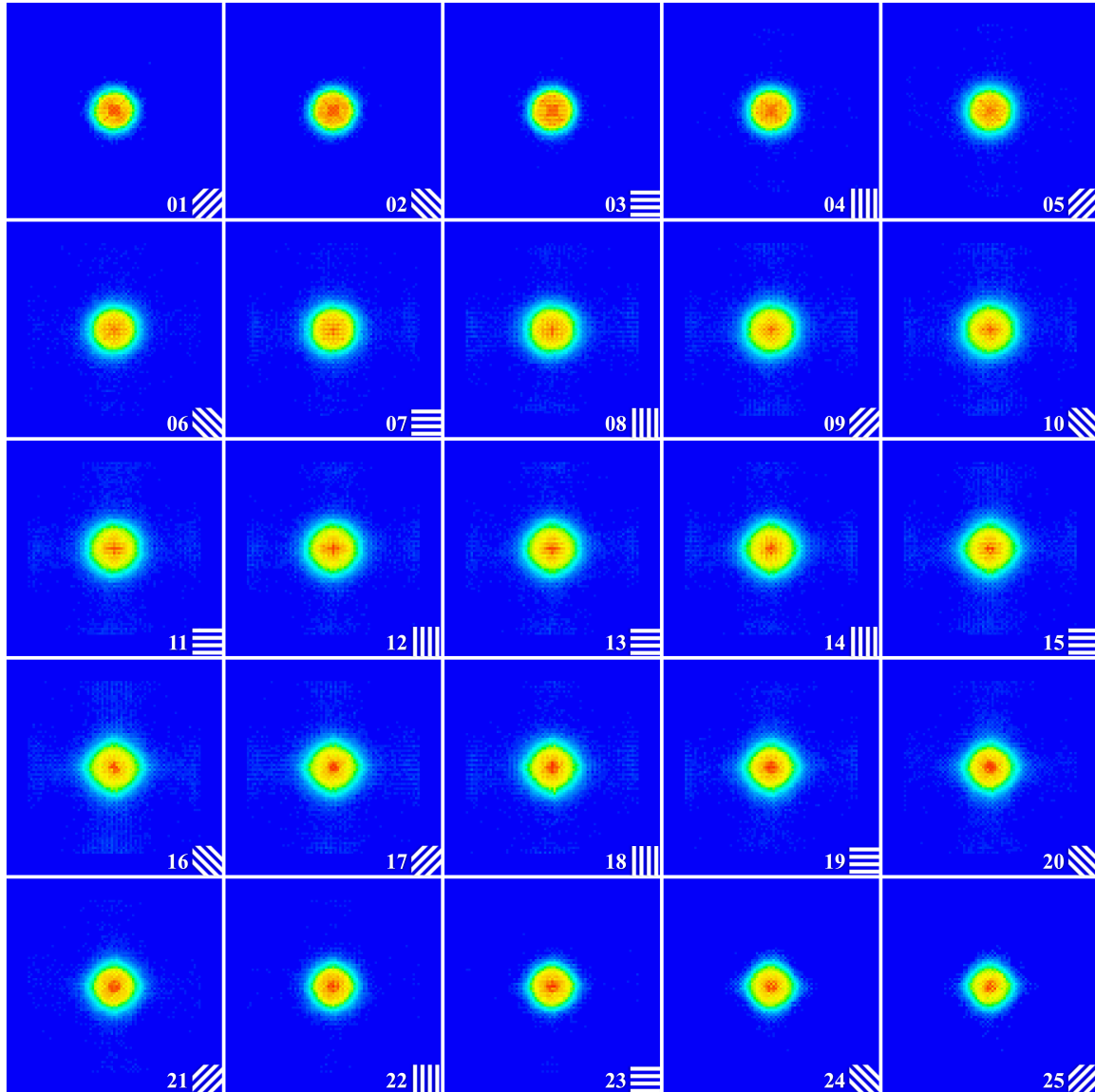


Figure 2-69: Ply-by-ply total damage predicted by PD04 approach for 262.5 in-lbf impact energy.

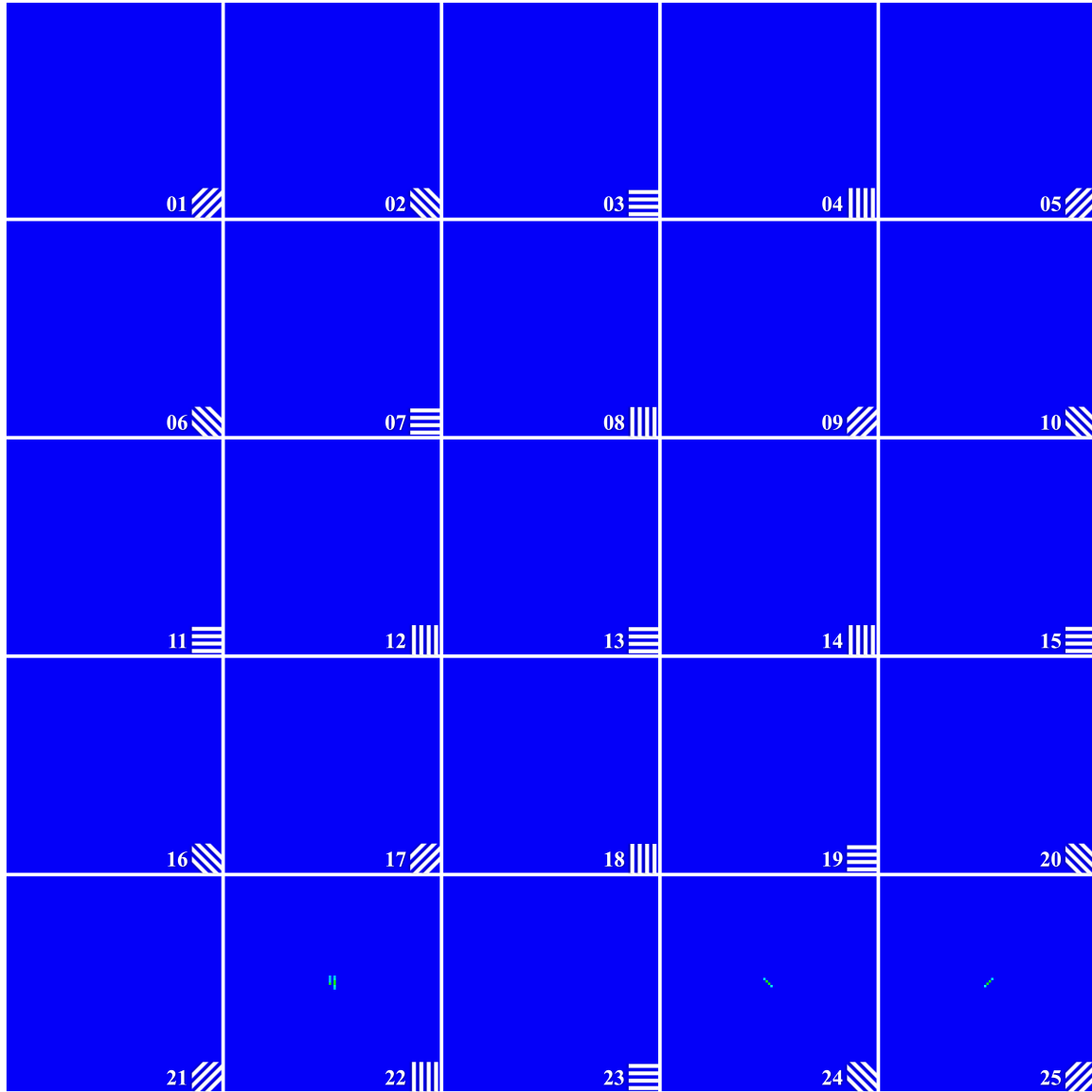


Figure 2-70: Ply-by-ply fiber damage predicted by PD04 approach for 150 in-lbf impact energy.

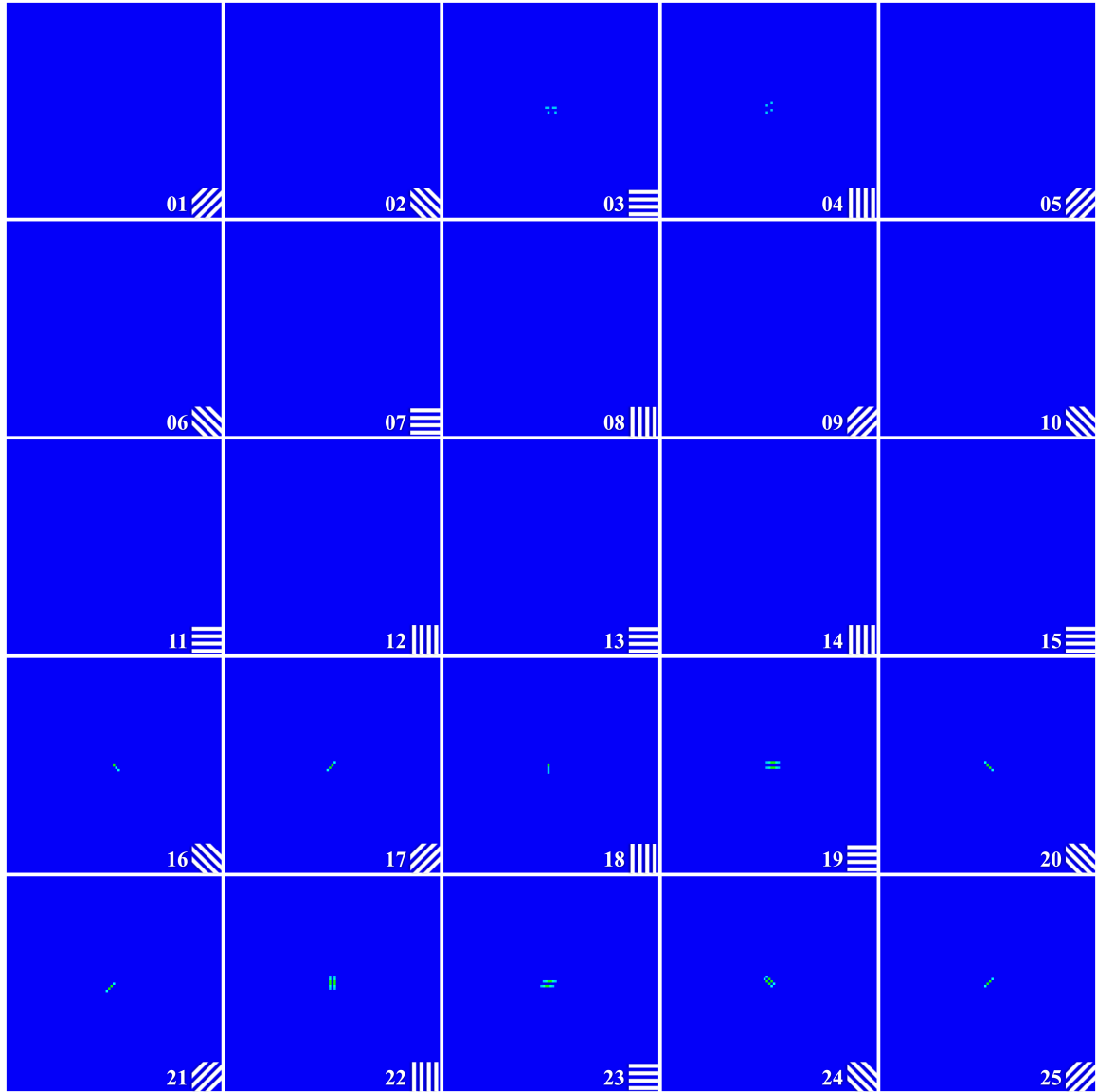


Figure 2-71: Ply-by-ply fiber damage predicted by PD04 approach for 187.5 in-lbf impact energy.

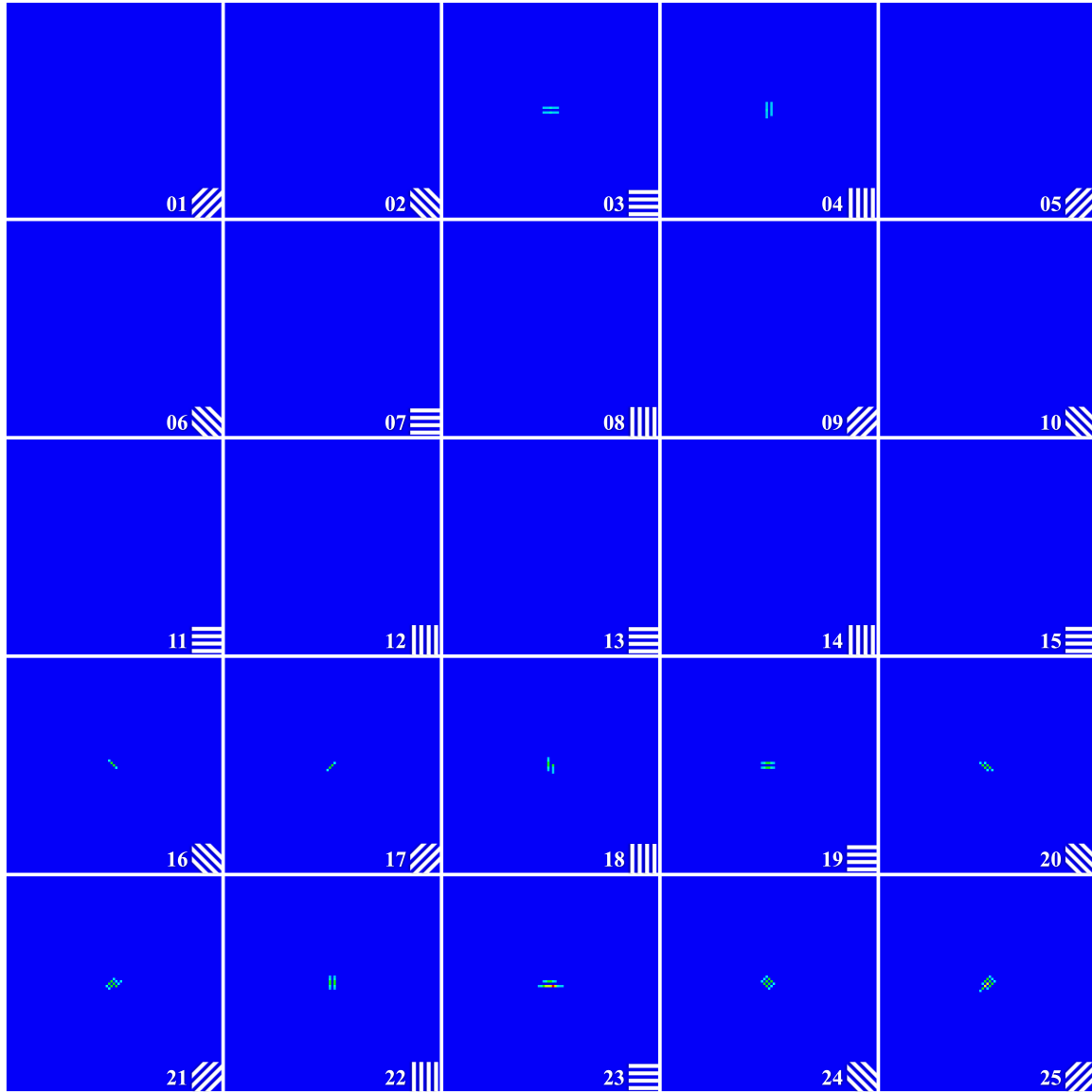


Figure 2-72: Ply-by-ply fiber damage predicted by PD04 approach for 225 in-lbf impact energy.

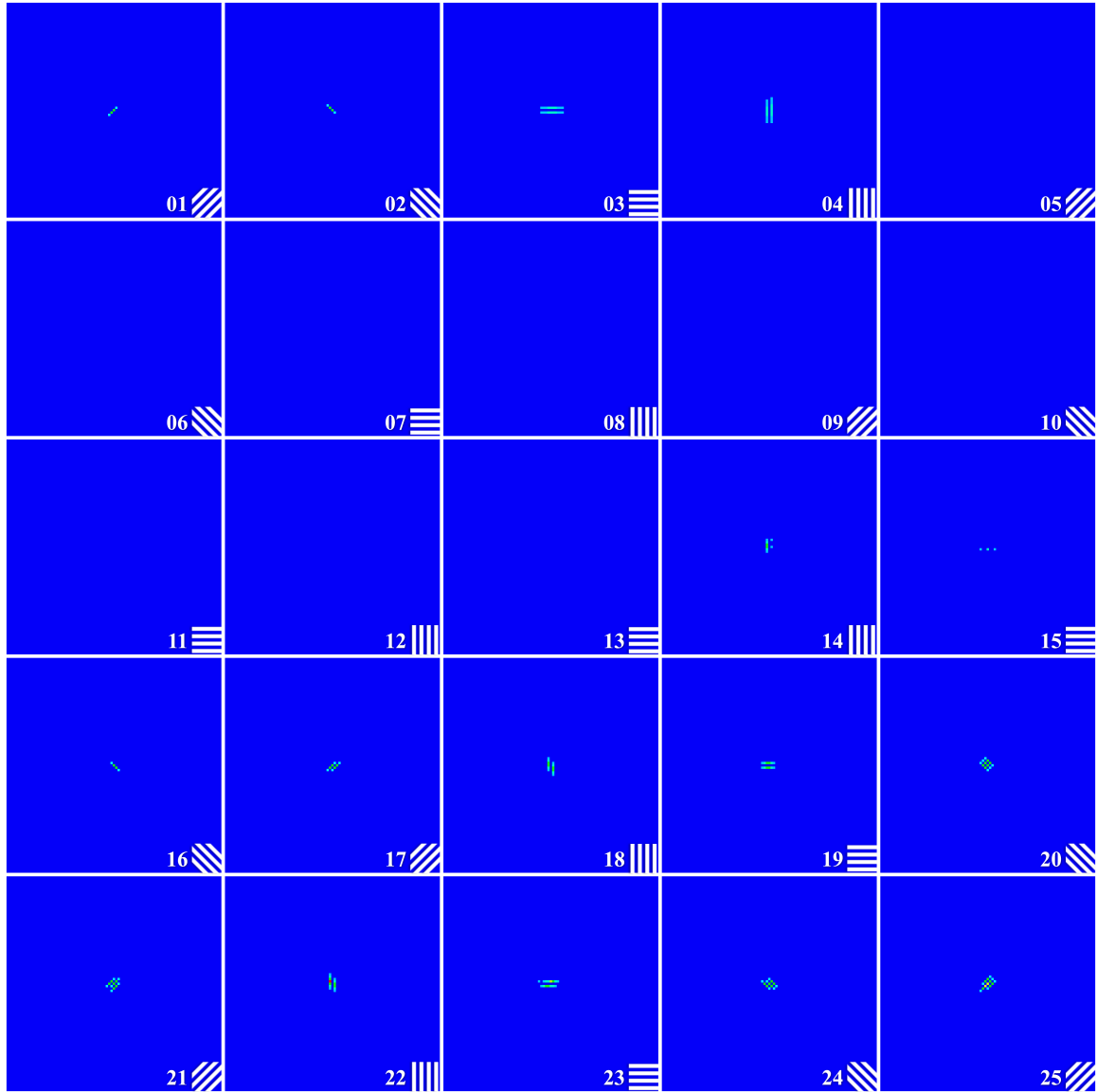


Figure 2-73: Ply-by-ply fiber damage predicted by PD04 approach for 262.5 in-lbf impact energy.

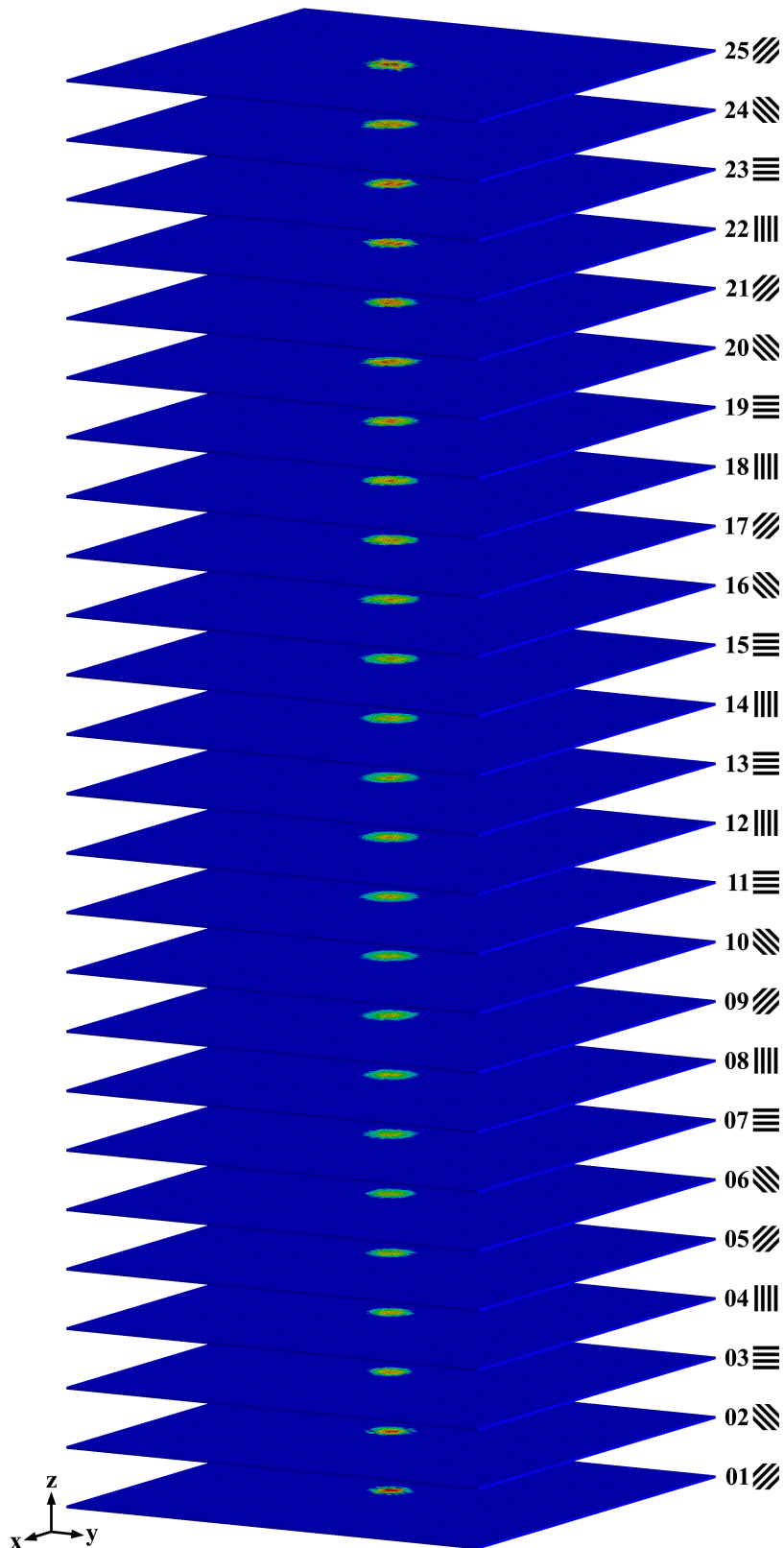


Figure 2-74: Ply-by-ply interlaminar damage predicted by PD04 approach for 150 in-lbf impact energy.

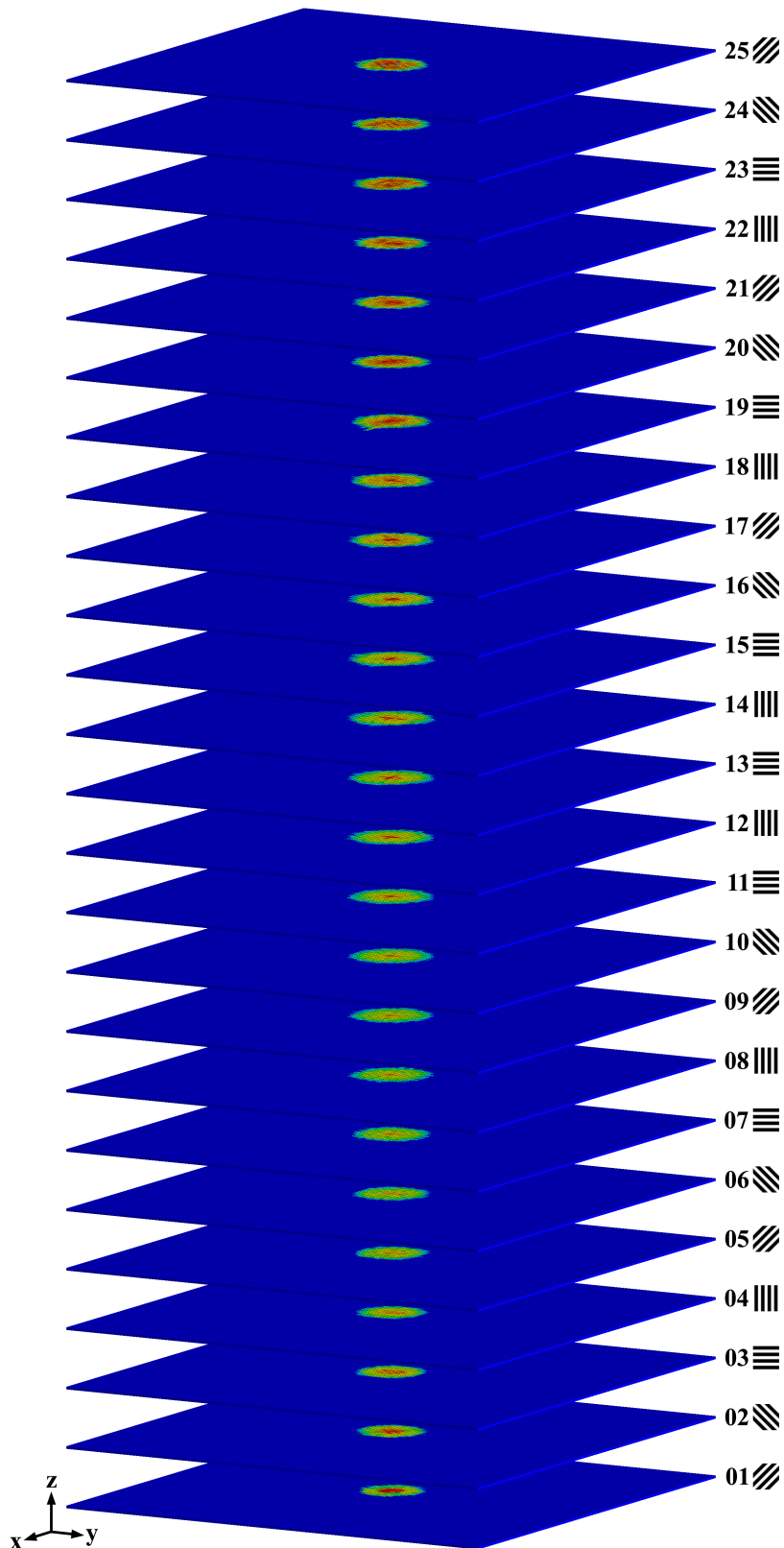


Figure 2-75: Ply-by-ply interlaminar damage predicted by PD04 approach for 187.5 in-lbf impact energy.

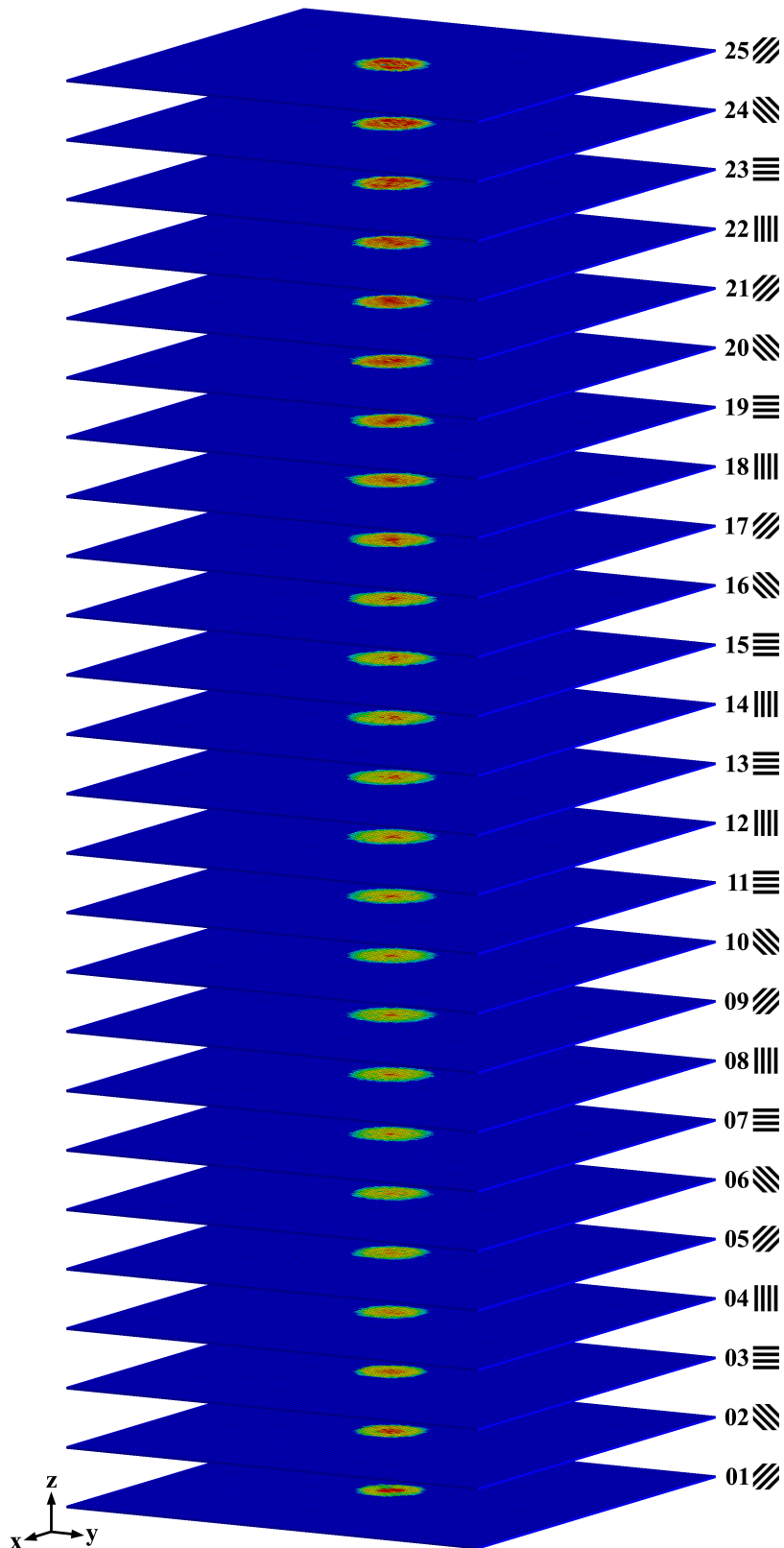


Figure 2-76: Ply-by-ply interlaminar damage predicted by PD04 approach for 225 in-lbf impact energy.

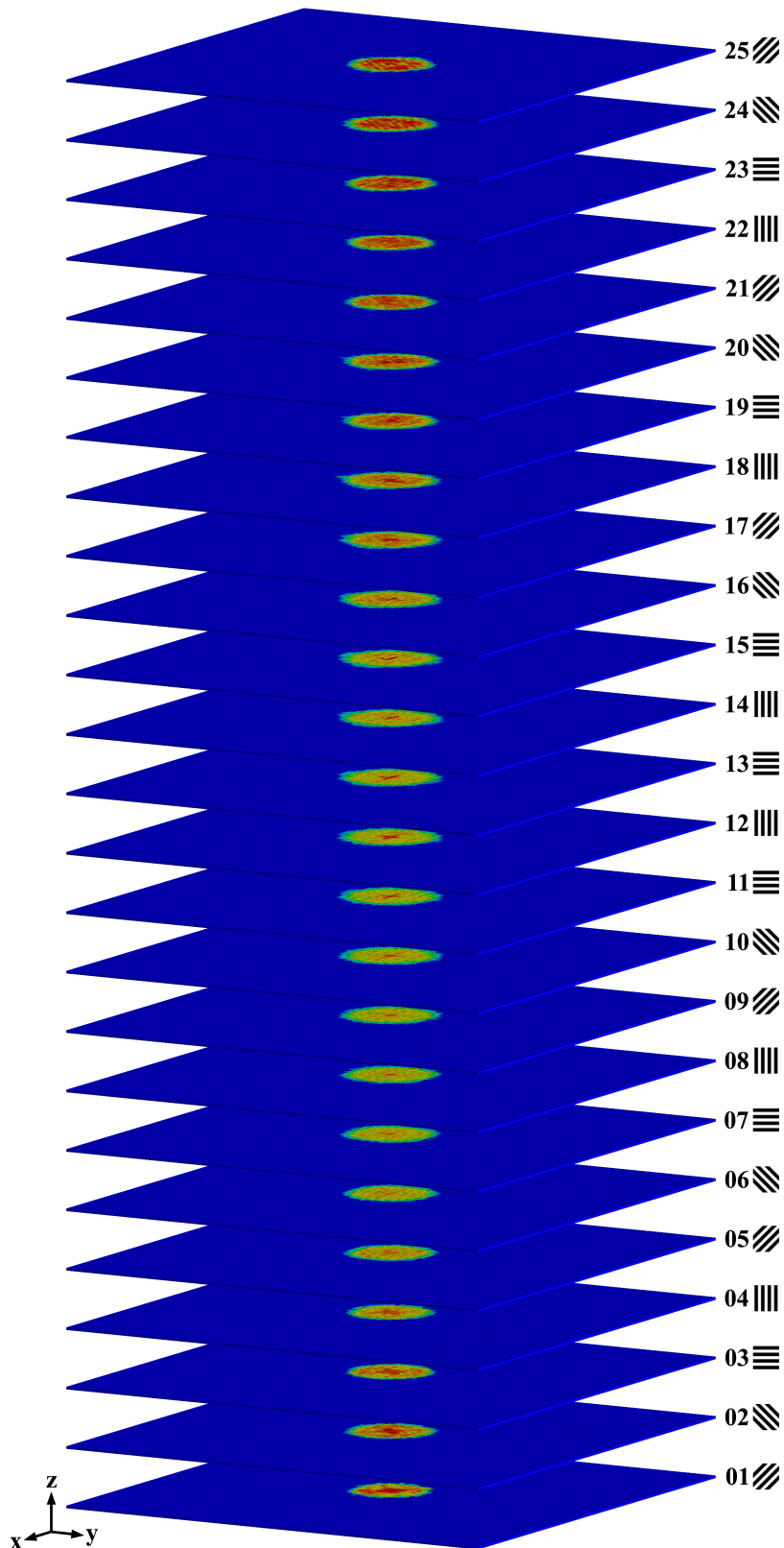


Figure 2-77: Ply-by-ply interlaminar damage predicted by PD04 approach for 262.5 in-lbf impact energy.

The PD simulations at the highest energy level were used to investigate the interaction of different damage mechanisms. A correlation between the force vs. time response, initiation of fiber damage, and the growth of interlaminar damage was observed. Prior to approximately 2.5 ms, the interlaminar damage is observed to grow almost linearly until a sudden, drastic increase, after which the damage plateaus (Figure 2-78(a) and Figure 2-78(c)). This sudden and dramatic damage growth occurs during the period containing a sharp drop in force, approximately 25 % over 70 μ s (Figure 2-78(a) - blue curve between locations 2 and 3). Similar to the interlaminar damage growth, an increase in fiber damage occurred during both of these events (Figure 2-78(b)).

While the overall fiber damage footprint does not drastically increase, the fiber damage initiates and propagates in several plies within this same short period of time (Figure 2-79(a, b)). Further demonstrating the interaction of mechanisms, plies containing more severe fiber damage appear to also have a larger interlaminar damage footprint (Figure 2-79(c, d)).

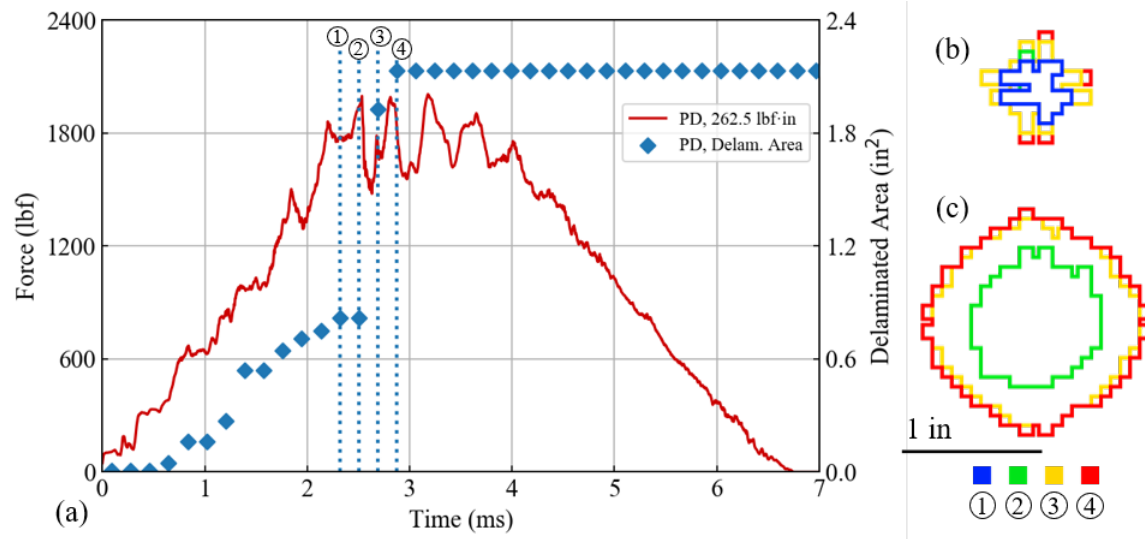


Figure 2-78: (a) Comparison of force response and delaminated area over time for 262.5 in-lbf impact energy (b) fiber damage footprint at selected times (c) interlaminar damage footprint at selected times.

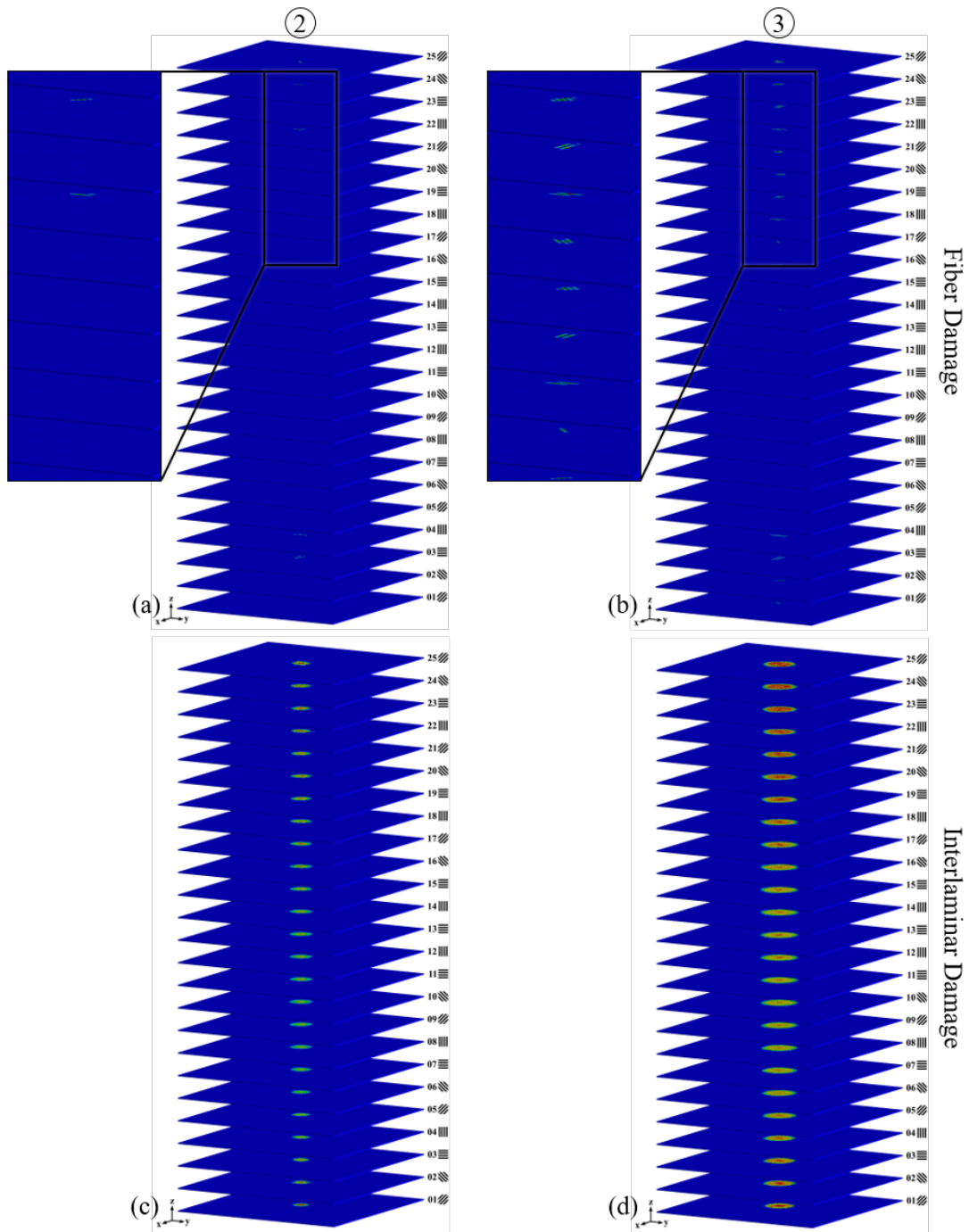


Figure 2.79: Ply-by-ply views of (a) fiber damage before event (b) fiber damage after event (c) interlaminar damage before event (d) interlaminar damage after event.

Quantitative Comparisons

A quantitative comparison of the maximum force, maximum displacement, delaminated area, and energy absorbed (E_a) is provided in Table 2.15 and is summarized visually in Figures 2.80 to 2.83.

Table 2.15: Quantitative comparison of experiments and PD simulations at all energy levels.

	150 in-lbf		187.5 in-lbf		225 in-lbf		262.5 in-lbf	
	PD	EXP	PD	EXP	PD	EXP	PD	EXP
Max Force (lbf)	1516.80	1469.58	1657.06	1620.42	1846.28	1849.95	2023.51	1977.20
Max Disp (in)	0.24	0.24	0.26	0.27	0.28	0.29	0.30	0.31
Delam. Area (in ²)	0.71	1.23	1.42	1.35	1.53	1.62	2.13	3.06
E_a (in-lbf)	28.80	41.42	51.09	43.67	73.15	51.61	81.69	188.40

In general, the PD simulations (Figure 2.80 - blue) slightly overpredict the experimental peak force (Figure 2.80 - black). The largest percent difference occurs for the first energy level (150 in-lbf), in which the PD simulation overpredicts the peak force by approximately 3%. The most accurate simulation was the third energy level; in this simulation, the experimental peak force is underpredicted by less than 1%. Alternatively, PD simulations slightly underpredict the peak displacement at each energy levels (Figure 2.81). The percent difference for each case ranges between -3% and -4%. It is believed that these simulation predictions show great accuracy in both the peak force and peak displacement.

Another interesting relationship that can be quantitatively analyzed is the relationship between the delaminated area (Figure 2.82) and the absorbed energy (Figure 2.83). The delamination area provides an indication of the areal extent of the damage in the composite and the absorbed energy gives insight into the intensity of the damage. Meaning, for example, a small concentrated damage site, could potentially have a higher amount of energy absorbed and a lower amount of delaminated area than a diffuse but large damaged

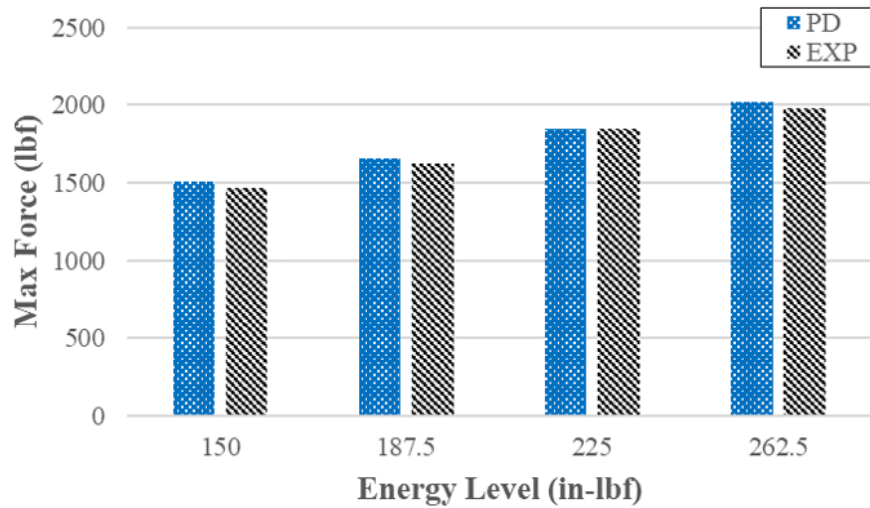


Figure 2-80: Quantitative comparison between PD (blue) and experimental (black) peak force (lbf) for each energy level.

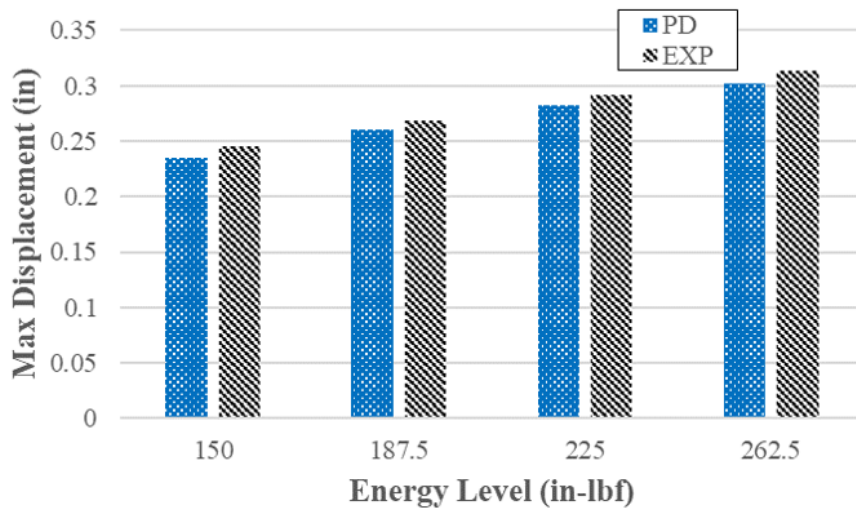


Figure 2-81: Quantitative comparison between PD (blue) and experimental (black) peak displacement (in) for each energy level.

region. From an experimental perspective, the intricacy of this relationship arises because of the interaction between intralaminar and interlaminar failure, such as delamination migration and matrix cracking [4]. The PD simulations tend to underpredict the delaminated area (Figure 2-82). However, because area is a squared quantity, the actual delaminated footprint is quite similar (Figure 2-62 - 2-65). Interestingly, while the delaminated area is

underpredicted, the absorbed energy is overpredicted for the 187.5 in-lbf and 225 in-lbf simulations. These scenarios where the absorbed energy is overpredicted are also the closest prediction in the delaminated area and implies that the damage for these simulations is highly concentrated. It is believed that the global bending response contributes to damage extending as opposed to simply increasing in intensity under the impactor. This intricate relationship can be explored through nonlocality in future work. While there are differences between the experimental results and PD simulation predictions, overall, the predictions are in remarkable agreement.

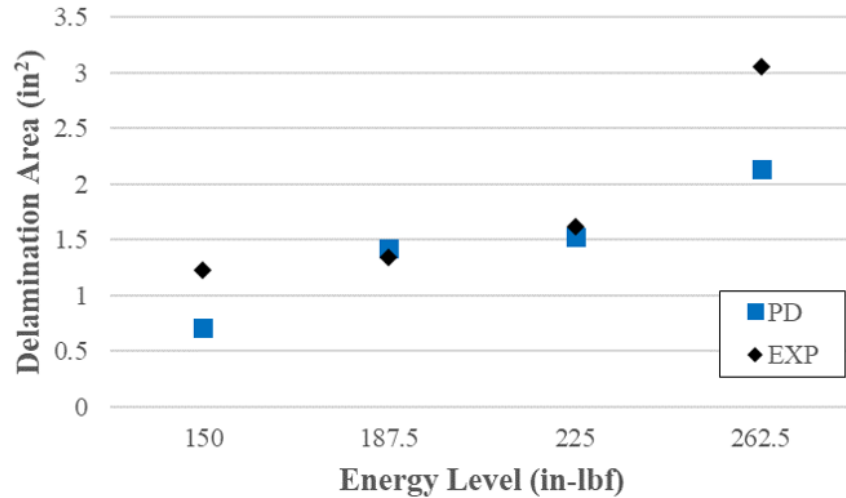


Figure 2-82: Quantitative comparison between PD (blue) and experimental (black) delaminated area (in²) for each energy level.

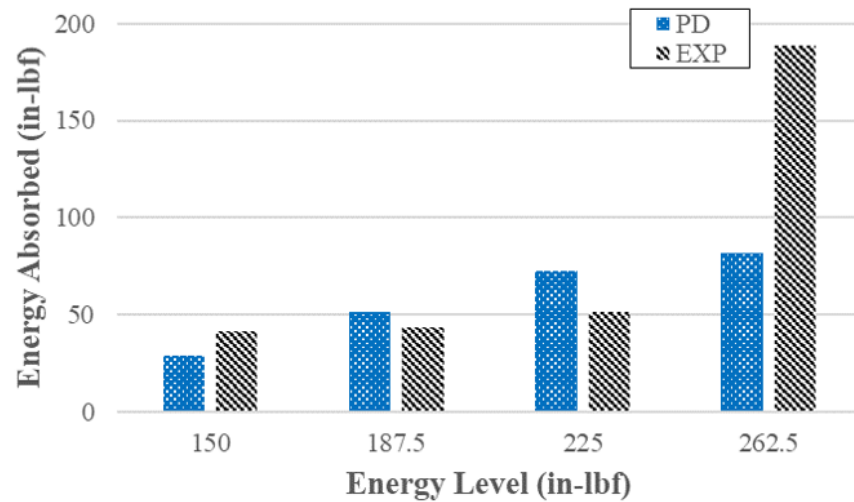


Figure 2-83: Quantitative comparison between PD (blue) and experimental (black) absorbed energy (in-lbf) for each energy level.

As mentioned in the earlier sections, the difference between the experimental and predicted response for the highest energy level (262.5 in-lbf) is related to the transition from BVID (barely visible impact damage) to VID (visible impact damage). At this transition, the failure morphology changes and the experiments show fiber splitting of the back face of the laminate. Fiber splitting causes the laminate to absorb approximately 70% of the impacting energy as the impactor slowly rebounds from the surface. The experimental force vs. time curve exhibits a sharp drop in force approximately 3 ms into the impact event (Figure 2-51); unfortunately, the PD04 approach does not capture this sharp drop. Because this is a threshold energy level, the simulation not capturing the change in behavior is unsurprising. Small modifications to the PD simulations could push the model into the VID regime and conversely, small changes to the experiments could push the results in the other direction back to BVID.

The threshold between BVID and VID was explored in two ways: increasing impact energy and decreasing longitudinal strength. By increasing the simulation impact energy, the sensitivity of the PD threshold was explored. Additionally, it provided insight into the interaction of PD damage mechanisms. Decreasing longitudinal strength helps to illu-

minate the sensitivity of fiber failure on the threshold, verifying that if more fiber failure occurs, the threshold will be reached at the experimental impact energy.

2.5.4 Increasing Impact Energy

Several additional impact energies greater than 262.5 (in-lbf) were explored by keeping the impactor mass constant and increasing the impactor velocity. All other simulation parameters were held constant. Increasing the impact energy to 282.42 in-lbf, an approximate 7.5% increase in impacting energy, produced a much different force vs. time response (Figure 2.84). This force vs. time response (red) is compared against the experimental 262.5 in-lbf (black) and the PD prediction at 262.5 in-lbf (blue). With a small increase in impacting energy, the peak force appears very similar, however, there is a sharp drop in force which is associated with fiber failure. The slope of the force drop and the subsequent unloading is very similar to the experimental curve at the 262.5 in-lbf energy level. This suggests that the PD model is very much within the same energy (BVID/VID) threshold as the experiments.

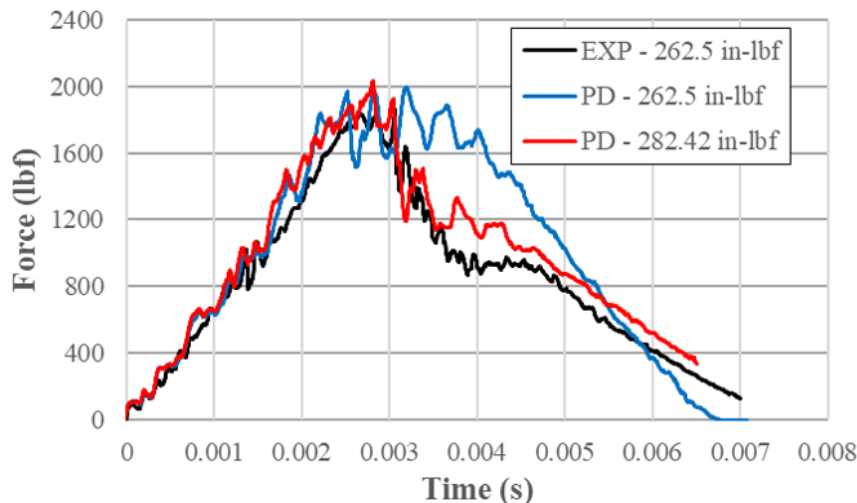


Figure 2.84: Force vs. time response prediction for 282.42 (red) in-lbf impact energy compared against experimental 262.5 (black) in-lbf and the PD prediction for 262.5 (blue) in-lbf.

The force vs. displacement prediction (Figure 2.85) at the higher energy level (red) also

follows very closely with the experimental 262.5 (black) in-lbf curve. The peak displacement at the higher energy level is very similar to the PD prediction and experimental results at the slightly lower energy level. This is another indication that the failure morphology is changing appropriately with increasing energy.

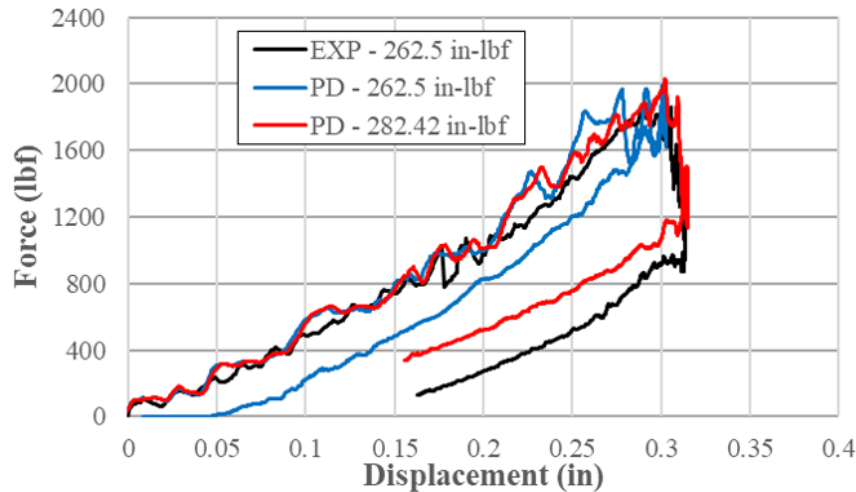


Figure 2.85: Force vs. displacement response prediction for 282.42 (red) in-lbf impact energy compared against experimental 262.5 (black) in-lbf and the PD prediction for 262.5 (blue) in-lbf.

Of all the metrics analyzed, the absorbed energy vs. time response (Figure 2.86) differs the most with the experimental results. As necessitated by the input energy, the peaks of the energy vs. time responses are different. However, as shown, while still underpredicting the absorbed energy response, it is in much better agreement with the experimental results.

The differences in delamination between the PD prediction at 262.5 in-lbf and 282.42 in-lbf (Figure 2.87) shows a slight increase in delamination (colored) and a significant increase in fiber damage (black). However, unlike the experimental results, while there is more significant fiber damage in the PD prediction at this energy level, the extent of the fiber damage is not as great.

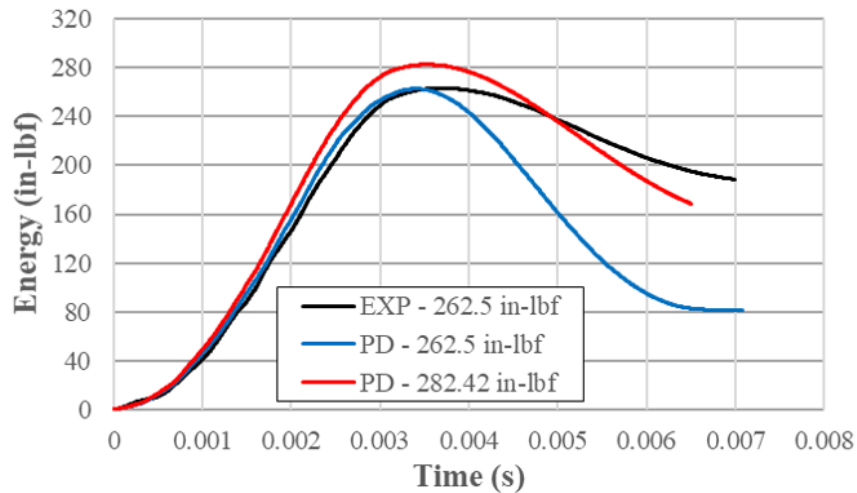


Figure 2-86: Energy vs. time response prediction for 282.42 (red) in-lbf impact energy compared against experimental 262.5 (black) in-lbf and the PD prediction for 262.5 (blue) in-lbf.

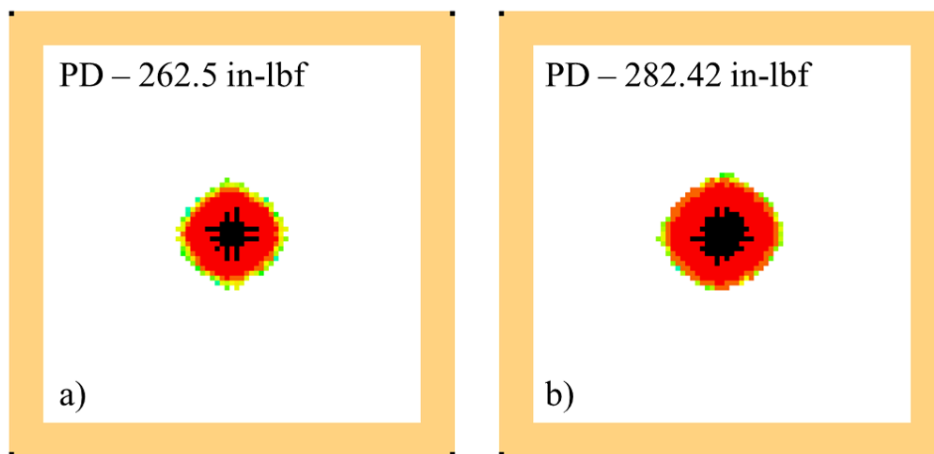


Figure 2-87: Delamination (color variation indicates ply depth from impact side and black indicates fiber failure) prediction at 262.5 in-lbf compared against prediction for 282.42 in-lbf impact energy.

2.5.5 Decreasing Longitudinal Strength

The PD simulation for the 262.5 in-lbf was repeated with the longitudinal strength, σ_{11}^f , reduced by 10% and 15% (Table 2.16). Both the 10% and 15% reduction in longitudinal strength captures the correct behavior of a sharp drop in force near 3 ms (Figure 2.88),

however, only the 10% reduction captures the maximum force value. Reducing the longitudinal strength demonstrates that there is sensitivity in fiber bond failure at the highest energy level and that the PD model, much like the experimental tests, is very close to a change in failure morphology at that energy level.

Table 2.16: Summary of decrease in longitudinal strength.

σ_{11}^f (ksi)	$0.9\sigma_{11}^f$ (ksi)	$0.85\sigma_{11}^f$ (ksi)
421	379	358

With relatively small decreases in the longitudinal strength, 379 ksi and 358 ksi, respectively, a significant change in the force-time response can be observed (Figure 2.88). The predicted failure with a 10 % decrease in longitudinal strength is very similar to that of the 7.5 % higher impacting energy scenario presented in the previous section. Fiber failure is a significant contributor to the change in the force response at this energy level. At the threshold energy level, small variations in the longitudinal strengths (still within bounds of experimental error) are enough to alter the force vs. time response. This indicates that a sensitivity study is needed when predictions are desired near this threshold.

As the longitudinal strength is decreased, the fiber bonds on the back surface begin to fail, leading to a drop in force. Similar to the experiments and the increased energy scenario, a recovery period occurs between 3 and 4 ms (Figure 2.89) the impactor finally rebounds from the surface. During this recovery period, the displacement increases with decreasing force (Figure 2.89).

The absorbed energy of the 10% decrease in longitudinal strength matches well with the experimental results (Figure 2.90), however, still slightly undershoots the final absorbed energy.

The failure predictions for 262.5 in-lbf (Figure 2.91 (a)) and 262.5 in-lbf with a 10 % decrease in fiber longitudinal strength (Figure 2.91 (b)) display some unique differences. First, as expected, decreasing the longitudinal strength increases the fiber failure extent and concentration (black squares). Additionally, an interaction between the fiber failure

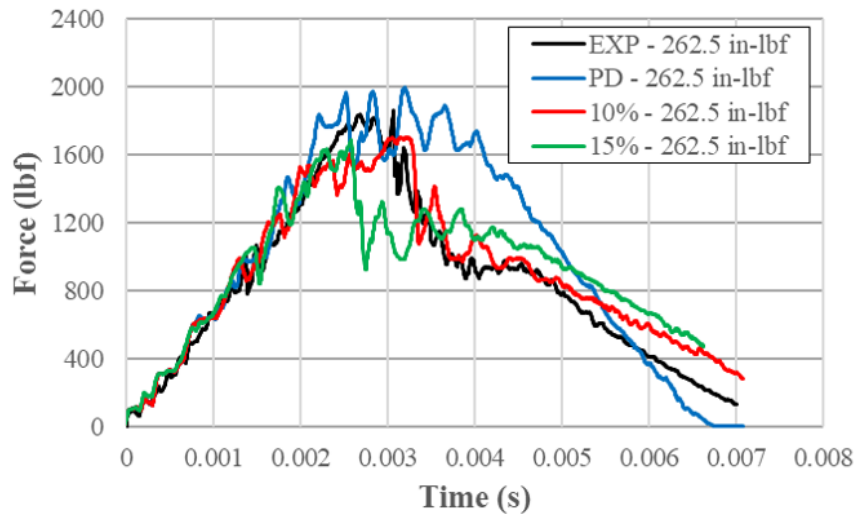


Figure 2.88: Force vs. time response predicted with 15% (green) less, 10 % (red) less, and original longitudinal strength (blue) compared against experimental measurements for 262.5 in-lbf impact energy.

and other failure mechanisms can be observed; specifically, the overall extent of damage (colored squares) is greater in the scenario with lower fiber strength, despite the same other failure parameters (matrix, shear, normal).

As a final verification of the BVID/VID threshold, the 10 % decrease was run at the third energy level. While the force vs. time response (Figure 2.88), force vs. displacement (Figure 2.93), and energy vs. time (Figure 2.94) differ slightly from the previous prediction, they are overall still in good agreement.

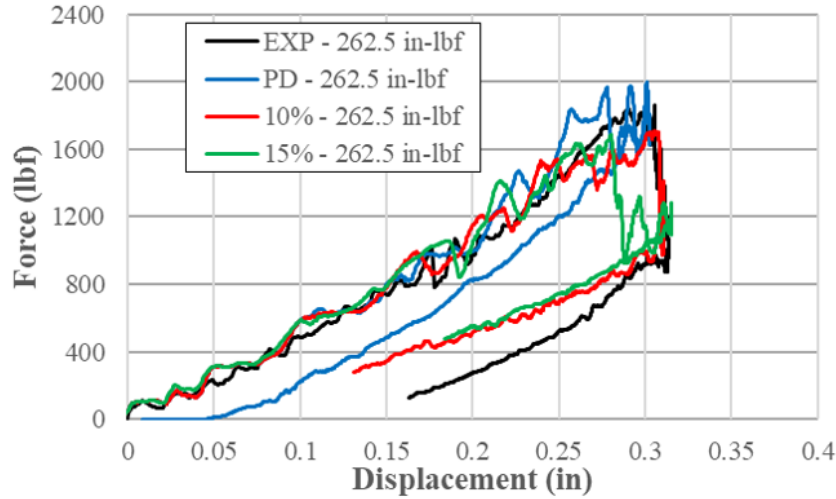


Figure 2-89: Displacement vs. time response predicted with 15% (green) less, 10 % (red) less, and original longitudinal strength (blue) compared against experimental measurements for 262.5 in-lbf impact energy.

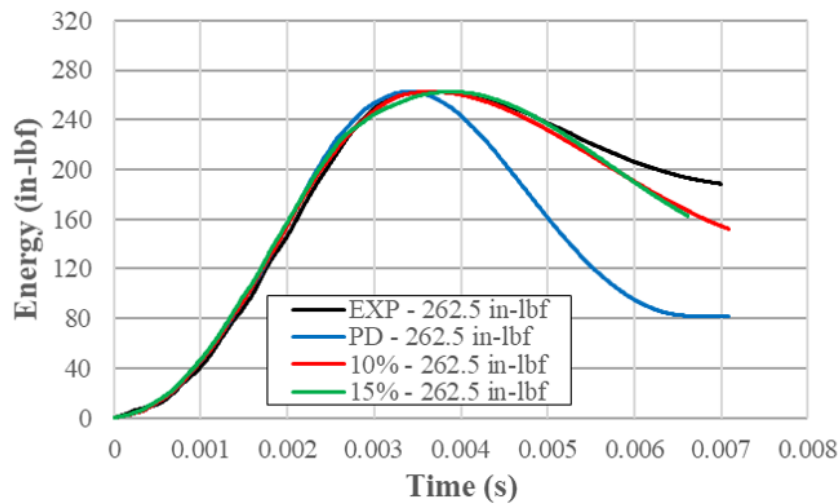


Figure 2-90: Energy vs. time response predicted with 15% (green) less, 10 % (red) less, and original longitudinal strength (blue) compared against experimental measurements for 262.5 in-lbf impact energy.

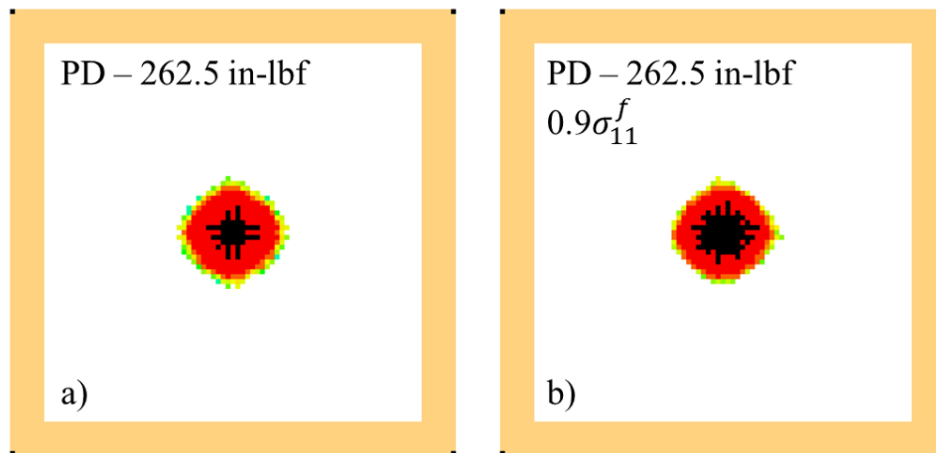


Figure 2.91: Delamination predicted with the original longitudinal strength (a) and with the 10% less longitudinal strength (b).

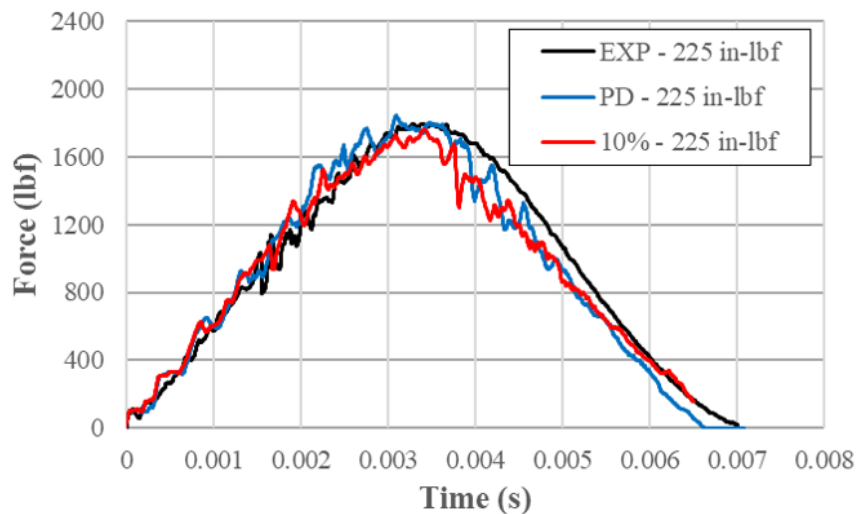


Figure 2.92: Force vs. time comparison of decreasing longitudinal strength at 225 in-lbf.

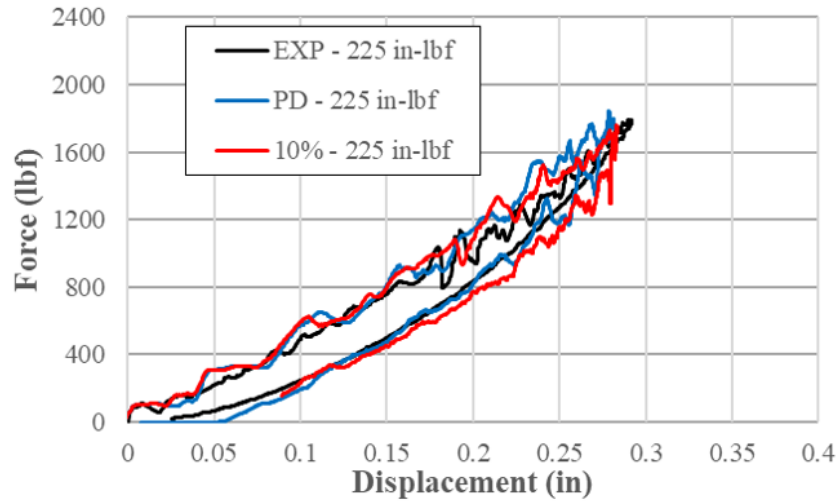


Figure 2-93: Force vs. displacement comparison of decreasing longitudinal strength at 225 in-lbf.

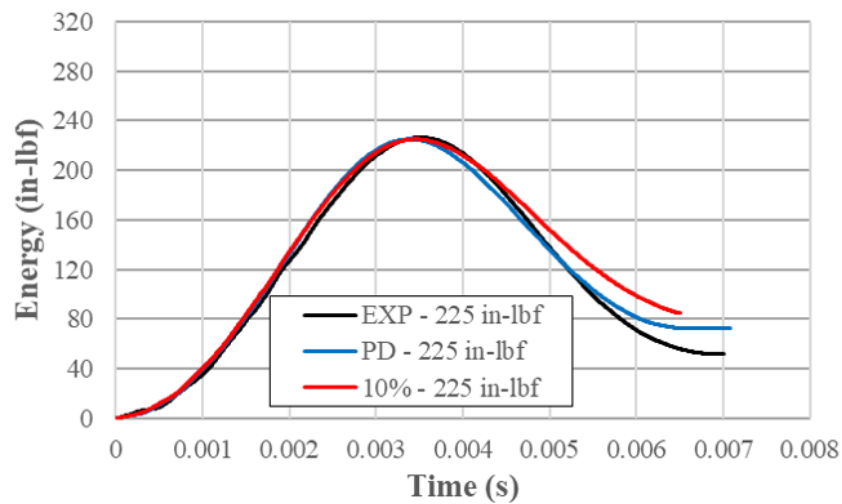


Figure 2-94: Energy vs. time comparison of decreasing longitudinal strength at 225 in-lbf.

2.5.6 Comparing Increased Energy with Decreasing Longitudinal Strength

Shown in the previous sections, increasing impact energy and decreasing longitudinal strength both produce similar force vs. time and force vs. displacement responses. While there is significantly more absorbed energy (Figure 2.95) in both scenarios (green and red) than the original scenario (blue), it still underpredicts the experimental result (black). This is a very interesting response, in particular because damage footprint of the higher energy case (Figure 2.96 (c)) is slightly larger than that of the lowered fiber strength (Figure 2.96 (b)) scenario. Because the absorbed energy is very similar, this implies that the fiber damage and perhaps the intensity of other damage mechanisms is contributing significantly to the absorbed energy. Importantly, correctly capturing the damage footprint and energy absorbed requires the correct capturing of the interaction of these different damage mechanisms.

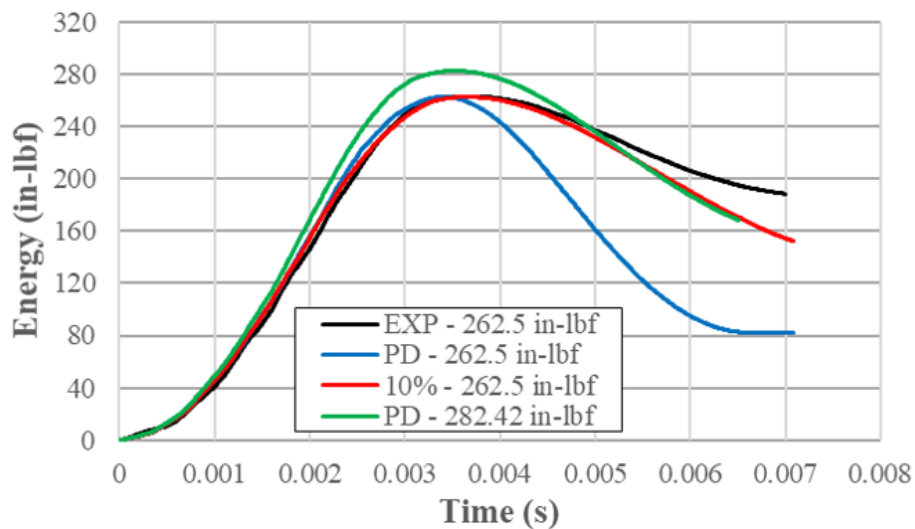


Figure 2.95: Energy vs. time response predicted with energy 282.4 in-lbf (green), 10 % (red) less longitudinal strength, and original longitudinal strength (blue) compared against experimental measurements for 262.5 in-lbf impact energy.

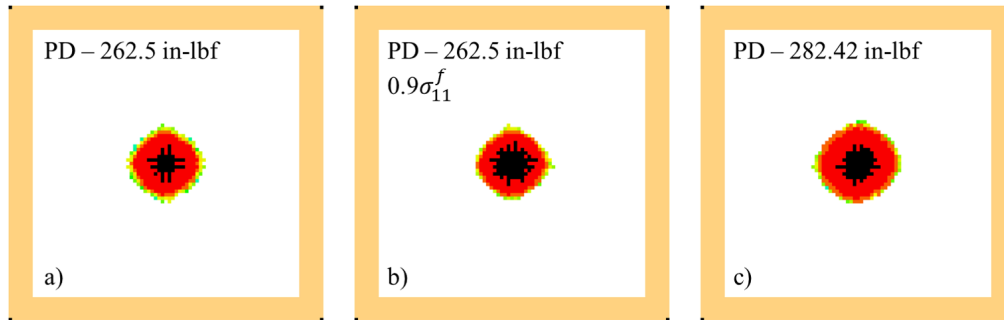


Figure 2.96: Delamination predicted with the original longitudinal strength (a) and with the 10% less longitudinal strength (b).

The fiber damage ply-by-ply prediction is compared (Figure 2.97 and 2.98) and shows that overall the fiber damage between the two scenarios is very similar. Fiber damage occurs on each ply and is oriented along the fiber direction. Both increasing the energy and decreasing longitudinal strength can push the simulation into the VID region, however, the simulations are still not able to capture the long extension of the fiber damage on the back face of the laminate. It is believed that the intralaminar discretization and the nonlocal horizons play a role in this fiber damage extension. These aspects of the simulations should be explored in future work.

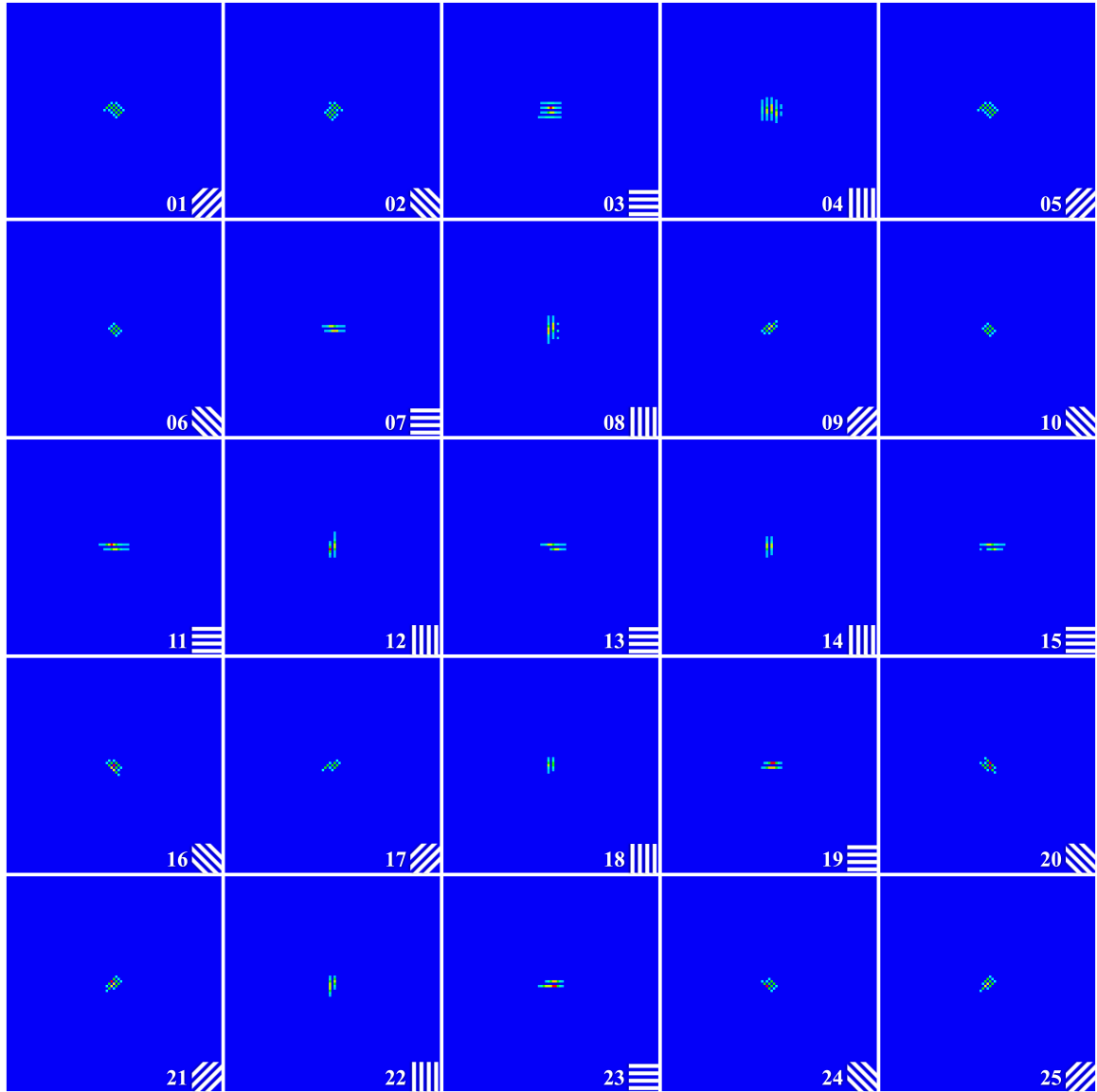


Figure 2-97: Fiber damage associated with a 10% decrease in longitudinal strength.

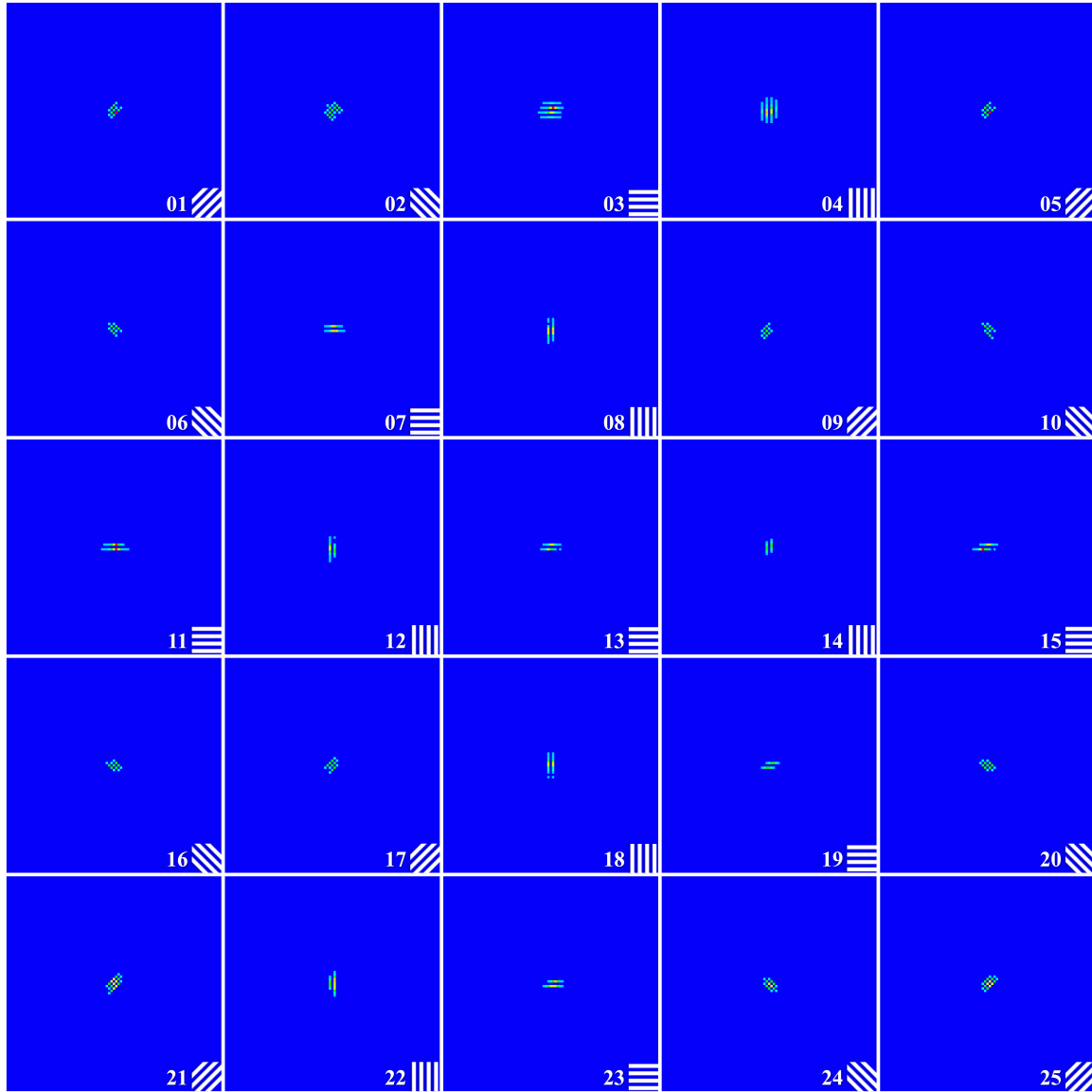


Figure 2-98: Fiber damage associated with an impact energy of 282.42 in-lbf.

2.6 Hat-Stiffened Panel Impact Simulation Results

A modeling approach was developed to simulate a hat-stiffened panel subjected to low velocity impact. The panel, with dimensions of 12 in. x 12 in., consisted of 25 plies with a [(45/-45/0/90)³/0/(90/0/-45/45)³] stacking sequence. A 1/2 in. rigid body hemispherical penetrator with a mass of 21.884 lbm and velocity of 72.83 in/s was used to impact the panel with 150 in-lbf of energy. The panel was impacted on the skin side 6 in. from the edge on the outer mold line and constrained using simply supported boundary conditions on the parallel edges. A three-dimensional isometric view of the hat-stiffener is reproduced in Figure 2-99 and hat-stiffener dimensions are provided in Figure 2-100.

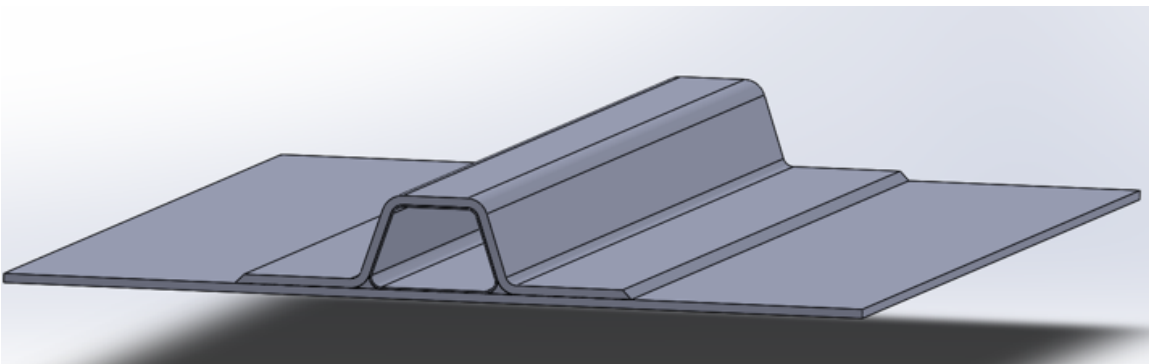


Figure 2-99: Hat-stiffened panel geometry.

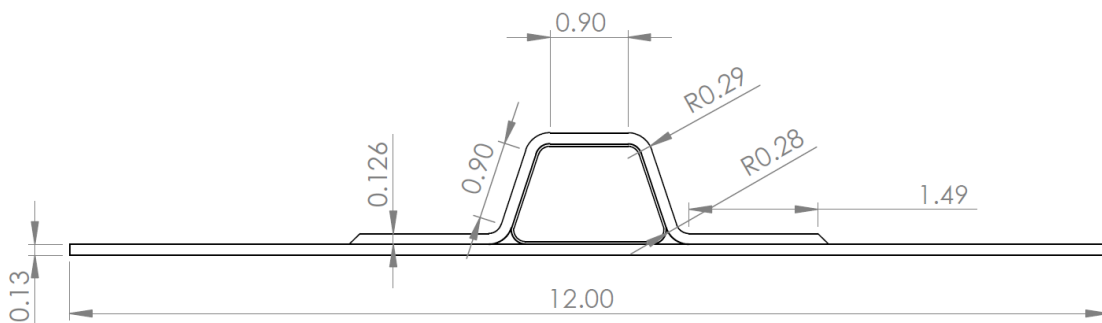


Figure 2-100: Hat-stiffened cross-section geometry.

The cross-section of the hat-stiffener was discretized (Figure 2-102) and extruded in the longitudinal direction (Figure 2-101). The discretization parameters of Table 2.11 were

used. Because the laminate dimensions increased from 7 in. \times 7 in. to 12 in. \times 12 in., the number of material points in the PD model increased to approximately 600,000. Additionally, the stiffener itself contained approximately 400,000 material points.

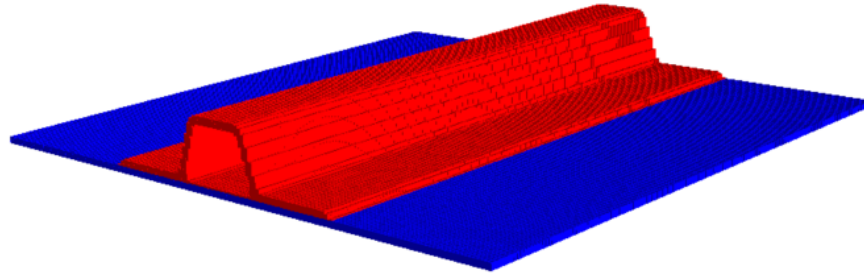


Figure 2·101: Discretized hat-stiffened panel with the hat-stiffener (red) and laminate (blue).

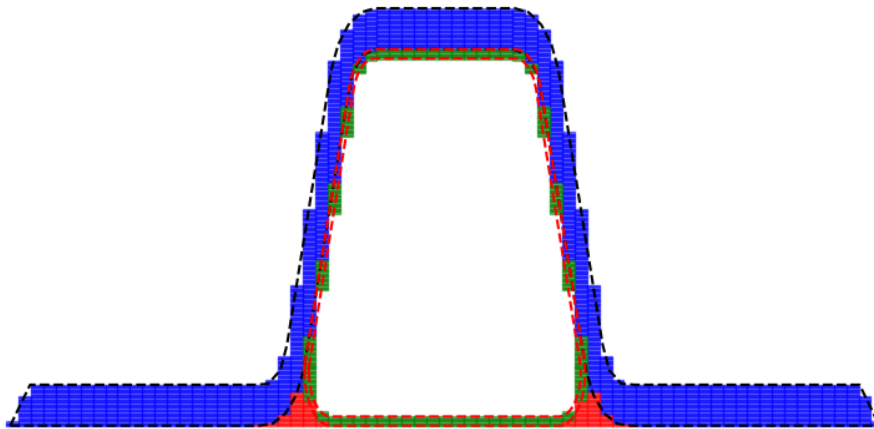


Figure 2·102: PD hat-stiffener cross-section discretization.

The increased geometry and lower impact velocity, as compared to the unreinforced simulations, lead to a much longer impact duration and a significantly more computationally demanding simulation. For simplicity, despite the stiffener being comprised of both a fabric and a noodle, only the fabric material properties are considered in the model.

The force vs. time curve (Figure 2·103), the force vs. displacement curve (Figure 2·104), and the energy vs. time curve (Figure 2·105) are provided for comparison purposes. Preliminary simulations have a peak force of approximately 1100 lbf at 6 ms. The

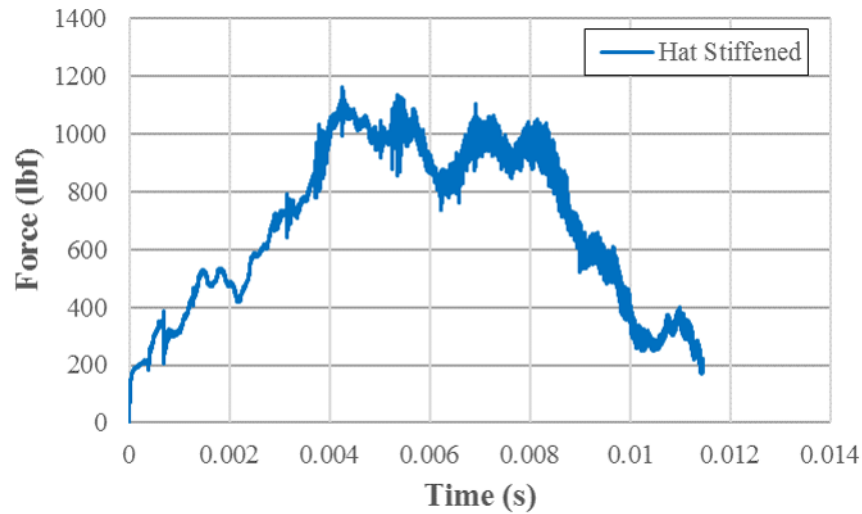


Figure 2-103: Force (lbf) vs. time (s) prediction for the hat-stiffened panel.

impact duration is approximately 12 ms with a peak force of approximately 1100 lbf at 6 ms. The predicted peak displacement is approximately 0.28 in. The energy vs. time curve (Figure 2-105) indicates the expected peak energy at 150 in-lbf, which is equal to the input energy, however, it is too early in the simulation to measure the absorbed energy in the panel. The z-displacement (Figure 2-106) of the hat-stiffened panel at the peak displacement exhibits the expected contour, but with a larger than expected local deformation under the impactor. A small circular damage directly under the impactor was predicted (Figure 2-107) in addition to some directionally dependent damage, possibly indicating fiber damage.

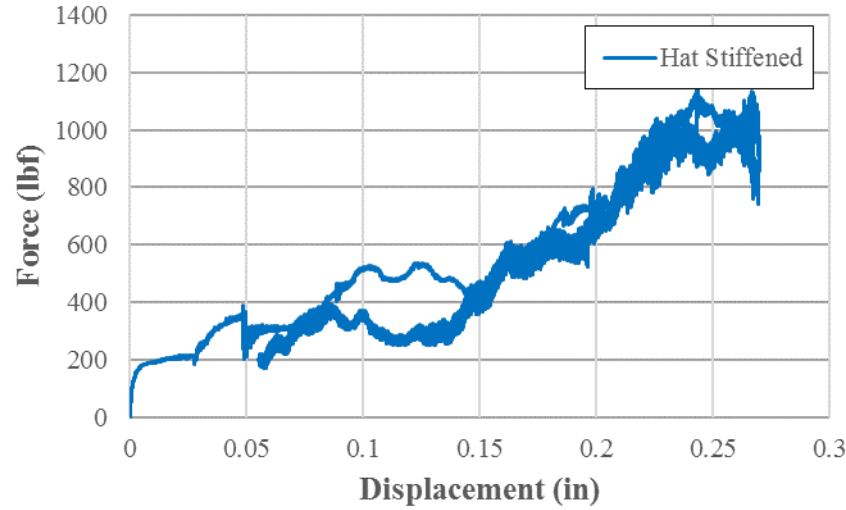


Figure 2-104: Force (lbf) vs. displacement (in) prediction for the hat-stiffened panel.

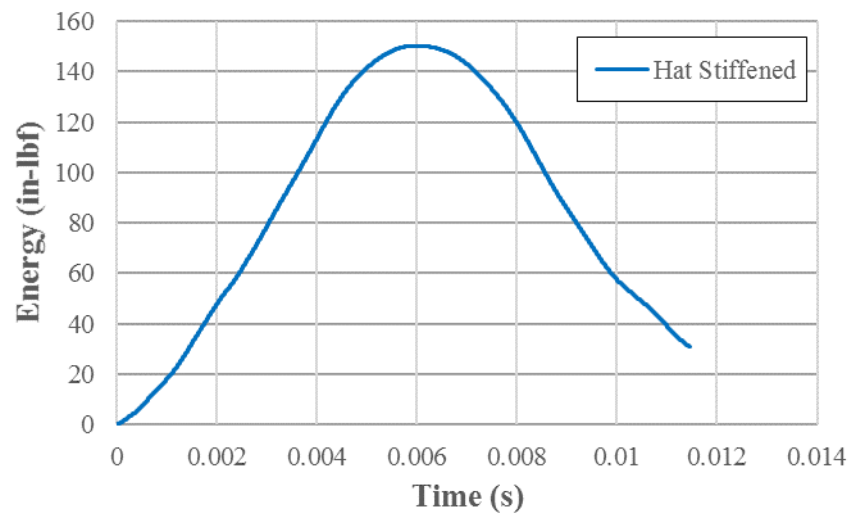


Figure 2-105: Energy (in-lbf) vs. time (s) prediction for the hat-stiffened panel.

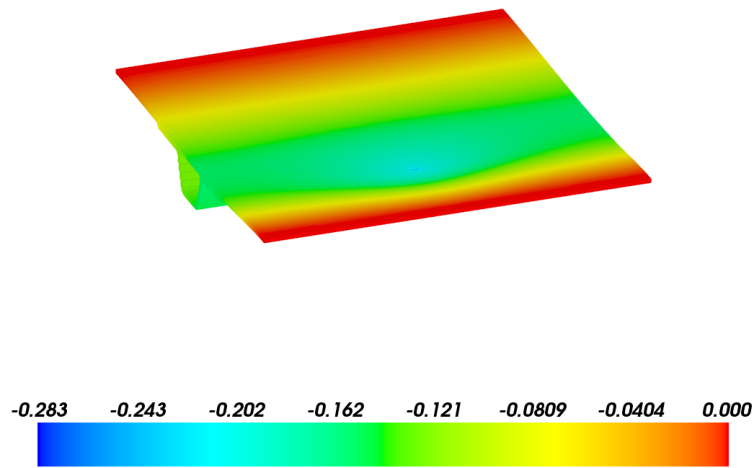


Figure 2-106: Z-displacement contours of the hat-stiffened panel.

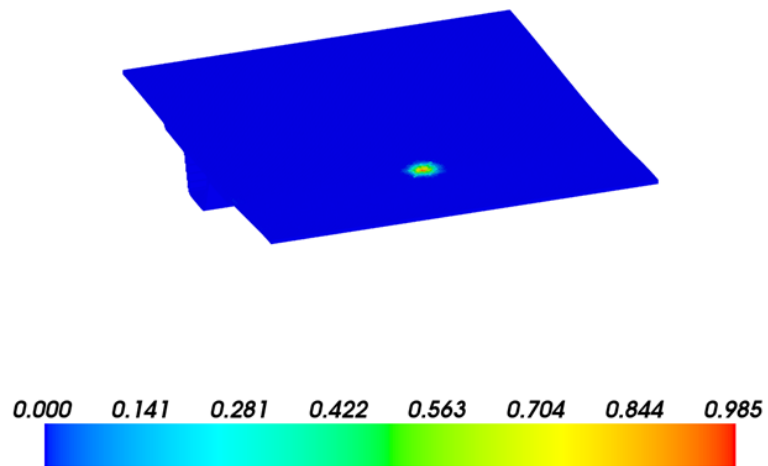


Figure 2-107: PD damage prediction in the hat-stiffened panel.

While the preliminary results are promising, more work is needed to accurately model the hat-stiffened panel. Most importantly, the PD model currently needs a uniform intralaminar discretization to incorporate shear bonds into the model. The curves of the hat-stiffener meant that the shear bonds could not be readily incorporated. This limitation can be overcome in the future by changing the shear bond reference system from z-based coordinate system to a ply number coordinate system. Introducing these shear bonds, with the same formulation as in the laminate itself, would allow the decoupling of the intralaminar and interlaminar response and the capturing of delamination between the hat-stiffener and laminate.

2.7 Through-Thickness Reinforcement Simulation Results

2.7.1 Considerations for Through-Thickness Reinforcement

An approach was developed for incorporating through-thickness reinforcements by representing stitches as embedded bonds. These bonds can be thought of as a duplication of existing interlaminar bonds (Figure 2-108)) with their own respective stitched based material parameters.

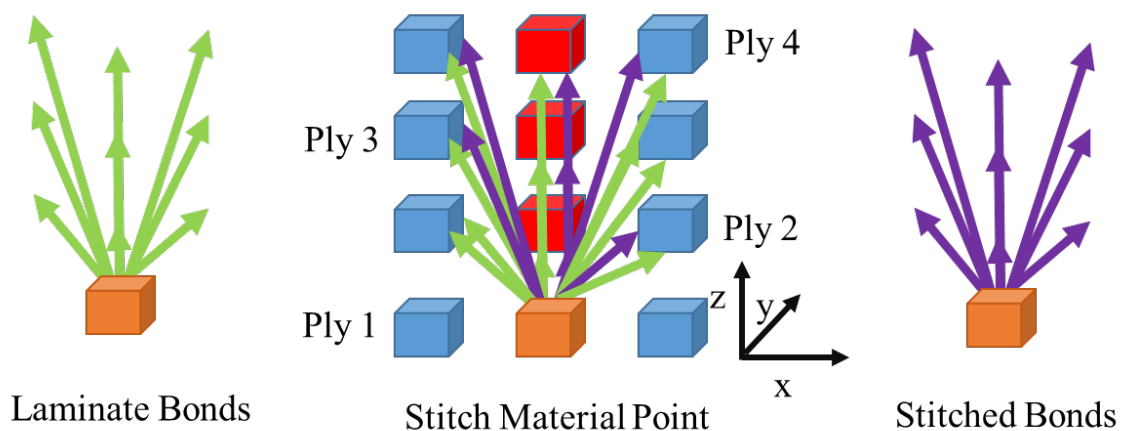


Figure 2-108: Schematic demonstrating the stitched bond approach.

To implement this approach, first the stitched material points are identified based on an

input pattern (Figure 2·109). The identified PD material points are written to file and are provided as input to the simulation.

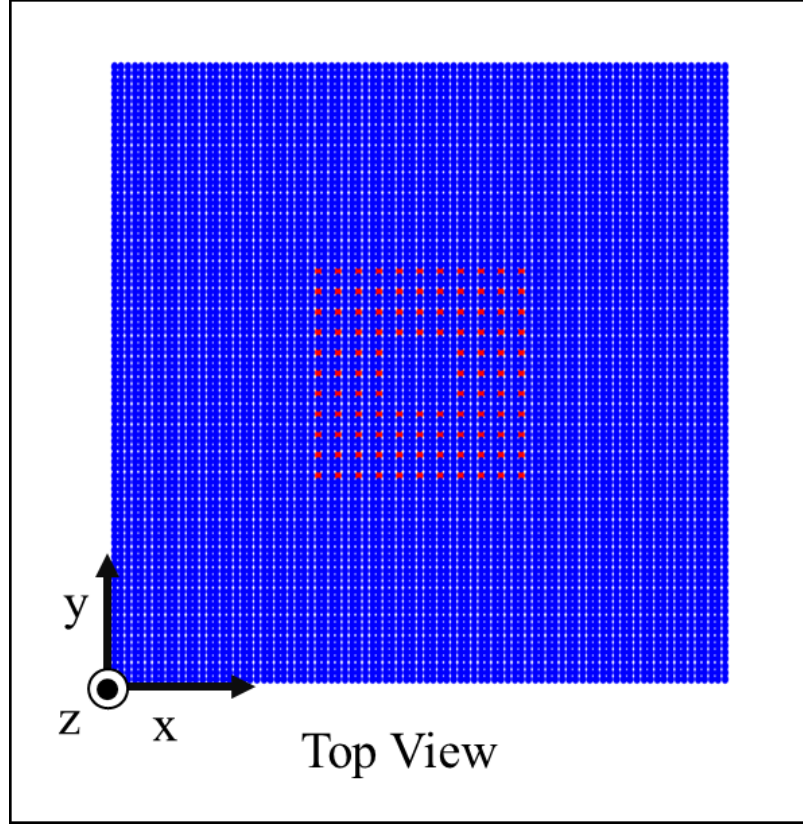


Figure 2·109: Example of a stitched pattern and the identified stitched PD material points (red) shown from a top view.

The stitched bonds influence the model by increasing the bond force density contribution. Mathematically, the bond force density f_{ij} relationship can be thought of as containing a laminate bond force density contribution f_{ij}^l and a stitched bond force density contribution f_{ij}^s .

$$f_{ij} = f_{ij}^l + f_{ij}^s \quad (2.107)$$

While the stitched bond force density contribution can take many different forms, in this work, as initial demonstration of concept, it is assumed to take a linear form. For interlaminar shear bonds, the constitutive relationship can be written as

$$f_{ij} = (k_s^l + k_s^s) \phi \Delta x^2 \frac{\delta}{r} \frac{y_j - y_i}{|y_j - y_i|} \quad (2.108)$$

where k_s^l is the interlaminar shear constant of the laminate and k_s^s is the stitched interlaminar shear constant. Similarly, for interlaminar normal bonds, the constitutive relationship can be written as

$$f_{ij} = (k_n^l + k_n^s) u_n \frac{\delta}{r} \frac{y_j - y_i}{|y_j - y_i|} \quad (2.109)$$

where k_n^l is the interlaminar normal constant of the laminate and k_n^s is the stitched interlaminar normal spring constant. A flow chart is provided (Figure 2.110) to summarize the steps taken to introduce a through-thickness response.

```

Require: List of identified stitched material points
Ni ← number of iterations
for i = 1 to Ni do
  m ← material points on processor
  for k = 1 to m do
    Determine if stitched material point
    Calculate stitched bond force density contribution
    Return updated bond force density
  end for
end for

```

Figure 2.110: Flow chart for introducing through-thickness reinforcements.

2.7.2 Through-Thickness Reinforcement Simulation Results

As discussed in the previous section, the through-thickness reinforcement is included by considering embedded bonds at stitched locations. The stitches were introduced in a frame pattern (Figure 2.111) with the outer and inner frame dimensions of 2.5 in. × 2.5 in. and 1 in. × 1 in., respectively. This distance between each stitch is 0.25 in. The frames are centered on the laminate.

The PD representation of (Figure 2.111) contains 11 stitched material points in the

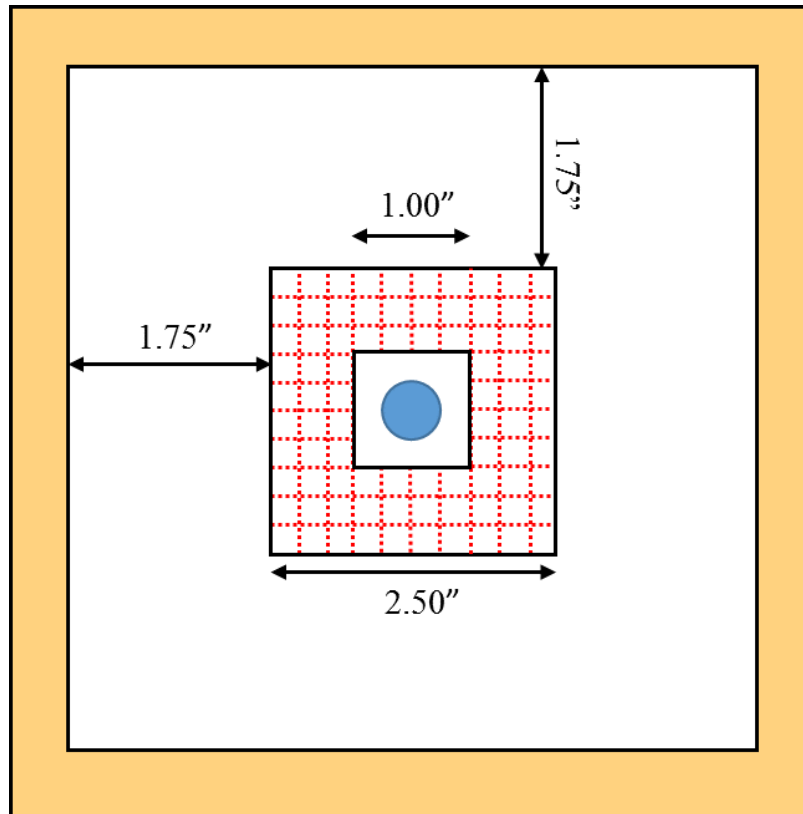


Figure 2-111: Stitch schematic showing the dimensions of the stitched frame with respect to the laminate.

x-direction and y-direction with no stitched material points in the interior 1 in. \times 1 in. inner frame (Figure 2-109). Both the material points and stitched pattern are uniform in the thickness direction.

Other aspects of the model such as the discretization (Table 2.11), PD material parameters (Table 2.12), and Ramberg-Osgood strain rate dependent parameters (Table 2.9) remain the same as in the previous sections. A piecewise linear stitched material response was provided in terms of force (lbf) and displacement (in) (Figure 2-112). Based on approximate values for the diameter D , cross-sectional area C_a , and the stitch length L_o (Table 2.17) the force displacement response (Figure 2-112) was converted into an axial stress vs. strain response (Figure 2-113).

As preliminary work, only the initial modulus of the stitched material was considered.

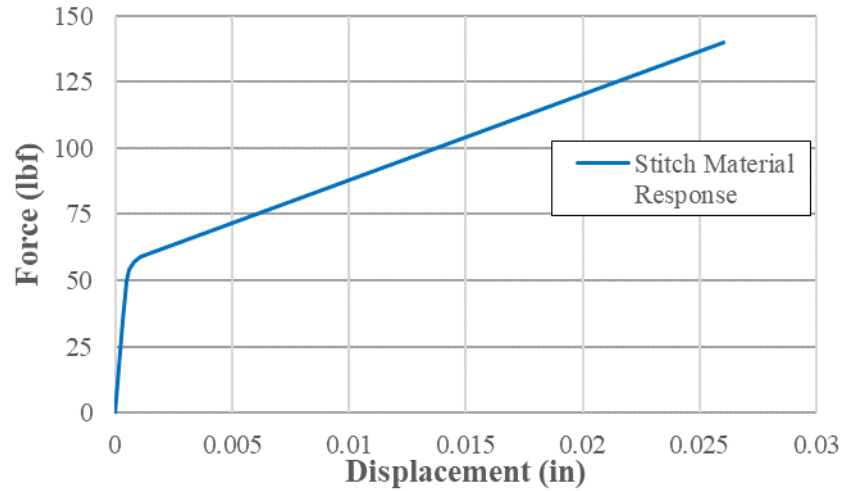


Figure 2.112: Force (lbf) vs. displacement (in) response for the stitch material.

Table 2.17: Approximate stitched geometric parameters.

D (in)	C_a (in ²)	L_o (in)
6.25e-2	3.07e-3	1.30e-1

Two scenarios were explored: scenario B has a stiffness approximately equal to the initial slope of (Figure 2.113) and is approximately 1.5 times stiffer than scenario A (Table 2.18).

Table 2.18: Normal and shear bond stitched material parameters.

Scenario	k_n^s (lbf/in ⁷)	k_s^s (lbf/in ⁵)
A	1.18e13	7.41e8
B	1.76e13	1.10e9

The stitched laminate was impacted with 225 in-lbf of energy using a 0.5” diameter tup. The force vs. time (Figure 2.114), force vs. displacement (Figure 2.115), and energy vs. time (Figure 2.116) simulation results were compared with the unreinforced laminate impacted under the same conditions. The introduction of a through-thickness reinforcement into the laminate slightly increased the peak force without changing the initial slope

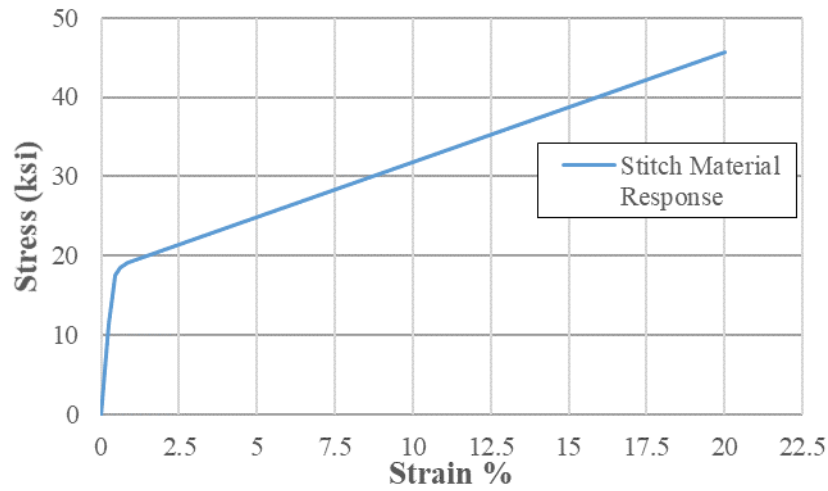


Figure 2-113: Converted stress (ksi) vs. strain (%) response of the stitched material.

of the force time curve (Figure 2-114), while the duration of the impact event remained approximately the same. Despite scenario B (green) having stitched material constants 1.5 times stiffer than scenario A (red), the force vs. time response and force vs. displacement response is very similar.

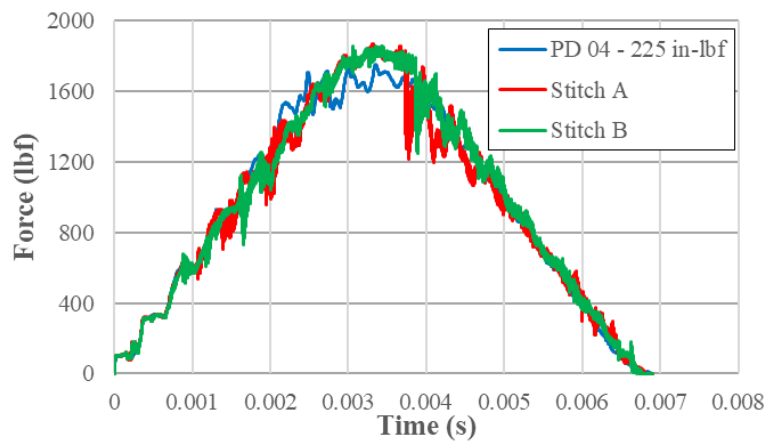


Figure 2-114: Comparison of stitch reinforced and unreinforced simulations at 225 in-lbf.

The most observable difference occurs in the energy vs. time plots (Figure 2-116). Scenario A has a significantly higher absorbed energy ~ 65.8 in-lbf compared to scenario B

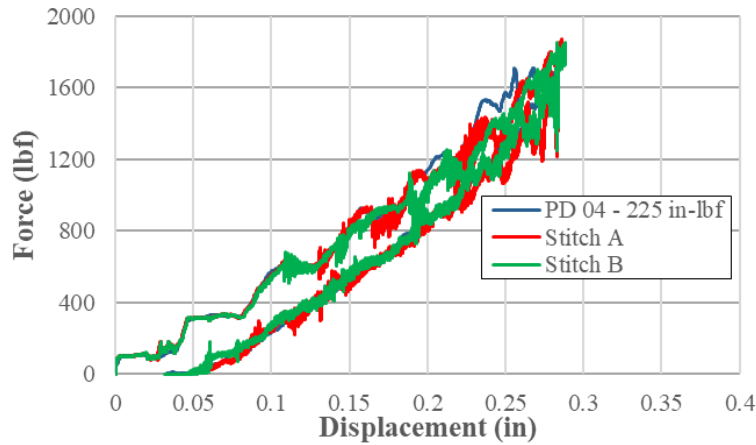


Figure 2-115: Force (lbf) vs. displacement (in) curve comparing a stitched laminate simulation with an unreinforced laminate simulation.

which has only ~ 54.7 in-lbf. Alternatively, when the stitch stiffness is decreased (Scenario B), the absorbed energy (Figure 2-116) response is very similar to that of the unreinforced case.

The differences in the absorbed energy response are naturally reflected in the delamination and damage contours (Figure 2-117). Stitch A has a much higher amount of damage and damage surrounding the location of the stitches. Alternatively, Stitch B and the unreinforced simulations have very similar delamination extents. While the delamination enters the stitch frame region denoted by the dashed black lines, it does not appear arrested.

Although the root cause of the increase in delamination with increasing stitched stiffness still needs further exploration, it is believed that there is an unnatural wave reflection that occurs when the stiffness of the stitched bonds is high. This can be thought of as similar to an additional boundary condition. It is thought that adding a mechanism for energy dissipation would more accurately capture the stitched response when embedded into the laminate.

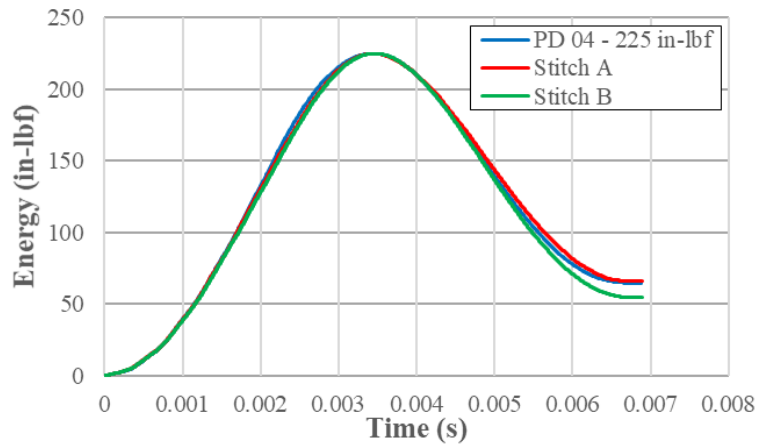


Figure 2-116: Energy (in-lbf) vs. time (s) curve comparing stitched and unreinforced PD simulations.

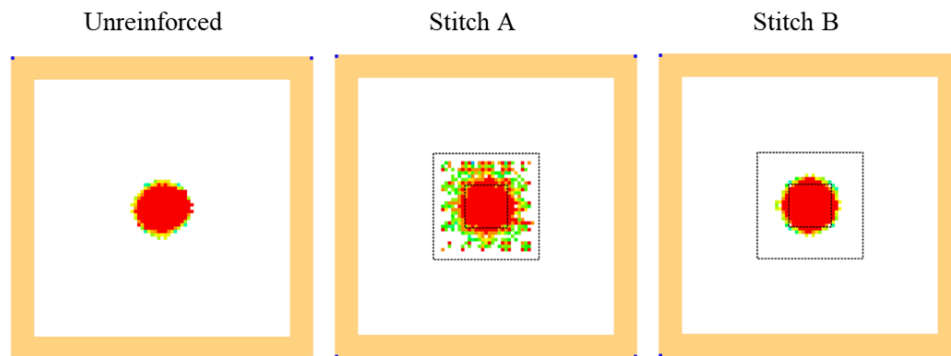


Figure 2-117: Comparison of stacked delamination between the two stitched scenarios.

Chapter 3

CNT Yarn Reinforced Polymer Composites

3.1 Background

Carbon nanotubes (CNTs) have been studied extensively for decades [46]. Although the measured nanoscale stiffness of CNTs has been reported on the order of 1 TPa [47–49] and the strength in the range of 50 - 100 GPa [49, 50], their envisioned use in the creation of a bulk scale composite with such properties has not been fully realized. One of the current challenges facing the aerospace structures community is to carry these nanoscale properties to the macroscale. A potential solution to this challenge is the development of CNT macro assemblages, in particular, CNT yarn. Recently developed manufacturing techniques have made CNT macro assemblages more readily available for aerospace applications [51].

In comparison to carbon fiber composites, CNT yarn-based composites have not been fully characterized. This lack of characterization can be traced back to advances in processing control. The large variety of processing parameters and post-processing procedures lead to a great diversity of microstructures. Experimental testing of each unique microstructural realization is simply not feasible. The expensive and time-consuming nature of experimental testing necessitates the advancement of simulation methodologies that can incorporate microstructural details. It is believed that such simulations could provide feedback to both synthesis and processing researchers, allowing a more targeted search for desirable structures.

Predicting and understanding the failure of materials has long been a challenging endeavor. Peridynamic theory has proven to be successful in capturing the failure and fracture behavior of a wide variety of material systems. Over the years, the failure prediction

capabilities of PD theory have been demonstrated on glass [27, 52, 53], metal [54], and carbon-fiber composite [22, 25] material systems. The theory is particularly adept at simulating failure in these material systems because of its integral formulation which, unlike its differential counterpart, does not give rise to the mathematical singularities associated with fracture [21].

In recent years, various PD approaches have been developed for carbon-fiber reinforced polymer (CFRP) composites [23, 25, 41]. Only a few researchers have explored the application of PD to CNT composites. In the early work [55], Bobaru et al. developed a 3D PD framework for carbon nanofiber networks and CNT composites. The authors demonstrated the ability of PD to capture complex failure behavior associated with the stretching of a fiber network and CNT pullout. Rahman et al. used a hierarchical multiscale modeling approach to link atomistic simulations with a coarsened state-based PD model [56]. In that work, the researchers explored deformation mechanisms associated with carbon nanofibers. More recent work [57] combined bond-based PD and Monte Carlo simulations to predict the mechanical properties for CNT-based nanocomposites.

A major distinction between previous PD CNT frameworks and the one proposed in this work is the length scale at which simulations are performed. In all of the above work, simulations were performed at the CNT/nanofiber length scale (nanometers). In the current work, the simulation domain is increased and simulations are performed at the CNT yarn length scale (micrometers).

This research aims to provide a systematic approach to incorporate microstructural information into the simulation process. In the current work, x-ray computed tomography (CT) is used to develop a simulation grid containing constituent level information. The composite microstructure is characterized using statistical and data clustering algorithms. A novel peridynamic approach for simulating CNT yarn composites has been developed to accurately capture the failure morphology and to investigate its origins. Finally, a framework was developed for creating synthetic microstructures through the use of probability density functions.

3.2 Experimental Work

In the previous work by Kim et al. [6], unidirectional CNT yarn polymer composites were fabricated from highly-densified CNT yarns (provided by Nanocomp Technologies, Inc.). Each yarn was composed of 4 plies of CNT roving. The 4-ply yarn has an irregular shape measuring an average of approximately 250 μm in diameter. Cyanate ester (RS-16) resin from Tencate Advanced Composites was diluted with methyl ethyl ketone (MEK) to a 65 wt. % MEK solution. A 100 to 9 mix ratio between resin solution and curing agent was used. The resin solution was applied to the CNT yarns by a wet winding method using a custom-built filament winder, with an applied winding tension of 13.34 N [51]. The CNT yarn was passed through a resin bath followed by direct winding onto a custom-made solid aluminum plate (width of 15.24 cm and height of 10.16 cm) as shown in Figure 3-1. The as-wound materials were sandwiched between two steel plates and then cured with a 4 hr hold at 113° C followed by a 1.5 hr hold at 135° C under a cure pressure of 10.34 MPa. The final composite panel dimensions were 10.16 cm (height) \times 2.54 cm (width) \times 383 μm (thickness). The resin and void contents of the composite were 19 wt. % and 2 %, respectively.

Tensile properties of tabbed unidirectional composite specimens (10 cm (height) \times 0.5 cm (width)) were measured using an MTS-858 test stand equipped with a laser extensometer and pneumatic grips. P180 sandpapers were glued to the ends of the composite specimens using cyanoacrylate. A crosshead speed of 0.5 mm/min was used during the test. Table 3.1 lists the material properties associated with the yarn, resin and composite. The diameter variations found in the CNT yarn prevent accurate measurement of yarn properties in volume-based units. Instead, linear density-based tex units are used (1 tex = 1 g/km) for the reported specific strengths and moduli, 1 N/tex = 1 GPa/(g/cm³).

High resolution nondestructive evaluation of as-prepared unidirectional CNT yarn/polymer composites was conducted using a micro focus x-ray computed tomography (CT) system (Nikon Metrology) with a maximum resolution of 5 μm and magnification of up to 160 \times . A Perkin-Elmer 16-bit amorphous silicon digital detector with a 2000 \times 2000 pixel array

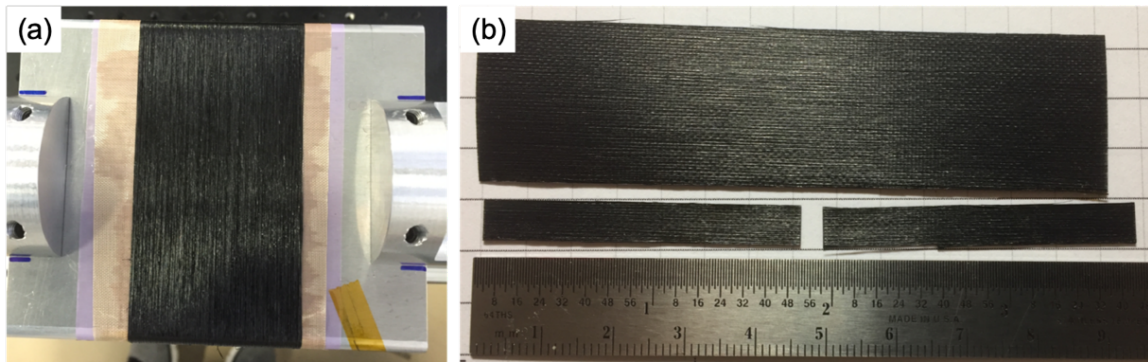


Figure 3.1: (a) Custom-made aluminum fixture and (b) unidirectional CNT yarn/cyanate ester composite.

was used to collect radiographs at each rotation angle as the x-ray path intersected the sample (360 degrees in 0.11 degree increments). The three-dimensional reconstruction of the collected radiographs produced tomographic data that could be viewed along any plane in the sample volume.

Table 3.1: Material properties of CNT yarn polymer composite. ^aAs reported by the manufacturer.

Material	Density (g/cm ³)	Specific Strength MPa/(g/cm ³)	Specific Modulus GPa/(g/cm ³)
Yarn Units	tex	N/tex	N/tex
Resin: Cyanate Ester ^a	1.19	67	2.5
Yarn: 4 ply ^a	26.89	1.63	96.3
Composite	1.14	1130	72.3

An experimentally obtained, representative stress vs. strain curve is presented in Figure 3.2. The initially observed stress stiffening is attributed to the elimination of slack and an increase in alignment of the CNT yarns as the load is applied. The softening behavior observed prior to failure is attributed to partial damage to the yarns before the complete failure of the specimen or originated from the typical mechanical response of CNT assemblies such as yarns and sheets. Figure 3.3 shows the fully failed specimen. The fully failed

specimen shows failure in multiple locations of the specimen and a yarn pullout failure morphology.

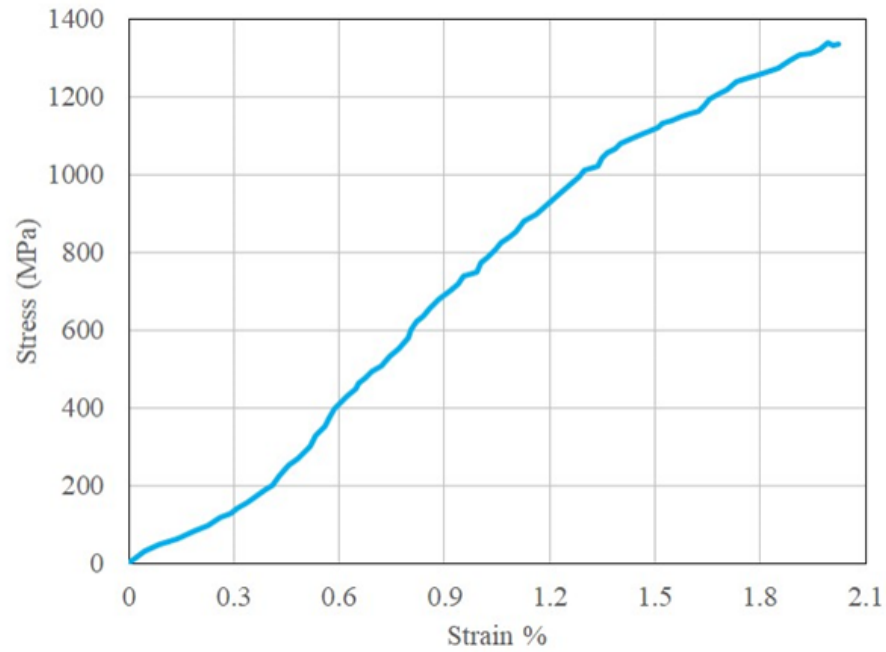


Figure 3-2: Experimentally obtained representative stress vs. strain curve.



Figure 3-3: Fully failed CNT yarn composite specimen.

3.3 Microstructure Characterization

A procedure was developed to convert x-ray CT bitmap (BMP) images into a PD simulation grid to incorporate structural features in the model. Features associated with the grids were then characterized using simple statistical methods and data clustering algorithms.

3.3.1 X-ray CT Imaging

The reconstruction of the CNT yarn composite sample characterized using micro x-ray CT produced a data set with dimensions of 2000 (width) \times 722 (height) \times 1999 (length) pixels and a reconstructed pixel resolution of approximately 3.6 μm in each direction. This data set served as the foundation for the PD simulation grid. Figure 3-4 presents a grayscale cross-sectional view of the composite obtained after the scanning process and demonstrates several directly observable features such as surface undulation, resin rich regions, and porosity.

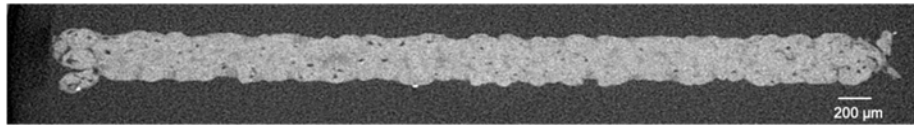


Figure 3-4: Cross-sectional x-ray CT BMP image of a unidirectional CNT yarn polymer composite.

3.3.2 Thresholding Process

Data obtained from the x-ray CT was post-processed using ImageJ [58] and converted from its native file type into a series of BMP images. Python scripts were used to segment these BMP images based upon pixel grayscale value. Following the work of Kim et al. [6], the threshold set point was obtained in ImageJ through manual adjustment and visualization of the porosity. During thresholding, grayscale values below the set point were discarded while higher values were kept. This initial thresholding effectively separated the foreground and background of each BMP slice, whereas internally discarded pixels indicated the presence of voids.

The retained pixels became the PD simulation grid. Figure 3-5 compares a single BMP slice against its segmented counterpart. For visualization purposes, lighter shades of gray coming from the BMP image are shown in the PD grid as orange/red colors, while darker shades of gray are green/blue in color

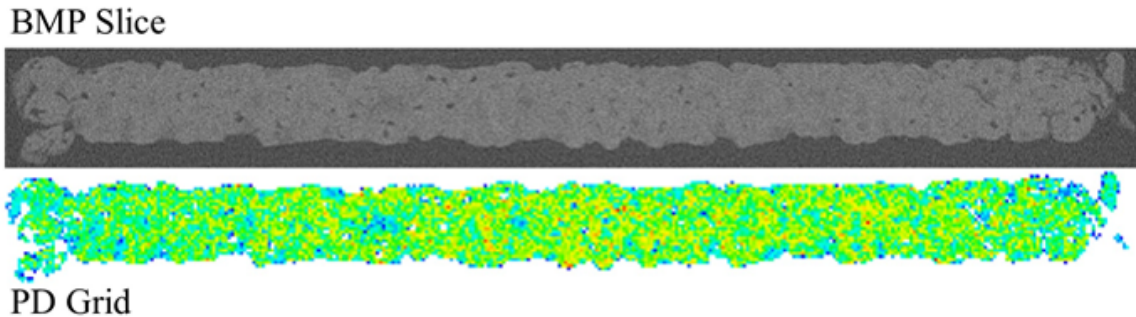


Figure 3-5: Comparison of BMP image and PD simulation grid after the thresholding process.

The final step in the grid generation process was to assign pixels as either CNT yarn or resin material. This was accomplished using a second threshold. The value of the secondary threshold was allowed to vary for each individual BMP slice. This variability arises as a result of contrast differences within the data set and is an artifact of the x-ray CT. To account for the variation in contrast, a series of thresholds were iterated through for each slice. The threshold set point was optimized by minimizing the difference between the calculated and experimentally measured resin volume fraction. Figure 3-6 shows a cross-sectional view after the thresholding procedures. In this figure, blue and red squares represent yarn and resin material points, respectively.

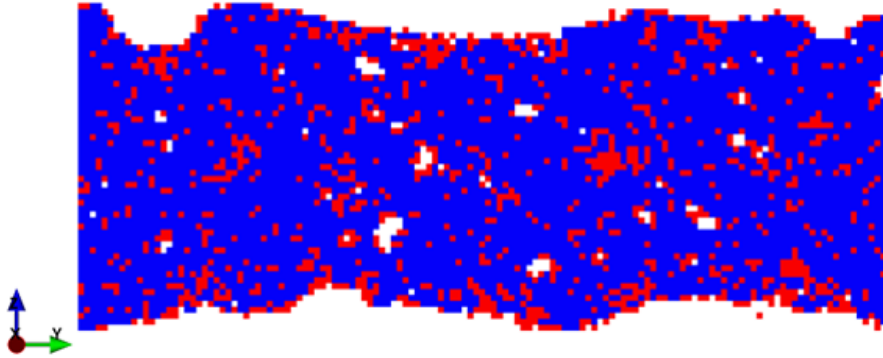


Figure 3-6: Example of determining constituent materials by means of a secondary threshold.

3.3.3 Manipulation of the Grid Spacing

A consequence of the thresholding approach is that the image resolution, the pixel to pixel distance, becomes the effective PD grid spacing. The grid spacing Δx can be controlled by manipulating the pixel dimension P_d . Equation (3.1) expresses the relationship between the physical size of the image P_s the pixel dimension P_d and the resolution P_r . With a desired grid spacing in mind, an updated pixel dimension U_d can be found as shown in Equation (3.2). This simple image manipulation allows for the creation of grid spacings larger than the native resolution.

$$P_s = P_d \cdot P_r \quad (3.1)$$

$$U_d = \frac{P_d \cdot P_r}{\Delta x} \quad (3.2)$$

Changing the resolution of the BMP image has significant influence over a pixels grayscale value. As a result, standard image processing resampling techniques were used to interpolate for a new grayscale value when manipulating the resolution. Specifically, a Lanczos resampling filter [59] was used to adjust grayscale value with changing resolution. This resampling filter was implemented through the use of the Python Image Library (PIL) [60] and the default kernel size was used.

Figure 3-7 shows several PD refinements of a BMP slice that can be obtained through manipulation of Equations (3.1) and (3.2) and demonstrates the effectiveness of the Lanczos resampling filter. Table 3.2 corresponds with Figure 3-7 and lists the approximate total number of material points in the corresponding three-dimensional PD model with each of the different grid spacings.

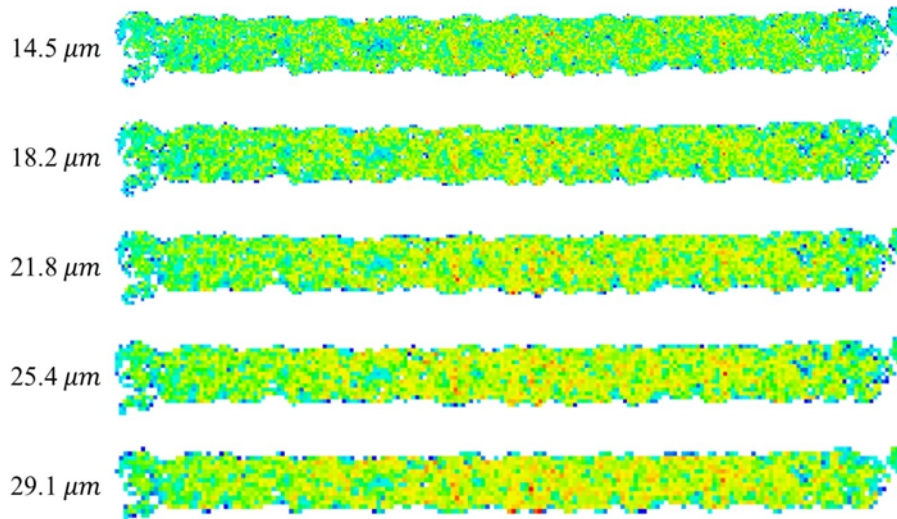


Figure 3-7: Comparison of differing levels of refinement. Notation on the left side of the image indicates grid spacing.

Table 3.2: Number of material points extracted from BMP images with changing grid spacing.

Multiple of Resolution	Grid Spacing (μm)	Number of points (10^6)
4	14.5	4.2
5	18.2	2.2
6	21.8	1.2
7	25.4	0.8
8	29.1	0.5

The BMP image is converted into a 2D PD grid Figure 3-8 (b) which contains yarn (blue) and resin (red) material points in addition to voids (white). Voids are represented

in the model by not including a material point at that specific location. This process of generating 2D slices is repeated for each BMP image and then stacked in the x-direction Figure 3-8 (c) to obtain the full simulation domain shown in Figure 3-8 (d). In all images, the yarn is oriented along the x-direction. Additionally, from this reconstruction it is clear that resin is continuous in the x-direction and most prevalent on the top and bottom surfaces. Another observation is that the resin material tends to cluster at regular intervals throughout the specimen.

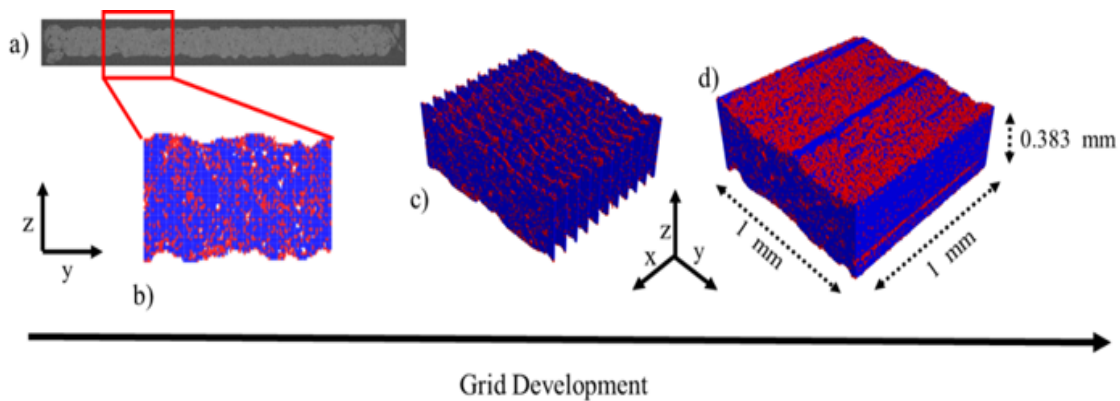


Figure 3-8: (a) BMP image containing yarn, resin, and void pixels. (b) A 2D PD slice of the composite specimen with yarn (blue) and resin (red) material points. (c) Stack of 11 different 2D PD slices with an exaggerated spacing in the x-direction. (d) A fully reconstructed section of the composite specimen.

After the conversion of the BMP images into a PD simulation grid, the domain was characterized using simple post-processing routines. These routines characterized aspects of the microstructure such as resin fraction, void fraction, number of resin/void clusters per unit area, and the average resin/void cluster sizes. This characterization is important because it will provide future insight into the failure mechanisms and stress vs. strain behavior of the composite. In the remainder of the text, these 6 different aspects are referred to as descriptors as they statistically describe the microstructure.

3.3.4 Characterization of Segmented X-ray CT Data

The x-ray CT data set was partitioned into four quadrants and four separate cells were created at 7.27 micrometer grid spacing. This permitted a high level of microstructural detail without exceeding available computational resources. Figure 3.9 (a) shows the locations of the cells on the x-ray CT domain. Cells were selected to exclude any boundary effects and were positioned to obtain a representative sampling of the entire specimen. Each cell has dimensions of approximately $1 \text{ mm} \times 1 \text{ mm} \times 0.4 \text{ mm}$ and contains approximately 900 thousand material points with a grid spacing of $7.27 \mu\text{m}$. An isometric view of Cell 1 is provided in Figure 3.9 (b), where red and blue voxels represent resin and yarn material, respectively. Figure 3.9 (c) shows the same isometric view of the cell, but colored by z-coordinate location. The alternating sequence of coloring on the top surface demonstrates the surface undulation present in the composite. Finally, Figure 3.9 (d) shows a cross-sectional view of the composite. From this orientation, one can clearly see clustering of the resin material.

After separation into distinct cells, the structural features of each cell were characterized. The features under consideration include: the number of material points, the average thickness, the resin volume fraction, and the void fraction.

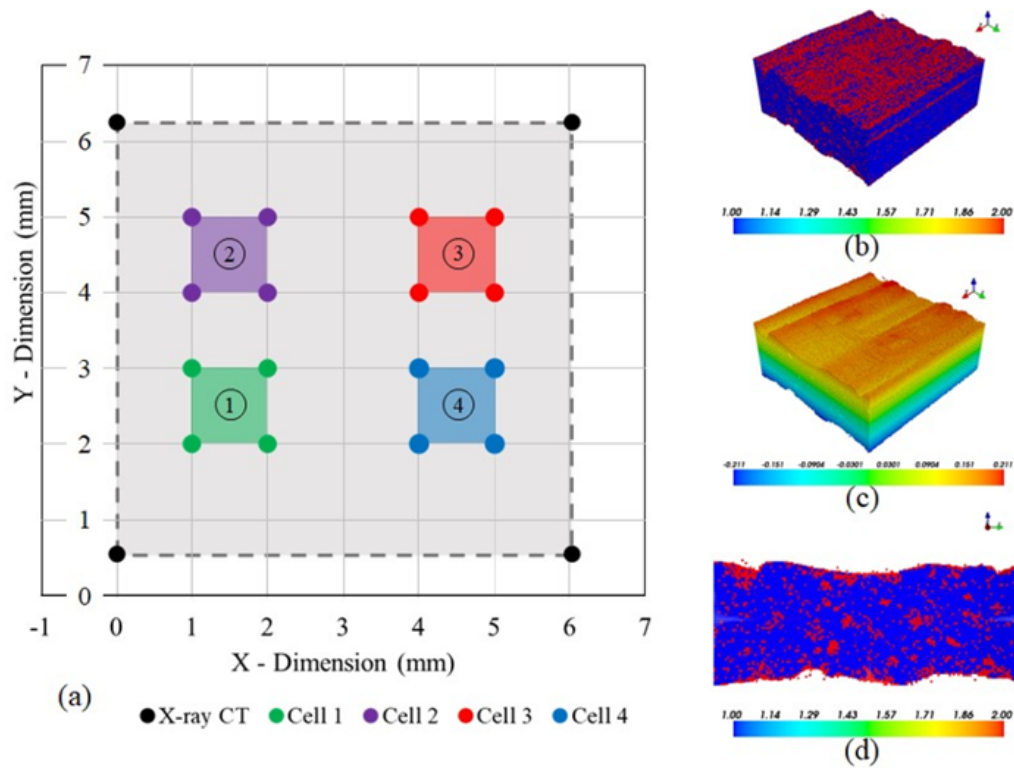


Figure 3-9: Partitioning of x-ray CT into four distinct cells of high resolution.

Number of Material Points

In each cell, the material point identities were tabulated. A bar chart of this quantification is given in Figure 3-10 with the horizontal axis representing each cell and the vertical axis displaying the number of material points. As shown, each cell contains approximately 900 thousand material points, the majority of which are of CNT yarn type. Cell 2 and cell 3, both located on the upper half of the x-ray CT specimen, have more yarn points than cells 1 and 4.

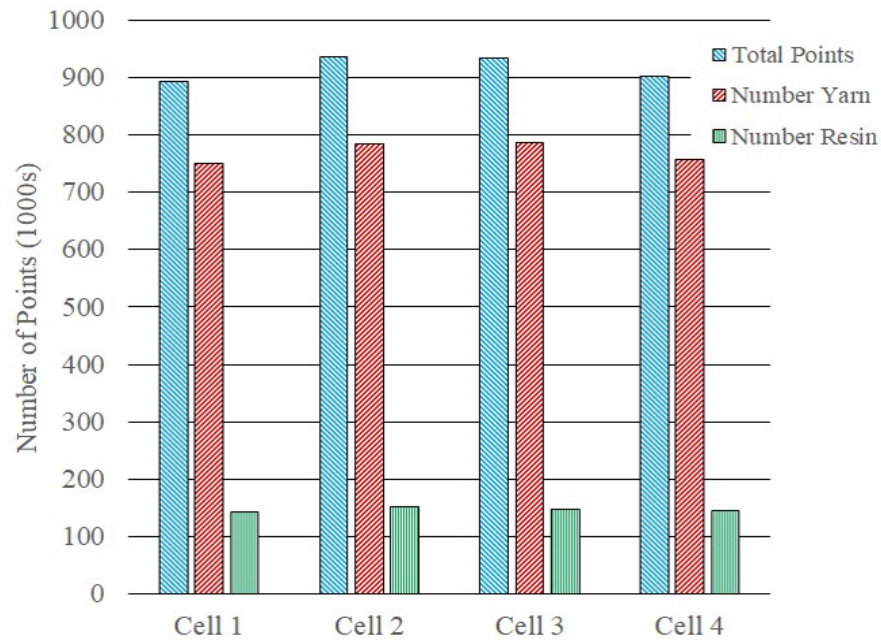


Figure 3-10: A comparison of the number of material points in each cell.

Average Thickness

Figure 3-11 compares the average thickness of each cell. The surface undulation associated with the structure naturally led to two different methods of approximation as shown in Figure 3-12. The blue bar, method 1, computes the thickness as simply the difference between the maximum and minimum z-positions of the surface. The red bar, method 2, calculates the thickness of a BMP slice as the difference between the average top and bottom surfaces. In both methods, the representative thickness for the cell was calculated by averaging the individual thicknesses of each BMP slice. Each cell has a similar thickness. Additionally, the difference in thickness between method 1 and method 2 is quite high due to the large amplitude in the surface undulation.

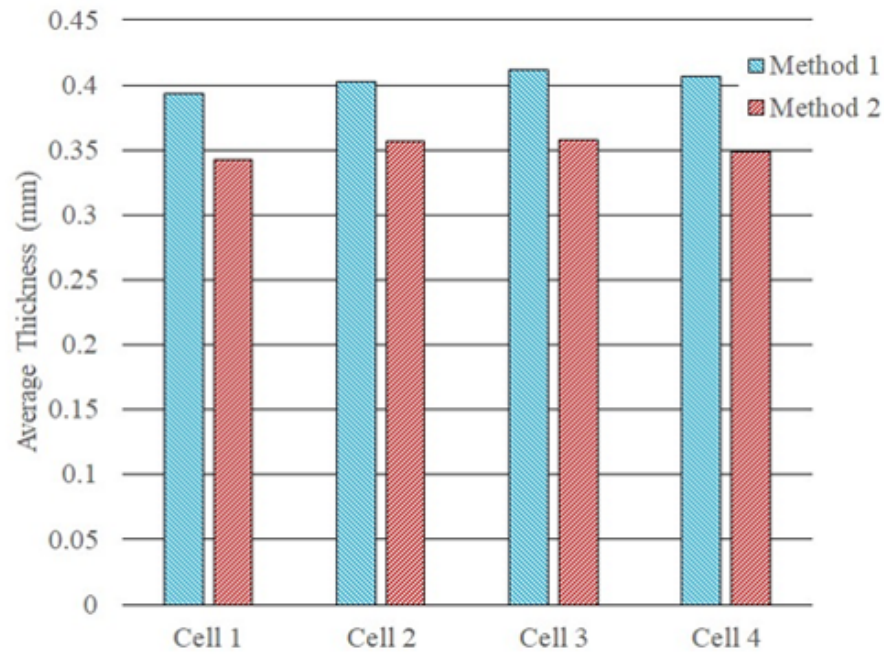


Figure 3-11: A comparison of the average thickness of each cell.

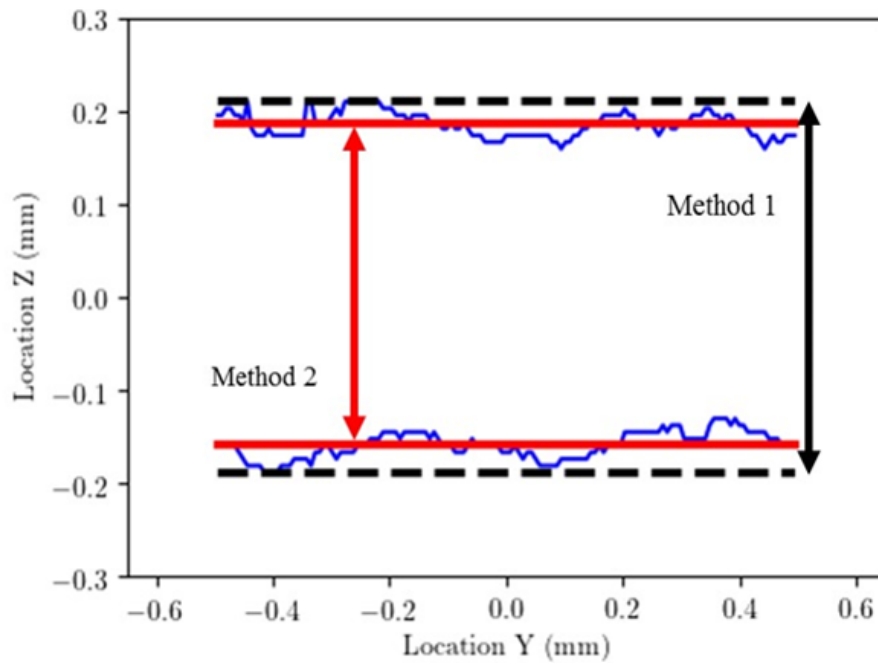


Figure 3-12: Visualization of the two different methods used for approximating the thickness of each BMP slice.

Resin Volume Fraction

The resin volume fraction for each slice was calculated by counting the number of resin points and dividing by the total number of material points. The volume fraction for the cell was then calculated by averaging together the volume fraction of each slice. With a similar notation to the previous charts, results from the process are given in Figure 3.13. The resin volume fraction for each slice was very consistent and has an approximate value of 0.16.

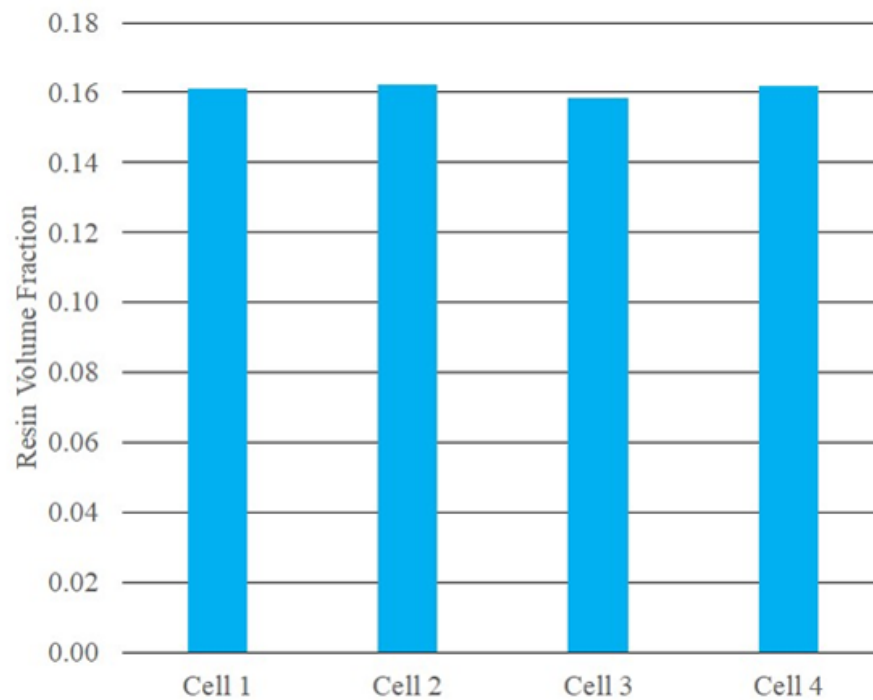


Figure 3-13: A comparison of the volume fraction of each cell.

Surface Undulation

One important feature observed throughout the BMP slices is the undulation of the surface. Figure 3.14 illustrates this undulation by coloring the material points by z-coordinate position. The alternating color on the top surface, progressing from yellow/orange to red, is sinusoidal in nature. This sinusoidal behavior can be visualized clearly on the YZ plane as shown in the rightmost image in Figure 3.14.

To approximate the surface undulation, a nonlinear least squares optimization routine was used to fit a sinusoidal function to the top and bottom surfaces of each BMP slice. Equations (3.3) and (3.4) show the top and bottom fitted expressions respectively, where A_i is the amplitude, f_i the frequency, ϕ_i the phase, and D_i the offset for a given slice, i . Figure 3-15 shows an example of this optimization procedure performed on a slice. The black dashed lines show the extremes of the surface, the red dashed lines show the average top and bottom surfaces, and the purple scatter shows the converged sinusoidal fit for the top and bottom surfaces.

$$z_i^t(x) = |A_i^t| \sin(f_i^t x + \phi_i^t) + D_i^t \quad (3.3)$$

$$z_i^b(x) = |A_i^b| \sin(f_i^b x + \phi_i^b) + D_i^b \quad (3.4)$$

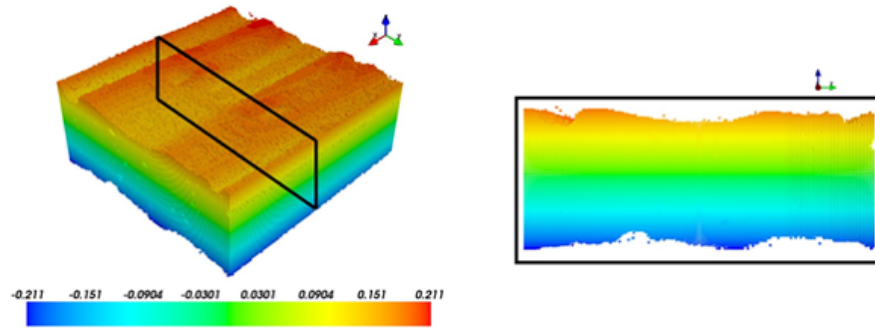


Figure 3-14: Visualization of the surface undulation colored by z-coordinate position.

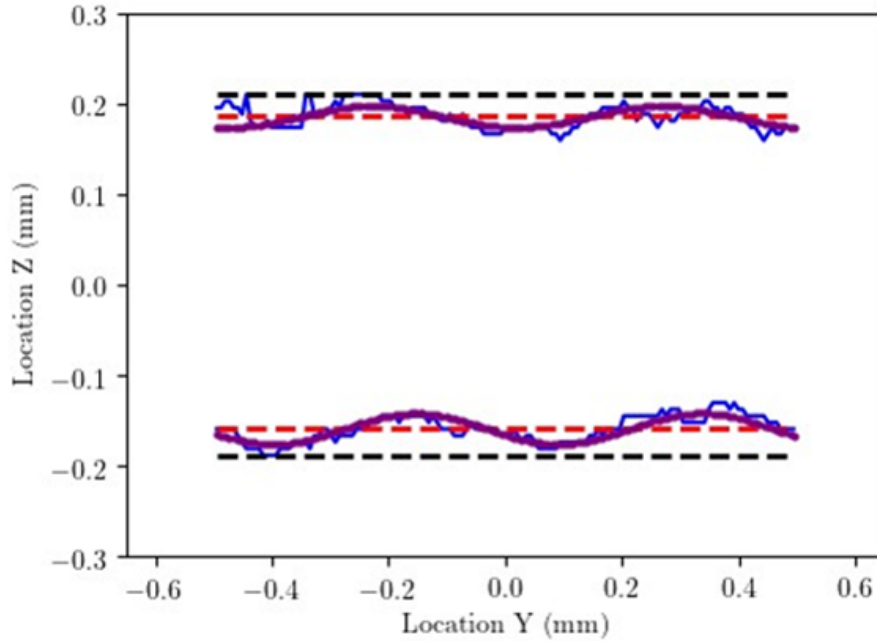


Figure 3-15: Approximating the undulation of the surface.

Void Fraction

The void fraction, V_f is approximated using Equation (3.5), where N_m is the actual number of material points for a cell and N_t is the number of points assuming a completely full domain.

$$V_f = 1 - \frac{N_m}{N_t} \quad (3.5)$$

A full domain is detected by overlaying a uniform grid on the top of the PD slice. The yellow cells of Figure 3-16 show a visualization of the voids detected using this method.

Figure 3-17 shows a comparison of the calculated void fraction for each cell. Cells 2 and 3 have lower void fractions than cells 1 and 4. It should also be noted that cells 2 and 3 contain the highest number of yarn material points (Figure 3-10).

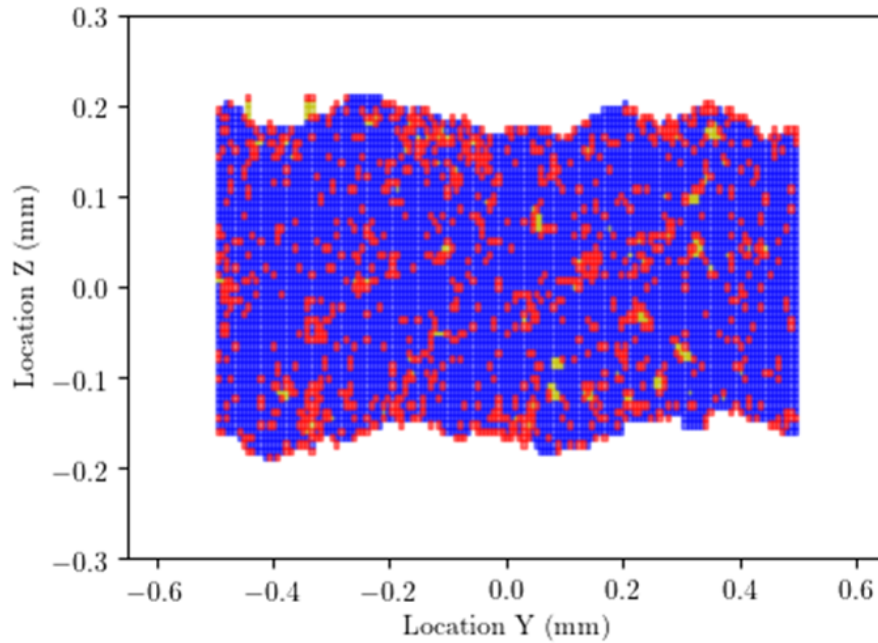


Figure 3-16: Visualization of void fraction on a slice.

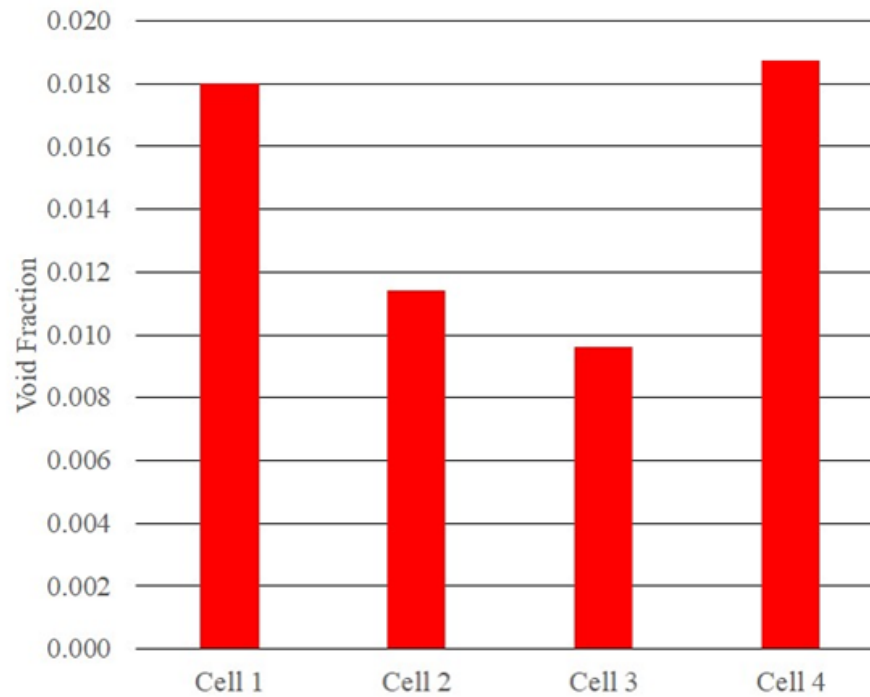


Figure 3-17: A comparison of the void fraction of each cell.

Quantification of Resin and Void Clusters

Two distinct algorithms were used to identify and characterize the groupings (clusters) of resin/void material on each individual slice. After assignment of resin/void material points, a K-nearest neighbors algorithm [61] was applied to detect the resin/void material points. The K-nearest neighbors routine identifies the resin/void material points to be placed into separate clusters, and performs an initial removal of noise from the data set. It is worth noting that it does not separate the points into clusters. Subsequently, a data clustering algorithm called Density Based Spatial Clustering of Applications with Noise (DBSCAN) was applied to detect and quantify individual void/resin clusters. This algorithm, first presented by Ester et al. in [62], is well suited for this task because of its ability to discover clusters of arbitrary shape and its ability to distinguish noise within the data set.

The clustering process is demonstrated by considering an example slice shown in Figure 3-18 with the yarn, resin, and void material points. In this instance, first the K-nearest then the DBSCAN algorithm were applied to identify the resin clusters of the slice (red points in Figure 3-18). Figure 3-19 shows the result of the process itself. In this instance, the algorithm detected 26 different resin clusters of various sizes. For visualization, each uniquely classified resin cluster is assigned a different color and the center of the cluster is shown using a red triangle. Also shown by the black crosses are resin material points considered by the algorithm to be noise and therefore not associated with any of the clusters. This procedure is performed on every BMP slice of the data and the resulting information about resin and void clusters is stored.

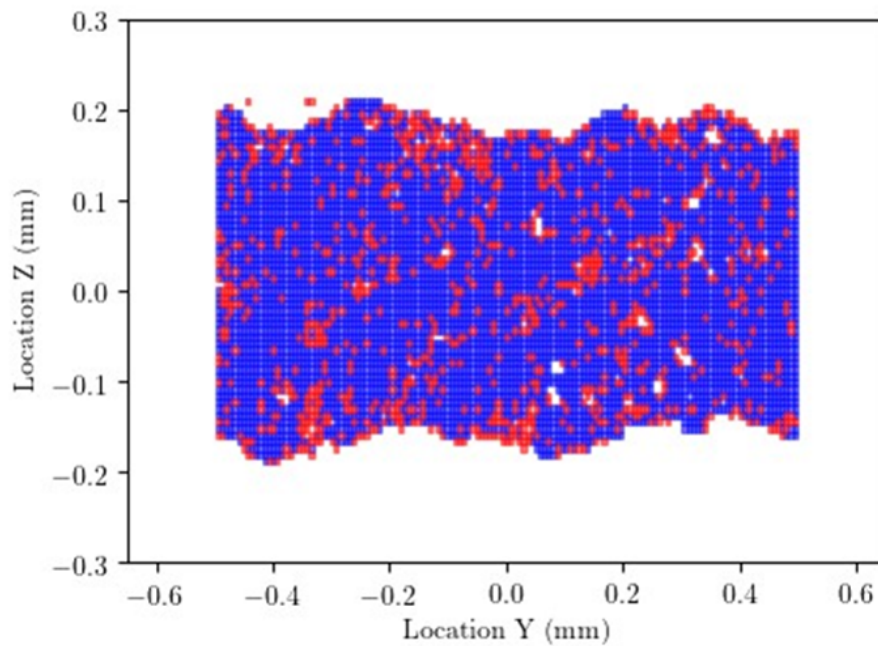


Figure 3-18: Visualization of yarn, resin, and void material on a slice.

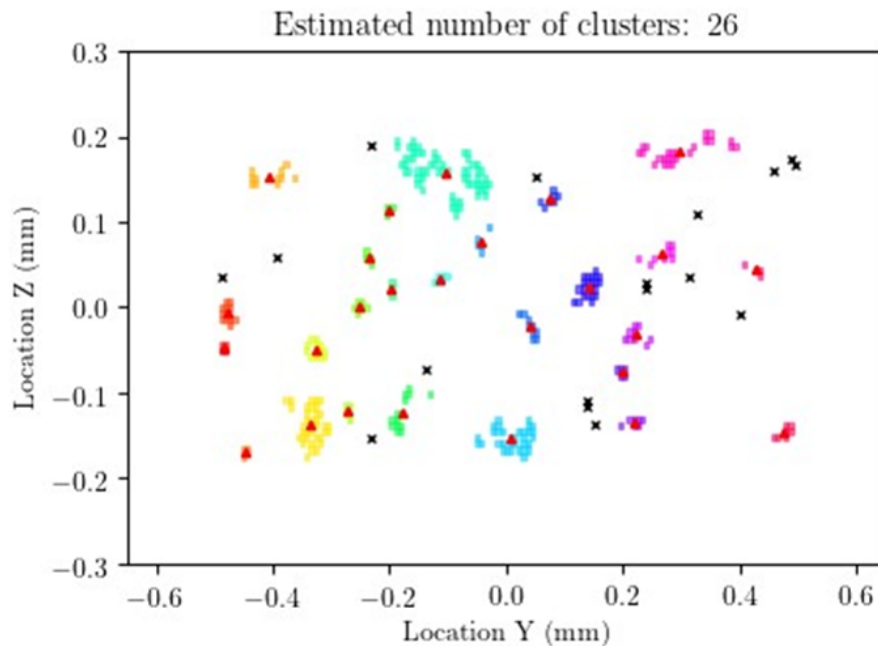


Figure 3-19: The resulting clusters identified by application of first the K-nearest then the DBSCAN algorithm to detect shape, size, and quantity of resin clusters of the microstructure.

3.4 Peridynamic Modeling Approach

Several modifications to the traditional bond-based PD method were needed to properly simulate the explicit yarn and resin material regions extracted from the x-ray CT data. These modifications are necessary to introduce the anisotropic material behavior of unidirectional composites. Similar to the CFRP methodology presented in Section 2.1, to develop anisotropy in the PD model, bonds were categorized based on material associations. Based on bond type categorization, bonds were given different constitutive properties.

3.4.1 Bond Types

Based on material association (yarn/resin) and alignment, several bond types were considered. (Table 3.3) shows the relationship between material association, alignment and behavior for these various bond types. The start and end point material association of a bond are given in the second and third column, respectively. The first set of bond type variations, labeled (1a-1c), are considered yarn-yarn bonds. For these three variations, alignment is an important consideration and is given in the fourth column. The first variation, 1a, is a yarn-yarn bond that is perfectly aligned with the yarn direction. In this scenario, the bonds behavior is governed by the yarn bond constant. The second variation, 1b, is a yarn-yarn bond that is oriented perpendicular to the yarn direction. In this instance, the bond behavior is governed by the resin bond constant as the yarns are only connected to each other through resin in that direction. Finally, the third variation is a bond that is oriented in between the parallel and perpendicular directions. For this scenario, the bonds have a material constant in between the yarn and resin bond constant and are governed by the off-axis modulus function.

The next variations considered were bonds consisting of one resin and one yarn material point. These bonds are treated as interface bonds and do not have any direction dependent properties. While classified as interface bonds for completeness, in the current work they use the same bond constant as the resin bond. Finally, the third variation is resin-resin bonds. Like the interface bonds, they do not have any directional dependency and are

governed by the resin material properties.

Table 3.3: Relationship between material association, alignment, and behavior for various bonds.

Bond Type	Material Point 1	Material Point 2	Alignment	Behavior
1a.	Yarn	Yarn	Parallel	Yarn
1b.	Yarn	Yarn	Perpendicular	Resin
1c.	Yarn	Yarn	Off-axis	Off-axis
2a.	Yarn	Resin	NA	Interface
2b.	Resin	Yarn	NA	Interface
3.	Resin	Resin	NA	Resin

Figure 3-20 pictorially illustrates the bond types that are possible within the model and their associated behavior. In this figure, blue squares represent yarn material points and the red squares represent the resin material points. Two separate scenarios are drawn. The first scenario is a yarn point located at the center, while the second is that of a resin point located at the center. The possible interaction behaviors are shown using different colors, interface in green, resin in red, yarn in blue, and off-axis in purple.

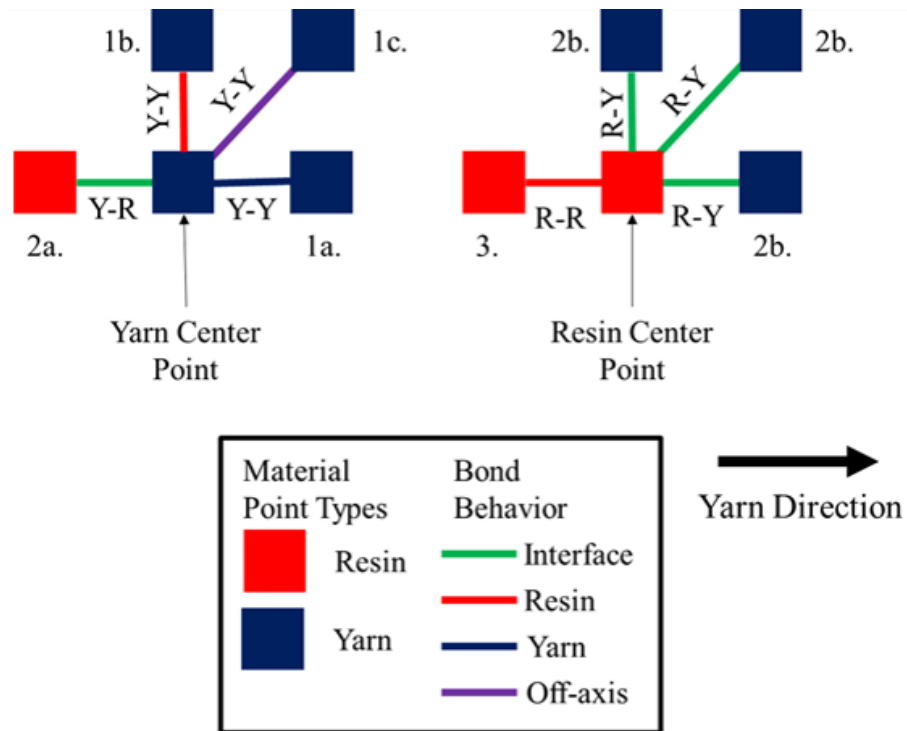


Figure 3-20: Schematic showing the possible bond types.

3.4.2 Off-Axis Modulus Function

Figure 3-21 shows the constitutive relationships associated with each bond type. For simplicity, each constitutive relationship is of a linear form and can be fully described by two material parameters: a bond constant and a critical stretch. The bond constant is the slope of the force-stretch curve while the critical stretch is a strength related parameter. The deformation of the bond may continue to a value that leads to its breakage. The stretch value at this state is called the critical stretch. The yarn constitutive relationship is given in blue and has a higher bond constant and lower critical stretch as compared to the other bond types. At the other extreme, the resin constitutive relationship, shown in red, has the lowest bond constant and the highest critical stretch. The interface constitutive relationship in green follows the resin behavior in this study. Finally, the off-axis yarn constitutive relationship in purple falls between the yarn and resin relationships. Equations (3.6 - 3.8) show the bond force vs stretch relationship for each bond type.

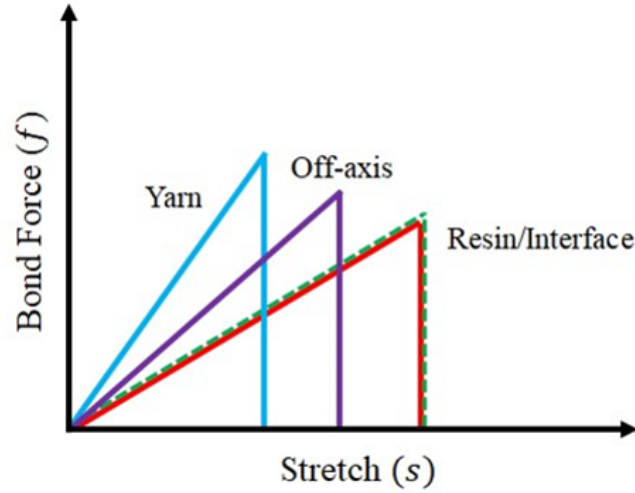


Figure 3-21: Schematic representation of the constitutive relationships.

$$f_y = c_y s \quad (3.6)$$

$$f_r = c_r s \quad (3.7)$$

$$f_o = \phi_c c_y s \quad (3.8)$$

The c_y and c_r constants can be determined by applying load along the yarn direction and then subsequently along the transverse direction. The composite specimen was only experimentally tested in the yarn direction so its behavior in the transverse direction is not currently known. Because transverse properties in uniaxial composites are generally matrix dominated, the transverse modulus was assumed to be that of the resin material.

The anisotropic material behavior was included in the model through the application of an off-axis function. The form of the off-axis function is given by Equation (3.9). This Gaussian function is used to ensure that yarn bonds oriented along the loading axis are attributed yarn material properties and bonds oriented off-axis are assigned a reduced bond constant. A bond perpendicular to the yarn direction is attributed the ratio of resin to yarn bond constant c_r/c_y . This ensures that, upon multiplication with the yarn bond constant,

the material property degrades back to the resin bond constant. Also in this equation, the variable w represents the width of the gaussian function and θ is the bond angle with respect to the yarn axis.

$$\phi_c = \left(1 - \frac{c_r}{c_y}\right) \exp\left(\frac{(\cos\theta - 1)^2}{2w^2}\right) + \frac{c_r}{c_y} \quad (3.9)$$

A sampling methodology was developed to find an expression for the PD elastic constants in a heterogeneous domain. In this method, a statistical representation of material point families was obtained by repeatedly sampling the interior points. Statistical sampling is necessary because the composition of a material points family is unique and based on the x-ray CT grid generation process.

3.4.3 PD Material Constants

A relationship between engineering constants and the peridynamic material parameters for each of the constituent materials is needed to describe the behavior of the different bond/interaction types. Traditionally, the classical continuum mechanics (CCM) engineering constants are related to nonlocal peridynamic material parameters through the strain energy density of a material point [22, 34, 35]. An expression for the peridynamic strain energy density of a material point is developed and simple loading conditions are applied to a family of material points positioned away from the domain boundaries. The strain energy density for the CCM representation is calculated and the PD nonlocal material parameters are chosen so that the PD strain energy density is equal to the CCM counter-part.

For each sampled point i , a displacement field was imposed on the sample. This is done first along the yarn direction x and then in the transverse direction y . The displacement field is imposed via an applied strain ϵ_x as shown in Equation (3.10). The superscript indicates

that the displacement of each bond in the family varies with the original bond length.

$$\begin{Bmatrix} u_x^b \\ u_y^b \\ u_z^b \end{Bmatrix} = \begin{Bmatrix} \varepsilon_x r_x^b \\ 0 \\ 0 \end{Bmatrix} \quad (3.10)$$

After imposing the displacement field on the family of point i , an initial guess is made for both the yarn spring constant k_y and the resin spring constant k_r . The spring constants k_y and k_r with units of N/m^7 can be related to the bond constants c_y and c_r with units of N/m^6 through Equations (3.11) and (3.12)

$$k_y = \frac{c_y}{\delta} \quad (3.11)$$

$$k_r = \frac{c_r}{\delta} \quad (3.12)$$

where δ is the horizon. The material point i is first associated with yarn material and the local strain energy density of the point is found through Equation (3.13). In this equation the summation index b represents an individual bond in the family of the sampled point i . Depending on material association and orientation, these bonds can take on resin or yarn constitutive behavior as shown from the decomposition. Accordingly, the strain energy density of each bond is summed to obtain the strain energy density of the material point i .

$$W_{(i)}^Y = \frac{1}{2} \sum_{b=1}^{N_r} \frac{1}{2} k_r (u_x^b)^2 V_b \frac{\delta}{r_b} + \frac{1}{2} \sum_{b=1}^{N_y} \frac{1}{2} k_y \phi_{c(b)} (u_x^b)^2 V_b \frac{\delta}{r_b} \quad (3.13)$$

Alternatively, material point i can be envisioned as having resin material association, as denoted by the superscript R in Equation (3.14). Under this circumstance, each bond b in the family of i will have resin material properties. The strain energy density of point i can be then calculated with just the resin associated terms.

$$W_{(i)}^R = \frac{1}{2} \sum_{b=1}^{N_r} \frac{1}{2} k_r (u_x^b)^2 V_b \frac{\delta}{r_{ij}} \quad (3.14)$$

The rule of mixtures is then applied to obtain an approximation of the composite strain

energy density in the longitudinal direction as shown in Equation (3.15), where m_r is the resin mass fraction.

$$W_{PD-X} = (1 - m_r)W_{(i)}^Y + m_r W_{(i)}^R \quad (3.15)$$

The entire process is then repeated with loading in the transverse direction to obtain an approximation of the composite strain energy density in the transverse direction. In this scenario, a transverse displacement field is applied as shown in Equation (3.16).

$$\begin{Bmatrix} u_x^b \\ u_y^b \\ u_z^b \end{Bmatrix} = \begin{Bmatrix} 0 \\ \varepsilon_y r_y^b \\ 0 \end{Bmatrix} \quad (3.16)$$

The strain energy density of yarn and resin points with this new displacement field is then calculated. As written below, the only change in Equations (3.13) and (3.14) is the exchanged relative displacement term u_y^b .

$$W_{(i)}^Y = \frac{1}{2} \sum_{b=1}^{N_r} \frac{1}{2} k_r (u_y^b)^2 V_b \frac{\delta}{r_b} + \frac{1}{2} \sum_{b=1}^{N_y} \frac{1}{2} k_y \phi_{c(b)} (u_y^b)^2 V_b \frac{\delta}{r_b} \quad (3.17)$$

$$W_{(i)}^R = \frac{1}{2} \sum_{b=1}^{N_r} \frac{1}{2} k_r (u_y^b)^2 V_b \frac{\delta}{r_b} \quad (3.18)$$

The strain energy density of the composite associated with the transverse load is then calculated using Equation (3.19) where $W_{(i)}^Y$ and $W_{(i)}^R$ are the strain energy densities of yarn and resin points, respectively, due to a transverse strain ε_y .

$$W_{PD-Y} = \left(\frac{(1 - m_r)}{W_{(i)}^Y} + \frac{m_r}{W_{(i)}^R} \right)^{-1} \quad (3.19)$$

The PD strain energy density terms are then compared with their classical continuum mechanics counterparts, Equations (3.20) and (3.21).

$$W_{CCM-X} = \frac{1}{2} E_x \epsilon_x^2 \quad (3.20)$$

$$W_{CCM-Y} = \frac{1}{2} E_y \epsilon_y^2 \quad (3.21)$$

A nonlinear least squares optimization routine was then used to optimize the yarn and resin spring constants with the following objective function.

$$\min(\Psi) = (W_{PD-X} - W_{CCM-X}) - (W_{PD-Y} - W_{CCM-Y}) \quad (3.22)$$

This optimization procedure finds the optimal k_y and k_r for a particular material point i . The heterogeneity of the microstructure means that this solution will be different for each sampled point i . For this reason, 10,000 different material points were sampled and the constants were found for each sampled point.

Figure 3-22 provides a flow chart for obtaining the yarn and resin constants and Figures 3-23 and 3-24 show a histogram of the variation in fiber and matrix constant obtained from the optimization process. The vertical axis shows the frequency while the horizontal axis shows the bond constant value in units of mN/mm^7 . The average bond constant values from these histograms were used in the subsequent simulations.

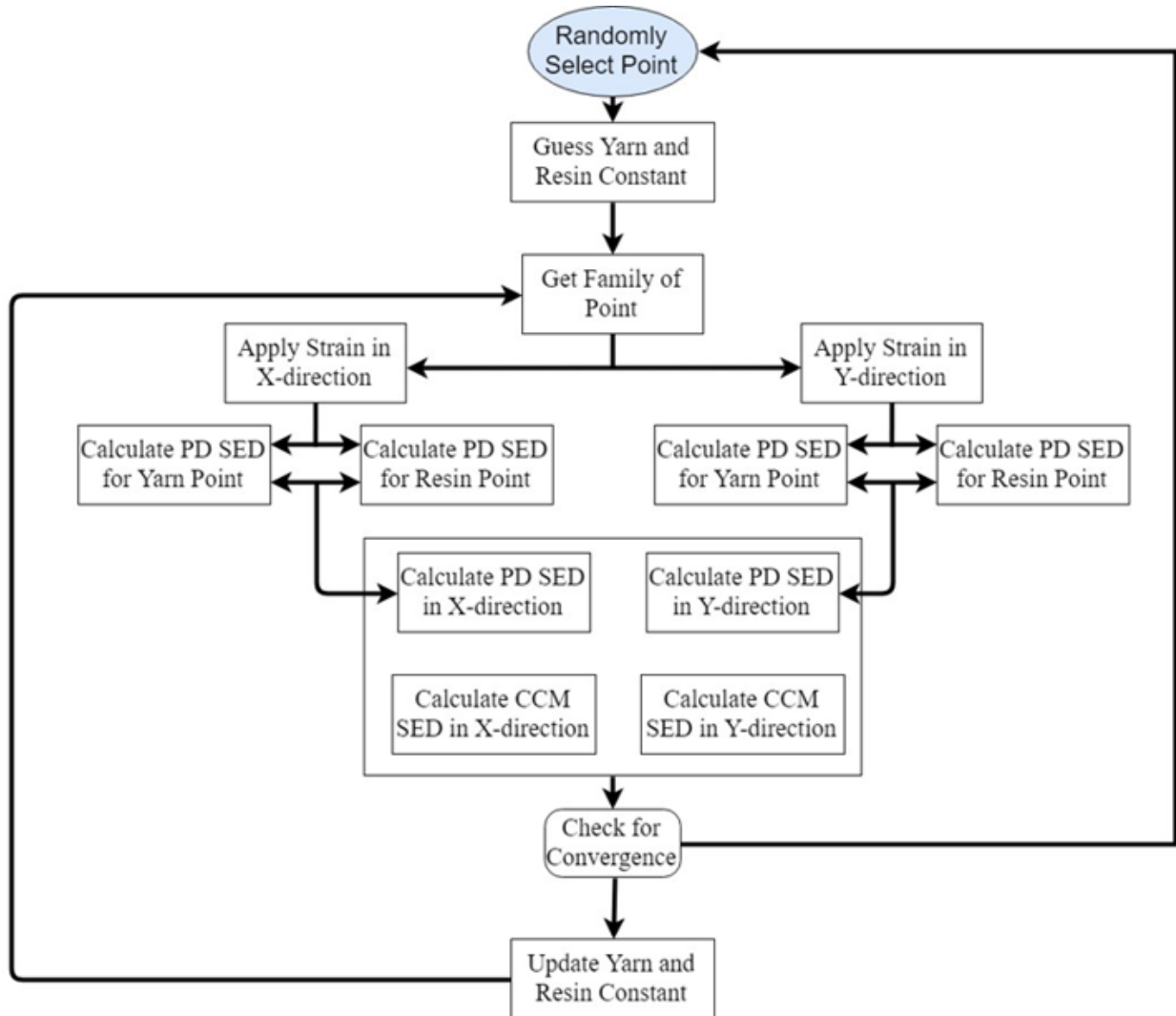


Figure 3.22: Flow chart for obtaining elastic constants.

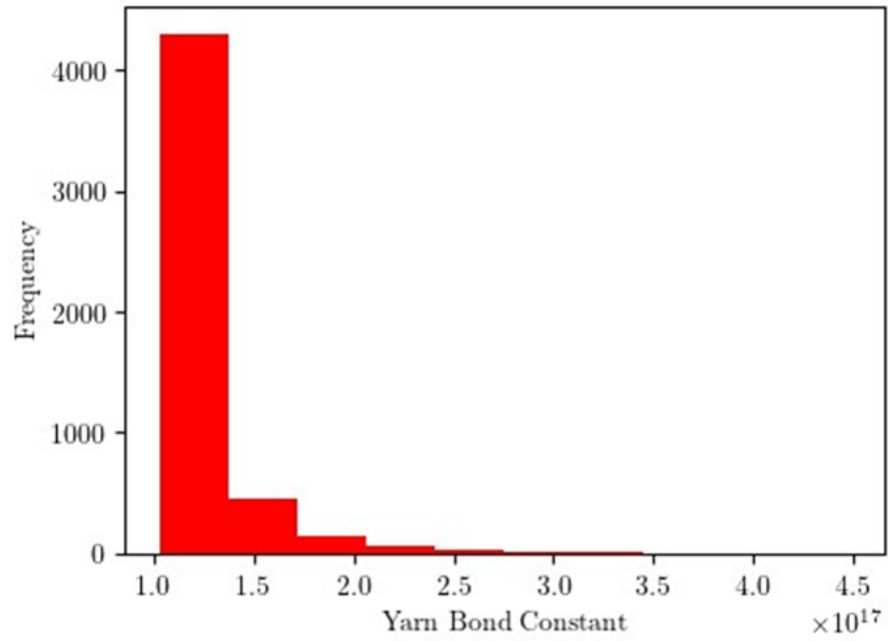


Figure 3-23: Variation in yarn material constant.

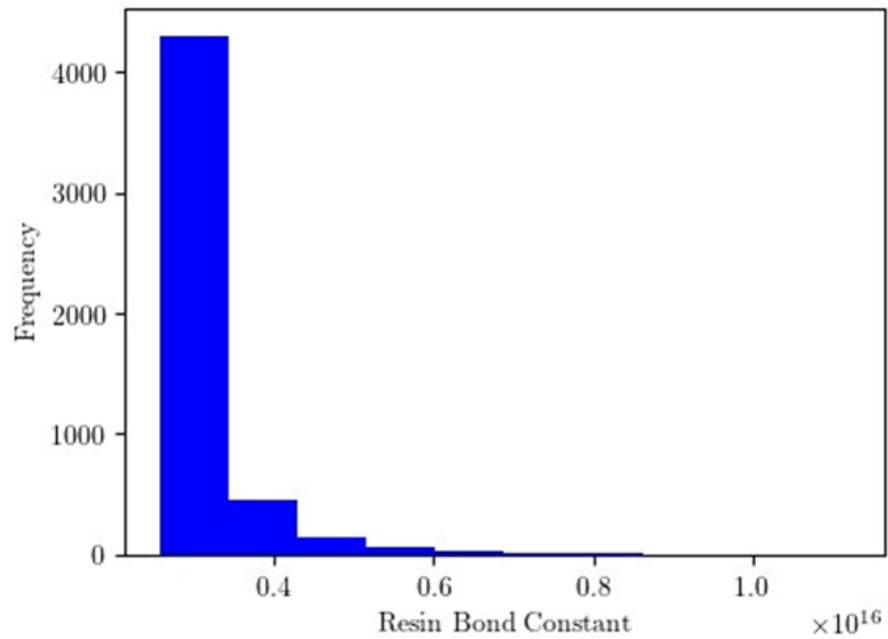


Figure 3-24: Variation in matrix material constant.

3.4.4 Simulation Procedure

The experimentally generated stress vs. strain curve was simulated by dividing the loading curve into multiple load steps. The blue curve of (Figure 3-25) shows the experimental stress vs. strain curve, while the red points show the chosen load steps for the simulation. The strain associated with each load step was converted into a displacement and applied as the boundary condition.

Within each load step, a dynamic relaxation procedure was followed [22]. A quasi-static solution was obtained for each load step by applying a small constant viscous damping coefficient to the velocity of each material point in the system. After equilibration, bonds were allowed to fail progressively until no further damage accumulated, after which, the next load step was entered. A complete description of the dynamic relaxation procedure can be found in [44].

Within each load step, the displacement boundary condition was ramped over 10,000 timesteps. The internal force of the specimen was monitored for the duration of the simulation by placing an imaginary force plane in the middle of the tensile specimen and summing each of the bond forces crossing the plane. Engineering stress was determined during post-processing by dividing the equilibrated internal force of each load step by the specimen cross-sectional area.

3.4.5 PD Simulation Results

Figure 3-26 shows the stress-strain responses for each individual cell and their comparisons to the experimental work of Kim et al. [6]. As expected, the heterogeneity and uniqueness of each cell gives rise to some minor fluctuations in the response. Figure 3-26 shows that the largest difference in the response can be observed in the failure strain. Failure of the cells is determined to occur when the internal force measured through the force plane drops to 0. Although further refinement in the load step increment is needed to determine the exact strain at failure, the first and the fourth cells fail between the 2.0 % and 2.2 % strain load steps while, the second and the third cells fail between the 2.2 % and 2.4% strain

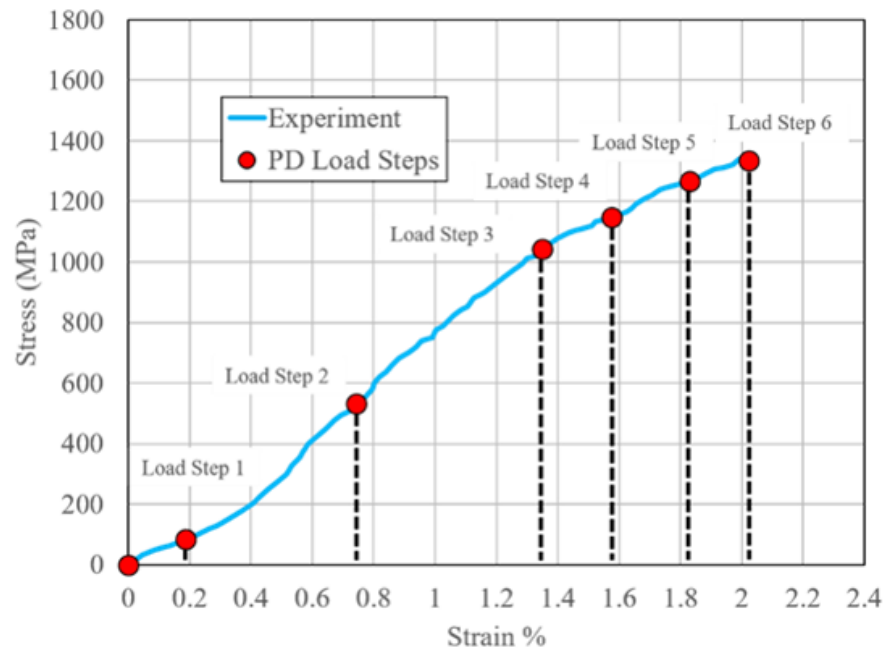


Figure 3-25: Demonstration of load steps.

load steps. Another observation is that unlike the experimental stress-strain curve, which exhibits a softening behavior in the stress vs. strain response after approximately 1.5 % strain, the simulated stress-strain curves are all linear. This response can be explained by the linear-elastic constitutive relationship employed in the PD simulation approach. While the PD simulations slightly overpredict the tensile strength, an overall good agreement is observed between the experimental and numerical results.

A comparison of the stress vs. strain simulation results with the microstructural characterization, contained in Section 3.3, lead to a few readily apparent trends. First, the total numbers of material points in the cells are very similar. This could be one possible explanation for the similarity in the stress-strain curves themselves. Additionally, a minor variation exists between cells 2 and 3, and cells 1 and 4 in both the total number of material points and the stiffness in the stress vs. strain response. Second, the two cells that fail at a higher strain %, cells 2 and 3, also have the lowest void fraction. The low void content of these cells could explain the higher failure strain and indicate that voids in the PD model influ-

ence the failure behavior. For these particular models, a 0.8 % decrease in void fraction increases the failure strain by 0.2 %.

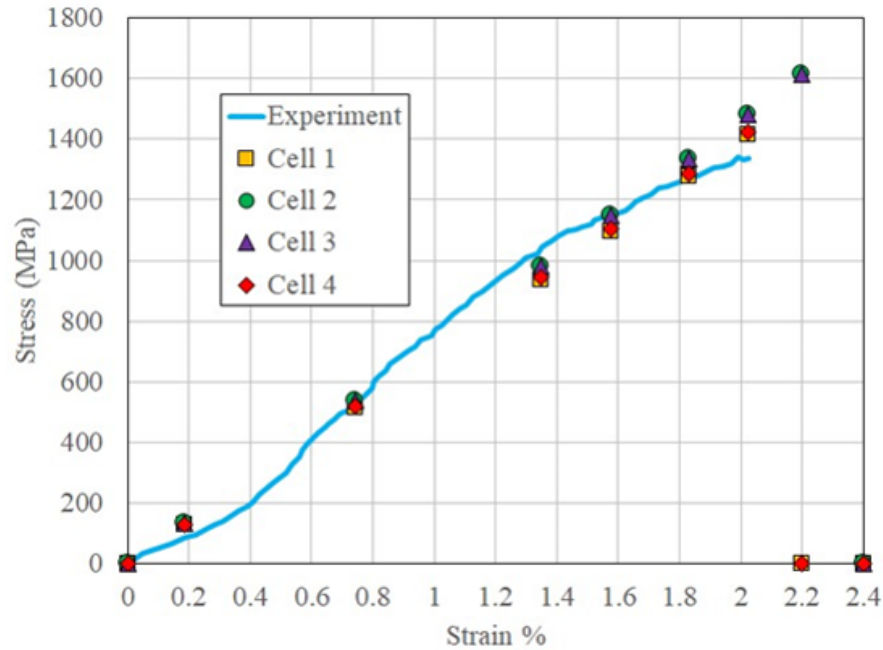


Figure 3-26: Peridynamic stress-strain % curves.

Peridynamic theory is well suited for investigating complex failure morphology. Figure 3-27 shows a set of damage contours in each of the four cells from three distinct perspectives with the yarn oriented along the x-direction. In this image, damage of a material point is colored on a scale ranging from 0 (blue) to 1 (red). Colors close to blue indicate less damage while colors close to red indicate a heavily damaged material point. The columns in this image show the damage in each cell. The first row shows an isometric view of the damage contours in each cell. From this orientation, only damage on the external surfaces is visible. For this reason, an internal slice of the specimen is provided in the second row. From this slice, an internal section along the yarn direction is visible. Finally, the middle view in the third row shows the specimen after being sectioned at the midplane. These contours demonstrate that failures, while not the same in each cell, share some common characteristics. First, in all cases, the specimens are highly damaged on the surfaces and

damage is oriented along the longitudinal (yarn) direction. Additionally, damage is present in the entirety of the specimen and is not limited to the surfaces. Overall, the damage observed in the PD simulations matches well with the experimentally observed failure as shown in Figure 3-3.

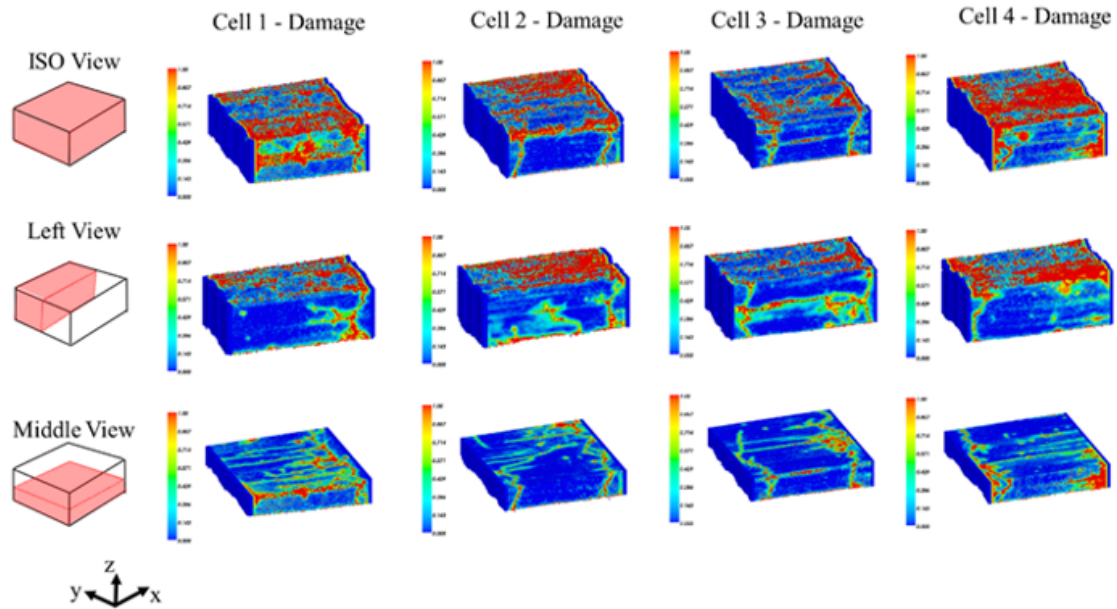


Figure 3-27: Damage contours at the failure strain of each cell at various orientations.

To better understand the relationship between the microstructure and the developed damage, an overlay was created for various YZ planes of the specimen with X-axis being the yarn direction. Each row of (Figure 3-28) shows a different YZ plane, highlighted in red, of the specimen: left, middle, and right. In this orientation, yarn is perpendicular to the plane. The middle column of the figure shows the microstructure of the slice. In this image, blue voxels represent yarn, gray voxels represent resin, and white voxels represent voids. The right most column shows accumulated damage on the slice. Undamaged material points of the slice have been removed and the remainder is plotted with the color representing the intensity of damage with red indicating the most damaged areas. The left column shows an overlay of the material association and the damage. For visualization purposes, transparency was added to the image. From the overlay, it is observed that

streaks of damage connect both resin and voids. Damage is observed to accumulate most around the void clusters and at the surfaces of sharp undulation. Additionally, damage is spatially located in similar locations on each slice indicating a continuity of the damage in the out-of-plane direction.

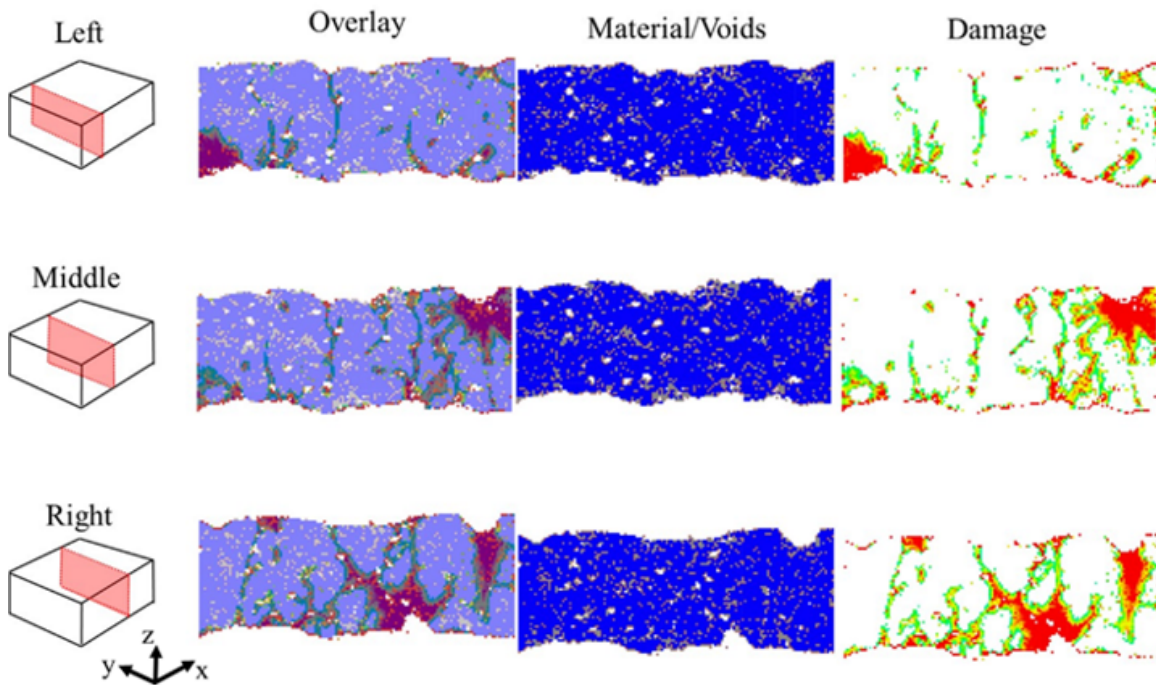


Figure 3-28: Damage overlay in different YZ planes for cell 1.

A similar set of overlays are shown in Figure 3-29. These figures show snapshots of the damage progression in the YZ-planes. From top to bottom (1-7) the snapshots show the damage process during the final load step. The progressive nature of the failure (snapshots 1-7) occurs as a result of the load redistribution during the failure process. In the fourth row of the left column, damage is first observed in the voids closest to the surface. In the next image, damage has extended towards the surface while following the closest voids. In the middle plane, damage is observed not only at the voids closest to the surface, but also at the top right surface where there is a sharp gradient in the surface waviness. As observed in the left plane, damage extends from the voids closest to the surface to the internal voids. Finally, in the rightmost plane, there are two sharp gradients in the surface

waviness. Damage initially accumulates in both of these sites (sequences 3 and 4).

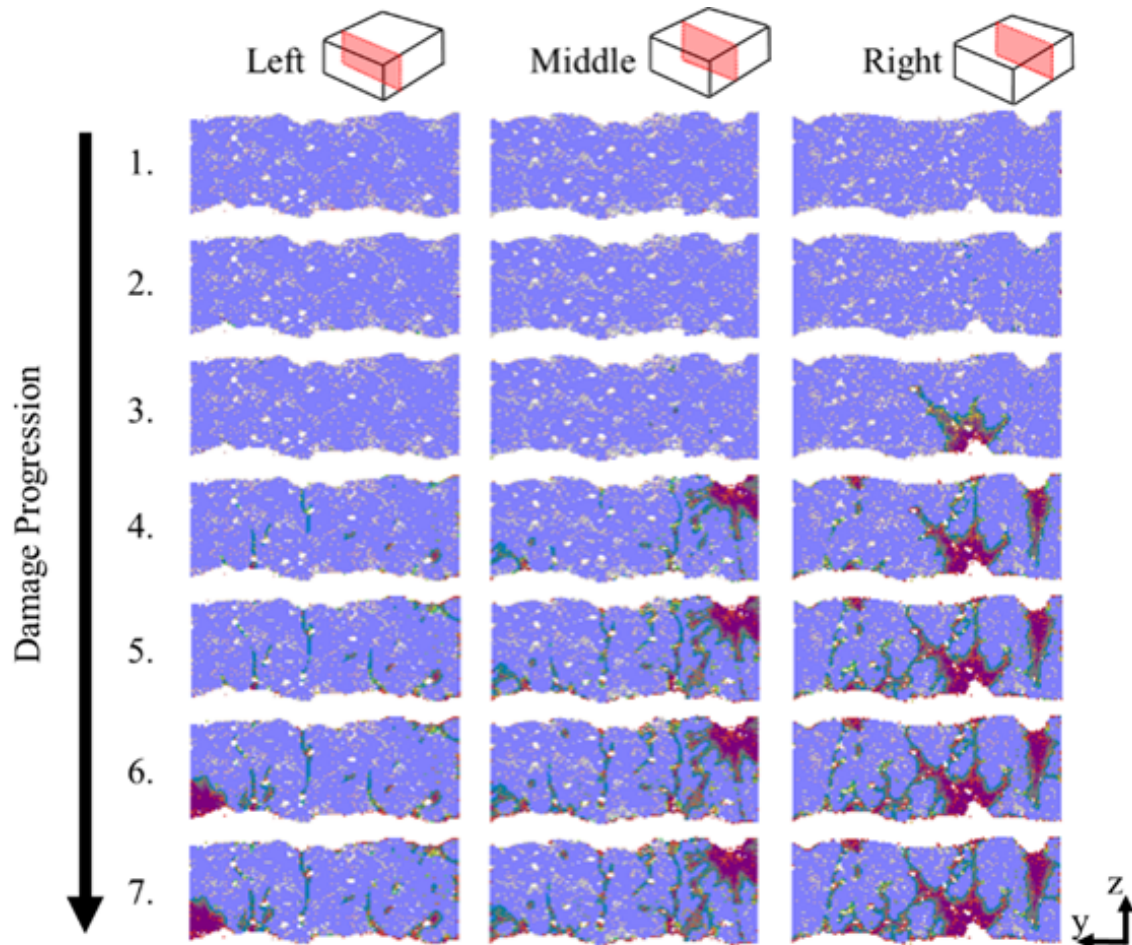


Figure 3-29: Damage initiation for cell 1 at different YZ planes.

Damage and material association overlay snapshots as the damage progresses for cells 2, 3 and 4 are presented in Figures 3-30, 3-31, and 3-32, respectively. Many of the observations detailed for cell 1 are also valid in cells 2-4. The most notable similarity being that damage initiates at the sharp undulations in the surfaces. A key difference between the microstructures can be observed in cells 2-3 (Figures 3-30-3-31) which have noticeably lower void fractions. Without voids to guide the fracture path, damage appears to follow the resin clusters. This is most apparent when comparing Figure 3-30 with Figure 3-32. Figure 3-30, a microstructure with few voids, fails at a higher strain percent and has damage that

follows the resin clusters. In contrast, Figure 3-32, a microstructure with more significant void fraction, fails at lower strain percent and has damage that follows the void clusters.

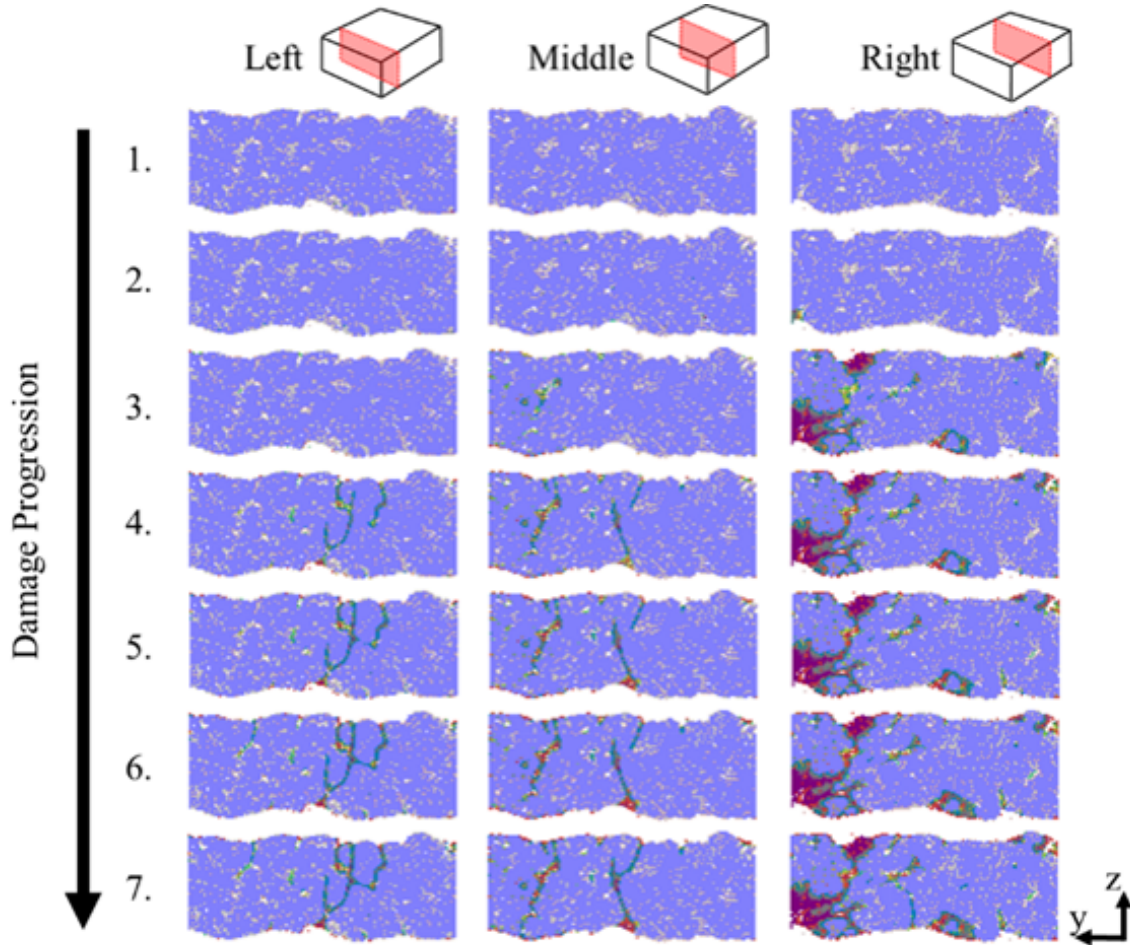


Figure 3-30: Damage initiation for cell 2 at different YZ planes.

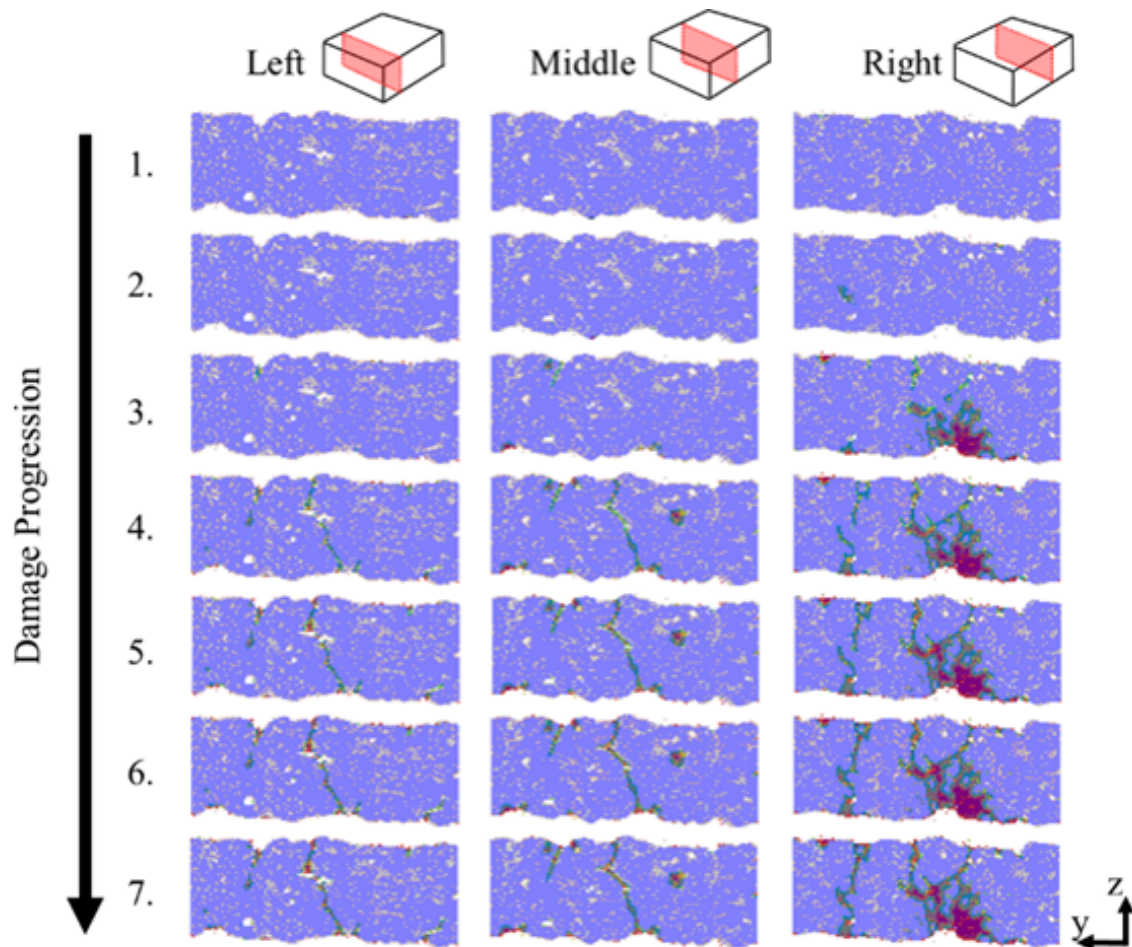


Figure 3-31: Damage initiation for cell 3 at different YZ planes.

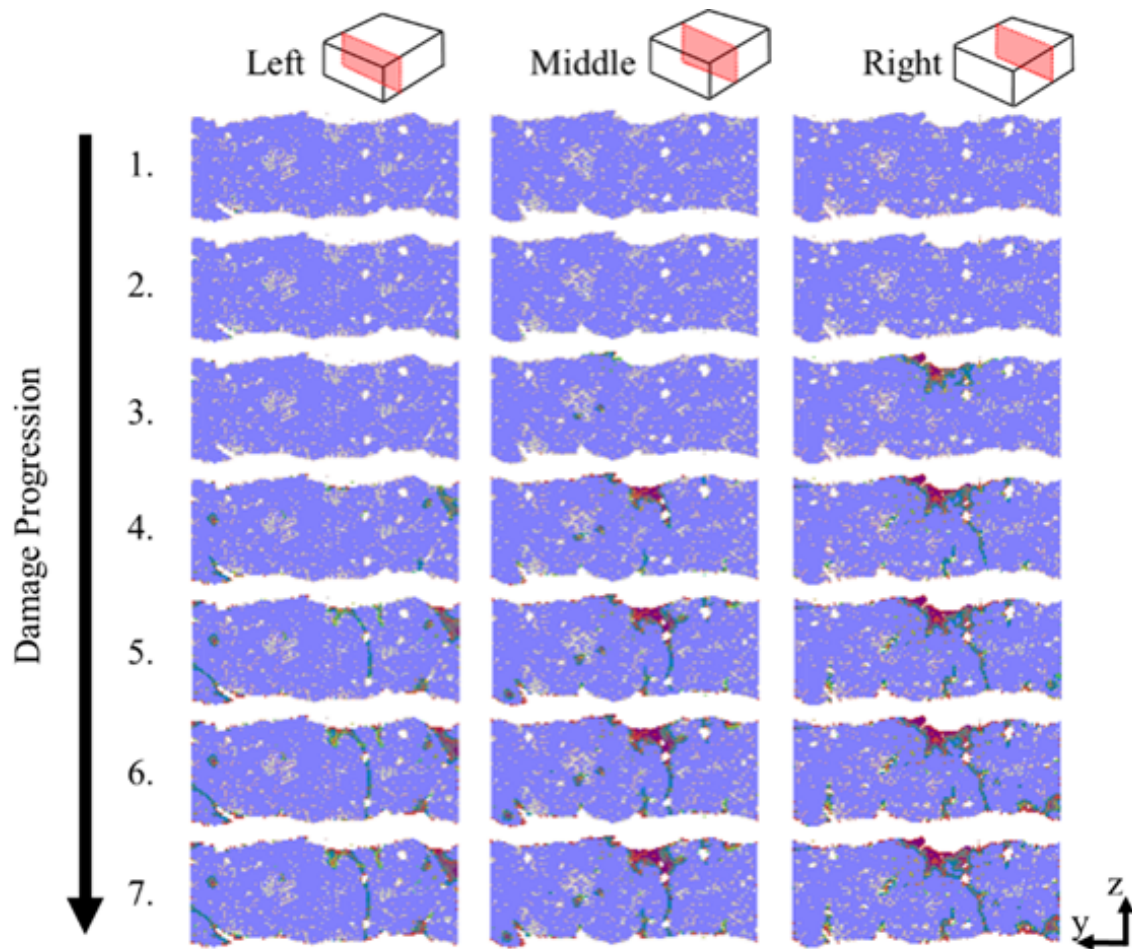


Figure 3-32: Damage initiation for cell 4 at different YZ planes.

3.5 Synthetic Microstructure Reconstruction

For the final aspect of this work, a methodology is presented for creating synthetic microstructures that are structurally similar to the experimental sample. Such reconstruction can provide insight into the structural features that heavily influence the mechanical response. Recall the characterization work presented in Section 3.3. The microstructure descriptors presented in this portion of the dissertation will be used heavily in the remaining sections.

Probability Density Functions

Synthetic reconstruction is accomplished through the representation of the microstructure as a series of probability density functions (PDFs). Using the statistical information from the characterized x-ray CT images, a PDF was created using Equation (3.23)

$$p(x) = \frac{1}{\sqrt{2\pi\sigma^2}} \exp^{-\frac{(x-\mu)^2}{2\sigma^2}} \quad (3.23)$$

where x is the statistic of interest, σ the standard deviation of the statistical set, and μ the mean. This PDF was then randomly sampled to generate a synthetic structure. Figure 3.33 shows an example of the types of PDFs generated. This example utilizes the cluster statistics gathered in Section 3.3.4.

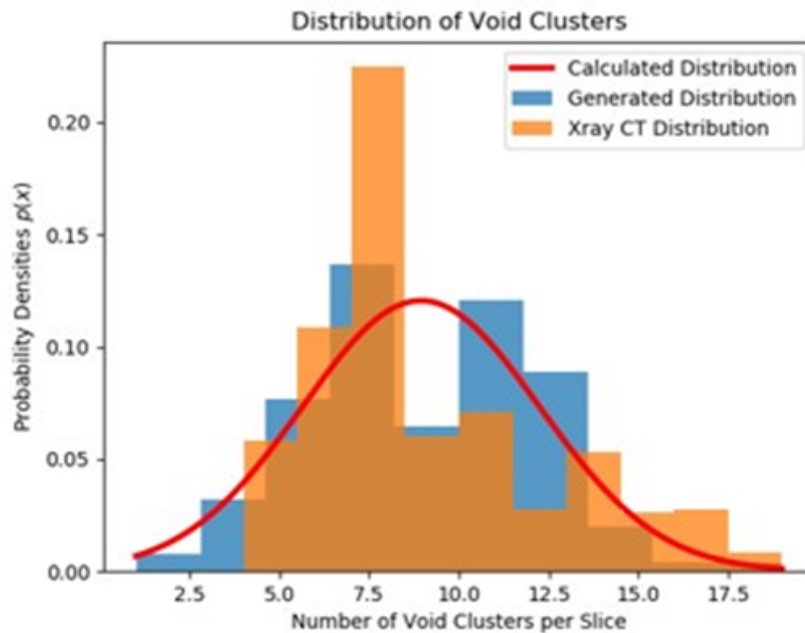


Figure 3-33: Example of PDF generation and comparison with sampled statistics for synthetic reconstruction.

In Figure 3-33, the orange histogram shows the distribution obtained directly from the x-ray CT data, the red curve shows the calculated PDF of this data, and the blue histogram shows a randomly generated distribution obtained by sampling the red PDF. It should, of course, be noted that probability is at play in the sampling of the red curve; the blue distribution will change with each realization of the microstructure. Meanwhile, the red and orange distributions come directly from the x-ray CT data and therefore are fixed.

A PDF can be generated for each microstructure descriptor and is summarized in functional form through Figure 3-34. The left column shows the statistics associated with the resin material such as the (a) resin fraction, (c) number of resin clusters per unit area, and (e) the average size of the resin clusters with the unit being the number of material points. The right column shows the same types of statistics though associated with void regions. The PDFs of (Figure 3-34) can be used to create each of the 2D slices of the structure as shown in Figure 3-35. As shown, the PDFs can be used to replace the x-ray CT information from Figure 3-8.

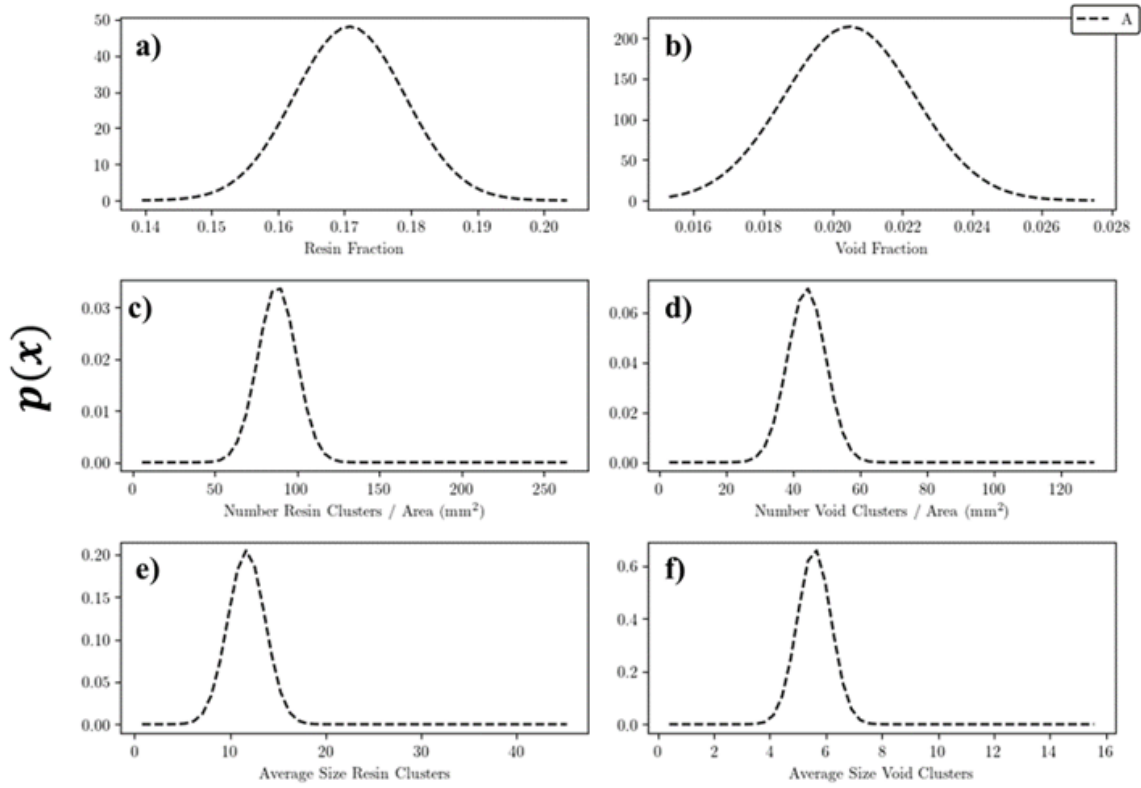


Figure 3-34: Probability density functions for each microstructural descriptor.

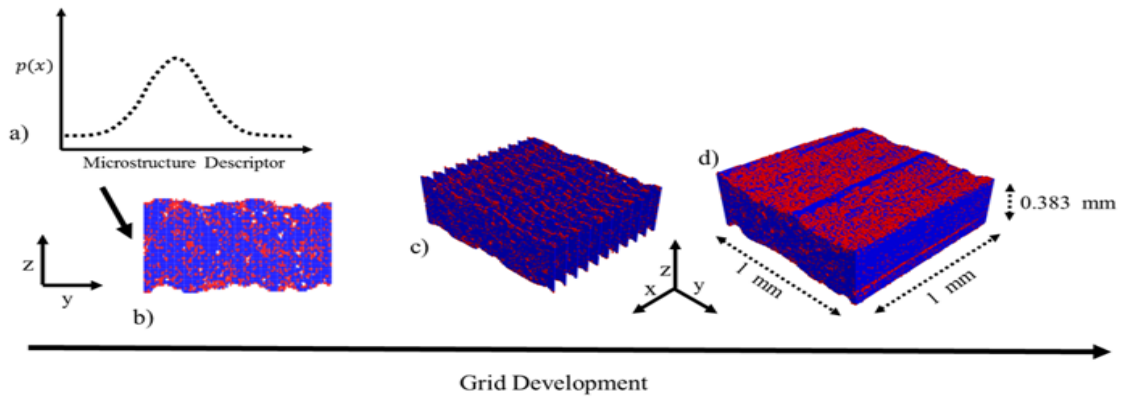


Figure 3-35: PD grid development using PDFs.

Synthetic Generation Procedure

Figure 3-36 shows a procedure for constructing a synthetic microstructure from the PDFs. A uniform rectangular cross-section for the slice is first created, Figure 3-36 (a). In Figure

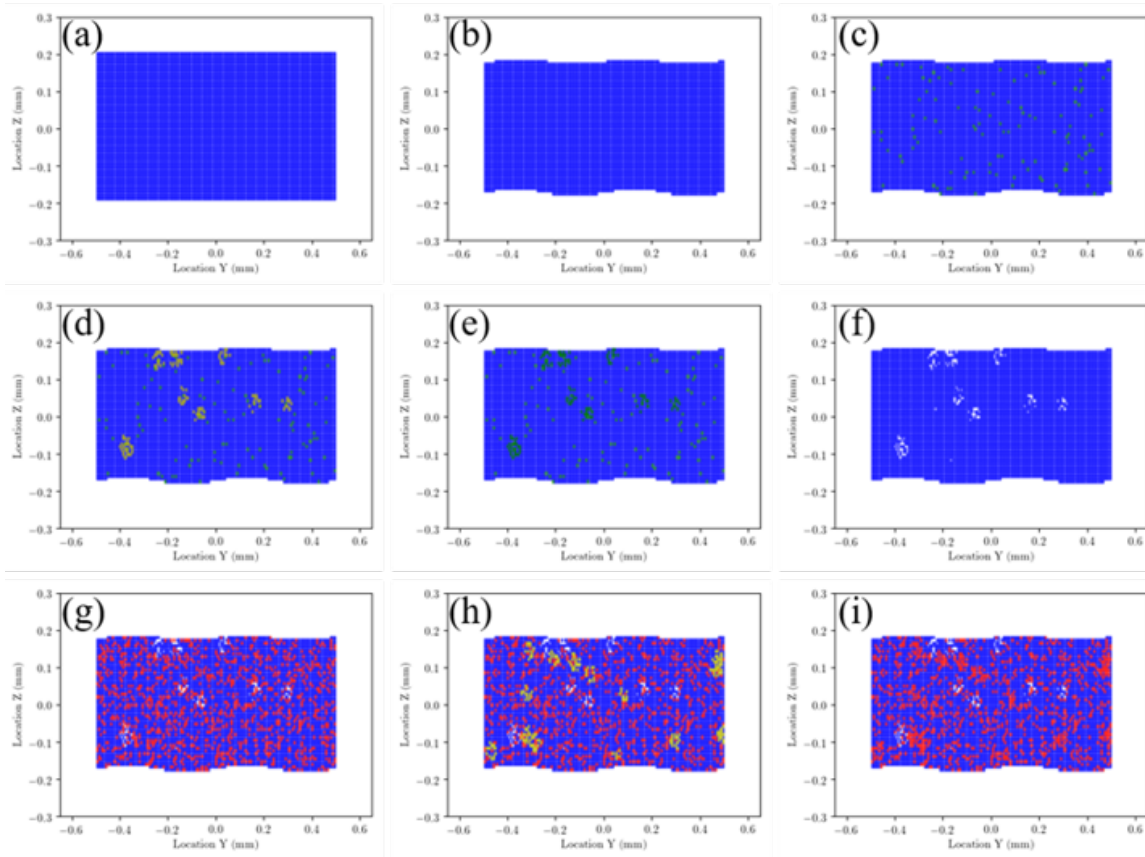


Figure 3-36: Synthetic reconstruction process.

3-36 (b), the surface undulation obtained from the microstructure characterization is applied to the top and bottom of the slice.

Next, utilizing the previously generated PDFs, isolated voids and void clusters are introduced into the domain, Figs. 3-36 (c) and 3-36 (d), respectively. The increase in the void fraction that occurs after introducing the void clusters is accounted for by converting a portion of the seeded voids back into material, Figure 3-36 (e). The void/void cluster configuration is finalized as shown in Figure 3-36 (f). In a similar manner, isolated resin material points (Figure 3-36 (g)) and resin clusters are introduced (Figure 3-36 (h)) into the slice. The fully reconstructed slice is then obtained by matching the resin volume fraction as shown in Figure 3-36 (i).

The methodology of introducing resin/void clusters into a reconstructed cell is outlined

in Table 3.4. The initial step is to seed the fraction onto the slice. If the void clusters are under consideration, then material points are removed in order to match the void fraction. Alternatively, if resin clusters are under consideration, then the material association is modified to match the resin volume fraction. Based on the statistics found from the DBSCAN algorithm, such as the number of clusters and the size of the clusters, a point is chosen as a nucleation site. The cluster is then grown from this nucleation site and allowed to grow with an arbitrary shape until the desired cluster size is reached. Finally, material points are added back to the model to match the void fraction and assigned yarn/resin material association to match the mass fraction. Figure 3-37 demonstrates the resin clustering procedure on a particular slice. The leftmost image, Figure 3-37 (a), shows the initially seeded resin volume fraction. This image shows a resin mass fraction with little resin clustering. In the middle image, Figure 3-37 (b), clusters are introduced and are shown by the yellow voxels. Finally, Figure 3-37 (c) shows the final step of ensuring mass fraction with resin clusters themselves. In this step, points are converted from resin association to yarn association to ensure that the resin clusters do not artificially increase the mass fraction on the slice. A very similar methodology was used to introduce void clusters into the cell.

Table 3.4: Incorporation of clusters into the model

Cluster Implementation Procedure	
1	Randomly seed to match resin/void fraction
2	Choose material point locations to nucleate clusters
3	Adjust association of points to match resin/void fraction
4	Repeat for each slice

To nucleate the clusters into the model, first an approximate area of the cluster C_A was calculated as shown in Equation (3.24), where N_A is the number of points in the cluster, and Δx is the size of the void in the x and y directions.

$$C_A = N_A \Delta x^2 \quad (3.24)$$

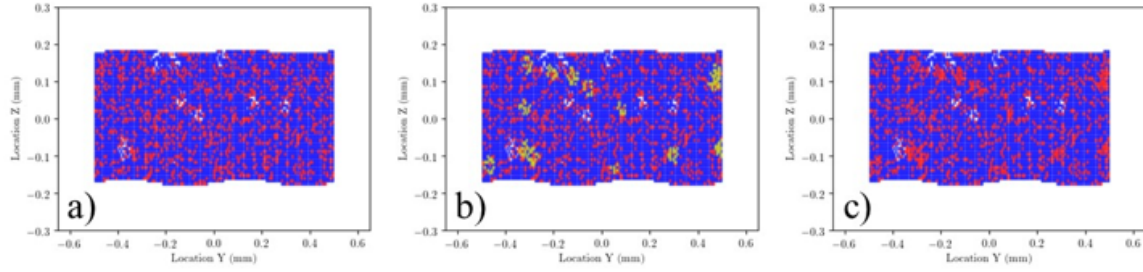


Figure 3-37: Demonstration of cluster implementation.

An approximate radius of the cluster was calculated following Equation (3.25).

$$r_A = \sqrt{\frac{C_A}{\pi}} \quad (3.25)$$

To account for the truncated size of the cluster arising from the thresholding process, the approximate radius of the cluster was increased by 2 times the grid spacing as seen in Equation (3.26).

$$r_B = r_A + 2\Delta x \quad (3.26)$$

Finally, the number of points to add for the cluster is increased proportionally as shown in Equation (3.27).

$$N_B = \frac{N_A}{r_A} r_B \quad (3.27)$$

Additionally, the x-ray CT displayed continuity of the voids through the length of the specimen, which is the yarn direction. In order to mimic this characteristic of the microstructure, the location of the point chosen to nucleate is kept constant for each slice along the length of the composite. However, the shape and size of the void are allowed to vary.

The advantage of representing the microstructure as a series of PDFs is that each PDF can be systematically explored and evaluated. Each microstructure descriptor can be independently modified through its PDF. Figure 3-38 shows an example of such artificial modification of the PDFs. In this example, the original PDFs are shown in black and a new statistical scenario is shown using red circular scatter points. The only difference between

the two scenarios is the size of the average resin clusters (Figure 3-38 (e)). For this particular PDF, the average of the size of the resin clusters μ is doubled between scenarios while the standard deviation σ is kept constant. This parameter change in the PDF ultimately manifests as a curve shift to the right that maintains the same shape.

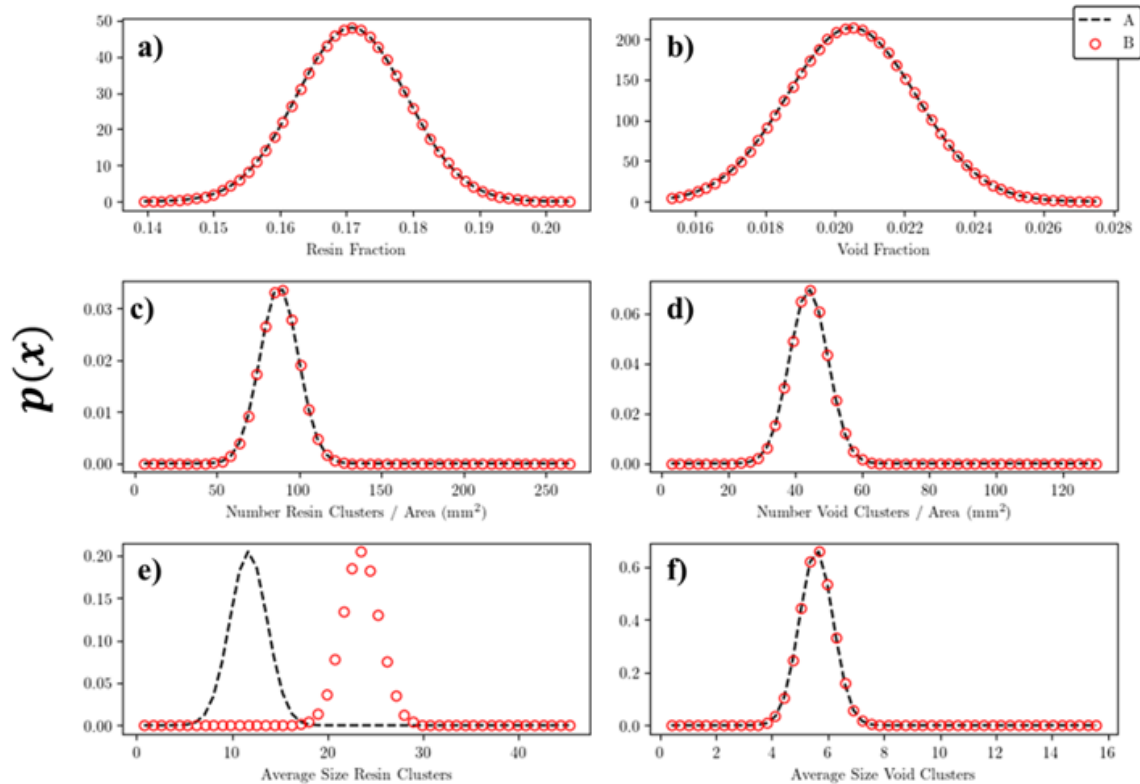


Figure 3-38: Comparison of the original PDFs (A) and modified PDFs (B).

The reconstruction of the microstructure with the new PDF will produce an entirely unique structure that reflects the shift in the PDF. Figure 3-39 compares the first slice of each of the different scenarios. In Figure 3-39 (b), the average size of the resin clusters has doubled. Because the resin fraction has not changed, there are fewer isolated number of resin material points. These points have become a part of the clusters themselves. Additionally, because the PDF associated with the number of resin clusters per unit area has not changed, the number of resin clusters are similar between the two structures (i.e. only their size has changed).

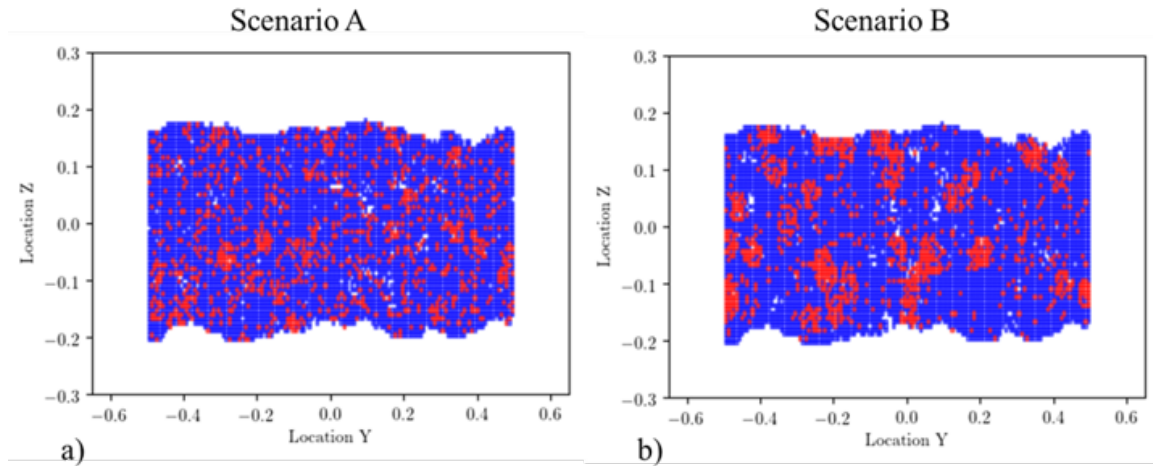


Figure 3-39: Visualization of PDF modification and the resulting microstructure on a 2D slice.

In this work, eight different simulations were considered to explore the influence of each microstructure descriptor. A description of each simulation is provided in Table 3.5. In each scenario, the mean of the PDF μ was modified. Figure 3-40 provides a visualization of these parameter modifications.

Table 3.5: Summary of simulations performed to explore the structure.

Scenario	Description of Microstructure Modification
x-ray	Simulation grid obtained directly from x-ray CT
A	Original synthetic realization
B	Double the mean resin cluster size per unit area
C	Double the mean void cluster size per unit area
D	Double the mean number of resin clusters per slice
E	Double the mean number of void clusters per slice
F	Double the mean resin fraction per slice
G	Double the mean void fraction per slice

Figure 3-40 (a) shows the variation in the number of material points for each of the microstructures. The size of the simulation domain remains constant between each scenario

and as a result, the total number of material points is very similar. Scenarios A-E do not change the resin fractions and have very similar number of yarn and resin material points. Scenario F doubles the resin fraction average in the PDF and as a result, the number of yarn material points decrease and the number of resin material points increase. One of the major modifications to the microstructure is the average size of the resin and void clusters. These statistics are compared in Figure 3-40 (b). The size of the resin clusters are dramatically increased in scenario B and the size of the void clusters are increased in scenario C. Figure 3-40 (c) compares the average resin and void fraction for the microstructures. As expected, these remain constant until scenarios F and G. The final comparison is the number of resin and void clusters Figure 3-40 (d). In scenario D, the number of resin clusters is doubled and in scenario E, the number of void clusters are doubled.

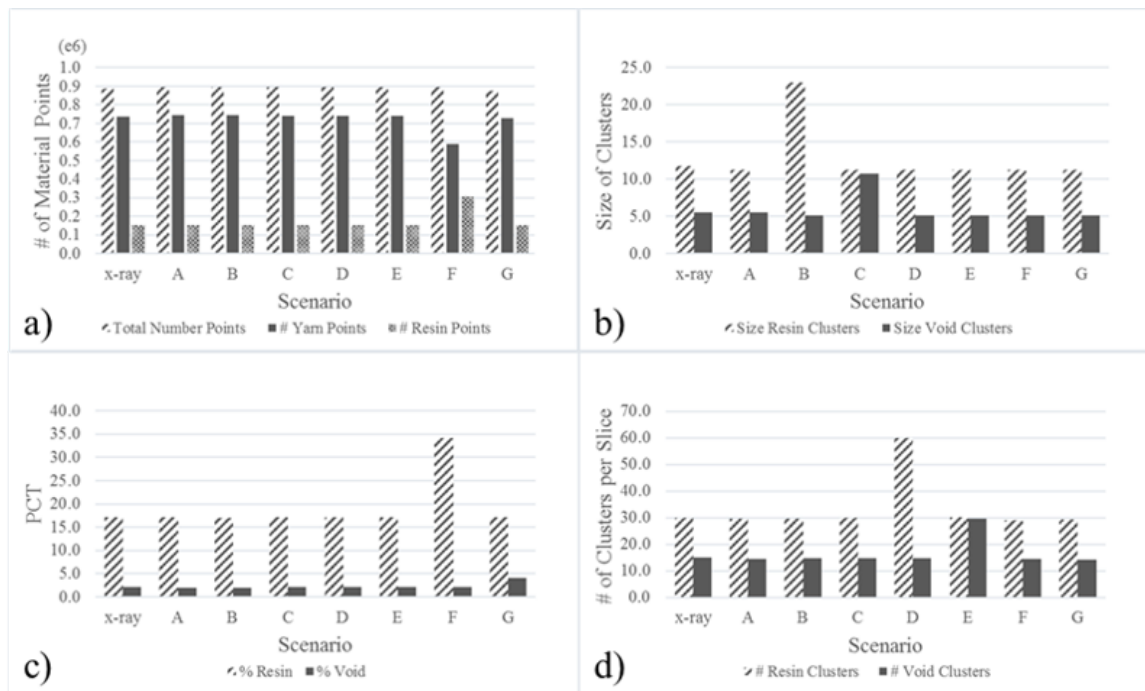


Figure 3-40: Visualization of microstructure descriptors for each simulation scenario.

Figure 3-41 is provided to help visualize each of these modifications and their influence on the actual microstructure. The top left image labeled x-ray CT shows the microstructure

obtained directly from the x-ray CT data. The top-right image, A, displays the PDF generated structure using the statistics obtained from the x-ray CT data. These two structures are statistically equivalent according to the current microstructure descriptors and only differ in the manner in which they were created. The leftmost column (B, D, and F) shows the modifications to the PDFs associated with resin material and the rightmost column (C, E, and G) shows the modifications to the PDFs associated with voids. It is important to note that this is only a single slice of the structure and is intended only to help visualize the changes in the structures. A 3D simulation domain is obtained following the grid development procedure explained through Figure 3-35 and Figure 3-36. Additionally, only a single realization of the structure was created for each scenario. Multiple realizations can be made that still match the overall statistics of the PDFs. In future work, additional realizations will be considered to learn more about the significance and establish bounds.

A total of eight simulations were completed each with a distinct microstructure (Figure 3-41). Peridynamic load steps were performed at 0.7, 1.3, 1.4, 1.5, 1.6, 1.7, 1.8, and 1.9% strain intervals. After applying the displacement to the boundary regions, equilibrium was found using a dynamic relaxation routine. The solution was then allowed to fail progressively until no further damage accumulated. Engineering stress was found by monitoring the internal force in the middle of the specimen. The specimen was considered to fail if the measured internal force dropped to 0.

Figure 3-42 provides an overview of damage in each of the different microstructure scenarios. Each material point in the model is colored on a scale between 0 (blue) and 1 (red). A damage value of 1 indicates that all of the interactions for that material point have failed. An isometric orientation of the specimen Figure 3-42 (a) and a sectioned view Figure 3-42 (b) are provided to visualize both the external and internal damage of the specimens. Each panel shows the damage at the final failure strain. For reference, the failure strain for each scenario is provided at the bottom of each panel.

As shown, the x-ray CT scenario has more damage on the surface than the other microstructures. One possible explanation for this difference is that the x-ray CT generated

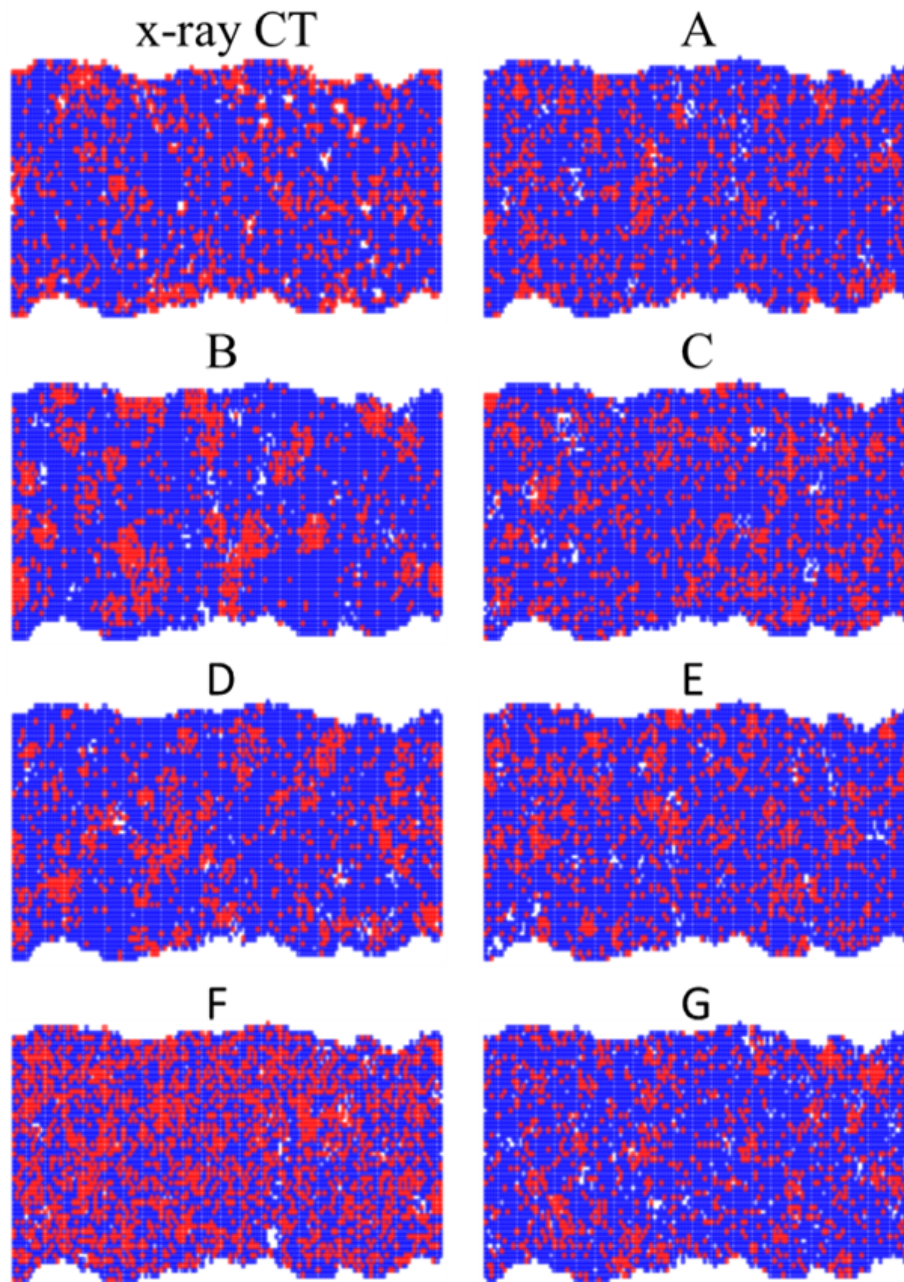


Figure 3-41: Visualization of microstructure modifications on 2D PD slices.

microstructure has more resin material points on the surface. There are two different damage features for the x-ray CT scenario. The first is damage that occurs transverse to the loading direction near the right boundary region. The second damage pattern is in the longitudinal yarn direction and spans the entire length of the specimen. Both damage pat-

terns exist through the thickness of the specimen and indicate complete separation of the material.

Unlike the x-ray CT scenario, most of the realizations exhibit damage that extends along the transverse direction of the composite but does not have much extension in the longitudinal direction. Scenarios D and E are an exception to this, as they have damage that extends longitudinally originating from the left side of the specimen. These two scenarios have an increase in the number of resin/void clusters and have a higher failure strain as compared to the other scenarios.

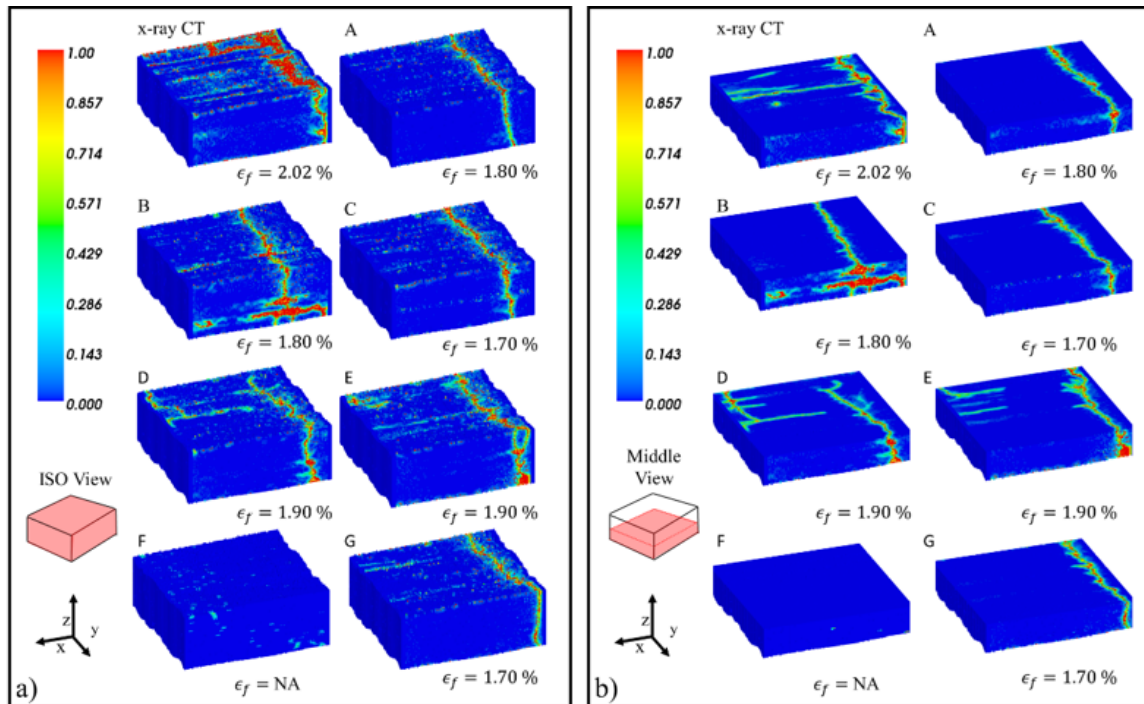


Figure 3-42: Overview of the final damage contours for each microstructure scenario.

Figure 3-43 shows the stress vs. strain curves for each of the artificially modified PDF scenarios compared against scenario A. The synthetically generated structures match well with the experimental stress/strain curves except that they underpredict the strain to failure. The lowest failure strain in the models was 1.70% while the experimental sample failed at just over 2% strain. The stress vs. strain curves for scenarios A-E Figure 3-43 (a-

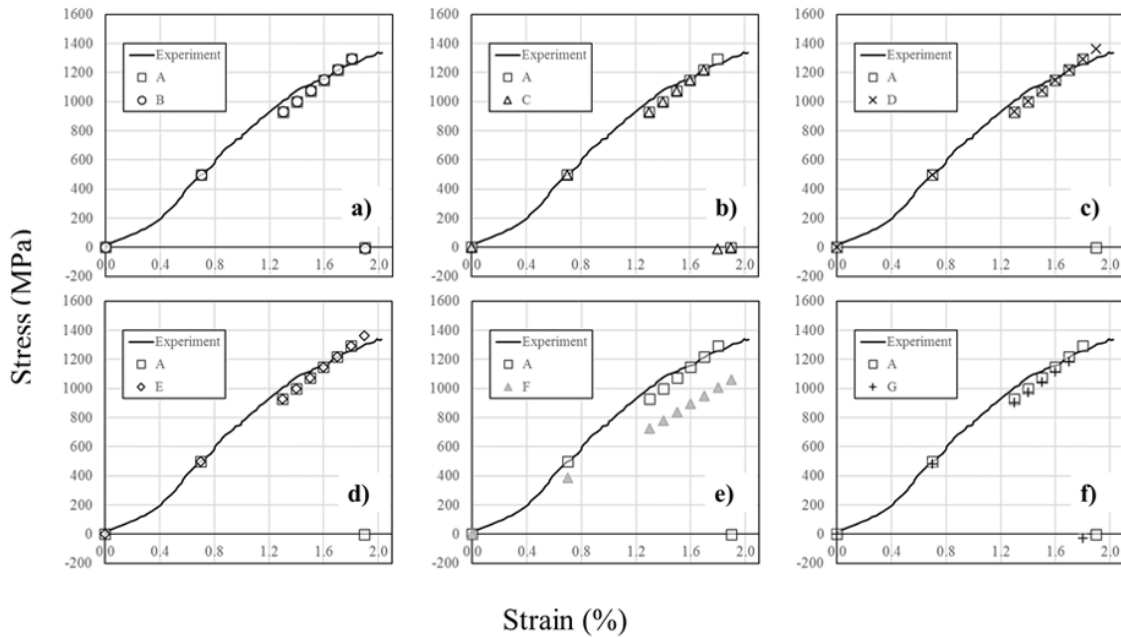


Figure 3-43: Stress vs. strain curves for each simulation scenario compared against the original PDFs (scenario A).

d) are nearly identical except for their failure strains. The similarity in stiffness is most likely a result of the total number of material points and the distribution of yarn/resin being nearly equal for these cases Figure 3-40 (a). Alternatively, in scenario F the average resin fraction was doubled and the number of resin material points was increased. This produced a composite with a lower stiffness and a composite that did not fail at the final simulation load step as observed in Figure 3-43 (e). Similarly, the stiffness of scenario G (Figure 3-43 (f)) drops as the total number of material points decreases with an increase in the void fraction. However, in this scenario, the specimen failed at a failure strain of 1.70%.

Chapter 4

Conclusions and Future Work

This dissertation is intended to provide the community with a systematic approach for using PD theory to predict the material response in polymer matrix composite systems. Two completely different types of composites were explored: carbon fiber and carbon nanotube yarn. For CFRP composite systems, a laminate based approach was systematically verified and validated. The developed approach was used to explore the damage mechanisms induced by low-velocity impact. While the core of the PD approach remained the same for the CNT yarn reinforced composites, actual x-ray CT data was used to develop the simulation domain. This process of using x-ray CT data and synthetic reconstruction is not limited to PD theory and can be used in a multitude of modeling approaches. The remainder of this dissertation reiterates the work that was performed for each composite system and provides some guidance into the direction of future work.

CFRP Conclusions

In this work, a direct numerical approach was developed for the calculation of nonlocal PD material constants with an explicit representation of fiber and matrix material regions. The approach was demonstrated by simulating uniaxial tension tests on a IM7/8552 composite system and compared against the experimental results of [37]. The versatility and advantage of the developed approach was demonstrated by modifying the discretization of the system. The approach was extended to include nonlinear constitutive relationships by reformulating as an optimization problem. Both a Ramberg-Osgood and a hyperbolic nonlinear constitutive relationship were demonstrated at various off-axis orientations and found to be in good agreement with experimental and analytical results. A method for re-

lating nonlocal stretch rate to strain rate was developed which enabled strain rate dependent constitutive responses to be simulated. A 45° off-axis dynamic tension test was simulated to validate the PD strain rate formulation developed.

Four different low-velocity impact energy levels were simulated and compared against the provided experimental results at 150, 187.5, 225, and 262.5 in-lbf. All of the PD simulations compared well with the experimentally observed force vs. time, force vs. displacement, and energy vs. time behaviors. Simulations predicted circular damage regions with delamination extents within the experimental bounds. The model was found to be particularly sensitive to fiber bond failure and a 10 % decrease in the longitudinal failure strength showed a significant load drop in the force vs. time curve similar to the experiments. The legacy PD approach, with calibrated PD elastic and strength constants, tended to overpredict both impact peak force and impact duration while underpredicting the peak displacement. Using the numerical approach led to a more accurate peak force and impact duration, however, still overpredicted the initial slope of the force vs. time curve. Adding shear nonlinearity decreased the initial slope of the force vs. time and force vs. displacement curves and overall made the most significant contribution in improving the experimental vs. simulation comparison.

A preliminary hat-stiffened panel model was developed and used to simulate a 150 in-lbf impact on the outer mold line. While computationally expensive, the initial response appears promising. Additionally, a through-thickness reinforcement approach was developed to simulate stitched composites. While the initial results did not show an improvement in the resistance to delamination, the model development provided further avenues of exploration.

CFRP Future Work

Future work should consider exploring the relationship between the intra- and interlaminar nonlocal horizon values. Because of the intricate experimental relationship between intra- and interlaminar failure mechanisms, the extent of these PD horizons may affect the predicted interaction. Additionally, an investigation of fiber bond failure sensitivity should

be conducted. The PD work in this project revealed that the interlaminar shear behavior has a profound influence on the bending near the impactor, which in turn affects the impact force and impact duration. The current approach uses the intralaminar Ramberg-Osgood as a starting point and extracts PD material parameters of a linear-flat response for the interlaminar shear bonds. A material model for interlaminar shear bonds that is based on experiments directly focusing on the interlaminar shear deformation would further improve the current approach. Additionally, experimental observation of the influence of interlaminar shear on the bending response (e.g., 3D DIC) would add to the knowledge base.

CNT Conclusions

This work describes the development of a method for accurately predicting the deformation and failure of CNT yarn polymer composites using PD theory. The heterogeneity of the microstructure and the resulting anisotropic behavior were accommodated within the PD framework by using explicitly defined bond types for CNT yarn and polymer resin. Additionally, an off-axis modulus function following a Gaussian variation has been utilized to account for CNT bundles that are not aligned with the major yarn direction. A number of PD models were generated using new techniques for processing x-ray CT reconstructions.

Characterization of the x-ray CT data was extended by constructing probability density functions for yarn, resin, and void materials within each slice. Further, the DBSCAN algorithm was employed to detect shape, size, and quantity of resin and void clusters. This additional characterization effort provided information needed to generate synthetic PD models that share the characteristics of the x-ray CT-based models, qualitatively and quantitatively. Tension test simulations of CNT yarn polymer composites were performed using the generated PD models.

The following conclusions are drawn:

- X-ray CT-based heterogeneous peridynamic model simulations capture the experimentally observed stress vs. strain response as well as the failure strain with good agreement

- Results reveal that the damage is most prevalent on the exposed surfaces and primarily aligned with the yarn direction, which is consistent with the experiment
- Sharp gradients on the surface provide preferential sites for failure initiation
- Clusters of resin and voids facilitate failure propagation
- Synthetically-generated heterogeneous peridynamic model simulations also capture the stress vs. strain response. The failure morphology shows damage aligned with the yarn direction
- The surface damage in synthetic models is not as pronounced as that seen in the x-ray CT-based models

CNT Future Work

There are two main differences between the x-ray CT-based and synthetically generated PD models: (1) the x-ray CT-based model, and thus the actual specimen, has a higher concentration of resin at the exposed surfaces and (2) the x-ray CT data indicates continuity of void and resin clusters along the yarn direction, which was not captured in the synthetic models. These differences lead to the discrepancy between the failure morphologies predicted. Although the specimen level stress vs. strain response and failure strain are both predicted with good agreement, in order to effectively utilize the synthetic models for exploration of the design space to maximize stiffness and strength, the synthetic models need to more closely represent the actual microstructural characteristics. The continuity of clustering could be influential in fully capturing the material response. With this in mind, future work should consider incorporating the continuity of clusters into the synthetic microstructure realizations. Additionally, because the generation process is inherently stochastic, multiple realizations at each structural modification should be created. Finally, only a normally distributed PDF was used in this work. To fully capture the inherent stochasticity of the structure, future work should consider alternative PDFs to fully explore both microstructure and model sensitivities.

Bibliography

- [1] Autar K. Kaw. *Mechanics of composite materials*. CRC press, 2005.
- [2] Philip E. Irving and Costas Soutis. *Polymer composites in the aerospace industry*. Woodhead Publishing, 2019.
- [3] Adrian P. Mouritz. *Introduction to aerospace materials*. Elsevier, 2012.
- [4] Markus G. R. Sause. *In situ monitoring of fiber-reinforced composites: theory, basic concepts, methods, and applications*. Springer, 2016.
- [5] Michael F. L. De Volder, Sameh H. Tawfick, Ray H. Baughman, and A. John Hart. Carbon nanotubes: present and future commercial applications. *Science*, 339(6119): 535–539, 2013.
- [6] Jae-Woo Kim, Godfrey Sauti, Russell A. Wincheski, Roberto J. Cano, Benjamin D. Jensen, Joseph G. Smith, Kristopher E. Wise, and Emilie J. Siochi. Unidirectional carbon nanotube yarn/polymer composites. *NASA/TM-2018-220081*, 2018.
- [7] A. Jumahat, C. Soutis, F. R. Jones, and A. Hodzic. Fracture mechanisms and failure analysis of carbon fibre/toughened epoxy composites subjected to compressive loading. *Composite Structures*, 92(2):295–305, 2010.
- [8] P. Berbinau, C. Soutis, and I. A. Guz. Compressive failure of 0° unidirectional carbon-fibre-reinforced plastic (cfRP) laminates by fibre microbuckling. *Composites Science and Technology*, 59(9):1451–1455, 1999.
- [9] M. O. W. Richardson and M. J. Wisheart. Review of low-velocity impact properties of composite materials. *Composites Part A: Applied Science and Manufacturing*, 27(12):1123–1131, 1996.
- [10] Weicheng Cui and M. R. Wisnom. A combined stress-based and fracture-mechanics-based model for predicting delamination in composites. *Composites*, 24(6):467–474, 1993.
- [11] Amar C. Garg and Yiu-Wing Mai. Failure mechanisms in toughened epoxy resins - a review. *Composites Science and Technology*, 31(3):179–223, 1988.
- [12] G. A. O. Davies and R. Olsson. Impact on composite structures. *The Aeronautical Journal*, 108(1089):541–563, 2004.

- [13] Markus Sause. *Identification of failure mechanisms in hybrid materials utilizing pattern recognition techniques applied to acoustic emission signals*. PhD thesis, University of Augsburg, 2010.
- [14] Helmut Schürmann. *Konstruieren mit faser-kunststoff-verbunden*. Springer, 2005.
- [15] Yani Zhang, Lianxi Zheng, Gengzhi Sun, Zhaoyao Zhan, and Kin Liao. Failure mechanisms of carbon nanotube fibers under different strain rates. *Carbon*, 50(8):2887–2893, 2012.
- [16] G. T. Camacho and M. Ortiz. Computational modelling of impact damage in brittle materials. *International Journal of Solids and Structures*, 33(20-22):2899–2938, 1996.
- [17] T. Belytschko and T. Black. Elastic crack growth in finite elements with minimal remeshing. *International Journal for Numerical Methods in Engineering*, 45:601–620, 1999.
- [18] Ted Belytschko, Hao Chen, Jingxiao Xu, and Goangseup Zi. Dynamic crack propagation based on loss of hyperbolicity and a new discontinuous enrichment. *International Journal for Numerical Methods in Engineering*, 58:1873–1905, 2003.
- [19] Shreyas Suryakant Joglekar. *Modeling and simulation strategies for thickness reinforced composites*. PhD thesis, North Carolina State University, 2017.
- [20] Vipul Ranatunga and Stephen B. Clay. Cohesive modeling of damage growth in z-pinned laminates under mode-I loading. *Journal of Composite Materials*, 47(26):3269–3283, 2012.
- [21] S. A. Silling. Reformulation of elasticity theory for discontinuities and long-range forces. *Journal of the Mechanics and Physics of Solids*, 48(1):175–209, 2000.
- [22] Erdogan Madenci and Erkan Oterkus. *Peridynamic theory and its applications*. Springer, 2014.
- [23] Ebrahim Askari, Jifeng Xu, and Stewart Silling. Peridynamic analysis of damage and failure in composites. In *44th AIAA aerospace sciences meeting and exhibit, Reno, NV*, 2006.
- [24] Wenke Hu, Youn Doh Ha, and Florin Bobaru. Modeling dynamic fracture and damage in a fiber-reinforced composite lamina with peridynamics. *Journal for Multiscale Computational Engineering*, 9(6):707–726, 2011.
- [25] Erkan Oterkus and Erdogan Madenci. Peridynamic analysis of fiber-reinforced composite materials. *Journal of Mechanics of Materials and Structures*, 7(1):45–84, 2012.

- [26] Erkan Oterkus, Erdogan Madenci, Olaf Weckner, Stewart Silling, Philip Bogert, and Alexander Tessler. Combined finite element and peridynamic analyses for predicting failure in a stiffened composite curved panel with a central slot. *Composite Structures*, 94(3):839–850, 2012.
- [27] B. Kilic, A. Agwai, and E. Madenci. Peridynamic theory for progressive damage prediction in center-cracked composite laminates. *Composite Structures*, 90(2):141–151, 2009.
- [28] Y. L. Hu, N. V. De Carvalho, and E. Madenci. Peridynamic modeling of delamination growth in composite laminates. *Composite Structures*, 132:610–620, 2015.
- [29] Olaf Weckner, Abe Askari, Jifeng Xu, Hamid Razi, and Stewart Silling. Damage and failure analysis based on peridynamics-theory and applications. In *48th AIAA/ASME/ASCE/AHS/ASC Structures, Structural Dynamics, and Materials Conference*, 2007.
- [30] Yi-le Hu, Yin Yu, and Hai Wang. Peridynamic analytical method for progressive damage in notched composite laminates. *Composite Structures*, 108:801–810, 2014.
- [31] Jifeng Xu, Abe Askari, Olaf Weckner, and Stewart Silling. Peridynamic analysis of impact damage in composite laminates. *Journal of Aerospace Engineering*, 21(3), 2008.
- [32] S. A. Silling and R. B. Lehoucq. Peridynamic theory of solid mechanics. *Advances in Applied Mechanics*, 44:73–168, 2010.
- [33] S. A. Silling, M. Epton, O. Weckner, J. Xu, and E. Askari. Peridynamic states and constitutive modeling. *Journal of Elasticity*, 88(2):151–184, 2007.
- [34] Walter Herbert Gerstle. *Introduction to practical peridynamics: computational solid mechanics without stress and strain*, volume 1. World Scientific Publishing Company, 2015.
- [35] S. A. Silling and E. Askari. A meshfree method based on the peridynamic model of solid mechanics. *Computers & Structures*, 83:1526–1535, 2005.
- [36] Mark Flores, David Mollenhauer, Vipul Runatunga, Timothy Beberniss, Daniel Rapping, and Mark Pankow. High-speed 3d digital image correlation of low-velocity impacts on composite plates. *Composites Part B: Engineering*, 131:153–164, 2017.
- [37] Imran Hyder, Joseph Schaefer, Brian Justusson, Steve Wanthal, Frank Leone, and Cheryl Rose. Assessment of intralaminar progressive damage and failure analysis methods using an efficient evaluation framework. In *Proceedings of the American Society for Composites: Thirty-Second Technical Conference*, 2017.

- [38] Steven Wantha, Joseph Schaefer, Brian Justusson, Imran Hyder, Stephen Engelstad, and Cheryl Rose. Verification and validation process for progressive damage and failure analysis methods in the nasa advanced composites consortium. In *Proceedings of the American Society for Composites: Thirty-Second Technical Conference*, 2017.
- [39] Hamid Razi, Joseph Schaefer, Steven Wantha, Jordan Handler, Gary Renieri, and Brian Justusson. Rapid integration of new analysis methods in production. In *Proceedings of the American Society for Composites: Thirty-First Technical Conference*, 2016.
- [40] Forrest Baber, Vipul Ranatunga, and Ibrahim Guven. Peridynamic modeling of low-velocity impact damage in laminated composites reinforced with z-pins. *Journal of Composite Materials*, 52(25):3491–3508, 2018.
- [41] Kyle Colavito. *Peridynamics for failure and residual strength prediction of fiber-reinforced composites*. PhD thesis, The University of Arizona, 2013.
- [42] Autar K. Bucciarelli, Louis L. *Engineering mechanics for structures*. Dover Publications, 2009.
- [43] Travis A. Bogetti, Christopher P. R. Hoppel, Vasyl M. Harik, James F. Newill, and Bruce P. Burns. Predicting the nonlinear response and progressive failure of composite laminates. *Composites Science and Technology*, 64(3-4):329–342, 2004.
- [44] B. Kilic and E. Madenci. An adaptive dynamic relaxation method for quasi-static simulations using the peridynamic theory. *Theoretical and Applied Fracture Mechanics*, 53(3):194–204, 2010.
- [45] I. M. Daniel, B. T. Werner, and J. S. Fenner. Strain-rate-dependent failure criteria for composites. *Composites Science and Technology*, 71(3):357–364, 2011.
- [46] Marc Monthieux and V. L. Kuznetsov. Who should be given the credit for the discovery of carbon nanotubes? *Carbon*, 44:1621–1623, 2006.
- [47] M. M. J. Treacy, T. W. Ebbesen, and J. M. Gibson. Exceptionally high young's modulus observed for individual carbon nanotubes. *Nature*, 381, 1996.
- [48] Eric W. Wong, Paul E. Sheehan, and Charles M. Lieber. Nanobeam mechanics: elasticity, strength, and toughness of nanorods and nanotubes. *Science*, 277:1971–1975, 1997.
- [49] Rodney S. Ruoff, Dong Qian, and Wing Kam Liu. Mechanical properties of carbon nanotubes: theoretical predictions and experimental measurements. *Comptes Rendus Physique*, 4(9):993–1008, 2003.

- [50] Min-Feng Yu, Oleg Lourie, Mark J. Dyer, Katerina Moloni, Thomas F. Kelly, and Rodney S. Ruoff. Strength and breaking mechanism of multiwalled carbon nanotubes under tensile load. *Science*, 287:637–640, 2000.
- [51] Jae-Woo Kim, Godfrey Sauti, Roberto J. Cano, Russell A. Wincheski, James G. Ratcliffe, Michael Czabaj, Nathaniel W. Gardner, and Emilie J. Siochi. Assessment of carbon nanotube yarns as reinforcement for composite overwrapped pressure vessels. *Composites Part A: Applied Science and Manufacturing*, 84:256–265, 2016.
- [52] Florin Bobaru, Youn Doh Ha, and Wenke Hu. Damage progression from impact in layered glass modeled with peridynamics. *Central European Journal of Engineering*, 2(4):551–561, 2012.
- [53] Youn Doh Ha and Florin Bobaru. Studies of dynamic crack propagation and crack branching with peridynamics. *International Journal of Fracture*, 162(1-2):229–244, 2010.
- [54] Dennj De Meo, Ning Zhu, and Erkan Oterkus. Peridynamic modeling of granular fracture in polycrystalline materials. *Journal of Engineering Materials and Technology*, 138(4), 2016.
- [55] Florin Bobaru and Stewart A. Silling. Peridynamic 3d models of nanofiber networks and carbon nanotube-reinforced composites. In *AIP Conference Proceedings*, volume 712, pages 1565–1570, 2004.
- [56] R. Rahman and J. T. Foster. Bridging the length scales through nonlocal hierarchical multiscale modeling scheme. *Computational Materials Science*, 92:401–415, 2014.
- [57] J. Decklever and P. Spanos. Nanocomposite material properties estimation and fracture analysis via peridynamics and monte carlo simulation. *Probabilistic Engineering Mechanics*, 44:77–88, 2016.
- [58] Caroline A. Schneider, Wayne S. Rasband, and Kevin W. Eliceiri. Nih image to imagej: 25 years of image analysis. *Nature Methods*, 9(7):671–675, 2012.
- [59] Pascal Getreuer. Linear methods for image interpolation. *Image Processing On Line*, 1:238–259, 2011.
- [60] Fredrik Lundh, M. Ellis, et al. Python imaging library (pil), 2012.
- [61] Fabian Pedregosa, Gaël Varoquaux, Alexandre Gramfort, Vincent Michel, Bertrand Thirion, Olivier Grisel, Mathieu Blondel, Peter Prettenhofer, Ron Weiss, Vincent Dubourg, Jake Vanderplas, Alexandre Passos, and David Cournapeau. Scikit-learn: machine learning in python. *Journal of Machine Learning Research*, 12:2825–2830, 2011.

- [62] Martin Ester, Hans-Peter Kriegel, Jörg Sander, and Xiaowei Xu. A density-based algorithm for discovering clusters in large spatial databases with noise. In *KDD-96*, pages 226–231, 1996.